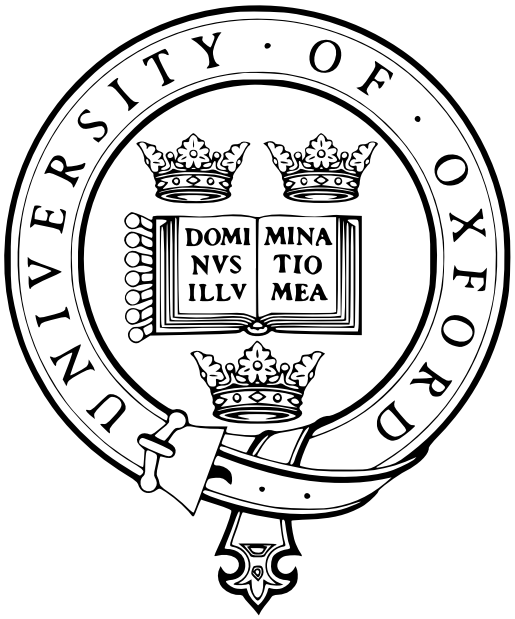

Motility Induced Phase Separation: Numerical and Experimental Approaches towards the High Péclet Regime

Lachlan C. Alexander

Christ Church
University of Oxford

Supervisor: Prof. Dirk G. A. L. Aarts

A thesis submitted for the degree of
Doctor of Philosophy

11/01/2022

Abstract

Active particles, those able to self-propel, have been shown to phase separate if they interact via a repulsive interaction [1, 2]. This is called motility-induced phase separation or MIPS. It was initially observed in systems of bacteria [3] but, as is often the case in the study of active matter, many have gone on to examine the phenomena in numerical simulations [2] and in theory [4]. Although active Brownian dynamics simulations, the numerical approach of choice when it comes to active particles, are decently understood and have been used extensively [1, 2, 5, 6], there remain issues related to the stiffness of interaction potentials in certain conditions [2, 5]. By nature, experimental systems can often be difficult to create let alone extend into a whole phase diagram [7, 8]. In this work, we tackle issues to do with MIPS both in simulation and experiment. We show how by using an empirically derived interaction, we are able to extend the Péclet/density phase diagram and discover that MIPS is hindered when the persistence length of particle trajectories are large. When no rotational coupling is included in simulation, particles are able to escape clusters with no resistance after they have rotated. The crystallinity of the dense phase locking particles in place couples with an imbalance of particle orientations from the random nature with which particles join a cluster to create the rotation.

Experimentally, we show that induced-charge electrophoretic particles are excellent for tunable phase separating active systems. We manipulate the conditions of our system such that we control the velocity and interaction of our particles. We show that an experimental phase diagram is possible and similar to simulated ones. Cluster dynamics also play an important role in the phenomena we observe experimentally. We add dipolar interactions in our simulations to show that we recover experimental behaviours when particles align. We foresee that this work could be a much needed bridging point between active matter in simulation and experiment whilst also providing multiple directions to advance the field further in both cases. Our interaction potential can be used to create simulated systems with strong attractions between particles. The experimental conditions we use can be a starting point for creating more complex systems by changing electric field frequency or particle size for example.

Declaration

This thesis is submitted for the degree of Doctor of Philosophy in Physical and Theoretical Chemistry at the University of Oxford. No part of this thesis has been accepted or is currently being submitted for any degree, diploma, certificate or other qualification in this University or elsewhere. This thesis is wholly my own work, except where indicated.

Contents

Abstract **i**

Declaration **iii**

1 Introduction **1**

1.1 Soft Matter and Colloidal Particles 1

1.2 Active Particles and Active Matter 2

1.2.1 Experimental Active Particles 4

1.2.2 Simulated Active Matter 6

1.2.3 Motility-Induced Phase Separation 7

1.3 Scope of the Thesis 8

2 Optimising Brownian Dynamics Simulations of Hard Disks **11**

2.1 Introduction 12

2.1.1 The Grand Ensemble, Canonical Ensemble and Pairwise Interactions . . . 12

2.1.2 Hard Interactions 14

2.1.3 Simulations of Hard Disks 21

2.2 Methods 24

2.2.1 A Scaled Contact Potential 24

2.2.2 Brownian Dynamics Simulations 28

2.2.3 Monte Carlo Simulations of Disks 29

2.2.4 Pair Distribution Function 29

2.2.5 Measuring a Pair Potential 30
2.2.6 Calculating Mean Squared Displacement 31
2.3 Results 32
2.3.1 Comparisons of Pair Distribution Functions 32
2.3.2 Comparisons of Mean Squared Displacements 36
2.4 Summary and Conclusions 37

3 Motility-Induced Phase Separation at High Péclet Numbers 39

3.1 Introduction 40
3.1.1 Ballistic Motion 40
3.1.2 A Theory of Motility-Induced Phase Separation 42
3.1.3 Feedback Mechanism Description 49
3.1.4 A Kinetic Approach to Determining the Transition 50
3.1.5 Spinodal Decomposition vs Nucleation and Growth 51
3.1.6 Characterising MIPS and Related Phenomena 53
3.2 Methods 58
3.2.1 Delauney Triangulation and Voronoi Tessellation 61
3.2.2 Static Structure Factor 62
3.2.3 Bond-Orientational Order Parameter 62
3.2.4 Polar Order Parameter 64
3.2.5 MIPS Development Parameter 64
3.2.6 Cluster Identification and Tracking 65
3.2.7 Determination of Cluster Torque and Rotation 69
3.2.8 Creating Sticky Disks 71
3.3 Results 72
3.3.1 Comparing MIPS with Different Potentials 72
3.3.2 Properties of MIPS via the SCP method at usual Péclet Numbers 75

3.3.3 Dynamics in MIPS at High Péclet Numbers . . . 84
3.3.4 Adding Rotational Friction into the System . . . 94
3.4 Summary and Conclusions . . . 99
3.5 Appendix . . . 102

4 Motility-Induced Phase Separation: Experiments of Phase Separating Active Particles 103

4.1 Introduction . . . 104
4.1.1 Colloidal Interactions . . . 104
4.1.2 Motility-Induced Phase separation in Experiment . . . 107
4.1.3 Induced-Charge Electrophoretic Particles . . . 110
4.2 Experimental Methods . . . 119
4.2.1 Experimental Setup . . . 119
4.2.2 Reflection Microscopy . . . 121
4.2.3 Particle Detection . . . 122
4.3 Results . . . 123
4.3.1 Péclet Number vs Density Phase Diagram in Experiment . . . 123
4.3.2 Dynamics of Clusters . . . 135
4.4 Summary and Conclusions . . . 140

5 Active Brownian Dynamics Simulations with Additional Interactions 143

5.1 Introduction . . . 144
5.2 Methods . . . 145
5.2.1 Quadrupolar Interactions between Spheres . . . 145
5.2.2 Maintaining Velocities by a Modification of the SCP Method . . . 146
5.3 Results . . . 147
5.3.1 Head to Tail Attraction . . . 147
5.3.2 Predator Prey Interactions . . . 151

5.3.3 Altering the SCP Method by Collision Angle 152

5.4 Summary and Conclusions 153

Summary, Conclusions and Outlook **155**

Bibliography **161**

Acknowledgements **179**

Chapter 1

Introduction

1.1 Soft Matter and Colloidal Particles

For matter to be considered soft, it needs to be deformable under the effect of weak forces. These are normally on the scale of those created by thermal fluctuations. Energies in these types of systems are measured in terms of k_BT, where k_B is the Boltzmann constant [1] and T is the absolute temperature. Alongside the forces and energies, the particles or components which form these systems also have characteristic length-scales and are typically smaller than 10 µm. Being so small and common, these particles are the building blocks for a lot of matter. Therefore, having an understanding of the dynamics and interactions of atoms (∼1 Å), molecules (∼1 nm) and colloidal particles (∼1 µm) is crucial to the study and development of new materials [9, 10].

Atoms and molecules are very difficult to probe due to their size and the fact that the timescales of their motions are typically under 1 ns. To directly observe them, one must use complex set ups which often involve X-rays, neutron scattering or atomic force microscopy [11, 12]. However, a practical solution arose in the beginning of the 20th century based on the observations of those such as Jean Perrin and Albert Einstein, which then became the foundation of the field of soft condensed matter [13, 14]. Colloidal particles, those on the larger side of the soft matter family, defined as solid particles suspended in a molecular fluid phase, were found to behave as scaled up versions of atoms (as seen in the structures in figure 1.1). Therefore, one can expand on the knowledge of soft matter as a whole by creating controlled systems of colloids.

[1] $k_B = 1.380\,648\,52 \times 10^{-23}\,\mathrm{m^2\,kg\,s^{-2}\,K^{-1}}$.

The typical length-scales of colloids are larger than the wavelength of visible light and the time-scales of their motion are slower than the typical sensitivity of human vision (∼60 Hz [15]), allowing for them to be observed using simple optical microscopy.

The study of soft matter grew to encompass many types of systems including gels [16], interfaces [17] and liquid crystals [18] whilst also becoming embedded in industry [19]. The advancements in our understanding of colloidal particles have shown that their interactions and dynamics remain central to extrapolating properties of systems as a whole.

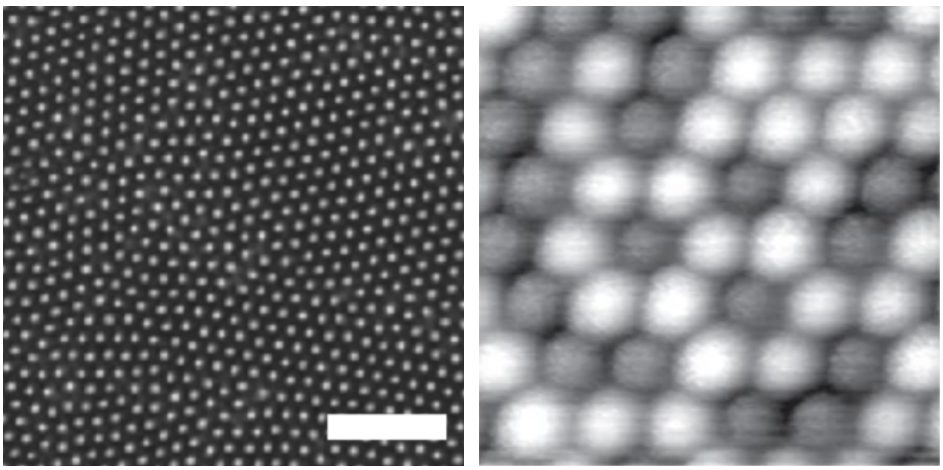

(a) **(b)**

Figure 1.1: Similar crystalline structures of colloidal and atomic systems. (a) A bright field microscopy image of a colloidal polycrystalline monolayer of melamine-formaldehyde spheres. The scale bar represents 20 µm. From the work of Lavergne *et al.* [20]. (b) Topographic image of a surface alloy composed by Si, Sn and Pb atoms blended in equal proportions on a Si(111) substrate. Image dimensions are 4.3 nm by 4.3 nm. From the work of Sugimoto *et al.* [12].

1.2 Active Particles and Active Matter

An active particle is defined to be one which consumes energy to create localised directed motion [21]. Finlayson and Scriven were the first to postulate that novel mechanisms could arise from the spontaneous conversion of internal energy to kinetic energy and that these mechanisms could be linked to phenomena at the cellular level [22]. The study of active particles had previously been confined to microbiology, which then had been classed simply as the study of microswimmers [23]. The development of the physics of active motion into a specific field of research was yet to occur.

The study of materials which include active particles, otherwise known as active matter, arose

from the incorporation of active particles into the field of soft matter. This happened because the most common and practical examples of motile particles exist on the colloidal length scale. The interest in this field was driven by the creation of simple models which could describe self-propelled systems at many scales and was not, like many other aspects of research, initially motivated by the desire to explain experimental phenomena [24–26]. However, in contrast to the typical approaches used to generate an understanding of soft matter systems, where physics is characterised by equilibrium dynamics [27], active matter requires novel approaches because the conversion of internal energy into kinetic energy necessarily removes systems out of equilibrium [28, 29].

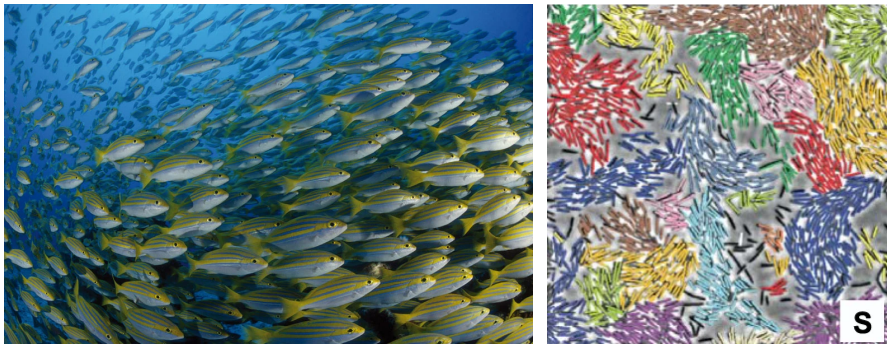

(a) **(b)**

Figure 1.2: Examples of biological swimmers. (a) A shoal of blue-striped snappers. Taken from the work of Conradt [30]. (b) Snapshots of monolayer bacterial swarms with different aspect ratios and densities, representative of motile phases. From the work of Be'er *et al.* [31].

Active matter became an interdisciplinary field due to an increase in attention after the late 1990s. The principles of self-propulsion and the resulting mechanisms reached into the domains of robotics [32], social transport in traffic and crowds [33], biomedicine when looking at nano-motors [34], biology (such as understanding foraging) [35] and finally statistical physics in the quantitative studies of collective motion [36]. Systems which were able to exhibit collective effects became centrepieces in the field. Experimental examples include the motions of flocks of birds, shoals of fish (figure 1.2 (a)) and dense samples of bacteria (figure 1.2 (b)), whilst numerical phenomena include the "Viscek model" (figure 1.3), motility-induced phase separation and many others [1, 36–38].

The use of active matter research may stem or be motivated by from one of three perspectives [4]. The first, as with all research, is to expand the current knowledge. Unlike many other types of research, active matter provides us with one of the few avenues to investigate non-equilibrium systems and create new branches of physics. The second, a more far-fetched idea, is that of being

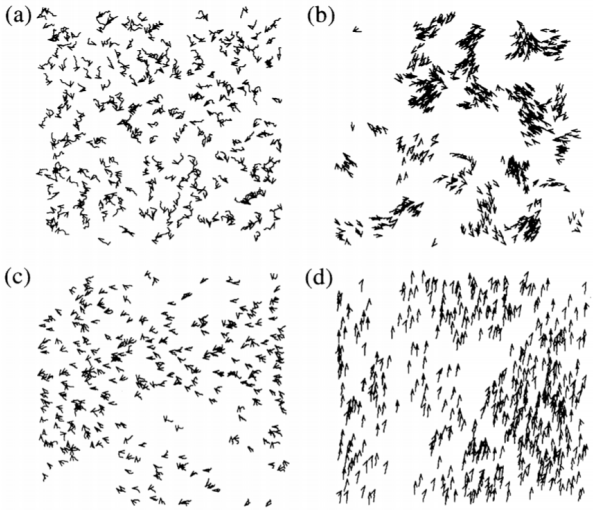

Figure 1.3: Collective dynamics in the Vicsek model. Snapshots of simulations. (a) A dilute system with large noise shows no correlations. (b) For small densities and noise the particles tend to form groups moving coherently in random directions. (c) After some time at higher densities and noise the particles move randomly with some correlation. (d) For higher densities and small noise the motion becomes ordered. From the work of Vicsek *et al.* [37].

able to create smart materials, such as an alternative to liquid crystal displays, or targeted drug delivery systems. The final approach, the one which will most likely have the most value in the short term, is that of understanding natural phenomena with a strong focus on those created by microswimmers, such as the formation of biofilms which pose a constant threat in the form of infections, contamination and antibiotic resistance [39]. The study of microswimmers remains the largest sector of active matter science as they are very common and efficient whilst playing a large role in medicine, sewage treatment and other key aspects of human life [40]. Because of its importance, its safety and its simplicity, the study of active matter at the colloidal length scale has become fully integrated in physical and biophysical research sectors [41–43]. However, one of the challenges in active matter remains the creation of functional experimental systems and representative simulations [44].

1.2.1 Experimental Active Particles

Experimental systems often suffer from common faults, all of which revolve around the concept of control parameters. Many synthetic examples consume fuel inefficiently preventing the creation of dense systems. This promotes the use of biological systems in experiment, such as flagellated bacteria, which have been optimised for active motion by evolution [44]. We will discuss examples of common active systems in this section.

Biological Systems

Biological active matter spans many orders of magnitude in length scales. The smallest examples are systems driven by proteins, such as intracellular motor proteins [45]. Active matter also encompasses behaviours on the level of the organism such as flocks of birds or shoals of fish (figure 1.2 (a)) [46]. Many of these, however, require more complex models to describe them. As a consequence, the largest component of active matter study which is based in biology is the study of microswimmers (figure 1.2 (b)) [44]. Not only are they simpler to model, they also benefit from being within the colloidal domain which facilitates manipulation, production and the simultaneous observation of large numbers of swimmers [40, 44, 45].

Synthetic Particles

Despite the advances in genetic manipulation, which enables selective tuning of biological examples of active particles, we are still limited in how far these changes can go. This is where synthetic active particles come into the picture. Only limited by synthesis techniques, synthetic particles in theory could provide us with simpler experimental systems than biological ones.

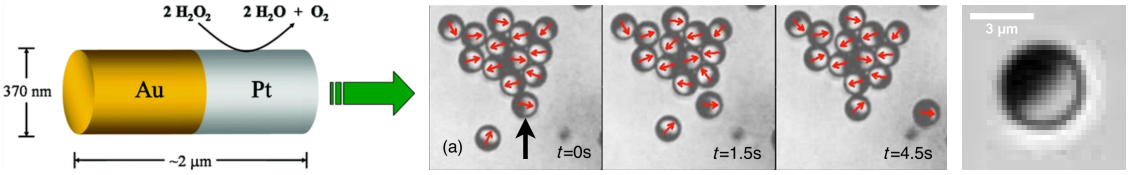

Figure 1.4: Examples of typical active Janus particles. (a) A scheme of a diffusiophoretic Janus rod. Taken from the work of Paxton *et al.* [47]. (b) Consecutive close-ups of a cluster of diffusiophoretic Janus particles. Adapted from the work of Buttinoni *et al.* [48]. (c) A picture of an electrophoretic Janus particle used in this work (4.28 µm silica bead with 35 nm titanium and an additional 15 nm silica coated on one side).

There already exists a diverse portfolio of synthetic particles in the literature. Janus particles, which have two sides with different chemical or physical properties [49], are the most common examples. They can be propelled by various mechanisms including diffusiophoresis (figure 1.4 (a) and (b)) [50, 51], thermophoresis [8, 52], Quincke rotation [53–55] and induced-charge electrophoresis (figure 1.4 (c))) [7, 56, 57]. These examples are the most common as they perform the best in experiment with each system having advantages and disadvantages. Each active system requires a fuel and the diffusiophoretic hydrogen peroxide system cannot be active indefinitely and slows down as fuel is used. On the other hand thermophoretic active systems can have unwanted flows and do not function well in dense phases.

Despite advances in the creation of particles, it is still common to use biological entities. They are efficient and directly relevant to phenomena we wish to unravel. However, they are not always fully controllable and often bring unwanted biological issues which complicate experiments from a physical perspective. Another option is to go in the opposite direction and make use of the ever expanding availability of computational power to create numerical simulations where interactions can be explicitly defined and tuned.

1.2.2 Simulated Active Matter

Simulations are based on many theoretical descriptions of motion [58]. The most common modes of locomotion used in simulation are "Run and Tumble Particles" (RTP) and "Active Brownian Particles" (ABP) as seen in figure 1.5. The first is based on the motion of flagellated bacteria, who periodically change their orientation to favour moving up concentration gradients of nutrients [59]. The second is based on colloidal swimmers. On top of a classical description of motion, where the dissipative nature of drag in a suspension balances out the thermal noise of motion of a particle, otherwise known as Brownian motion, a constant and active force is added to all particles [60].

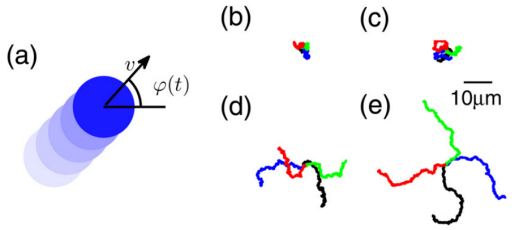

Figure 1.5: Active Brownian particles in two dimensions. (a) An active Brownian particle is characterized by an orientation along which it propels itself with speed v while it undergoes Brownian motion in both its position and orientation. Trajectories of active particles are shown at right for (b) $v = 0\mu ms^{-1}$, (c) $v = 1\mu ms^{-1}$, (d) $v = 2\mu ms^{-1}$, and (e) $v = 3\mu ms^{-1}$, all with zero angular velocity. With increasing v, the particles move longer distances before the direction of their motion is randomized; four different $10s$ trajectories are shown for each velocity. From the work of Volpe *et al.* [60].

Through simulation many phenomena have been investigated. The motion of active particles near boundaries [61], the effect of particle shape [62–64], coupling with attractive [65] and repulsive interactions [1] and the effect of orientation correlations [37, 38]. Simulations form a large section of active matter research because it is often easier to create virtual systems than experimental ones. Chapters 2 and 3 cover simulations of particles in more depth.

1.2.3 Motility-Induced Phase Separation

Many active matter systems either interact with complex environments or have intricate interactions between the active particles themselves; namely in systems of animals whose sentience has obvious complexity. Collective behaviour and other phenomenologies are uniquely attributable to the interaction of activity with other simple particle interactions. A crucial advancement in the explanation of collective motion, driven by observations of flocking and shoals of fish, was the Vicsek model [37]. The Vicsek model, which created polar steady states from large numbers of locally aligning particles, became a landmark model in simulated active matter.

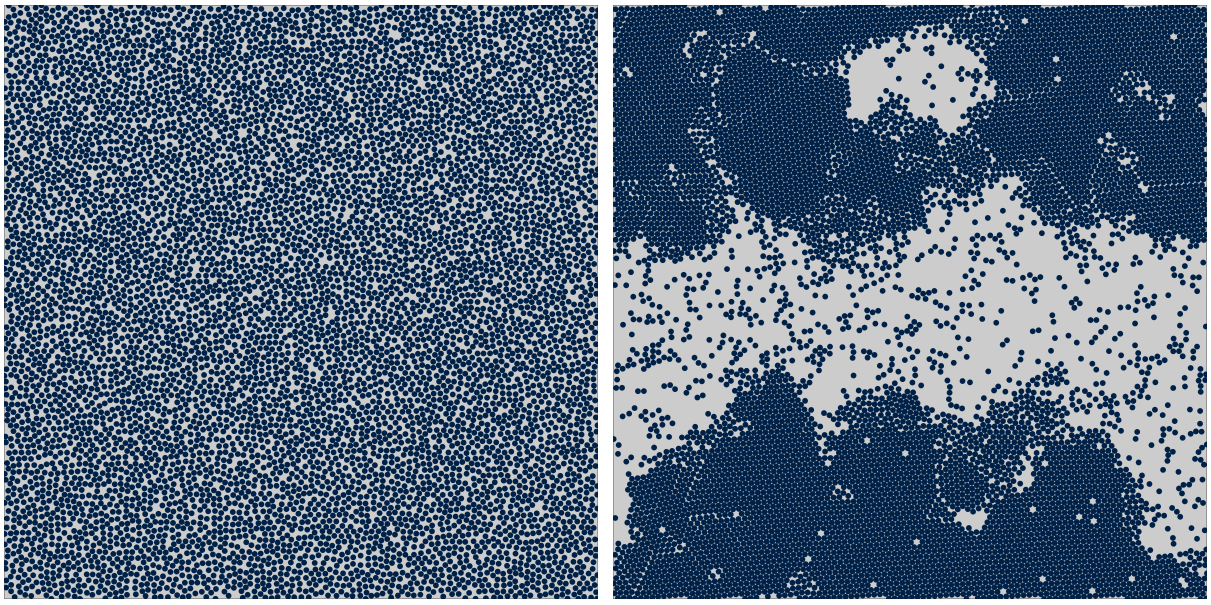

(a) **(b)**

Figure 1.6: An example of Motility-Induced Phase Separation. (a) An initial configuration of particles before the onset of activity. (b) A phase separated system in the steady state with a dense and a dilute region. (More information on this topic can be found in chapter 3).

One of the simplest interactions is a short range and repulsive one due to links with many real and experimental systems which use electrostatic repulsion and excluded volumes [66]. Self-propelled particles with purely repulsive interactions lead to systems which can phase separate at relatively low densities (figure 1.6) [1, 5, 67–69]. Phase separations in passive systems are usually attributed to either attractive interactions, such as depletion, or high densities, making such systems perfect examples of the novelty of phenomena created by active systems.

"Motility-Induced Phase Separation" (MIPS) is the name given to the creation of dense and dilute regions in a system of repulsive particles due to activity. It can be thought of as a traffic jam as the velocity of the particles in the system is linked to their local density. As particles

collide they are unable to overlap leading to their activities opposing each other and no net movement is achieved.

MIPS was first predicted numerically for systems of run and tumble particles [3]. This, as with a lot of active matter research, was inspired from the motility of bacterial microswimmers. Bacteria, such as *Bacillus subtilis* are able to behave collectively due to their excluded volume [70]. Along with the analogy, traffic jams and crowds can have similar properties to the dense phases of phase separated systems [71]. MIPS was then, from a coarse grained "thermodynamic" perspective, described by Tailleur and Cates who found that active particles accumulate when their velocities are reduced [3, 4, 72, 73]. A more detailed description of this theory is laid out in the introduction of chapter 3.

Repulsive ABPs have since been extensively studied in numerical simulations of systems which undergo MIPS [1,5,67–69,74–77]. Finally, it has also been shown that active particles can undergo phase separation in a variety of experimental systems [7, 48, 57, 78]. More information on MIPS in simulation and experiment can be found in chapters 3 and 4 respectively.

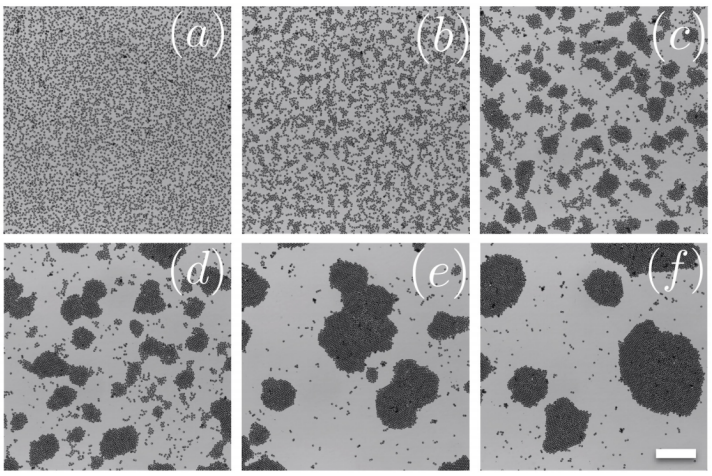

Figure 1.7: Aggregation kinetics in a system of induced-charge electrophoretic self-propelled Janus colloids. From (a) to (f): successive time steps ($t = 0.02, 0.4, 2, 5, 20$ and $68s$) following the onset of activity. The scale bar in (f) is 100 µm. From van der Linden *et al.* [7].

1.3 Scope of the Thesis

With common issues of creating experimental systems of active particles in mind, we set out with this work to optimise an experimental system of induced-charge electrophoretic Janus particles

to create motility induced phase separated systems [2]. With this system, we wanted to dissect each of the contributing factors to the motions of both the individual particles and their eventual dynamics in the phase separated state. For this we also develop a method of creating a hard interaction between particles which allows us to explore the effects of high particle velocities (compared to their Brownian motion) and attractive interactions. By providing a concrete method of simulating hard particles and a tunable experimental system, we aim to further bridge the gaps between MIPS in experiment, simulation and theory.

Chapter 2 introduces a new method of simulating systems of hard disks with Brownian dynamics simulations via a "Scalable Contact Potential" (SCP). We will begin with an overview of current theories and methods of creating simulated hard systems. Through comparison with other potentials used to mimic hard systems, which are commonplace in the literature on Brownian dynamics, we will determine its effectiveness. We will continue to use this method in simulating the particles in the subsequent chapters.

With our novel method of dealing with hard particle interactions in dynamical simulations, we will test its efficacy in active simulations in chapter 3. We will then create stable systems of active disks in all conditions using an appropriate scaling of the simulation time-step. We will move on to investigate hitherto unexplored regions of the MIPS phase diagram of hard disks; highlighting the effect of secondary phenomena in such systems on the phase diagram itself; and the stability of clusters. We will explain the phenomena from multiple angles in line with the current theories explaining MIPS. We will then test our results by introducing a friction interaction between the particles.

To extend our results from simulation, we will investigate the dynamics of an experimental system of induced-charge electrophoretic particles in chapter 4. We are able to control swimming velocity by tuning the frequency and magnitude of the AC electric field used to propel the particles and increase it to compare the system to our numerical results. Through a study of the linear and angular motions of the particles we will present a way of measuring the dynamics of particle motion and show its dependency on the parameters of the electric field. We will also present the dynamics of clusters of particles in experiment.

Finally, in chapter 5, we will show how our new method of dealing with particle interactions enables us to create systems with more complex particle interactions whilst keeping the

[2] More information can be found in chapter 4.

radius of our particles intact. The system of choice is that of hard disks each with electrostatic quadrupoles. We also investigate the effect of changing the interaction of particles to attempt to reduce the amount by which particle velocities reduce during collisions in an attempt to make motile clusters in line with experimental observations.

Chapter 2

Optimising Brownian Dynamics Simulations of Hard Disks

Abstract

We introduce a novel approach to simulating hard disks with Brownian dynamics. By considering the particle overlap created by the motion of the particles, we derive a potential which is scalable with the time-step used in simulations. By comparing it with currently widely used particle interactions and Monte Carlo algorithms, we are able to investigate how effective our methods are in approximating a discontinuous potential with a semi-continuous numerical method.

2.1 Introduction

This chapter contains the methodology and analysis for creating Brownian dynamics simulations of disks which we use throughout the thesis. After introducing the general physics involved in the structure and dynamics of two dimensional ensembles of monodisperse "hard" particles [1], we lay out, in detail, the way in which we have chosen to optimise hard particle interactions and how one can analyse such systems. We then move onto using these methods to study whether our novel method provides us with the expected results for a system of hard disks which move via Brownian motion.

Further details on the topics covered in the introduction of this chapter can be found in "Colloidal Dispersions" by Russel *et al.* [79], "Theory of Simple Liquids" by Hansen and McDonald [80] and "Computer simulation of liquids" by Allen and Tildelsley [81].

2.1.1 The Grand Ensemble, Canonical Ensemble and Pairwise Interactions

The grand ensemble is a description of an open system of particles with a marginally fluctuating number of particles N and mean energy E [80, 82]. Each microstate of a system, i.e. one of the possible states in which the system can be, can be explicitly defined by the position and momentum of all its particles. Such a description has commonly been used for colloidal systems because a single field of view, as seen under a microscope, follows the same rules [83].

Each microstate has a probability of occurring and an associated energy. This can be calculated from the probability density function (PDF) of said microstate for which N, the number of particle is fixed:

$$P(\vec{p}^N, \vec{r}^N; N) = \frac{1}{\Xi h^{sN}} exp\big(- \frac{1}{k_B T}(H_N(\vec{p}^N, \vec{r}^N)) - N\mu\big), \tag{2.1}$$

where $\vec{p}^N$ are all of the particle momenta, $\vec{r}^N$ all of the particle positions, Ξ a normalisation factor (the sum over all microstates), h the Planck constant, s the system dimensionality, $k_B T$ the thermal energy, H_N the Hamiltonian and μ the chemical potential. Systems where the number of particles is fixed are also known as the canonical ensemble [83].

[1] The concept of a hard particle is further described in section 2.1.2.

The probability density function can be reduced to a configurational PDF since the classical Hamiltonian is a sum of kinetic K_N and potential U_N energy:

$$H_N(\vec{p}^N, \vec{r}^N) = K_N(\vec{p}^N) + U_N(\vec{r}^N), \tag{2.2}$$

and

$$P_c(\vec{r}^N; N) = \frac{z^N}{\Xi} exp\big(- \frac{1}{k_B T} U_N(\vec{r}^N)\big), \tag{2.3}$$

where $z = \exp(\mu/k_B T)/\lambda_B^n$ is the reduced activity in n dimensions and $\lambda_B = \sqrt{h^2/2\pi m k_B T}$ is the de Broglie wavelength.

Therefore, to obtain a measurement of the energy of a system one must dissect the contributions to the potential energy of the system:

$$U_N(\vec{r}^N) = \sum_i u^{(1)}(\vec{r}_i) + \sum_i \sum_{j>i} u^{(2)}(\vec{r}_i, \vec{r}_j) + \sum_i \sum_{j>i} \sum_{k>j} u^{(3)}(\vec{r}_i, \vec{r}_j, \vec{r}_k) + ..., \tag{2.4}$$

where $u^{(1)}(\vec{r}_i)$ depends on the positions of individual particles, $u^{(2)}(\vec{r}_i, \vec{r}_j)$ depends on the positions of pairs of particles and $u^{(3)}(\vec{r}_i, \vec{r}_j, \vec{r}_k)$ depends on the positions of triples of particles etc.

The first term in equation 2.4, $u^{(1)}(\vec{r}_i)$, is only affected by external fields such as electric or magnetic ones. One can adjust the chemical potential of the system to give a desired particle number density such that this term can be ignored in uniform systems. The second term, $u^{(2)}(\vec{r}_i, \vec{r}_j)$ reflects the interactions between two isolated particles and is known as the pair potential. Terms after the pair potential are often ignored. Their contributions to the energy of the system are negligible except in a few cases [84].

Instead of using the individual particle positions to define a pair potential, it is often the case that defining a centre of mass, $\vec{R}_{ij} = (\vec{r}_i) + \vec{r}_j)/2$, and a relative position, $r_{ij} = \vec{r}_i - \vec{r}_j$, creates a more simplified approach; this being the case for particles with radially-symmetric interactions [2]. This results in a potential energy for a homogeneous system given by:

$$U_N(\vec{r}^N) = \sum_i \sum_{j>i} u^{(2)}(r_{ij}). \tag{2.5}$$

[2]Such as disks or spheres.

Despite in theory being able to know or measure the interaction potential, with optical traps for example [85–87], direct calculations of the properties of an equilibrated fluid using P_c can be troublesome. This is because the configuration space depends on all the particles and their degrees of freedom leading to burdensome calculations. Alternative approaches have therefore been developed such as molecular simulations.

2.1.2 Hard Interactions

The simplest system of particles is that of the perfect gas; particles have no volume and do not interact. Their dynamics are purely dependent on the thermal properties of the system [88]. It is only able to describe real systems when in the dilute limit, where particles rarely come into contact. Therefore, to describe the interactions of particles with volumes under a first approximation, the concept of the "hard" interaction developed. It is based on the idea that particles have volumes and cannot overlap. One can describe the interaction potential for disks or spheres using the following equation [89]:

$$U_H(r) = \begin{cases} \infty & r < \sigma, \\ 0 & r \geq \sigma \end{cases} \tag{2.6}$$

where r is the distance between two particles and σ is the diameter of the particles. This interaction, due to its simplicity and its resulting behaviours, is commonly used as a backbone for theoretical descriptions of real systems. Because particles interacting via a hard potential do not overlap, nor do they interact when apart, the free energy of a system of hard particles at equilibrium is only affected by entropy and kinetic energy. Transitions to more ordered states are possible due to the compensation of a loss in organisational entropy by increased translational motion [90].

Over the twentieth century, the idea of whether or not a system of spheres with only purely repulsive interactions, a three dimensional system of hard particles, could undergo a disorder-order transition was highly contentious [91–93]. It was only in 1968 that the first order liquid to crystal transition for hard spheres was convincingly determined by Hoover and Ree in their work using Monte Carlo simulations [3] [94]. The particles in a crystalline phase sit upon a regular

[3] The determination of energies or configurations of a system via a stochastic sampling procedure usually involving arithmetic or logical operations.

infinite lattice and relate to one another via bond orientations. A system can be characterised by the fluctuations from said lattice. In contrast to the crystalline phase, where both long range positional order and long range orientational order exist, order in the liquid phase decays exponentially as a function of distance [95].

Surprisingly, the phase behaviours of systems of hard disks, those confined to two dimensions, still remains unconfirmed [96–102]. Despite this, it is understood that in a two dimensional system, due to the relative larger significance of thermal fluctuations to the structure, a crystal cannot be formed. Instead they can form solids [103–105]. Solids are characterised by the decay of positional correlations as a power law which reaches zero at large distances. This is coined as "quasi-long-range" order. However, solids do maintain their orientational order [95].

There exists a third phase in the two dimensional case, the "hexatic" phase. In this case the positional order decays exponentially, like in the liquid phase, but its orientational order is quasi-long-range similar to the positional order in a solid. The hexatic phase has been recently shown to occur by Bernard and Krauth via Monte Carlo simulations [66, 101, 106].

The debate on the phase transition of hard disks has been between a first order transition between the liquid and solid states and the theory proposed Kosterlitz, Thouless, Halperin, Nelson and Young (KTHNY) [107–110]. In their work, which appeared in the early 1970s, they suggested a two step transition via the hexatic phase. The first of the transitions being a first order transition between the liquid and hexatic phase and the second a continuous second order transition between the hexatic and solid phases [66]. The liquid-hexatic transition has been determined to be from $\phi \approx 0.702$ to $\phi \approx 0.716$ [102].

Structure of Two Dimensional Hard Systems

It is often more useful to describe a system in terms of the probabilities of finding n particles at given positions instead of the configurational integral. This is because the former is an average over all configurations removing the need for explicitly determining the positions of all particles. They can be defined as:

$$\rho^{(n)}(\vec{r}^{n}) = \sum_{N=0}^{\infty} \frac{1}{N!}\left(\frac{N!}{(N-n)!}\right) \int P_c(\vec{r}^{N}; N) d\vec{r}^{(N-n)}. \tag{2.7}$$

The one-body density function $\rho^{(1)}(\vec{r}_i)$ depends on, in a uniform system, all the interactions the particle at position $\vec{r}_i$ has with all other particles in the system. For this reason, the many-body density functions of a perfect gas is simply a product of one-body density functions; thus, due to the lack of particle interactions:

$$\rho_{pg}^{(n)}(\vec{r}^n) = \prod_{i=1}^{n} \rho_{pg}^{(1)}(\vec{r}_i). \tag{2.8}$$

This can then be used to help us in describing systems with interactions as it can be factored out of $\rho^{(n)}(\vec{r}^n)$ to create distribution functions $g^{(n)}(\vec{r}^n)$ which quantify the deviations from perfect gas behaviour. Because higher body interactions are not in the scope of this work we will only introduce the pair distribution function [80]:

$$g^{(2)}(\vec{r}_1, \vec{r}_2) = \frac{\rho^{(2)}(\vec{r}_i, \vec{r}_j)}{\rho_{pg}^{(1)}(\vec{r}_i)\rho_{pg}^{(1)}(\vec{r}_j)}. \tag{2.9}$$

Following the derivations in Ref. [111–113], one can rewrite this function in terms of a conditional probability and therefore distance between both particles, which gives us an experimentally useful tool to describe the structure of a uniform system with isotropic and pairwise interactions:

$$g^{(2)}(r_{ij}) = \frac{\rho^{(1)}(r_{ij})}{\rho}, \tag{2.10}$$

where ρ is the average density of the system and $g^{(2)}(r_{ij})$, which from here onwards in this thesis we will write as $g(r)$, is known as the radial distribution function.

In figure 2.1, we show a typical radial distribution function for a system of hard disks with an area fraction of ϕ =0.5. Between $r = 0$ and $r = \sigma$, $g(r)$ is equal to 0 as particles cannot overlap. The peaks in the distributions correspond to the coordination shells around particles. The heights of successive peaks diminish due to a lack of long range order in this system. As r tends to infinity, the radial distribution function converges to 1. This is because the particle correlations diminish.

Radial distribution functions and configurational probability density functions require systems to be in equilibrium because of the definition of the grand ensemble [4]. For this reason they do not describe the temporal evolution of a system. For example, these descriptions are invalid for active systems because they continually consume energy and result in non-equilibrium steady

[4]Marginally fluctuating E an N.

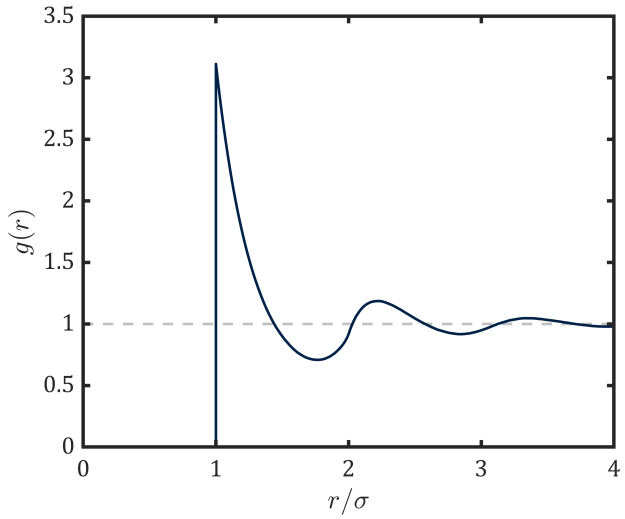

Figure 2.1: An example of a radial distribution function. A radial distribution function of hard spheres at $\phi = 0.5$. The curve is generated by measuring a Monte Carlo simulation by particle insertion (see sections 2.1.3 and 2.2.4 for more details).

states. Therefore, the dynamics of colloidal systems are also of importance in this work.

Dynamics of Colloidal Particles

A key feature of the colloidal length scale is that particles perform Brownian motion. This stochastic process is named after the botanist Robert Brown from his observations of suspended pollen particles. The first theoretical breakthrough came from Albert Einstein and Sutherland in 1905 [14]. Einstein devised a model whereby the motion of a particle was determined by the numerous collisions it has with the molecules in its surroundings. Each of the many collisions changes the position of the particle resulting in a perceived random motion. The equation of motion, based on Newton's law of motion, was devised by Paul Langevin in 1908, [114]:

$$m\frac{d\vec{v}}{dt} = \vec{F} + \vec{f}(t) - \lambda\vec{v}, \tag{2.11}$$

where m is the mass of the particle, $\vec{v}$ its instantaneous velocity, t time, $\vec{F}$ the sum of external forces, $\vec{f}(t)$ a rapidly fluctuating random force and λ a friction term. For a sphere, this is given by Stokes Law:

$$\lambda = 6\pi\eta a, \tag{2.12}$$

where η is the dynamic viscosity of the solvent and a the particle radius.

By considering a colloidal particle diffusing down a concentration gradient, we can determine characteristic properties of colloidal motion:

$$\vec{F} = -\nabla\mu = -\nabla\left(\mu^0 + k_B T ln\left(\frac{c}{c^0}\right)\right) = -\frac{k_B T}{c}\nabla c, \tag{2.13}$$

where μ is the chemical potential, k_B the Boltzmann constant, T the temperature of the solution, c the particle concentration, μ^0 and c^0 are the standard chemical potential and concentration respectively. In this example, we are in a steady-state of diffusion and at low Reynolds number ($Re << 1$) (the ratio of viscous to inertial terms):

$$Re = \frac{\rho v L}{\eta}, \tag{2.14}$$

where L is a characteristic linear dimension such as the particle diameter in the case of hard particles.

Being in the low Reynolds number regime means that viscous forces dominate in equation 2.11 and the inertial term, $m\frac{d\vec{v}}{dt}$, can be neglected. $\vec{f}(t)$ will average out to zero over a certain period of time, a characteristic of Brownian motion. Therefore:

$$\vec{F} - \lambda\vec{v} = 0. \tag{2.15}$$

This means that the flux, the flow rate per unit volume, of the system is given by:

$$\vec{J} = c\vec{v} = \frac{\vec{F}c}{\lambda} = -\frac{k_B T}{\lambda}\nabla c, \tag{2.16}$$

and by using Fick's first law $\vec{J} = -D_t\nabla c$ [115], we obtain the Einstein-Smoluchowski equation:

$$D_t = \frac{k_B T}{\lambda}, \tag{2.17}$$

where D_t is the translational diffusion coefficient [5].

This describes particles in a stead-state flow and not systems of particles in equilibrium. Particles in equilibrium do not feel a net external force, $\vec{F} = 0$. We can use the velocity

[5] $\lambda = 6\pi\eta a$ is the aforementioned Stokes law for a sphere.

autocorrelation function (equation 2.18) to identify the timescale over which $\vec{f}(t)$ tends to zero and therefore measure some of the dynamic properties of a system:

$$\langle \vec{v}(0) \cdot \vec{v}(t\rangle). \tag{2.18}$$

The equation for the velocity can be solved from equation 2.11 and using the general method of "variation of constants" [116]. This results in:

$$\langle \vec{v}(0) \cdot \vec{v}(t)\rangle = \langle v^2(0)\rangle \exp(-\lambda t/m). \tag{2.19}$$

From the Equipartition theorem we know that the mean kinetic energy $\langle \frac{1}{2} m v(0)^2 \rangle$ of a particle is $dk_BT/2$, where d are the quadratic terms in the Hamiltonian and therefore in three dimensions:

$$\langle \vec{v}(0) \cdot \vec{v}(t)\rangle = \frac{3k_BT}{m} \exp(-\lambda t/m). \tag{2.20}$$

This result is useful as it gives us a timescale; $\tau = m/\lambda$. A 1 µm silica bead has a value of τ around 1.25×10^{-7} s. This means that instantaneous velocities are impractical in practice because they average out on too short a timescale for direct observation [6]. Particle positions are therefore much easier to use experimentally.

The ensemble average $\langle \vec{r} \rangle$ is equal to 0 and means that simple positions are inadequate. The mean squared displacement, as proposed by Einstein, solves this problem as it returns a non-zero measurement. Mean squared displacement is linked to the width of the distribution of a particle's position and can also be related to the translational diffusion coefficient via:

$$\langle \vec{r} \cdot \vec{r} \rangle = \langle r^2 \rangle = \langle \int_0^t \vec{v}(t')dt' \cdot \int_0^t \vec{v}(t'')dt'' \rangle. \tag{2.21}$$

By changing the variables in the integrations, using equation 2.20 and the Einstein-Smoluchowski equation, we can come to a solution in three dimensions:

$$MSD_t^{(3)} = \langle r^2 \rangle = \frac{6k_BTt}{\lambda} = 6D_t t. \tag{2.22}$$

[6] Although they can be measured at long times via a marginally larger diffusion coefficient than expected.

A similar result can be achieved when looking at the rotational motion of a particle where:

$$\lambda_r = 8\pi\eta a^3, \tag{2.23}$$

$$D_r = \frac{k_B T}{\lambda_r}, \tag{2.24}$$

and:

$$MSD_r^{(3)} = \langle\theta^2\rangle = \frac{4k_B T t}{\lambda_r} = 4D_r t. \tag{2.25}$$

The aforementioned equations are only valid for spherical particles in three dimensions. In the two dimensional case, there are fewer degrees of freedom in both translational and rotational motion. This changes equations 2.22 and 2.25 to:

$$MSD_t^{(2)} = 4D_t t, \tag{2.26}$$

and:

$$MSD_r^{(2)} = 2D_r t. \tag{2.27}$$

A system reaches equilibrium through Brownian motion as particles are able to change their configurations. However, there may be other factors which prevent systems from doing so. The mean squared displacement equations are only valid in the dilute regime where particles do not interact with other. The equations can be generalised to:

$$MSD_x = 2nD_x t^{\gamma_x}, \tag{2.28}$$

where x denotes the type of motion, n the degrees of freedom of the motion, D_x the diffusion rate and γ_x the time exponent. γ_x is equal to one when the system is diffusive. It can be less than one when it is sub-diffusive and particles are considered to be crowded/confined, in spatial heterogeneity or have bond-like directional interactions between the particles [117]. Systems can also be super-diffusive ($1 < \gamma_x < 2$) or ballistic ($\gamma_x = 2$) [60, 118]. When γ_x is not equal to one, D_x can no longer be considered to be the diffusion coefficient but the diffusion rate. A final point is that the time-scale of any motion plays an important role in experimental systems and

measurements. For example, sub-diffusive regimes, where $\gamma_x < 1$, often occur at short time-scales [119] and can eventually be dominated by a reduced Brownian motion leading to different short and long time diffusion coefficients [120, 121].

2.1.3 Simulations of Hard Disks

As previously eluded to, there are many reasons for which integrating configurational probability density functions is too complex; namely large systems. To counter this, many have used numerical simulations since the advent of using computers in soft matter research. The need for simulations can also arise from impractical experimental systems. Recently, however, advancements in hardware and available software packages have sometimes made finding numerical solutions a go to approach. There are two common approaches to creating particle coordinates through numerical means; Monte Carlo methods and Brownian dynamics.

Monte Carlo

A general Monte Carlo (MC) method is one which uses a repeated random sampling technique [81,122]. By creating multiple sets of accepted microstates under the conditions of the simulation, an expected value of a property in a system can be measured such as the radial distribution function. Details on how MC algorithms are implemented can br found in "Computer simulation of liquids" by Allen and Tildesley [81].

MC algorithms run into difficulties when dealing with either more complex systems or with very large systems [123]. However, they remain one of the best methods for generating systems of disks with hard interactions due to the discontinuous nature of the inter-particle potential.

They are often used to describe static properties of a system through time-independent averages. However, in the limit where the trial displacement in a MC algorithm is small or if one rescales the MC time by the acceptance probability of the trial moves, MC simulations become equivalent to Brownian dynamics (BD) simulations [124–126].

Brownian Dynamics

Dynamical simulations have been used since the 1950s to understand systems of particles and a rapidly growing number complex systems have been investigated [127–130]. Many complex algorithms have been created to find solutions for specific cases [131].

Common dynamic simulations are discontinuous molecular dynamics in which interactions are only calculated upon collisions [81, 122]. These kinds of methods are beneficial from a computational aspect but their complexity drastically increases for non-spherical particles or multi-site hard core models [131–133].

Continuous methods of dynamic simulations still remain prevalent in the study of hard sphere systems despite novel techniques rising in popularity. There exist popular software packages which are optimised for large scale simulations [134–137]. In addition to this, supercomputers and GPU processing units are becoming rapidly affordable from a research perspective [138].

Brownian dynamics simulations are the methods of choice for studying colloidal systems and active Brownian particles. They are simultaneous calculations of the motion of particles based on the Langevin equations of translational and rotational motion [131]. In the case of passive particles these follow:

$$m_i \frac{d\vec{v}_i}{dt} = \vec{\eta}_t(t) - \frac{k_B T}{D_t}\vec{v}_i + \sum \vec{f}_i(t), \tag{2.29}$$

$$I_i \frac{d\omega_i}{dt} = \eta_r(t) - \frac{k_B T}{D_r}\omega_i + \sum \tau_i(t), \tag{2.30}$$

where I_i is the inertia of the particle, ω_i is the angular velocity, $\vec{\eta}_t(t)$ is the radial stochastic term, $\eta_r(t)$ is the angular stochastic term, $\vec{f}_i(t)$ are any other forces and $\tau_i(t)$ are any other torques.

Because we simulate particles in the low Reynolds number regime [7], we can assume that the inertial terms on the left hand side of both equations 2.29 and 2.30 are equal to zero. We can then rearrange the equations in terms of velocities [60, 131]:

$$\vec{v}_i = \frac{D_t}{k_B T}\vec{\eta}_t(t) + \frac{D_t}{k_B T}\sum \vec{f}_i(t), \tag{2.31}$$

[7] See section 2.1.2.

$$\omega_i = \frac{D_r}{k_B T}\eta_r(t) + \frac{D_r}{k_B T}\sum \tau_i(t), \tag{2.32}$$

and finally in terms of displacements via a conversion into a numerical approach via Ito calculus:

$$\vec{r}_i(t+\Delta t) = \vec{r}_i(t) + \sqrt{4D_t\Delta t}\vec{\chi}_i(t) + \frac{D_t}{k_B T}\sum \vec{f}_i(t)\Delta t, \tag{2.33}$$

$$\theta_i(t+\Delta t) = \theta_i(t) + \sqrt{2D_r\Delta t}\chi_i(t) + \frac{D_r}{k_B T}\sum \tau_i(t)\Delta t, \tag{2.34}$$

where $\vec{r}_i(t)$ is the position, $\theta_i(t)$ is the angle, Δt is the time-step, $\vec{\chi}_i(t)$ and $\chi_i(t)$ are uncorrelated Gaussian random numbers with zero mean and a standard deviation of 1.

Much like in MC simulations, BD simulations start with a certain initial configuration. Instead of moving a single particles, the positions of all the particles are updated at once using very small time-steps in equations 2.33 and 2.34. A key part of BD simulations is that the time-step, Δt, used is required to be shorter than the timescales associated with the motion and or interactions of the particles [8].

To create a system of repulsive disks, an inter-particle force needs to be introduced. The most common force is derived from the Weeks-Chandler-Anderson (WCA) potential [139], which is a cut and shifted form of the empirical Lennard-Jones potential [140, 141]:

$$U_{WCA}(r) = \begin{cases} 4\epsilon\left[\left(\frac{\sigma}{r}\right)^{12} - \left(\frac{\sigma}{r}\right)^{6}\right] + \epsilon & r < 2^{\frac{1}{6}}\sigma, \\ 0 & r \geq 2^{\frac{1}{6}}\sigma, \end{cases} \tag{2.35}$$

where ϵ is the energy parameter, σ is the particle diameter and r is the inter-particle distance.

This potential has been used extensively to reproduce data for hard interactions [142–145]. However, in many cases it has been shown to only be effective in an approximate manner. The most striking issue of which is that the equation of state or compressibility factor, a relation which relates the density of a system to its compressibility, depends on temperature; something which should not be the case for systems of hard spheres or disks [123].

A solution to the differences in compressibility depending on temperature has been to scale

[8] The characteristic distance of the motion caused by the interaction must be smaller than the size of the particle over the a time-scale.

the properties of the system by a Boltzmann diameter σ_B [146]:

$$\sigma_B = \sigma\left(\frac{2}{1+(T^*)^{\frac{1}{2}}}\right)^{\frac{1}{6}}. \tag{2.36}$$

where $T^* = k_B T/\epsilon$ is the reduced temperature.

Despite this fix, the WCA potential in simulations of spheres [9] still does not match what is expected theoretically from a hard sphere system [147].

In the work of Jover *et al.*, it was proposed to use a much steeper potential by modifying the Mie potential [148], equation 2.37 (from which the WCA potential is derived), to have much larger exponents λ_a and λ_b than the WCA potential, namely 50 and 49:

$$U_{Mie}(r) = \begin{cases} \frac{\lambda_b}{\lambda_b-\lambda_a}\left(\frac{\lambda_b}{\lambda_a}\right)^{\frac{\lambda_a}{\lambda_b-\lambda_a}}\epsilon\left[\left(\frac{\sigma}{r}\right)^{\lambda_b}-\left(\frac{\sigma}{r}\right)^{\lambda_a}\right]+\epsilon & r < \sigma\frac{\lambda_b}{\lambda_a}^{\frac{1}{\lambda_b-\lambda_a}}, \\ 0 & r \geq \sigma\frac{\lambda_b}{\lambda_a}^{\frac{1}{\lambda_b-\lambda_a}}, \end{cases} \tag{2.37}$$

$$U_{PHS}(r) = \begin{cases} 50(\frac{50}{49})^{49}\epsilon\left[\left(\frac{\sigma}{r}\right)^{50}-\left(\frac{\sigma}{r}\right)^{49}\right]+\epsilon & r < \frac{50}{49}\sigma, \\ 0 & r \geq \frac{50}{49}\sigma. \end{cases} \tag{2.38}$$

It was shown that the "pseudo-hard-sphere" (PHS) potential was an improvement on the WCA potential despite not becoming independent of temperature (although less). For a given reduced temperature of $T^* = 1.5$, it reproduces the equation of state of hard spheres to a greater degree of accuracy [123].

In this chapter, we set out to develop a method of creating Brownian dynamic simulations of hard disks which are independent of temperature so that they could be used in all situations.

2.2 Methods

2.2.1 A Scaled Contact Potential

Because hard interactions are discrete, using a continuous curve will never perfectly be able to mimic them. However we must, due to the nature of continuous dynamical simulations, such as

[9] In three dimensions.

Brownian dynamics simulations, use interactions which are continuous by nature.

In using both WCA and PHS, one must choose a time-step such that the movement of the particles does not lead to excessive overlap [10]. Because the PHS potential is a significantly steeper potential than WCA, it requires a finer slicing in time to avoid creating overlaps which lead to repulsive displacements significantly larger than the particle diameter. This therefore means that the PHS systems are often simulated with $\Delta t = \tau \times 10^{-6}$, $\tau = 1/D_t$ [2]. Not only is the interaction dependent on the inputs of the simulation (the time-step most notably) but they require increased computing power.

Because of the non-linear gradients of both the WCA and PHS potentials, the responses to particle overlap depend on the initial positions and movements of the particles. This makes collisions inconsistent; again minimised by a reduced time-step and requiring more computing power.

A final issue with previous methods has already been eluded to. They depend on the temperature of the system [11]. This means that when the system is varied, the compressibility of the system will vary.

For a more stable simulation and consistent interaction we propose three conditions:

1. The potential must be equal to 0 when $r = \sigma$ as in the hard interaction (assuming an approach from $r > \sigma$).

2. Each collision must be independent on the initial distance between particles and, therefore, the gradient of the force must not depend on r.

3. The magnitude of the repulsion must result in particles returning to contact such that no displacement caused by a repulsion between particles will extend past the cut-off value.

The first point is easy to implement by having a cut-off value equal to σ. For WCA it is equal to $2^{\frac{1}{6}}\sigma$ and PHS equal to $\frac{50}{49}\sigma$. The second point requires that the exponent of r in the potential must not exceed 2 such that the force and the displacement equations [12] are proportional to r. This results in a potential which does not over separate or under separate particles. For the

[10] Overlap which leads to significant deviations from hard behaviour in compressibility.
[11] Although this is also affected by the magnitude of the time-step.
[12] Which are related to each other by friction and the time-step.

third point be fulfilled, because the force on each particle must be equal and the displacement implemented to annihilate the overlap for each particle must be equal to half the overlap, the prefactor to r in the displacement equation must be $1/2$. Finally to align the displacement equation to be equal to 0 ar $r = \sigma$ we must add a constant to the displacement equation giving:

$$s_{SCP}(t) = -\frac{1}{2}r(t) + \frac{\sigma}{2}, \quad r(t) < \sigma \tag{2.39}$$

where $s_{SCP}(t)$ is the displacement of the "scaled contact potential" (SCP) method for a particle which overlaps with another at a given time in a simulation and $r(t)$ is the distance between the particles at time t. This, when divided by time, gives a velocity:

$$v_{SCP}(t) = -\frac{1}{2\Delta t}r(t) + \frac{\sigma}{2\Delta t}. \quad r(t) < \sigma \tag{2.40}$$

This can be converted to a force by a friction coefficient k_BT/D_t:

$$F_{SCP}(t) = -\frac{k_BT}{2D_t\Delta t}r(t) + \frac{k_BT\sigma}{2D_t\Delta t}, \quad r < \sigma \tag{2.41}$$

This then, once integrated, gives us a potential:

$$U_{SCP}(t) = \begin{cases} \frac{k_BT}{4D_t\Delta t}r^2(t) - \frac{k_BT\sigma}{2D_t\Delta t}r(t) + \frac{k_BT\sigma^2}{4D_t\Delta t} & r < \sigma \\ 0 & r \geq \sigma, \end{cases} \tag{2.42}$$

which can be seen with the other aforementioned potentials in figure 2.2.

There has been one similar approach to this in the literature. In a 1993 article by Heyes *et al.* [149] and later used by Ref. [150, 151], Brownian dynamics simulations were performed for systems under shear. In their case, they used a prefactor equal to 1 to ensure particles did not overlap in dense regions and did not extend their methodology for other systems. We choose to use a prefactor of $1/2$ which exactly shares the displacement amongst pairs of particles and keeps σ as an exact particle diameter. Heyes *et al.* noted that although these types of approaches are based on single collisions, due to the sharpness of the potentials used, multiple collisions remain rare even at higher densities.

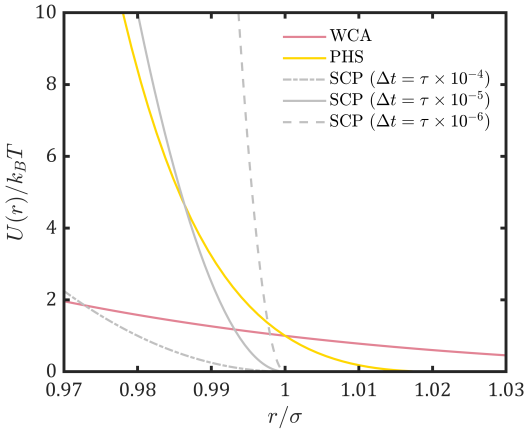

Figure 2.2: The form of all mentioned interaction potentials. The time intervals in the cases shown are in the legend. The Weeks Chandler Anderson potential is typically simulated with time intervals of $\Delta t = \tau \times 10^{-5}$ whereas the pseudo-hard sphere potential with $\Delta t = \tau \times 10^{-6}$.

Linking motion to the Time-Step

Previous works using the WCA and PHS potentials have had to choose a time-step such that the simulations remain stable. Choosing too small a time-step (less than $\tau \times 10^{-4}$) can lead to excessive particle repulsions in dense systems. Due to the harsh exponents of PHS and WCA potentials, when significant overlap occurs and the gradients of the potentials are large, the force separating the particles can lead to displacements larger than one particle diameter. The gradient of the scaling contact potential is linked to the time-step chosen for a simulation. Therefore, we must choose a time-step which gives an appropriate stiffness to our potential.

We do this by determining the degree of overlap as a percentage of particle diameter caused by the motions of the particles. For example, a diffusive type of motion will lead to a Gaussian profile of displacements which depends on the time-step. In figure 2.3 we show typical profiles of displacements for typical time-steps. The smaller we choose the time-steps, the smaller the width of the profile becomes. For $\tau \times 10^{-5}$, we can see that nearly all the possible displacements are less than 1 % of particle diameter. In the limit of $\Delta t \to 0$, the displacements will reach zero, no overlap will occur and the potential is hard but the number of steps required to reach equilibrium for example is vast. Choosing the threshold in our case was done to the limit of our computation power at $\Delta t = \tau \times 10^{-5}$.

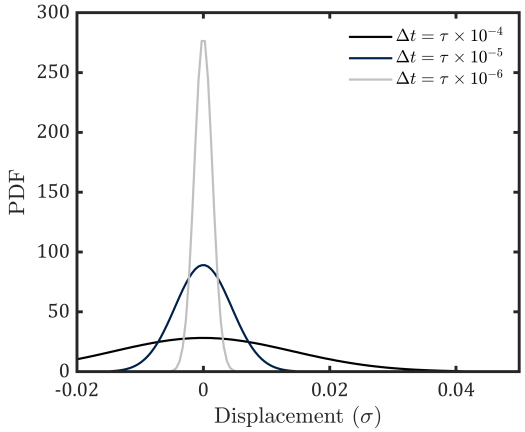

Figure 2.3: The magnitudes of displacements in simulations. The diffusion coefficient used in this figure is equal to $1\sigma^2/\tau$.

2.2.2 Brownian Dynamics Simulations

In this work, we use a simple custom algorithm in which we first determine the distances between all the particles, add displacements via Brownian and or active motion finally implementing the pair potential for particles which are closer than the cut off distances of equations 2.35, 2.38, 2.42 for each time-step. We then allow for one step of physical motion, Brownian and active, before saving the coordinates. The reason for this extra step (not used in traditional methods) will be explained in the beginning of the results section. There are other types of simulations, including Verlet leap-frog mechanisms [152], however, we choose to employ a simple method for computational speed as we use unoptimised custom algorithms. This also allowed us to use Nvidia GPU processors via CUDA (a C++ based coding language) on the Oxford supercomputer cluster called the Advanced Research Computing (ARC) systems.

For each simulation, we begin by creating a box with periodic boundary conditions containing 1024 or 8192 particles [13]. The dimensions of the box are chosen to give a desired area fraction. When using WCA or PHS potentials we use pre-equilibrated coordinates from MC simulations. When using the scaled contact potential, we equilibrate the system for 100τ.

We use reduced units of length $\sigma = 1$, energy $k_BT = 1$, viscosity $\eta = 1/3\pi$, time $1/D_t = \tau$. These are chosen to give the most constants equal to one. The diffusion coefficients follow Stokes'

[13] Depending on the simulation, the values will be stated in the graphs of the relevant data.

equations [60]:

$$D_t = \frac{k_B T}{6\pi\eta(\sigma/2)}, \tag{2.43}$$

and

$$D_r = \frac{k_B T}{8\pi\eta(\sigma/2)^3}. \tag{2.44}$$

2.2.3 Monte Carlo Simulations of Disks

For the work we present in this thesis, we only use the results of Monte Carlo simulations to compare with our results. Therefore, we will only present the single method we have exploited. More details on such methods can be found in Ref. [81, 153]. The simulations were kindly performed by Dr Adam Stones of the Aarts group following the work of Bernard *et al.* [154]. For completion we will briefly describe the methodology.

We implement an Event-Chain Monte Carlo algorithm for generating coordinates to measure exact pair distribution functions for hard sphere systems. Following the creation of an initial set of particle positions on a lattice, a random particle is chosen to be moved in a random direction until it collides with another. This disk then continues the displacement until a total distance or chain length l is met. All moves are accepted and the chain length is chosen to incorporate $\approx \sqrt{N}$ disks.

We simulate 1024 particles when the area fraction of the system is below the hexatic transition and marginally more if necessary to fit a lattice in a box. We use a periodic boundary condition to avoid finite size effects.

2.2.4 Pair Distribution Function

Binning Method

In this work, we make most use of the binning method of measuring a radial distribution function. We do this by calculating all the distances between all the particles at a given time then creating a histogram to generate a distribution of distances. We then normalise it by the area of the

ring determined by the size of the histogram binning, b_H, and divide it by the average density following:

$$g(r; b_H) = \frac{n(r; b_H)}{(\pi(r + b_H)^2 - \pi r^2)} \frac{s_f^2}{N^2}, \tag{2.45}$$

where $n(r; b_H)$ is the number of particles in a ring of width b_H at r, and s_f is the size of the simulation box or observation frame. An advantage of using the binning method is that it only requires particle coordinates.

Insertion Method

An interpretation of equation 2.10 is that the radial distribution function is the ratio of the probability of finding a particle at a distance r_{ij} in a system to the probability of finding a particle in a perfect gas at that same distance [155]. This is equivalent to saying that it is the ratio of the free energy differences in the grand ensemble of inserting a particle at a distance r_{ij}. We can use this to measure a pair potential by comparing the probability of inserting a particle in a set of coordinates, given we know their interactions [14], to the bulk insertion probability:

$$g(r) = \frac{\langle \exp(-\frac{1}{k_B T} P(r)) \rangle}{\langle \exp(-\frac{1}{k_B T} P) \rangle}. \tag{2.46}$$

This method of generating a radial distribution function is complementary to the binning method. It works best at low densities where there is available space for insertion. It is also beneficial as it does not depend on the arbitrary choice of bin sizes [155].

We implement this method by considering each particle in the system in turn and attempt particle insertions over many separations and angles. Code for the implementation of this method was provided for by Dr Adam Stones of the Aarts group.

2.2.5 Measuring a Pair Potential

Following the methods in Ref. [87], it is possible to combine both methods of determining the radial distribution function of a system in equilibrium to measure a pair potential between the particles in a system. Using a "predictor-corrector scheme", trial pair potentials are used in the

[14] In the hard disk case being unable to insert a particle at $r \leq \sigma$.

insertion method to generate a $g(r)$, which is then compared to the distribution obtained by binning. With an iterative procedure, this is then repeated to match both distribution functions such that a pair potential can be obtained. Code for the implementation of this method was provided for by Dr Adam Stones of the Aarts group.

2.2.6 Calculating Mean Squared Displacement

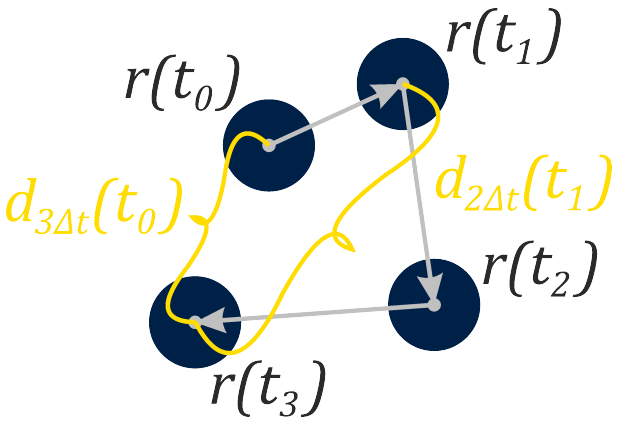

Figure 2.4: A scheme showing the distance over which a mean squared displacement curve is measured. The grey arrows show the movement of the particle and the yellow lines the distances used in the calculation.

Because we simulate our particles over given time-steps the motions of our particle are effectively discrete. This is similar to how in experiment (as in chapter 4), we record a series of images. To calculate the MSD of a set of a particles, we must first calculate the distances over which they move. These are done between all possible intervals; examples are shown in figure 2.4 as $3\Delta t$ and $2\Delta t$. These are then averaged over all displacements over all particles with each displacement having an equal weighting. This means that the statistics of the short time displacements are much larger than the long times. It is also common to average the displacements for each particle and then performing an average over all particles. This is done when particles have different behaviours, unlike in our simulated systems.

2.3 Results

2.3.1 Comparisons of Pair Distribution Functions

A more empirical approach of determining if our method is suited for BD simulations of passive particle is to compare measurable properties of the system. Because MC simulations are able to provide us with almost exact time independent properties of systems of hard disks, we can compare equilibrium structural properties generated by MC algorithms to those of our BD simulations.

We begin by comparing the radial distribution functions of BD systems near $r = \sigma$. The contact value, $g(\sigma)$, allows us to compare the compressibility and pressure of systems [82]. The closer the first peak of the $g(r)$ is to the real value measured by the MC simulation and particle insertion [155] the more a system is hard.

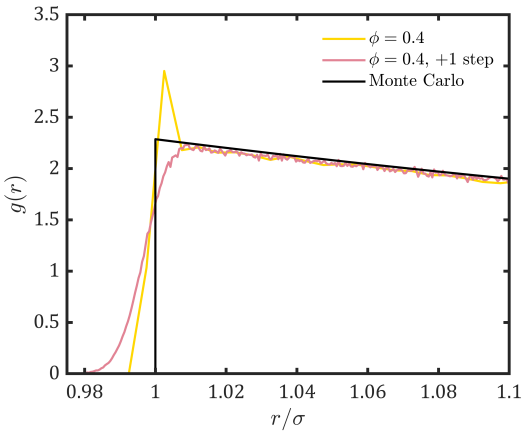

Figure 2.5: The extra displacement step before saving coordinates improves the structure of our systems. The radial distribution functions for simulations noted in the legend. Far from contact the difference is negligible but the extra displacement smooths the anomalous peak near contact at the expense of overlap.

In figure 2.5 we show a justification as to why we choose to have an extra displacement step before saving particle coordinates [15]. Without the extra step the contact value of the system is much larger than the value obtained from Monte Carlo simulations. The extra step reduces this value but does not significantly change the structure of the system at large distances.

In figure 2.6 the radial distribution function for the WCA system is as expected far away

[15] Essentially saving the coordinated after the Brownian step and not after the overlap resolution step as traditionally done.

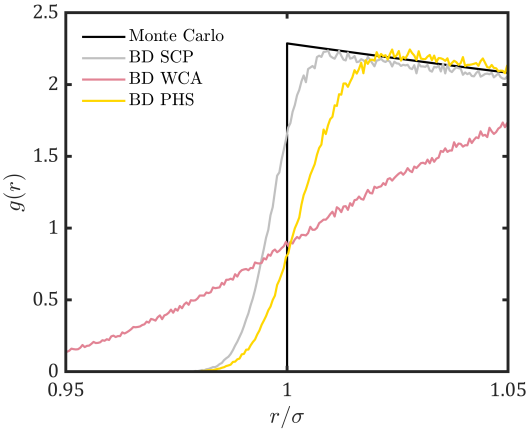

Figure 2.6: The steepness of the SCP curve shown by the pair distribution function near $\sigma = 1$. The pair distribution function, $g(r)$, of simulations of 1024 particles with time intervals of $\Delta t = \tau \times 10^{-5}$. The SCP method produces a pair distribution closer to that of the precise Monte Carlo method compared to the PHS potential and the very soft WCA potential.

from being hard (at least compared to the other potentials). More interestingly is how the SCP method compares to the PHS potential. The SCP curve is closer to the contact value at its peak (the most probable location to find a second particle). It also reaches 0 in a very similar position to the PHS curve. This would suggest that the SCP method does indeed provide us with a method to create harder systems than any in the literature.

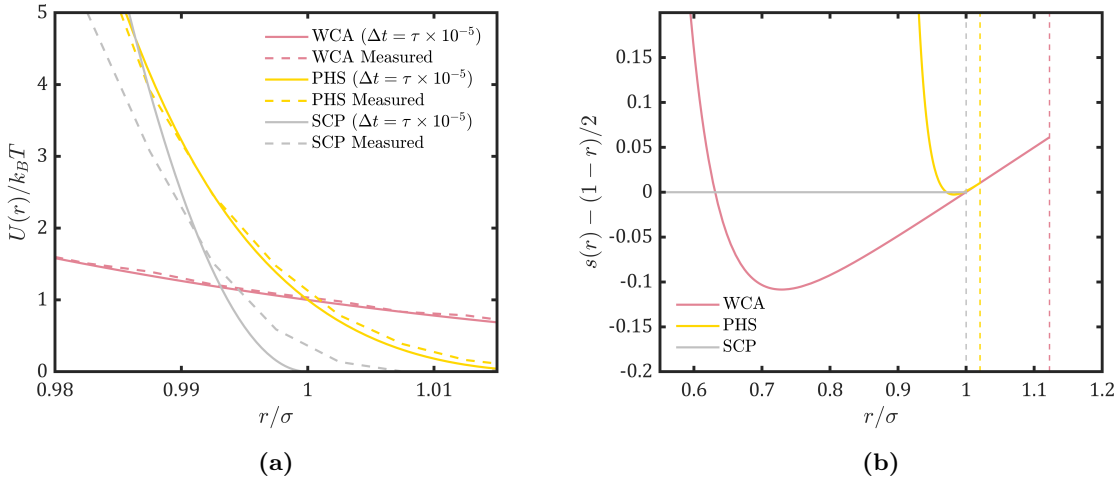

(a) **(b)**

Figure 2.7: The difference between input potential and resulting interactions in Brownian dynamics simulations. (a) The solid lines represent the input potentials used in Brownian dynamics simulations from which the interactions potentials are measured by particle insertion. Simulations of 1024 disks in two dimensions at an area fraction of $\phi_A = 0.4$ were run for 15×10^6 frames. The depreciation in the potential at lower distances can be attributed to our methodology of simulating which allows for partial overlap. (b) The theoretical displacements implemented in the BD algorithm normalised to half the overlap.

We use the insertion method to measure the pair potentials which are obtained from our

simulation method in figure 2.7(a). Here we see that all three measured potentials do not match the theoretical curves exactly. This is most significant in the case of SCP. This is because of the extra step which includes a Gaussian displacement effectively smoothing each potential. The WCA and PHS measurements are less affected by this step because of the distance dependent displacements shown in figure (b). Prior to the extra motion step the particles experience a range of overlaps where some have been over and some under separated depending on whether the curve in (b) is above or below 0 respectively. With the SCP method all the particles reach contact and therefore the difference in the distribution of overlaps from before the extra step and after is greater. Nevertheless, the SCP method still provides us with a harder potential for the same computational cost. One could argue that these differences are small because of the small time-steps. However, this has always been the reason why the empirical potentials have worked well in previous works.

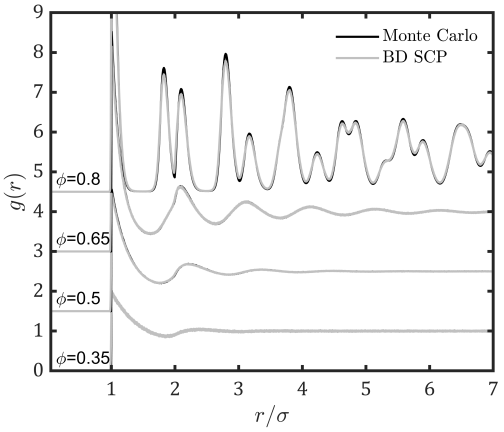

Figure 2.8: The consistency with which SCP simulations reproduce correct structure. The pair distribution function, $g(r)$, of simulations of 1024 particles with time intervals of $\Delta t = \tau \times 10^{-5}$. The distributions of each area fraction are shifted vertically to distinguish them. The grey curves follow the shape of the more precise Monte Carlo method over long distances and high area fractions.

Next we compare the long range structure. In figure 2.8 we compare the radial distribution function of the SCP method at 4 area fractions. We see that the SCP method correctly follows the shape of the MC curve for all area fractions and at large separations. Most notably it does so for a dense system which is past the hexatic transition. We do see the largest differences at the peaks and troughs. These arise because the SCP systems are not perfectly hard.

In practice, one can create systems at any area fraction from a random set of points and the SCP method prevents major disruptions to the simulation. At higher area fractions, instead of becoming unstable, as can be the case for the PHS potential (particles exploding out of the

simulation box), the SCP method prefers to jam as repulsion displacements are never larger than the overlap distance. Therefore, to simulate dense systems properly one still has to correctly choose an appropriate initial configuration.

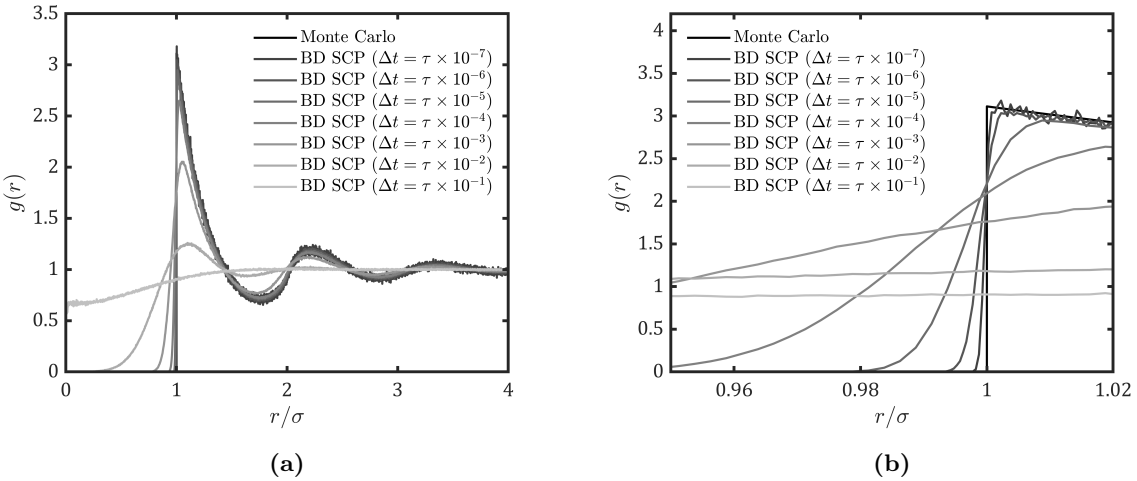

Figure 2.9: How the SCP method is dependent on the time interval used between simulation steps. The pair distribution function, $g(r)$, of simulations of 1024 particles. The distributions are shown to approach the correct Monte Carlo curve as the time interval between simulation step sis reduced. Therefore, the accuracy of the SCP method is limited either by the calculation speeds or the duration of a simulation.

In figure 2.9, we compare the radial distribution functions of SCP simulations at different time-steps. Because the hardness of the SCP method depends on the time-step, we see that those with larger time-steps become progressively softer. In figure 2.9 (b), we can see that the $\Delta t = \tau \times 10^{-7}$ simulation comes very close to the desired contact potential of the MC simulation. This means that as we stated in our methods section, the SCP method provides us with systems with hard interactions as the time-step tends to zero. These graphs show that although the choice of time-step is partially arbitrary, we are able to calibrate it to our needs and our computational power.

In figure 2.10 we present the pair distribution functions of SCP and PHS simulations at various temperatures. The times-steps, as described in our methodology, are dependent on the temperature of the system, as τ depends on the translational diffusion coefficient (see equation 2.17). We simulated both the PHS and SCP systems with the same set of rules. As described in the introduction to this chapter, WCA and PHS systems are only proposed to be hard systems at a specific reduced temperature [16] unless the diameter of the particles is scaled [123]. In

[16] $T^* = 1.5$ for PHS and $T^* = 1.25$ for WCA.

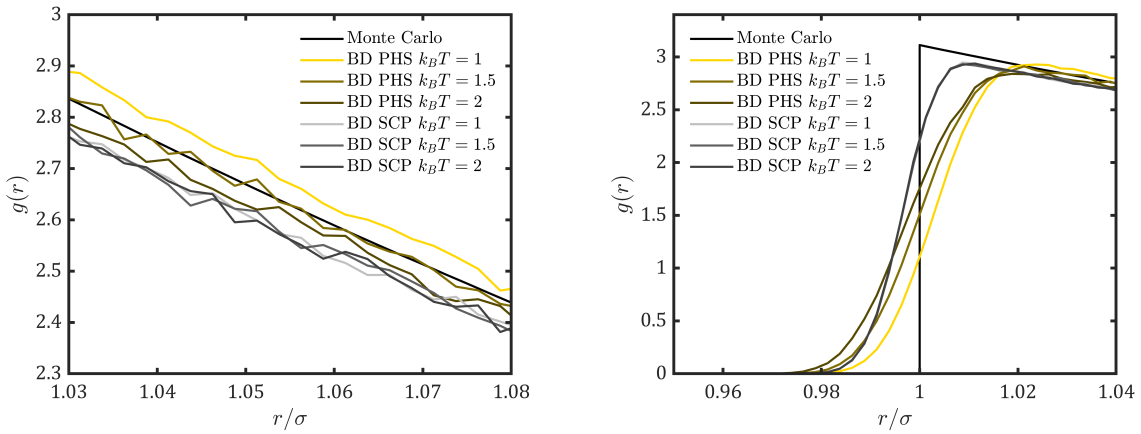

Figure 2.10: The consistent structure obtained with the SCP method despite changes in temperature. The pair distribution function $g(r)$ of simulations of 1024 particles with time intervals of $\Delta t = \tau \times 10^{-5}$. (a) and (b) show different regions of the curves. Over a range of temperatures the SCP method is unchanged whereas the structure of the PHS method varies. Hard interactions should remain unchanged as the energy of the system varies. The lines in (a) show that the PHS potential works best at $1.5k_BT$ as shown in its original publication [123]. The SCP method remains marginally softer than a true hard interaction and this is shown by how it remains below the Monte Carlo curve when the gradient is negative and above when the gradient is positive (as seen in figure 2.8).

figure 2.10(a) we can see that the PHS curve where $T^* = 1.5$ lies on top of the MC curve when using our algorithm. This shows that our methods do recreate the results of the original article where PHS was proposed [123]. We see, in figure 2.10(b), that the PHS curves vary in position, whereas the SCP curves do not. This means that the SCP method is consistent in generating the structure of the system whereas PHS is not. Therefore, one would never need to scale the diameter of the particles to compensate for changes in the system with the SCP method. The SCP curves again, as is the case in figure 2.9, are below the line around the first peak.

2.3.2 Comparisons of Mean Squared Displacements

Brownian dynamics stimulations allow us to also explore the time dependent properties of systems. Thanks to the attributes of the SCP method, we are able to probe the dynamics of high density systems.

Figure 2.11(a) shows the MSD curves for a range of area fractions. Here we see the expected trends of having straight lines at the lowest area fractions and a reduction in the displacements as area fractions rise [156]. For the highest area fraction shown, we can also see the beginning of the inflection caused by particles escaping the cage effect.

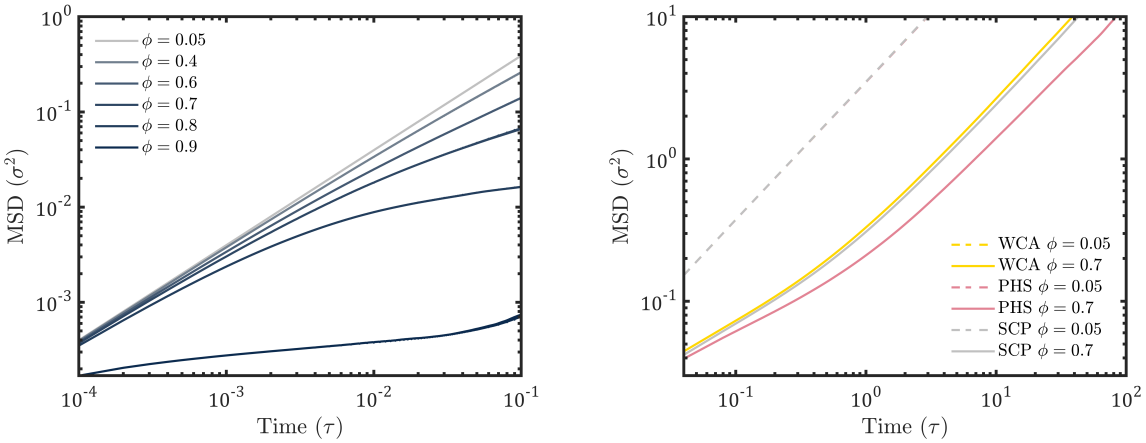

Figure 2.11: The mean squared displacement of particles simulated with the SCP method. The mean squared displacement (MSD) of simulations of 1024 particles with time intervals of $\Delta t = \tau \times 10^{-5}$. Displacement is in units of particle diameter (σ) and time in diffusion time ($\tau = \sigma^2/D_t$). The graphs show the reduction in the displacements due to the particle collisions. The SCP method produces stable simulations when the area fraction of particles is very large. All three dahsed lines in (b) lie on top of each other.

We see the inflections better in figure 2.11(b). All three potentials used have the same MSD at low area fractions (all dashed lines are superimposed). This is expected as there are very few collisions and it is exceedingly rare for particles to become trapped. However, we do not obtain the same curves for the larger area fraction. If we compare WCA to PHS, we can conclude that the stiffness of the PHS curve creates harder particles and stiffer cages for particles to be trapped in. A less obvious phenomenon to explain is that of the difference between SCP and PHS. One would expect SCP to prevent more motion than PHS due to it being a sharper potential. However, we must also consider that the PHS potential does not have a consistent particle diameter. The temperature in these simulations is equal to $T^* = 1$ and therefore the PHS particles have a marginally larger effective diameter which can have a drastic effect at such a high density of particles.

2.4 Summary and Conclusions

Using the "scaled contact potential" (SCP) method, we have compared the structure and dynamics of passive Brownian dynamics simulations to those using the pseudo-hard-sphere potential (PHS) and the Weeks-Chandler-Anderson potential (WCA). We also compare the structure of our systems to those generated using Monte Carlo algorithms which by definition provide us

with the expected configurations of truly hard disk systems.

Based on the observations of the radial distribution functions presented in the previous section, we can confidently say that the SCP method is successful in mimicking hard disk systems. It seems that it is also the case that it is an improvement on the PHS and the WCA potentials. Not only does it not produce errors when the time-step is large, never leading to excessive repulsion regardless of the conditions of the system, but it does so with an effective time-step typically much larger than those used in PHS systems ($\Delta t = \tau \times 10^{-5}$ vs $\Delta t = \tau \times 10^{-6}$ respectively). However, it remains the case that the PHS potential is superior at following the radial distribution function obtained from Monte Carlo methods only at $T^* = 1.5$. However, we would recommend that the SCP method could be used universally. The ability to calibrate the time-step means that any simulation can be stable. For example, a simulation with exceedingly large attractions can have its time-step calibrated to the interaction (and not the Brownian motion) such that overlap is never significant.

We can also see that the MSD of the particles with the SCP method does behave as expected. It highlights, when compared to the PHS potential, that there is no need for readjusting for particle radius as conditions change, a common approach when using the WCA potential.

Although the use of an algorithm which returns particles to contact is not entirely novel [149], the consideration of the percentage overlap from the motion of the particles and scaling the time step accordingly is a framework which to our knowledge has not been fully exploited and which enables tuning of the softness of particles in a simulation for an optimised amount of computing power with any behaviours.

Chapter 3

Motility-Induced Phase Separation at High Péclet Numbers

Abstract

We use the SCP method to investigate motility-induced phase separation (MIPS). We show that it creates consistent particle diameters regardless of the particles' active force. Because of this, we are able to create systems with much larger Péclet numbers where we find novel phenomena which are not described in current theory. To explain the phenomena we have developed a method to track clusters and grains over time. We end with a study of "sticky" active disks to confirm that the persistence of the swimming direction of hard active Brownian particles at high Péclet numbers leads to the disruption of MIPS.

3.1 Introduction

We begin this chapter by covering some theory of Brownian active particles, namely a description of the mean squared displacement of ballistic particles and the origin of the Péclet number for active particles. We then provide an overview of the current theoretical description of motility-induced phase separation based on an analogy of equilibrated systems which undergo spinodal decomposition. This theory was first constructed by Tailleur and Cates [4] and uses the Cahn-Hilliard equations. We also include a description based on the the rates of "evaporation and condensation" of particles at the edge of the dense phase [1]. We take the time to introduce these theories as we then test their main principles with our data. We finish the introduction section with a review of recently published articles on the topic of MIPS in simulation.

In the methods section, we explain the technicalities of using the SCP method for active particles and the tools we use to analyse our results. These analytical tools are also used in chapter 4 and 5. They include descriptions of the structure of the dense phase, angular correlations, cluster identification and tracking and the determination of torque and cluster rotation.

We then finish with the results from our ABP simulations. We first compare our results to those in the literature in terms of phase diagrams and temporal dynamics. This is to ensure that our SCP methods does not produce anomalous results at traditionally used Péclet numbers ($Pé < 300$). We then discover novel phenomena in our results at higher Péclet numbers ($Pé > 300$). A full phase diagram with snapshots can be found in the appendix of the chapter. To confirm our hypothesis we also examine simulations where the angular motion of our particles is hindered in the proximity of others.

3.1.1 Ballistic Motion

A commonly used method to describe or analyse ballistic motion is mean squared displacement (MSD). When an MSD curve has a squared dependency on time then it can be categorised as ballistic. However this merely touches on one aspect of such motion.

A velocity, as it is defined, is a vector. This means that there is an angular dependence to activity. Due to its links with colloidal particles, such as bacteria and synthetic microswimmers,

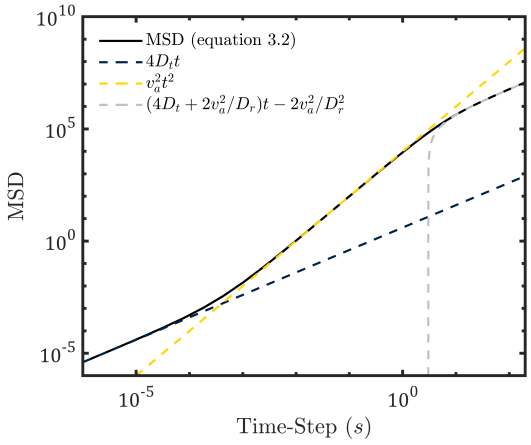

Figure 3.1: A characteristic mean squared displacement curve of an active Brownian particle showing multiple regimes. In this case $D_t = 1$, $v_a = 100$ and $D_r = 0.33$ in units of σ, s and rad.

the active Brownian particle model is one which is commonly used in active matter research. It describes particles which, alongside activity, also exhibit Brownian motion. Because of this, the Langevin equation (equation 2.11) can be modified to:

$$m\frac{d\vec{v}}{dt} = \vec{F}_a + \vec{f}(t) - \lambda\vec{v}, \tag{3.1}$$

where the external forces are now equal to the active force $\vec{F}_a$.

Following the work of Gomez-Solano *et al.* and Uhlenbeck *et al.* [157, 158], the MSD of an active Brownian particle in two dimensions follows:

$$MSD_t = 4D_t t + \frac{2v_a^2}{D_r^2}(D_r t + \exp(-D_r t) - 1), \tag{3.2}$$

where v_a is the active component of velocity and all other terms are as previously described. Because of various dependencies on time, this equation can be separated into different regimes (which are also shown in figure 3.1):

$$MSD_t \approx \begin{cases} 4D_t t, & \text{if } D_r t << 1 \\ v_a^2 t^2, & \text{if } D_r t < 1 \\ (4D_t + 2v_a^2/D_r)t - \frac{2v_a^2}{D_r^2}, & \text{if } D_r t >> 1. \end{cases} \tag{3.3}$$

Using the mean squared displacement as a tool to measure motion is practical in obtaining

the rotational diffusion coefficient by fitting the whole curve but can be erroneous: this may be because active systems are often not uniform in activity and an MSD curve is a global average which depends on time regimes. It is also the case, because the mean velocity is no longer equal to 0 as in the purely Brownian case, that simply determining velocity with a distance divided by a time interval is possible and often preferred (more information can be found in the results section of chapter 4). However, as described above, the velocity of the particles themselves do not suffice in describing the motion in the system.

In the case of active Brownian particles, a dimensionless parameter which is often used to describe the ratio of activity to Brownian motion is the Péclet number [159]:

$$Pé = \frac{\sigma v_a}{D_t} = \frac{3v_a}{\sigma D_r}, \tag{3.4}$$

where v_a is the velocity of the particle generated by the self-propulsion. The two versions of the equation are related via the Stokes–Einstein equation. The Péclet number encompasses both the velocity component and the angular diffusion. However, as has been shown in the work of Martin-Roca *et al.* [2] and as will be discussed later, it has certain flaws.

3.1.2 A Theory of Motility-Induced Phase Separation

Motility-Induced Phase Separation has been described for "Run and Tumble" (RTPs) [1] and active Brownian particles (ABPs) by Julien Tailleur and Michael E. Cates [3, 4, 73]. In their work, they derive a theory for the relation between velocity and particle density in many body systems which leads to a non-convex energy dependence on the mean density of the system based on the Cahn-Hilliard theory of phase separation in passive systems [160–163]. This result suggests that a system will spontaneously phase separate if within the spinodal of the energy curve. In this section, we will cover the main steps to deriving the key results of their theory, based primarily on Ref. [4], whilst highlighting key assumptions.

Thermodynamic Description

The Relation between Velocity and the PDF:

[1] A motion based on bacteria whereby a particle will swim in a straight line until it reaches a stochastic reorientation event before swimming again.

As previously defined in this thesis, the trajectory an active Brownian particle follows can be well described by an over-damped Langevin equation:

$$\dot{\vec{r}} = v_0\vec{u}(\theta) + \sqrt{2D_t}\vec{\xi}, \tag{3.5}$$

where $\vec{r}$ is the position of the particle, v_0 its active velocity, $\vec{u}(\theta)$ its orientation, D_t its translational diffusion constant and $\vec{\xi}$ is a Gaussian white noise term.

This equation only describes the motion of a single non-interacting active particle and analysis can only be done on a trajectory by trajectory approach. Instead it is more enlightening to describe the system from a probabilistic point of view using the probability of finding a particle at a given position and orientation; this given by the probability density function (PDF) of the particles in the system $P(\vec{r}, \vec{u})$. A relation for the PDF of a system with the movement of its particles can be derived from the Fokker-Planck (FP) equation which is typically used for passive Brownian particles (PBPs):

$$\dot{P} = -\nabla \cdot VP + \nabla \cdot D\nabla P, \tag{3.6}$$

where V is a drift term and D is a diffusivity term.

Both RTPs and ABPs, given sufficient coarse-graining, resemble diffusive random walks described by the typical behaviours of PBPs. This is because the diffusivity of the system, D, can be thought to be increased by the active component of the motion at a large scale (see equation 3.3). Therefore, by keeping our description of an active system with an explicit coarse-graining we can use the FP equation for basic active systems. We can generalise the equation for systems where the velocity of a particle depends on its position $v(\vec{r})$. This can arise in real systems where the medium of the swimmers is complex and therefore is a useful universal adjustment. This, for the case of ABPs with a rotational diffusion coefficient D_r, results in:

$$\dot{P}(\vec{r}, \vec{u}) = -\nabla \cdot \big[v_0(\vec{r})\vec{u}(\theta)P(\vec{r}, \vec{u})\big] + \nabla_{\vec{u}} \cdot \big[D_r\nabla_{\vec{u}}P(\vec{r}, \vec{u})\big] + \nabla \cdot \big[D_t\nabla P(\vec{r}, \vec{u})\big], \tag{3.7}$$

This general first step is useful and can be tuned to simplify our understanding. To do this we must solve the equation to remove the angular dependence. This can be done via finding its

angular harmonics [72]. The zeroth component is derived from the integral with respect to $\vec{u}$:

$$\psi(\vec{r}) = \int P(\vec{r}, \vec{u}) d\vec{u}, \tag{3.8}$$

where $\psi(\vec{r})$ is our new PDF with respect to only $\vec{r}$.

Following Ref. [72], it can be shown that the components of higher order than zero may be assumed to be zero in the limit where $1/D_r = \tau << t$ for a slowly varying $v(\vec{r})$. This gives us a PDF:

$$\dot{\psi}(\vec{r}) = \nabla \cdot \Big[\frac{-v_0(\vec{r})}{2D_r} \nabla \big(v_0(\vec{r}) \psi(\vec{r}) \big) \Big] + \nabla \cdot \big[D_t \nabla \psi(\vec{r}) \big]. \tag{3.9}$$

This equation can be rearranged in terms of the flux of the system $\vec{J}(\vec{r})$:

$$\dot{\psi}(\vec{r}) = -\nabla \cdot \vec{J}(\vec{r}), \tag{3.10}$$

where:

$$\vec{J}(\vec{r}) = \frac{-v_0(\vec{r})}{2D_r} \nabla \big(v_0(\vec{r}) \psi(\vec{r}) \big) - D_t \nabla \psi(\vec{r}). \tag{3.11}$$

Given that we are already confined to long times within the coarse grained approach, one can then use a steady state to simplify the problem. The simplest case is a flux-free steady state where $\vec{J}(\vec{r}) = 0$. Given this steady state, we can re-write equation 3.11 as:

$$-\Big(D_t + \frac{v_0^2(\vec{r})}{2D_r} \Big) \nabla \psi(\vec{r}) - \frac{1}{2} \psi(\vec{r}) \nabla \Big(D_t + \frac{v_0^2(\vec{r})}{2D_r} \Big) = 0, \tag{3.12}$$

which can be rearranged to give:

$$\nabla \ln \left[\psi(\vec{r}) \sqrt{D_t + \tfrac{v_0^2(\vec{r})}{2D_r}} \right] = 0, \tag{3.13}$$

which when integrated then implies:

$$\psi(\vec{r}) \propto \frac{1}{\sqrt{D_t + \frac{v_0^2(\vec{r})}{2D_r}}} \tag{3.14}$$

Here we have derived a relation between a spatially dependent velocity and a probability density. It implies that for an active system, at long times, particles accumulate when they are swimming slower. The equation also implies a specific relation $\psi \propto 1/v$.

This relation does not explicitly describe MIPS; it is the general case where velocity is spatially dependent. To bring it forward to a MIPS system, one has to relate the velocity to the reduction of velocities caused by the excluded volumes of the particles. One thing to note is that, although active systems are by definition not in equilibrium, the relations which we have stated so far are analogues to theory applied to passive equilibrated systems. This does not serve as a proof that active systems are in equilibrium but shows that they can be considered to be thought of as analogues of passive systems and presents a framework within which to study MIPS.

Converting the Dependence on Space to Density:

To derive a more complete description of MIPS, we move onto converting the aforementioned description in terms of local density. We begin by returning to the Fokker-Planck equation:

$$\vec{J} = -D\nabla\psi + V\psi. \tag{3.15}$$

From this and equation 3.11, we can write a diffusivity and a drift term explicitly:

$$D(\vec{r}) = D_t + \frac{v_0^2(\vec{r})}{2D_r}, \tag{3.16}$$

and,

$$\vec{V}(\vec{r}) = -\frac{v_0(\vec{r})\nabla v_0(\vec{r})}{2D_r}. \tag{3.17}$$

This in turn gives us the following relation:

$$\frac{\vec{V}(\vec{r})}{D(\vec{r})} = -\nabla \ln[v_0(\vec{r})]. \tag{3.18}$$

In equation 3.18, D_t, the translational diffusion, has not been included. This can be considered a decent approximation because it has been shown that the MIPS transition occurs around $Pé \approxeq 55$ in two dimensions [1], the terms relating to D_t are therefore typically an order of magnitude smaller than those of the activity in the regions of interest.

We can again compare these equations to the passive Brownian particle (PBP) case in an external potential, where $U(\vec{r}) = k_B T \ln[v_0(\vec{r})]$, and derive the stochastic equation of motion for the coarse-grained density $\rho(\vec{r})$ [164]:

$$\dot{\rho}(\vec{r}) = -\nabla \cdot \vec{J}_\rho(\vec{r}), \tag{3.19}$$

where $\vec{J}_\rho(\vec{r})$ is the flux of the density and:

$$\vec{J}_\rho(\vec{r}) = -D\nabla\rho(\vec{r}) + V\rho(\vec{r}) + \sqrt{2D\rho(\vec{r})}\vec{\Xi}, \tag{3.20}$$

where $D(\vec{r})$ and $V(\vec{r})$ obey equations 3.16 and 3.17 and $\vec{\Xi}$ is a vector-valued unit white noise. Equations 3.19 and 3.20 can then be generalized to the case where v and τ depend on ρ and therefore D and V also [3]. In the following equations, we will again take D_t to be zero as it does not affect the qualitative description. Using the Fokker-Planck equation for the many-body probability $P[r]$ we obtain:

$$\dot{P}([\rho]) = -\int dr \left(\nabla \frac{\delta}{\delta\rho(\vec{r})}\right)\left[V\rho(\vec{r}) - D\nabla\rho(\vec{r}) - D\rho(\vec{r})\left(\nabla\frac{\delta}{\delta\rho(\vec{r})}\right)\right]P([\rho]), \tag{3.21}$$

where $[\rho]$ denotes an arbitrary functional dependence on the coarse-grained density field $\rho(\vec{r})$. We can then bring this equation to an equilibrium-like steady state again giving:

$$\vec{J}\big[P_{eq}([\rho_{eq}])\big] = \left[V\rho(\vec{r}) - D\nabla\rho(\vec{r}) - D\rho(\vec{r})\left(\nabla\frac{\delta}{\delta\rho(\vec{r})}\right)\right]P_{eq}([\rho_{eq}]) = 0. \tag{3.22}$$

If we then assume that $P_{eq}([\rho_{eq}]) = \exp(-\mathcal{F}/k_B T)$ where $\mathcal{F}$ is the free energy of the system, there is a flux-free solution to equation 3.22:

$$\frac{\vec{V}([\rho],\vec{r})}{D([\rho],\vec{r})} = -\frac{1}{k_B T}\nabla\frac{\delta\mathcal{F}_{ex}}{\delta p}, \tag{3.23}$$

where $\mathcal{F}_{ex}$ is the excess free energy of the system, and:

$$k_B T \ln[v([\rho],\vec{r})] \equiv \mu_{ex}([\rho],\vec{r}) = \frac{\delta\mathcal{F}_{ex}}{\delta\rho}. \tag{3.24}$$

If all the assumptions and requirements made up to this point and equation 3.24 are kept, our description of the system remains an analogue of a PBP system with an external potential with

the free energy functional:

$$\mathcal{F}[\rho] = k_B T \int \rho(\ln[\rho] - 1) d\vec{r} + \mathcal{F}_{ex}[\rho]. \tag{3.25}$$

Deriving the Free Energy Density as a Function of a Density Dependent Velocity:

If we take a final step to limit the changes in ρ to depend only weakly on space and that the swim speed depends isotropically on ρ, then we can convert our velocity to:

$$v([\rho], \vec{v}) = v[\rho(\vec{r})], \tag{3.26}$$

which makes equation 3.24 always satisfiable with:

$$\mathcal{F}_{ex}(\rho(\vec{r})) = \int_0^{\rho} \ln[v(s)] ds, \tag{3.27}$$

where s is in units of density and the system becomes again equivalent to PBPs with:

$$\mathcal{F}[\rho(\vec{r})] = \int f(\rho(\vec{r})) dr, \tag{3.28}$$

and using equation 3.25:

$$\frac{f(\rho)}{k_B T} = \rho(\vec{r})(\ln[\rho(\vec{r})] - 1) + \int_0^{\rho} \ln[v(s)] ds. \tag{3.29}$$

For completion we can recover the terms in D_t [4]:

$$\frac{v \nabla v}{D_r(v^2/D_r + 2Dt)} = \nabla \frac{\delta}{\delta \rho} \mathcal{F}_{ex}, \tag{3.30}$$

If $v[\rho(\vec{r})]$ is strictly local, as we have used to derive our relations, only the speed (not D_r or D_t) must depend on the density to keep the condition for $\mathcal{F}_{ex}$ to still exist. The free energy then becomes:

$$\mathcal{F}_{ex} = \int f_{ex}[\rho(\vec{r})] dr, \tag{3.31}$$

with:

$$f_{ex}[\rho(\vec{r})] = \int_0^{\rho} \frac{1}{2}\big[v^2(s)/D_r + 2D_t\big]ds, \tag{3.32}$$

and:

$$f[\rho(\vec{r})] = \rho(\vec{r})(\ln[\rho(\vec{r})] - 1) + f_{eq}[\rho(\vec{r})]. \tag{3.33}$$

This theory gives us access to a free energy description of MIPS and predicts that equation 3.33 formally describes the transition to be spinodal due to the non-convex shape of $f[\rho(\vec{r})]$ giving (derivatives are with respect to density):

$$f''[\rho(\vec{r})] < 0 \Longleftrightarrow \frac{v^2}{D_r}\left(1 + \rho\frac{v'}{v}\right) < -2D_t. \tag{3.34}$$

For an exact measurement of the free energy of a MIPS system one must have access to the relation of v with ρ. In the work of Tailleur and Cates [4], they proposed that an example dependence could follow:

$$v^2(\rho) = v_0^2 + \big(v_1^2 - v_0^2\big)\big(1 - \exp(-\rho/\rho_l)\big), \tag{3.35}$$

where v_0 is an exponentially decaying dilute velocity which reaches v_1 on a characteristic density scale ρ_l. This equation is used as an example as its spinodals can be computed exactly (figure 3.2). However, it has been shown in previous works that the relation between velocity and density for ABP systems with soft interactions can be approximated by a linear relation: $v(\rho) = v_0[1 - \rho/\rho^*]$, where ρ^* is the extrapolated point at which v equals 0 which is close to the close packing threshold of ρ for disks [5].

Although this description is quite complete from a theoretical standpoint, many of the assumptions used in its derivation limit its applicability quantitatively. However, it has been shown that it qualitatively agrees with numerical measurements [4].

In this work, we concern ourselves with hard interactions of disks. This means that the assumptions that the change in velocity and density in space are not slowly changing because the interaction potentials are not. We also question the validity of the assumption that the

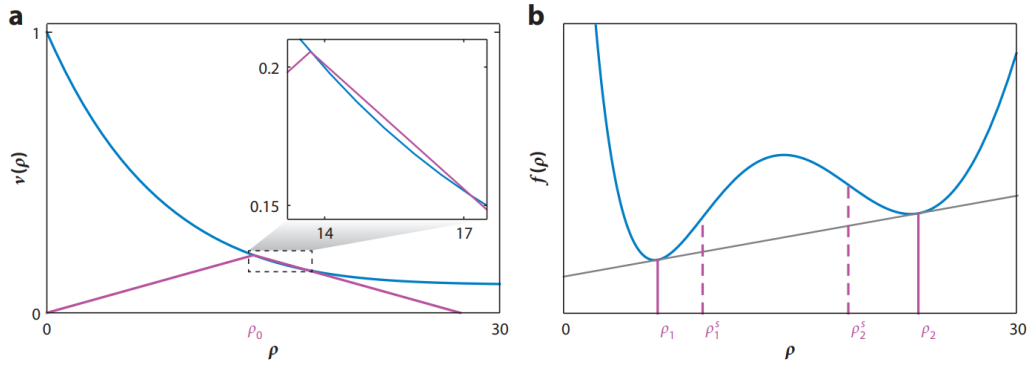

Figure 3.2: The construction of the effective free energy density $f(\rho)$. (a) If $v(\rho)$ decreases rapidly enough the resulting $f(\rho)$ (b) has a negative curvature (spinodal) region with the global equilibrium state comprising a coexistence of the binodal densities ρ_1, ρ_2. The condition for instability (equation 3.34) translates into the geometric construction shown in (a). The figures correspond to $v(\rho)$ given by equation 3.34, with $D_t \approxeq 1.4 \times 10^{-3}$, $v_0 = 1$, $v_1 = 0.1$, $\phi = 4$, $\tau = 2$ and $2\rho_0 = \rho_1^s + \rho_2^s$. From the work of Cates and Tailleur [4].

steric interaction between the particles is isotropic. Although the pairwise potential is radially symmetric, the collisions between particles in MIPS depend severely on the collision angle. As in most numerical simulations, in our case our simulation box is not large enough to necessarily be described by a coarse grained approach. More will be said on the relevance of this theoretical description throughout the chapter.

3.1.3 Feedback Mechanism Description

Although the description in the previous section covers most of the nature of MIPS, there exists an alternative perspective on the problem. A feedback mechanism from slight perturbations in density and velocity was also proposed by Cates and Tailleur [4].

We begin again with the relation between the PDF of a system as a function of position and velocity which is always a steady-state solution for isotropic processes:

$$\psi(\vec{r}) \propto \frac{1}{v_0(\vec{r})}. \tag{3.36}$$

In addition, if we consider that the dependence of the velocity of a particle could be a function of local density, which in a hard disks system of ABPs would arise from collisions, then it is feasible that MIPS originates from a positive feedback mechanism between the relations.

If one considers a small perturbation in the local density, $\delta\rho(\vec{r})$, around a mean density, $\rho_0 \equiv a/v(\rho_0)$, where a is proportionality constant, it would mean that the velocity is varying

and spatially dependent; $v[\rho_0 + \delta\rho(\vec{r})] = v(\rho_0) + v'(\rho_0)\delta\rho(r)$. The changes in density, $\delta\rho(\vec{r})$, and velocity, $\delta v(\vec{r})$, are in anti-phase as velocity decreases with density. Then the final density for a given velocity would be:

$$\rho_0 + \delta\rho' = \frac{a}{v(\rho_0) + v'(\rho_0)\delta\rho} \approxeq \frac{a}{v(\rho_0)}\left(1 - \frac{v'(\rho_0)}{v(\rho_0)}\delta\rho\right) = \rho_0 - \rho_0\frac{v'(\rho_0)}{v(\rho_0)}\delta\rho. \tag{3.37}$$

If the change in the perturbed velocity changes the density more than the initial density perturbation, then the system is destabilised. A linear instability arises whenever $\delta\rho' > \delta\rho$ and:

$$\frac{v'(\rho_0)}{v(\rho_0)} < -\frac{1}{\rho_0}. \tag{3.38}$$

3.1.4 A Kinetic Approach to Determining the Transition

Although both of the previous descriptions work well in many cases, they falter when it comes to explaining the dependency of MIPS on the Péclet number. Many numerical approaches have shown that the biphasic region of the $Pé/\phi$ phase diagram cuts off at a given $Pé$ which contradicts the previous descriptions which always predicts a spinodal decomposition for $\rho > \rho^*/2$ (ρ^* is the point where $v = 0$).

A final method to describe MIPS is able to account for this Péclet dependence. If one is to derive the kinetics of particles joining and leaving the dense region one can arrive to the conclusion that closely follows the binodal up to $Pé \approx 100$.

Following Ref. [1], we can derive the cluster fraction (the proportion of particles in the dense phase) in dimensionless parameters from the relation of the rates with which particles enter and leave the dense phase. It is plotted in figure 3.3 from the same article:

$$f_c = \frac{4\phi Pé - 3\pi^2\kappa}{4\phi Pé - 6\sqrt{3}\pi\kappa\phi}. \tag{3.39}$$

where κ is the average total number of particles in an escape event, ϕ is the average area fraction. κ has previously been measure to be around 4.5 [1] or 3 [69].

This description, unlike the previous two, does not have the constraints of needing to be coarse grained which is why it is able to account for the value of the Péclet number at the transition.

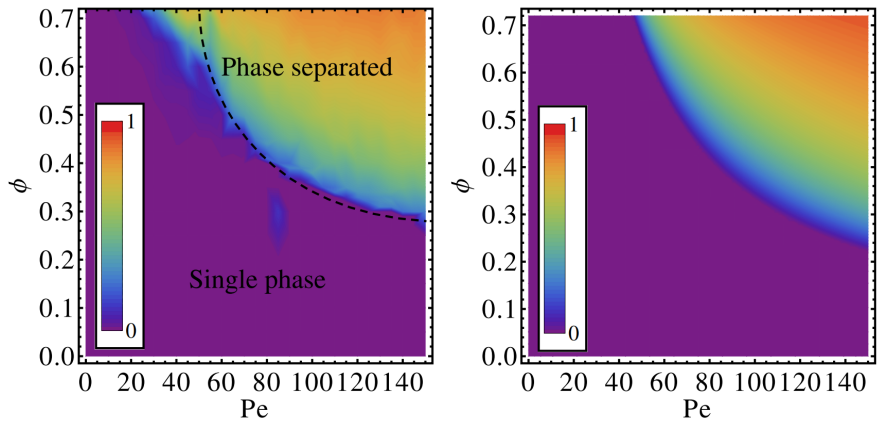

Figure 3.3: Cluster fractions of ABPs interacting via a WCA potential. Left: contour map of cluster fraction f_c measured from simulations. The dashed curve marks the approximate location of the binodal. Right: cluster fraction as predicted by analytic theory (equation 3.39). From the work of Redner *et al.* [1].

3.1.5 Spinodal Decomposition vs Nucleation and Growth

Phase separation can be described in two ways; nucleation and growth or spinodal decomposition. Both of these are not exclusive. A traditional thermodynamically equilibrated system which is quenched from a homogeneous fluid, will first have a large free energy barrier which prevents nucleation. However if that barrier is crossed when quenched from the dilute phase, then the dense domains will grow. This process is described by nucleation and growth [80, 161, 165, 166]. However if the system is quenched past the spinodal line, then the system becomes thermodynamically unstable with respect to any small fluctuation and spinodal decomposition occurs without the need for nucleation.

In the case of ABPs, quenching is equivalent to increasing the density of the initial configuration, or to increase the Péclet number of the particles.

Spinodal decompositions are detected using the static structure factor:

$$S(\vec{k}) = \frac{1}{N}\left\langle \sum_{i=1}^{N}\sum_{j=1}^{N} \exp(-i\vec{k}\cdot(\vec{r}_i - \vec{r}_j)) \right\rangle, \tag{3.40}$$

where N is the number of particles, $\vec{r}_i$ the position of particle i and $\vec{k}$ is the wave-vector related to the real space length scale L, the size of the simulation box, as $2\pi/L$ [80, 167].

In the work of Stenhammar *et al.* [6], it was shown that the continuum model as presented by Tailleur and Cates, in fact works excellently to describe a system of ABPs interacting via a

WCA potential. They showed this by comparing the typical length scales of the first minimum in the static structure factors measured from ABP simulations and the numerical solutions to the continuum model (figure 3.4).

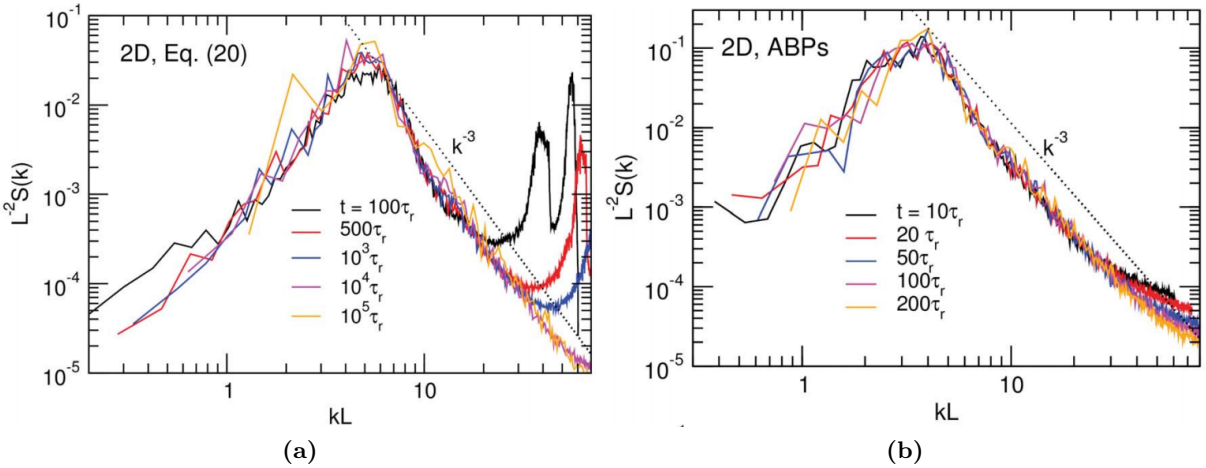

Figure 3.4: Mapping of the length scale of the first minimum in the static structure factor onto the continuum theory. Static structure factor $S(k)$ obtained at different times as indicated during ABP (left) and continuum (right) simulations in 2D. The curves have been rescaled in accordance with the dynamical scaling hypothesis according to Cahn-Hilliard scalings [160–163]. Dotted lines indicate the large-k behaviour predicted by Porod's law. The results show that the typical length scale in the system grows in time as with traditional spinodal decompositions. From the work of Stenhammar *et al.* [6].

For a description nearer to the spinodal/transition point in the $Pé/\phi$ phase digram we can again turn to the work of Redner *et al.* [1]. In their work, they required artificial seeding to promote MIPS to study the phase separation and showed that MIPS occurs via a nucleation and growth mechanism close to the transition. They also studied MIPS when it separates via spinodal decomposition. They showed that the mean cluster size scaled with $t^{0.5}$ with a corresponding length scale $L(t) \propto t^{0.25}$. The scaling with the length scale was also reported to be the same in two dimensions but not in three in the work of Stenhammar *et al.* [6]. These results confirm that using the Cahn-Hilliard theory on active repulsive particles is reasonable and MIPS is very similar to classical phase separation (although this still does no prove it). Because the difference in nucleation and growth and spinodal decomposition is hardly observable for systems with few particles and few growing domains we will, for the rest of this thesis, use language appropriate to nucleation and growth. This is to simplify reasoning and to remain consistent, something which the literature does not always achieve as the term spinodal decomposition has been loosely used [1].

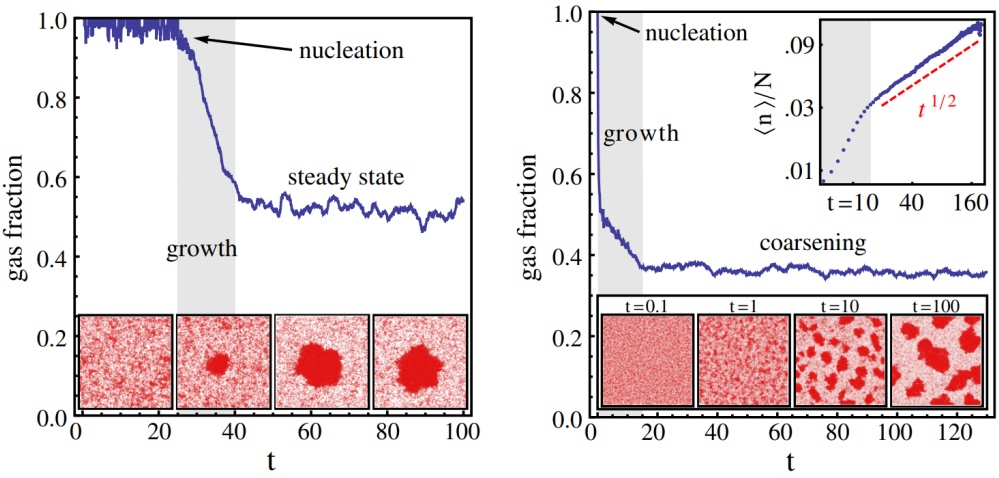

Figure 3.5: Dynamics of phase separation as shown by the gas fraction of a system. Left: a system with $Pé = 100$, $\phi = 0.45$ in which a delayed nucleation event leads quickly to steady state. For shallowly quenched systems, the nucleation time can be long enough that artificial seeding is needed to make nucleation computationally accessible. Right: a system with $Pé = 80$, $\phi = 0.6$ where separation leads to a coarsening regime which slowly evolves toward steady state. Inset shows mean cluster size scaling approximately as $t^{1/2}$. From the work of Redner *et al.* [1].

3.1.6 Characterising MIPS and Related Phenomena

Due to the simplicity of the ABP model, it is the most widely used in numerical simulations [1,2, 5,6,54,64,74,76–78,168–174]. However, there are simulations which involve other swimmers such as RTPs, squirmers and Quincke swimmers [54, 75, 78] [2]. More on swimmers with interactions can be found in chapters 4 and 5.

The second component of systems which undergo MIPS is their repulsive interaction. There have been many interactions used including: harmonic potentials [5,170,172], a Yukawa potential [168], a WCA potential [1, 6, 173] and a pseudo hard sphere potential [2]. The nature of the interaction is important to MIPS. Some systems, such as those used by Fily *et al.* [170], which include a soft harmonic potential, show how significant overlap up to particles passing over each other can alter the phase diagram of the system (figure 3.6(a)). Those who simulate their particle with harder potentials, such as in the works of Redner *et al.* [1] and Martin-Roca *et al.* [2], can make use of the structure factor (figure 3.6(b)) and the bond-orientational order parameter, an order parameter which can describe the hexagonal order in a system [175] [3], to characterise their systems due to the hexagonally arranged particles in the dense phases. Comparisons have

[2] Squirmers include a hydrodynamics interaction between swimmers which mimic those created by flagellated bacteria and Quincke swimmers, also known as rotators, move by a force created by a perpendicular electric field [53].

[3] A full description can be found later on in the methods section of this chapter.

been made on the stiffness of the interactions [2, 168]. Following the article by Martin-Roca *et al.*, where the WCA and PHS potentials were compared, it was clear that a harder interaction promoted phase separation. That investigation was done in collaboration with the work of this thesis and a more detailed description of this will be laid out in the first part of the results of this chapter.

Not only does the interaction affect the phase diagram itself, but it can have a significant effect on the dynamics of the dense phase. It has been shown in dense systems that the dense phase of active particles can behave as a glass with heterogeneous movement in a somewhat homogeneous structure [2, 168]. However, if activity is too high, then these glasses and initial configurations which are glass-like can be disrupted (figure 3.6(a)) [168, 170].

A common way to measure the progression of the dense phase is to use parameters such as cluster size, the cluster size distribution and the gas fraction (figure 3.5) [1, 69, 170]. This is because, even though deeper into the phase diagram the system will separate spontaneously, on the single particle level the formation of the dense region is indistinguishable from nucleation. MIPS is often therefore characterised in terms of phases and clusters. The first phase is "nucleation" where particles form the cores of clusters. Then there is cluster growth which is then followed by coarsening if multiple clusters are able to nucleate. The coarsening phase is where no new clusters can form as the dilute phase is too dilute for a nucleation event to occur and the smaller clusters evaporate slowly as the largest dense phase dominates.

All systems of moving particles can be described to have a pressure: the forces transmitted through a plane in the system. The pressure of the components of a phase separated system can be useful to described its nature. The pressure of active systems has been of particular interest in recent years [172]. It has been theoretically described in both dense and dilute systems and it has been shown that MIPS suppresses the pressure created by the motion of the active particles in the system.

Another aspect of phase separated systems are their interfaces. The interfaces of MIPS systems has been investigated by Patch *et al.* [173]. These interfaces show both equilibrium-like properties (an expected time-averaged density profile) and unusual behaviours such as a negative interfacial tension from the strong non-equilibrium fluctuations.

In a publication by Wysocki *et al.* [171], it was shown that there was an additional crucial

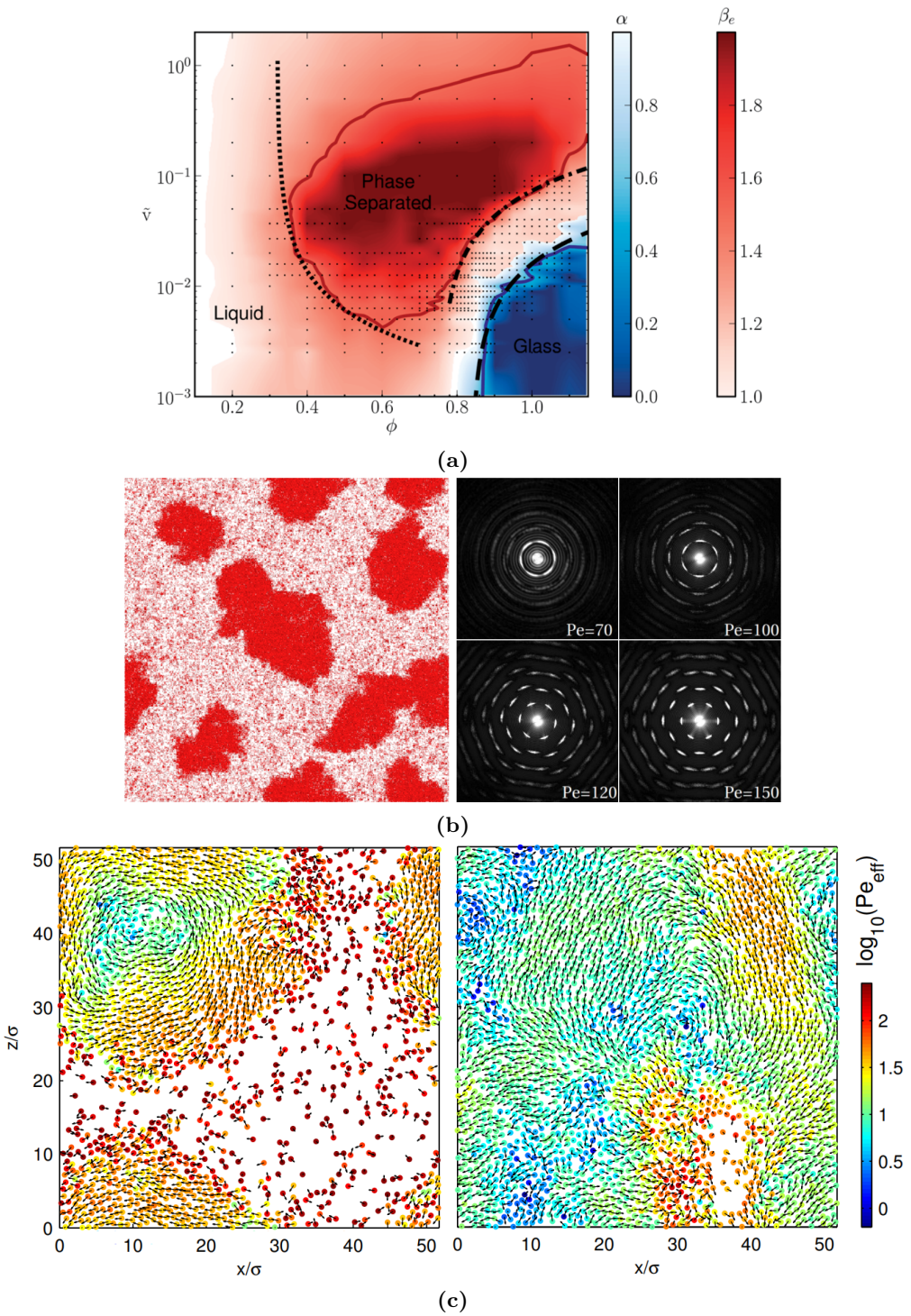

Figure 3.6: Behaviours in MIPS systems. (a) Colour map of the long-time MSD exponent α and local number fluctuation β_e in the (ϕ, v) plane showing the three phases of the system: homogeneous liquid, phase separated, and glassy. The phase separated and glass regions are disrupted at high velocities by particle overlap. From Fily *et al.* [170]. (b) A typical WCA simulation and the static structure factor restricted to the interiors of large clusters. The symmetric pattern on the right shows order. Adapted from Redner *et al.* [1]. (c) Collective dynamics in 3D system of active hard spheres at two average densities. From Wysocki *et al.* [171].

difference between systems in two and three dimensions. It was shown, with $Pé = 272$ [4] in 3D, that the dense phase was able to exhibit collective behaviour from the spatial sorting of particles with similar orientations near the interfaces of the dense phase (figure 3.6(c)). It was also stated that in 3D, high Péclet and high density systems are fluid, unlike in 2D ones which are crystalline [1]. This is explained in the ability for mono-disperse 3D phases to form glasses with internal currents which form under the inhomogeneous pressure of the clusters.

In a recent study by Caprini *et al.* [176], the spontaneous alignment of ABPs intaracting via a WCA potential was studied. They observed that the local correlation in the alignment of particles in the dense region of a MIPS system would increase with an increase in the persistence length of the particles. This observation, and others including those about pressure [177, 178], negative interfacial tension between the coexisting phases [173, 179], and different temperatures inside and outside of clusters [76], goes against the equilibrium based theory presented at the beginning of this chapter.

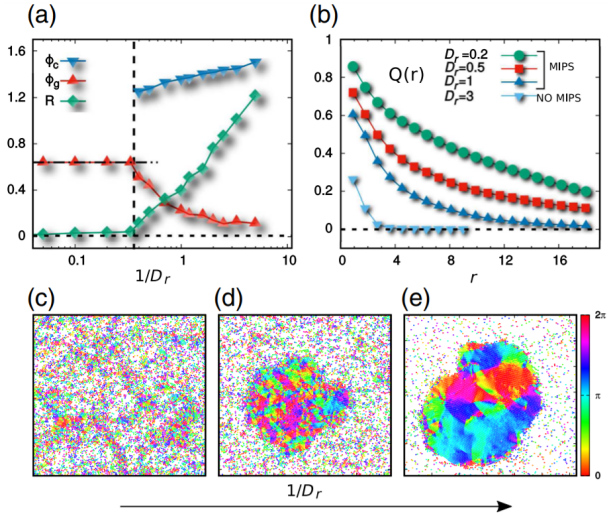

Figure 3.7: Correlations between the orientations of particles as the Péclet number increases. (a) Density, ϕ_g (red upper triangles) and ϕ_c (blue lower triangles) for the dilute and the cluster phase, respectively, as a function of $1 = D_r$. Velocity-alignment order parameter, R (green diamonds), as a function of $1 = D_r$. For presentation reasons, R is rescaled by a factor 6. Black dashed lines are guides for the reader: the vertical one identifies the value of $1 = D_r$ at which the MIPS transition occurs. Instead, the horizontal lines refer to the nominal density ($\phi = 0.64$) and the value of R in absence of velocity alignment (0). (b) Spatial correlation of velocity orientation function for different values of D_r, as shown in the legend, where we specify the presence or not of the phase separation. (c), (d), and (e) are snapshot configurations for three different values of $1 = D_r$. (c) is obtained for $D_r = 3$, panel (d) for $D_r = 1$, and panel (e) for $D_r = 0.2$. Colours are associated with the direction of the velocity of each particle. All the simulations are realized with numerical density $\phi = 0.64$, $v_0 = 50$ and the other parameters specified in the text. From the work of Caprini *et al.* [176].

It is unusual for systems with purely isotropic repulsive interactions to exhibit collective

[4] Defined as a high Péclet number in this article.

motion. Typically, an interaction which promotes alignment is needed [37, 180–184]. Systems which do this include the aforementioned Vicsek model which uses a specific interaction for alignment. However, it is possible to achieve collective motion via a more indirect method. By changing the shape of particles and exploiting self-assembly, similar to liquid crystalline systems [185], particles can align. This has been investigated by simulation for rod-like particles and dumbbells by van Damme *et al.* [64] and Suma *et al.* [182] respectively (figure 3.8).

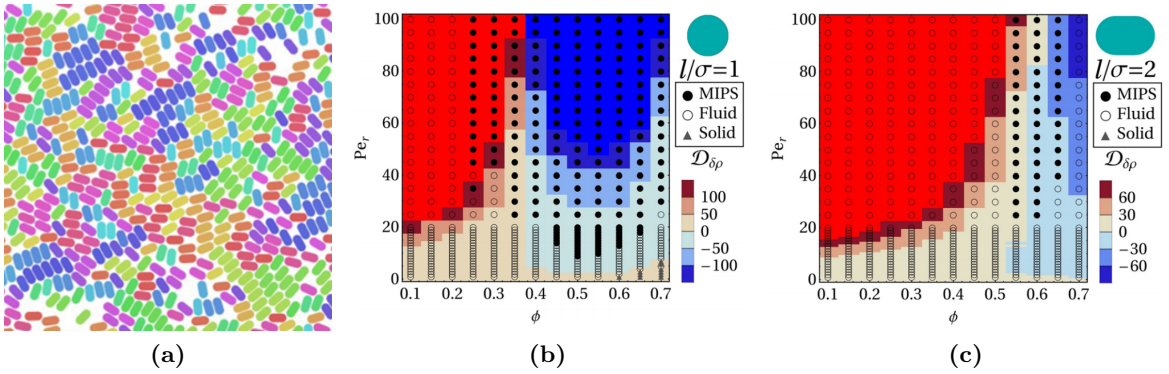

Figure 3.8: The suppression of MIPS by the alignment of active rods. (a) The dense phase of rods in a MIPS system. Phase diagrams of 2D self-propelled disks (b) and rods (c) as a function of *Pé* and ϕ. The colours indicate the diffusion constant of density fluctuations. From van Damme *et al.* [64].

Van Damme *et al.* showed that MIPS is suppressed beyond a given aspect ratio. Particle alignment prevents head on collisions and suppresses the reduction in velocities which cause the instability and the feedback mechanism for phase separation (figure 3.8). On the other hand, dumbbells promote MIPS and that the clusters formed are able to rotate and form a spiral-like pattern. They do this because there are inbuilt correlations between the two halves of the dumbbells and particles are not able to separate if hexagonal order is obtained (figure 3.9). These kinds of dynamics have also been seen in systems with simulated hydrodynamics, where MIPS can also either be enhanced or disrupted [54, 75].

Despite there being a breadth of literature on motility-induced phase separation there are many intricacies which require unravelling. A common feature among all previous results from numerical approaches is that they heavily rely on the particle interactions [2]. Although kinetic Monte Carlo methods have been used for systems of hard ABPs, they are limited in the method by the range of Péclet numbers they have access to [69]. In contrast to this, many previously studied systems of ABPs with repulsive interactions simulated with Brownian dynamics simulations have been unable to mimic truly hard systems and the competition between the motion of the particles and their interactions leads to other unwanted effects [2, 170]. This leaves pages

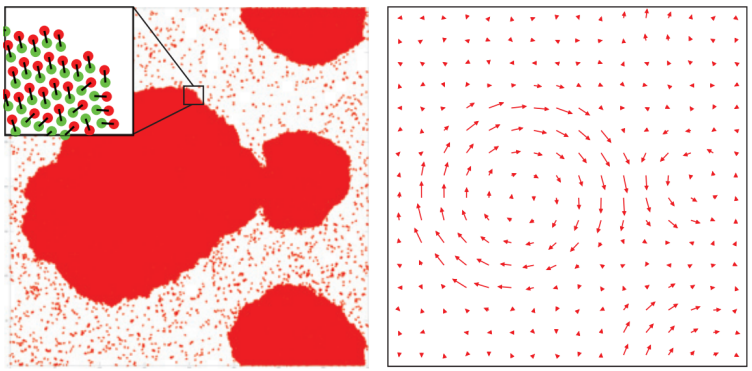

(a) (b)

Figure 3.9: Formation of active dumbbell rotating clusters. (a) Snapshot of a phase separated active dumbbell fluid with three clusters. (b) Coarse-grained velocity field corresponding to the snapshot in (a). From Suma *et al.* [182].

empty in the story of MIPS pertaining to truly hard particles at high Péclet numbers. Although attempts have been made to expand the phase diagram, by decoupling rotational and translational diffusion and only changing the rotational motion to change the Péclet number for example, it remains a difficult challenge to overcome.

3.2 Methods

Active Brownian Dynamics Simulations

To convert the equations of Brownian particles to active Brownian particles, the addition of an active force F_a in equation 2.33 is possible due to the additive relations in the Langevin equation. The active case therefore follows 1.5:

$$\vec{r}_i(t+\Delta t) = \vec{r}_i(t) + \sqrt{4D_t\Delta t}\vec{\xi}_i(t) + \frac{D_t}{k_BT}\vec{F}_a\Delta t + \frac{D_t}{k_BT}\sum \vec{f}_i(t)\Delta t. \tag{3.41}$$

For active simulations, the initial configurations were generated from the passive simulations. Activity is calculated as a displacement from a velocity in terms of particle diameter $s_a = v_a\Delta t/\sigma$ and applied along the orientation of the particle. Inter-particle interactions are calculated by differentiating the potentials from equations 2.35, 2.38 and multiplying them by the friction coefficient D_t/k_BT and the time-step Δt. For the SCP and SACP potentials, equations 2.39 and 3.42 are used. The positions of each particle are defined in (x, y, θ).

Because our simulations are intrinsically linked to the time-step, we are able to define time by what we call the "ideal displacement". It is the total distance a particle can travel with the given active velocity in a simulation if no collisions nor rotational diffusion occurs (the sum of all the active forces used on one particle) and is in units of σ, the particle diameter.

The Scaled Contact Potential in the Active Case

One of the conditions of our interaction requires us to create a potential which returns particles to contact, $r = \sigma$, after their overlap had been annihilated. When activity is added to a simulation, a constant force, then particles will have additional displacements when a collision occurs which must be considered.

There lies one major issue in the use of activity in Brownian dynamics which is one of the reasons why Brownian dynamics is used instead of other types of algorithmic approaches. Activity is implemented along the orientation of a particle. This means that from a displacement perspective, the particles are no longer isometric. Therefore, the degree of overlap between collisions depends on the angle of approach.

We trialled versions of simulations whereby we implemented a modification to the particle interaction which depended on relative orientation. However, due to the nature of motility-induced phase separation and dense phases, the collisions were not dependent on a single set of particles. Therefore, further complications would have needed to be resolved.

Instead we have opted to add a simple shift based on a head on collision. This is such that the contact position could be normalised in extreme cases. Because the total displacement of the active component of two particles is equal to twice the active velocity multiplied by the time we derived the following interaction (equal to zero if $r \geq \sigma + 2v_a\Delta t$):

$$s_{SACP}(t) = -\frac{1}{2}r + \frac{\sigma + 2v_a\Delta t}{2}, \quad r < \sigma + 2v_a\Delta t, \tag{3.42}$$

$$U_{SACP}(t) = \frac{k_BT}{4D_t\Delta t}r^2 - \frac{k_BT(\sigma + 2v_a\Delta t)}{2D_t\Delta t}r + \frac{k_BT(\sigma + 2v_a\Delta t)^2}{4D_t\Delta t}, \quad r < \sigma + 2v_a\Delta t. \tag{3.43}$$

The resulting potentials for both the passive (SCP) and the active (SACP) scaling contact potentials are shown in comparison to the WCA and the PHS potentials in figure 3.10.

For a simulation with a time-step equal to $\Delta t = \tau \times 10^{-5}$, the SCP potential is effectively steeper than the PHS potential which has been until now the interaction potential used in continuous dynamical simulations with the largest gradient. This means that changing the gradient by the prefactor works at least as well as changing the exponent. It is also the case that the SCP method will give the same particle interaction regardless of the simulation conditions given a certain time-step.

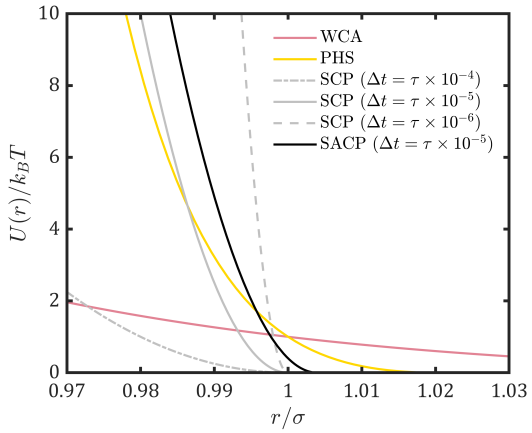

Figure 3.10: The scalable contact potential compared to commonly used potentials. The scalable contact potentials (SCPs) depend on the time interval chosen in simulation. The time intervals in the cases shown are in the legend. The Weeks Chandler Anderson potential is typically simulated with time intervals of $\Delta t = \tau \times 10^{-5}$ whereas the pseudo-hard sphere potential with $\Delta t = \tau \times 10^{-6}$. This means that using SCPs returns an improvement in both stiffness and computation time.

Linking motion to the Time-Step

Unlike in the passive case, we cannot simply only consider the Brownian motion; activity also contributes to overlap. Again using the case of a head-on collision the maximum total overlap will be equal to $2v_a\Delta t$. For a desired overlap threshold and therefore hardness, we consider which of either contribution is largest. This also extends for any interaction which leads to overlap (such as electrostatic attractions in chapter 5). In the simulations of this chapter, we define the time step to be the smallest of either $\tau \times 10^{-5}$ or $\sigma/v_a \times 2.5 \times 10^{-3}$; unless stated otherwise. This does mean that if for example v_a is extremely large, the disks will be "harder" from the perspective of the Brownian motion but the total overlap will be the same.

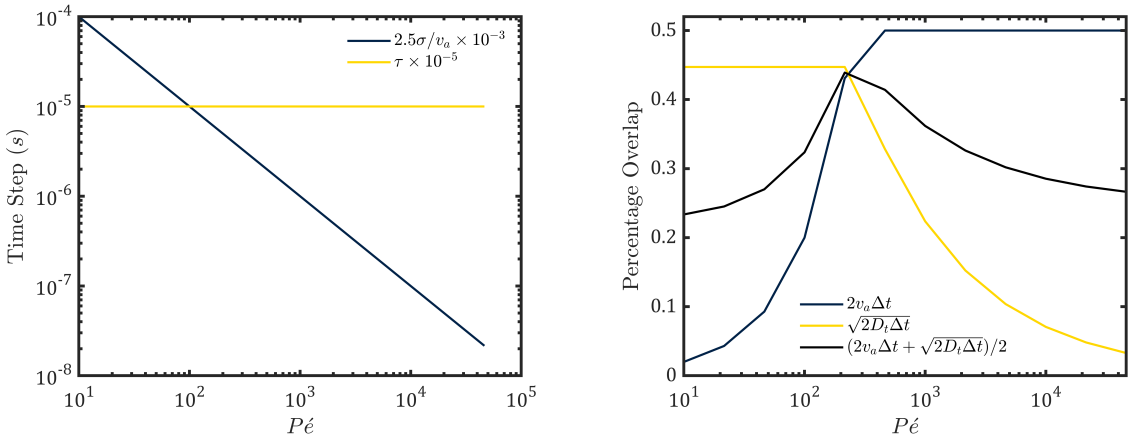

Figure 3.11: A comparison of time steps and displacements with both definitions. (a) A comparison of time steps using both definitions when changing v_a. (b) The comparison of probable displacements.

In figure 3.11(a) we show the value of the time step using both definitions. We see that the values cross at a given $Pé$ number. This converts to the displacements and therefore the likely percentage overlap in (b) which remains almost constant across all $Pé$ numbers; only varying less than 0.2 %. One could consider variations on the method to avoid using a cross-over for determining Δt. However, the steps one would take to move the crossover point will lead to an increase in computation time. For example, reducing the value of Δt in the active definition such that one uses the active form for all $Pé$ would lead to a substantial increase in computation time. On the other hand, increasing the passive value would lead to greater overlap. We therefore use this method as a balance of computation and hardness. Varying other parameters to change $Pé$ would lead to the same result as all displacements are relative to the value of the time step chosen as is shown in the beginning of the results section of this chapter.

3.2.1 Delauney Triangulation and Voronoi Tessellation

A Delauney triangulation is a geometrical method of determining nearest neighbour particles. It is defined to be a triangulation for which no point of a set of coordinates lies within its circumcircle. As an extension to this, once the centres of each circle defined by all of the triangulations are connected, a Voronoi diagram is created. In a Voronoi diagram, each point has an associated polygon which defines a region of closest proximity. By measuring the area of a polygon and taking its inverse, we can measure the local area fraction of a particle; we call

this ϕ_V.

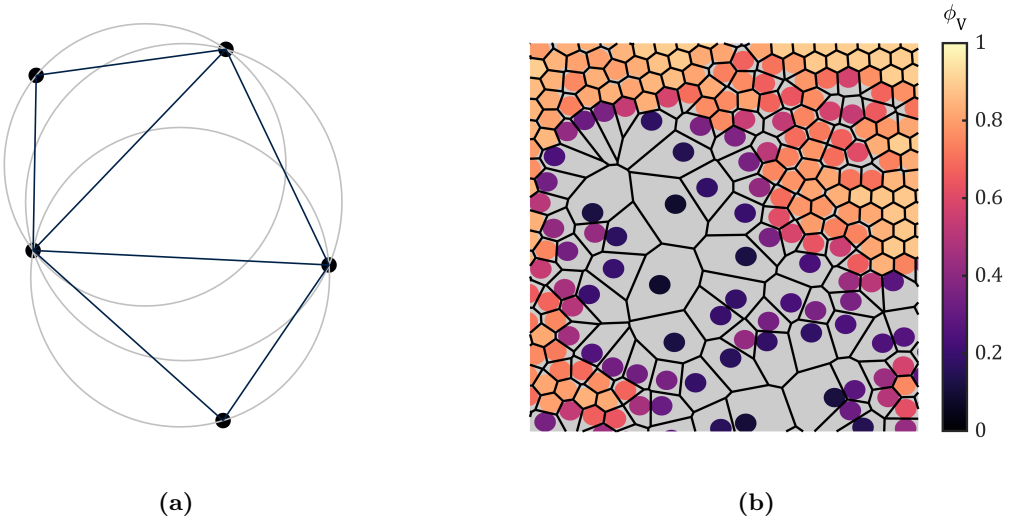

(a) **(b)**

Figure 3.12: The process of determining the local area fraction of a particle. (a) An example Delaunay triangulation on a set of 5 particles. The circumcircles of the triangles are shown in grey. (b) The local area fraction of a set of particles in an active Brownian simulation where MIPS occurs. The mesh denotes the areas of each particle determined by a Voronoi tessellation.

3.2.2 Static Structure Factor

Because both the static structure factor and the radial distribution function can be defined in terms of densities they can also be expressed in terms of one another [80]:

$$S(\vec{k}) = 1 + \frac{1}{N}\left\langle \sum_{i=1}^{N}\sum_{j=1}^{N} \exp(-i\vec{k}\cdot(\vec{r}_i - \vec{r}_j)) \right\rangle, \tag{3.44}$$

which in two dimensions can be written as:

$$S(\vec{k}) = 1 + 4\pi\rho \int_0^\infty r^2 g(r) \frac{\sin(kr)}{kr} dr, \tag{3.45}$$

which is the method we use to measure the structure factor in this work.

3.2.3 Bond-Orientational Order Parameter

Once a particle's nearest neighbours are defined, the local order around a particle can be determined. This is typically done by a bond-orientational order parameter for disks in two

dimensions:

$$\psi_6(\vec{r}_j, t) = \frac{1}{N_j(t)} \sum_{k=1}^{N_j(t)} e^{i6\Delta\theta_{jk}(t)}, \tag{3.46}$$

where $\Delta\theta_{jk}(t)$ is the angle between the x direction and the bond vector connecting the particle to its kth neighbour of the $N_j(t)$ total neighbours.

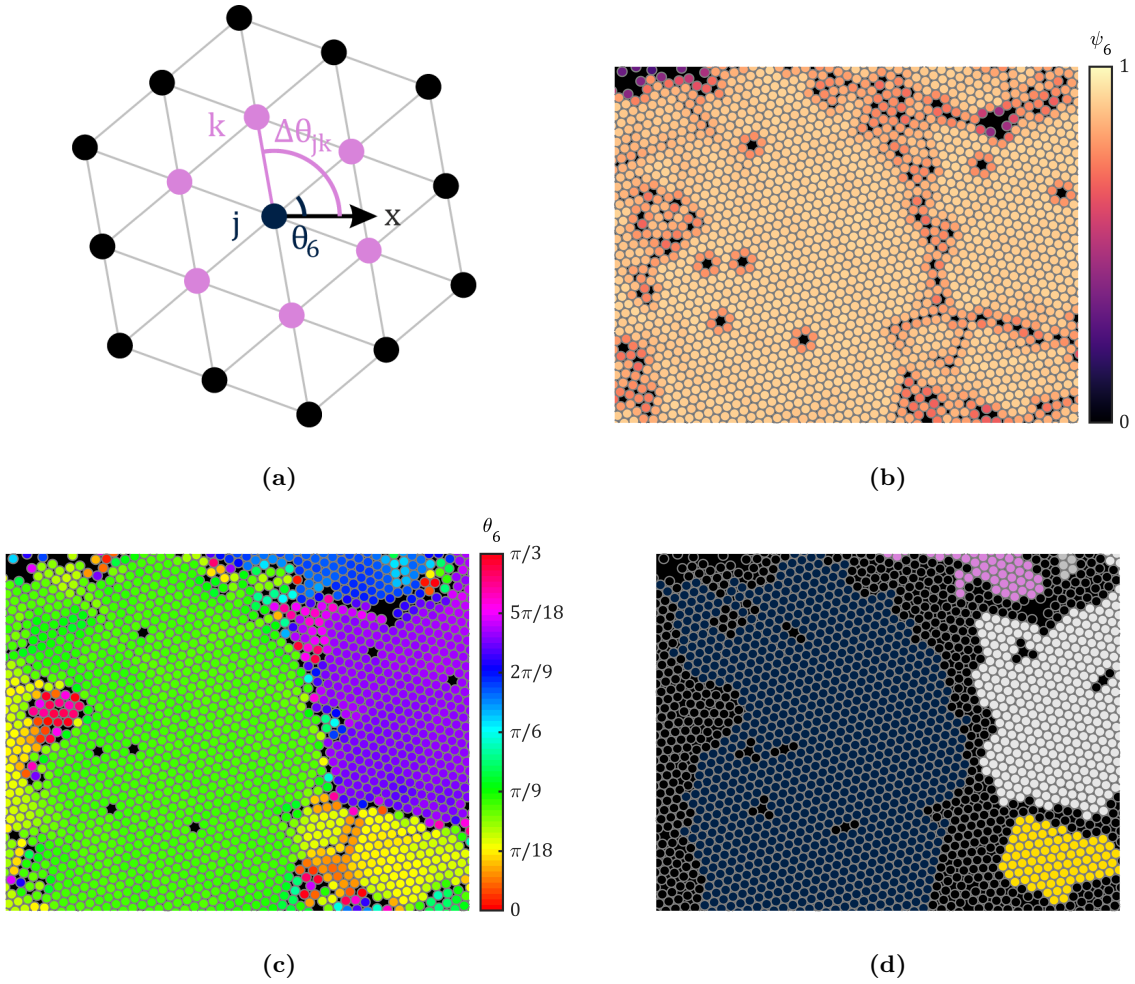

Figure 3.13: Procedure of determining crystallinity and grains. (a) A scheme of the nearest neighbours of a particle and the angle of its hexagonal organisation. (b) Local crystalline order parameter ψ_6, (c) local hexagonal orientation θ_6 and (d) detected grains in a dense phase of active particles. Particles which are not identified as grains are coloured in black.

The orientation of the hexagonal surrounding of the particles can be calculated by:

$$\theta_6(\vec{r}_j, t) = \frac{1}{6} arg(\psi_6(\vec{r}_j, t)), \tag{3.47}$$

which can vary between 0° to 60° due to the symmetry of the hexagonal structure of a 2D crystal.

A particle can be determined to be crystalline if its ψ_6 is above 0.7 [186]. Multiple crystalline particles in the same region all connected by crystalline nearest neighbours with the same hexagonal orientation can be defined as a grain. For the purpose of detecting grains we use a threshold of a difference of less than 0.75° in $\theta_6(\vec{r}_j, t)$ between three crystalline neighbours and require that a grain consists of more than 18 particles as 19 particles corresponds to the first two coordination spheres a particle can have (figure 3.13(a)).

3.2.4 Polar Order Parameter

In this chapter, we measure the correlations between particles as a function of distance. For this we use the polar order parameter between the particles a given distance from an initial particle. We then take the average for all the particles in the system:

$$P_\theta^{(1)}(r) = \frac{1}{N}\sum_{i}^{N}\frac{1}{N_r}\sum_{i\neq j}^{N_r}\cos(\theta_j - \theta_i), \tag{3.48}$$

where N is the number of particles i in the system, N_r is the number of particles j within a distance r of particle i and θ_i and θ_j are the angles of the particles.

If all the particles were to be aligned then $P_\theta^{(1)}(r) = 1$, $P_\theta^{(1)}(r) = 0$ if they are randomly misaligned and $P_\theta^{(1)}(r) = -1$ if they make an angle of π with respect to particle i.

3.2.5 MIPS Development Parameter

There have been many methods used to identify whether a system has phase separated due to motility. The most common method is to use the probability distribution of local area fractions of the system. Because particles separate into a dense phase and a dilute phase, two peaks arise in the distribution [1, 2]. Others have used parameters such as the variance of the packing fraction in given windows of a system [172], morphological transformations [171] or number fluctuations [170]. All of these methods use the structure of the system to determine if MIPS has occurred. This means they have two flaws. The computation time of the parameters depends on the number of particles and their diameter which as explained previously, for all currently used interactions, does not remain constant.

A final method was developed in the work of Martin-Roca *et al.* [2]. As a system phase

separates the displacements of the particles depend on which phase they are in and therefore the distribution of all displacements deviates from a Gaussian. A "non-Gaussian parameter" can therefore be defined:

$$\alpha_2(t) = \frac{< \Delta r^4(t) >}{2 < \Delta r^2(t) >^2} - 1. \tag{3.49}$$

As explained in chapter 1 and as will be covered in the first part of the results section of this chapter, we keep a constant particle radius and therefore area when using the SCP method. We also limit out simulations to 8192 particles at most which means that the computation time of structural parameters is not limiting.

Because our particles do not need a rescaled effective radius, the PDF of the local area fractions is quantitative. We therefore choose to define a MIPS development parameter:

$$\omega_M = \frac{\int |P_{\phi_V}(\phi_V|Pe,\phi) - P_{\phi_V}(\phi_V|0,\phi)| d\phi_V}{2}, \tag{3.50}$$

where $P_{\phi_V}(\phi_V|Pe,\phi)$ is the probability distribution of Voronoi area fractions for a given Péclet number and average area fraction, ϕ is the average area fraction and ϕ_V is the local Voronoi area fraction.

3.2.6 Cluster Identification and Tracking

A common method to measure the progress of phase separation is to determine the gas fraction/cluster fraction of the system [1, 5]. This can be done by taking the number of particles with a local area fraction beyond a certain threshold; for example using the mean area fraction. The drawback of these kinds of analyses is that they are global and do not tell us about the nature of the progression.

Others have reported using data pertaining to the size of clusters and their morphologies [171]. To determine if particles are in a given cluster it is common to use a distance cut-off between nearest neighbours.

In this chapter we use two methods of determining clusters on information which can be gathered about phase separating systems. To do this we employ various methods:

1. *Distance Cut-off:* The first method is to use a distance threshold. By taking the first minimum in the pair distribution function, a value of 1.2σ in our systems, we associate particles together and give them a cluster identification number.

2. *Minimum Crystallinity:* By determining the crystallinity of a particle using ψ_6, we then can filter out particles which are hexagonally ordered beyond a given threshold. We choose to use a $\psi_6 = 0.7$ cut-off as is commonly used in determining grains [20]. We then only allow particles which are considered "crystalline" to be part of clusters. Any particles with too low a value of ψ_6 are then given their individual cluster number.

3. *Using Grains:* Using the procedure to detect grains in a crystal laid out in the previous section, we can then associate a cluster number to a grain.

4. *Covering Grain Boundaries:* Because grains can be connected via a grain boundary in a single crystal, we also choose to provide a method via which grains can connect. By allowing each crystalline particle to have a second particle associated with it by proximity regardless of its crystallinity, a grain and therefore cluster can be joined to another. This allows for a final cluster to be composed of many grains.

When we discuss a cluster, we identify them using a distance cut-off, a minimum crystallinity and connect them over grain boundaries. When a grain is discussed it is defined as simply a grain. Typically a grain is limited to a minimum of 19 particles, enough for 2 coordination shells. However, because we identify clusters with particle IDs we do not include this limit in our analysis unless absolutely necessary.

A more complex problem than the identification of a cluster for a given time, is to be able to track them. The question of what defines a cluster and how fast its properties can change over time is not obvious [5]. For example, the centre of mass of a cluster, determined solely by particle proximity can drastically change if two clusters of approximately equal size collide. Their shape can also add complexity to that description.

One could take the perspective of identifying a cluster by the identity of the particles which it contains. This, although it seems at first glance to solve the problem, has issues when for example the particle which was at the source of the cluster's original nucleation leaves the cluster. One could try to confine the definition of a cluster over time with a plethora of properties but

[5] Much like the mythological/philosophical problem of the ship of Theseus

each one of them would require a set of thresholds which could vary depending on the conditions of the system.

We choose to combine the idea of using the particle IDs and the composition of a cluster over time from those IDs. By initially defining each particle to be in a cluster on its own at $t = 0$ we can then extrapolate an identity of a cluster over time by referring to a log of the particles which it contained. We implement this according to the flow chart in figure 3.14. The steps taken are to ensure that certain events do not prevent losing the identity of clusters due to events in the system. They go as follows:

1. We introduce a time-cut off threshold which corresponds to the amount of time beyond which we do not take the history of a cluster into account. This is to avoid having a bias of time over cluster size for long simulations. It must be long enough to avoid quenching events which we consider to be cluster behaviour but not too short for IDs to change rapidly due to collisions. We use a time it would take for particle to move 200σ due to its active component if it had no rotation.

2. We define a priority list when determining which clusters take IDs by priority. We first consider the frequency all the particles in a given cluster have had the ID of the cluster and then their size. If there are equal clusters in both of these parameters, the one with the lowest temporary ID [6] takes priority. This is to avoid IDs jumping around due to frequent collisions of large clusters.

3. Clusters which need new IDs once the highest priority cluster has been tracked then are given the ID of the particle closest to its centre of mass. This means that the ID should remain as long as possible.

4. The final consideration is when a particle with the same ID of a cluster leaves the cluster, leaving behind a large cluster of particles which take the ID by priority. This leaving particle then retroactively gets given a fresh unique particle ID.

5. All clusters in a given frame must end up with a unique tracked ID.

This procedure works as well regardless of the method we use to determine a cluster in a given frame. Previous works on MIPS have not had to implement such procedures. Data such

[6] The cluster ID of a given frame.

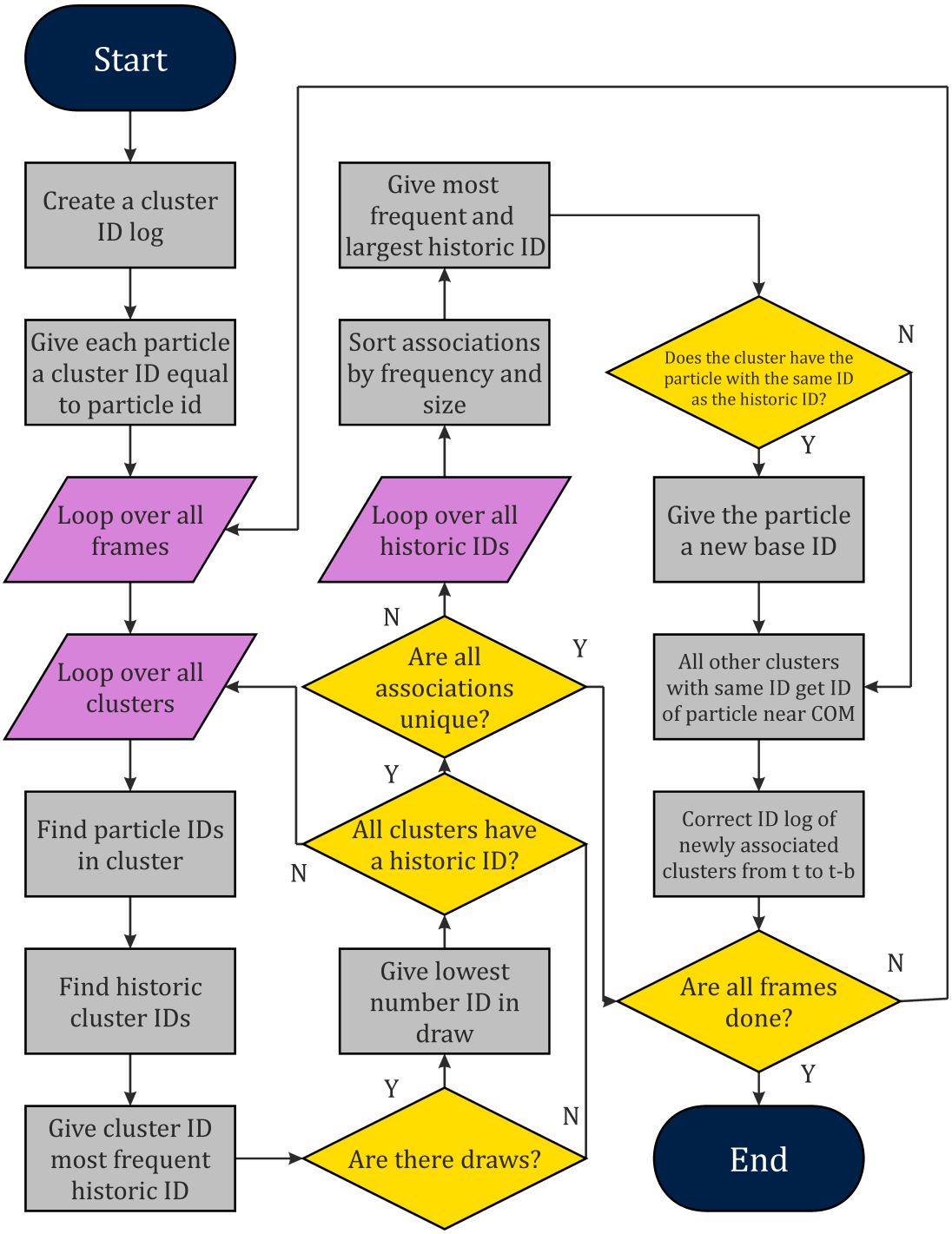

Figure 3.14: A flow chart of the procedure to track clusters.

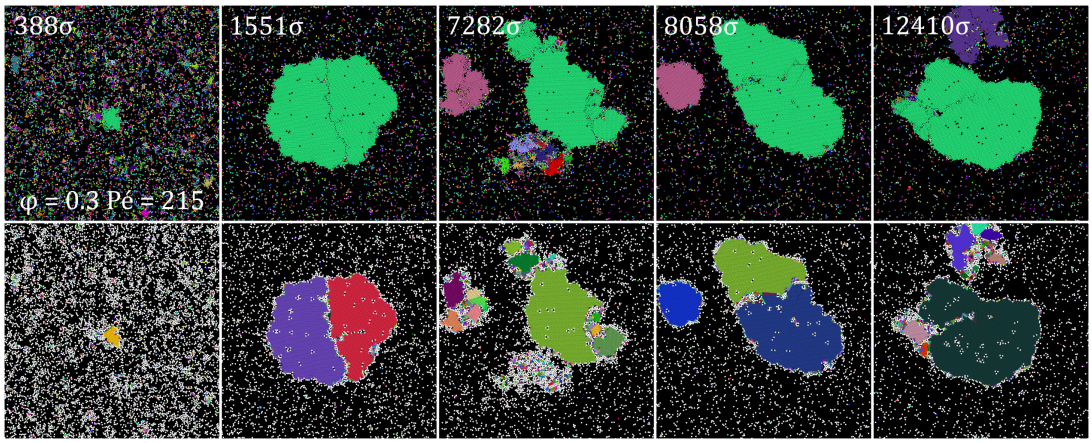

Figure 3.15: Examples of the results of tracking clusters. A series of images over the progression of a single simulation at $\phi = 0.3$ and $Pé = 215$ showing the identification of clusters (top) and the identification of grains (bottom) over time. Each colour represents an ID number. The green cluster retains its ID over time even with clusters breaking off. The grains however have much richer dynamics and change their ID due to breaking and rearranging.

as the cluster size distribution over time tracks frames and not individual clusters over time.

3.2.7 Determination of Cluster Torque and Rotation

Thanks to the crystallinity of a grain or cluster, we can use the orientation of the grains which make up a group of particles in the dense phase as a means of cluster angle. Therefore, tracking the angular velocity of a cluster is relatively trivial. This however does not give us any extra information about the behaviour of a cluster. We therefore also introduce a method of analysing the centre of rotation of a cluster.

Each particle in a cluster will act on the cluster via its propulsion force. Therefore, a torque can be estimated by summing all the tangential forces in a cluster. To calculate this, a centre of rotation is needed. By considering the displacement of the particles between two frames we can construct a set of vectors perpendicular to the lines which approximately go to the centre of rotation (figure 3.16). If one takes the centre of mass of all the intersections of the lines then one can obtain an approximate location for the centre of rotation of a cluster. When a grain is concerned we take the mode of the probability density of the intersections. The reason for the final step is that we are unable to decouple a translation of a cluster whilst a cluster rotates without more extensive procedures, which for this work are not needed.

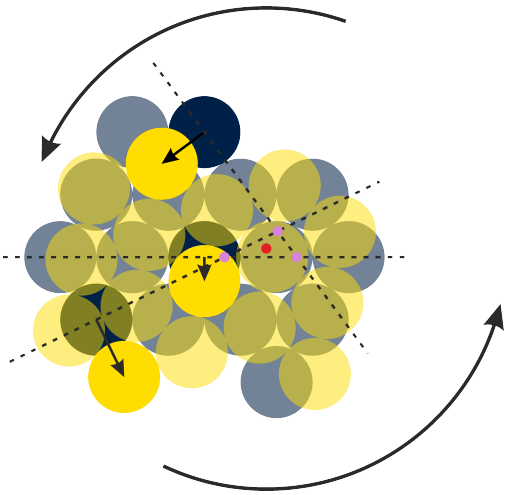

(a)

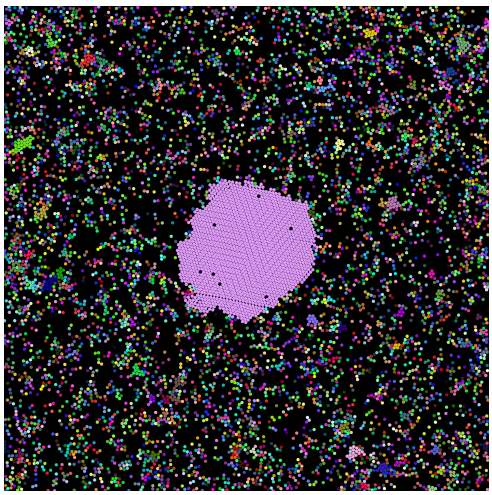

(b)

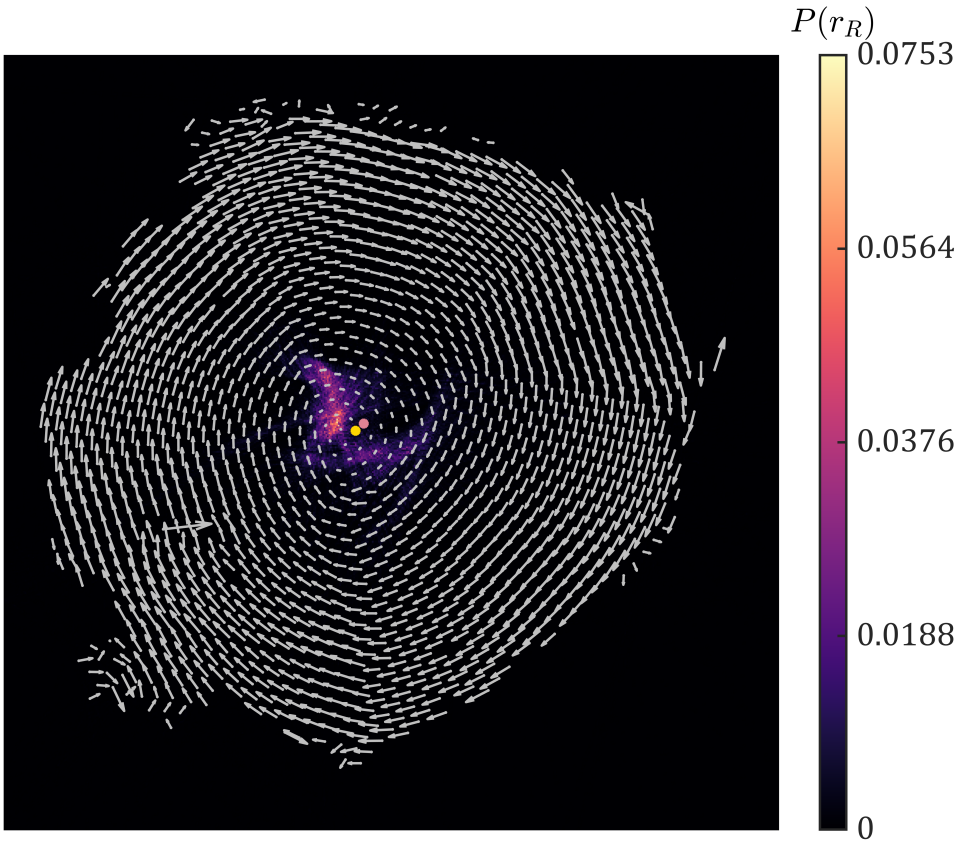

(c)

Figure 3.16: A scheme demonstrating how to estimate the centre of rotation of a cluster. (a) Some of the displacements from blue to yellow are shown with arrows and the centre of rotation is shown in red. (b) An image of a cluster in a simulation with $\phi = 0.3$ and $Pé = 4162$ during growth. (c) The probability distribution of the intersections calculated using the aforementioned method with the velocity vector diagram of the particles behind one ideal displacement (arrows scaled by a factor of 2 for the diagram). The centre of mass is shown in pink and the centre of rotation in yellow.

The torque of a cluster then becomes:

$$T = \sum_{i}^{N} \vec{F}_a \times (\vec{r}_i - \vec{r}_R), \tag{3.51}$$

where N is the total number of particles in a cluster, $\vec{F}_a$ is the active force, $\vec{r}_i$ is the position of particle i and $\vec{r}_R$ is the centre of rotation.

3.2.8 Creating Sticky Disks

In the second half of the results we compare the phase diagrams of ABPs with and without rotational friction. We create "sticky disks" using the following equation during our simulations:

$$\delta\theta_j(t+\Delta t) = \sum_{i}^{N(\sigma_f^*)} -\frac{\mu_f N(\sigma_f^*)}{6}\left(\frac{\hat{u}_j(t+\Delta t)\cdot(\vec{r}_j(t+\Delta t)-\vec{r}_i(t+\Delta t))}{|\vec{r}_j(t+\Delta t)-\vec{r}_i(t+\Delta t)|} - \frac{\hat{u}_j(t)\cdot(\vec{r}_j(t)-\vec{r}_i(t))}{|\vec{r}_j(t)-\vec{r}_i(t)|}\right), \tag{3.52}$$

where $\delta\theta_j(t+\Delta t)$ is the total angle change due to friction, $N(\sigma_f^*)$ is the number of neighbours determined by a distance threshold of $\sigma_f^* = 1.1\sigma$, μ_f is a dimensionless friction coefficient which we only used as 1, $\hat{u}_j(t)$ is the velocity vector of particle j, $\vec{r}_j(t)$ its position and $\vec{r}_i(t)$ the position of particle i where i is a neighbour of particle j.

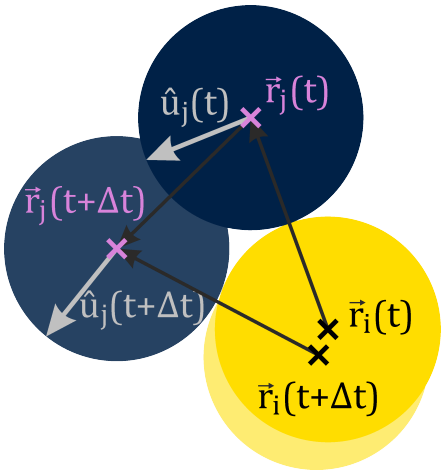

Figure 3.17: A scheme demonstrating the vectors associated with creating sticky disks. Particle j is in blue and i in yellow.

In simple terms this reduces the relative change in angle between a particle's orientation and the orientation of its local environment created by its neighbours. If a particle has six particles

then the relative difference cancels out any other angular motion. This step in the simulation is always done last such that all other contributions to angular changes are affected.

This approach, whilst using a value of σ_f^* much larger than contact, is a simplified way capture hydrodynamic coupling and particles locking to each other.

3.3 Results

3.3.1 Comparing MIPS with Different Potentials

As in the previous chapter, we must check whether our novel particle interaction is suitable for the simulations we wish to investigate. For this we compare $Pé/\phi$ phase diagrams of SCP systems with those of WCA and PHS systems, shown in figure 3.18. The phase diagrams for the latter two potentials are from the work of Martin-Roca *et al.* [2], an article in collaboration with this work.

In figure 3.18(a), we compare the SCP method with a $\Delta t = \tau \times 10^4$ to phase diagrams of particles with a WCA interaction. This is because the WCA potential is softer than the PHS potential (more information on this can be found in chapter 2). In figure 3.18(b), we compare the SCP method with a $\Delta t = \tau \times 10^5$ to phase diagrams of particles with a PHS interaction. As in line with Ref. [2], we show the many phase diagrams for each potential and some methods of varying the Péclet number is changed. Because the Péclet number [7]:

$$Pé = \frac{3F_a D_t}{\sigma k_B T D_r}, \tag{3.53}$$

depends on the active force, the translational diffusion coefficient and the rotational diffusion coefficient, any of the three are viable options to vary $Pé$ [8]. All three of the phase diagrams have a common Péclet number equal to 16 where $k_BT/\epsilon = 1.5$, $D_r = 4.5$, $D_t = 1.5$ and $F_a\sigma/\epsilon = 24$ from which any of the three values is changed. When changing D_r in this case, the Stokes-Einstein relation between D_t and D_r is broken such that only D_r is changed.

As can be seen by the slight variations in the phase diagrams, the method with which one

[7] Where F_a is the active force, D_t is the translational diffusion coefficient, k_B is the Boltzmann constant, T is the temperature and D_r is the rotational diffusion coefficient

[8] Equation 3.53 is an alternative form of the equation which was presented at the start of this chapter.

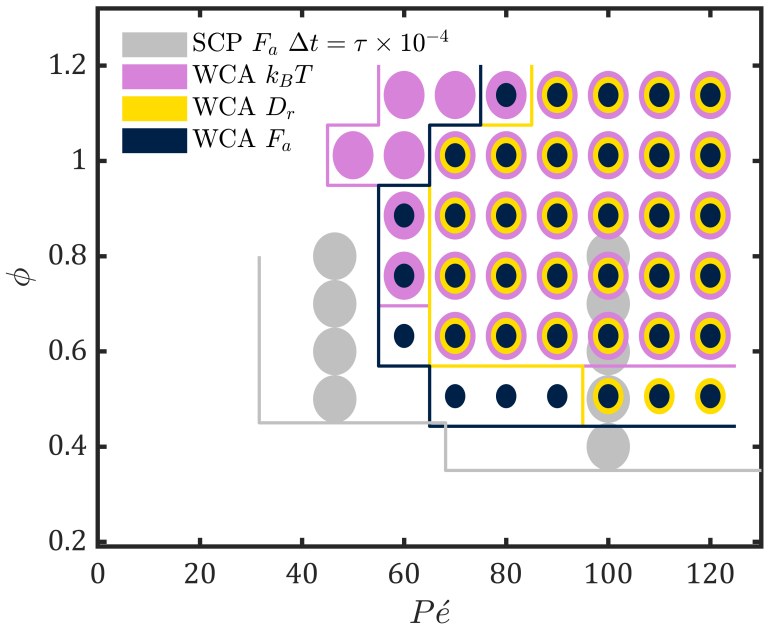

(a)

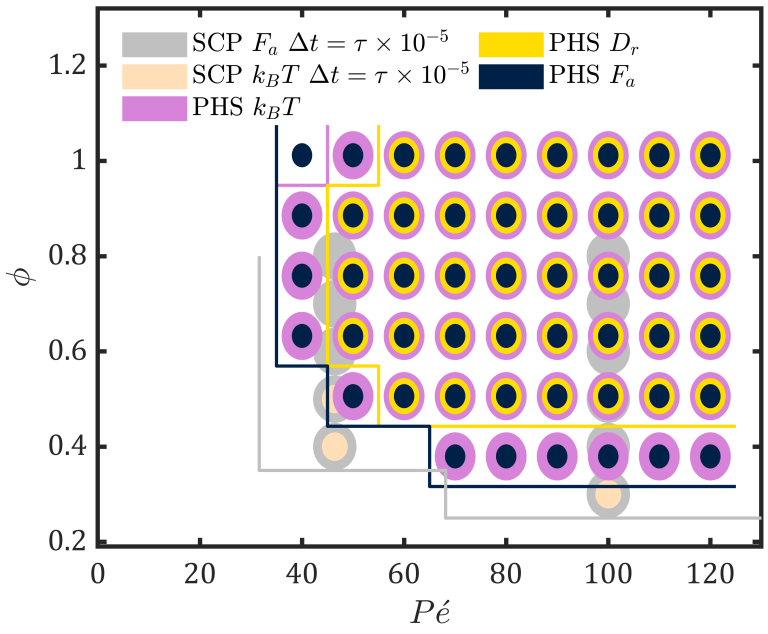

(b)

Figure 3.18: Phase diagrams in $Pé/\phi$ space using different potentials and methods for changing $Pé$. (a) Phase diagrams of the softer potentials, as laid out in the legend of the figure, where we can compare our results using a softer version of the SCP method to previous data with a WCA potential. (b) Phase diagrams of harder potentials including SCP $\Delta t = \tau \times 10^{-5}$ or $\Delta t = 2.5\sigma/v_a \times 10^{-3}$ and PHS. Each dot represents a data point where MIPS was observed. The lines correspond to the midpoint between the last non MIPS point and the first MIPS point, and approximation of the binodal.

changes the Péclet number is important for MIPS. One can take the phase diagram where D_r is changed as the base case to explain the differences. Changing a rotational component of the system will not affect the relation between density and velocity which are both translational.

When k_BT is changed, in this case by reducing its magnitude, the MIPS region starts at lower $Pé$. This can be attributed to a reduction in translational diffusion which allows for particles to become more jammed when near a surface [9]. When F_a is changed, the MIPS region moves to lower $Pé$ and ϕ because the collision forces from the activity grow relative to the repulsion force and the translational diffusion, and as such the particles overlap more they become more jammed and effectively reduce in diameter.

If we then compare the results with the PHS potential to those using the SCP potential, we can see that not only does MIPS occur at lower $Pé$ and ϕ for the SCP method, which can be attributed to the increased hardness of the particles and their constant radius, but the results do not vary when changing either k_BT or F_a. The second point is an important result as it confirms that relating all the forces which are felt by the particles (namely activity, repulsion and diffusion) to the time-step such that the particle remain almost as hard as each other regardless of the conditions can be achieved and is important to keeping the whole phase diagram consistent.

The effect of how consistently hard the particles are in simulations using the SCP method can be seen in figure 3.19. In (a) we show the probability density profiles of the Voronoi densities of the particles in simulations with a total area fraction of $\phi = 0.6$. We see that as the $Pé$ number increases, the distribution widens until it obtains the characteristic double peaked shape of MIPS. In (b) we show the same but for a constant $Pé$ and varying ϕ. In both cases we not only see that the maximum of the peak in the dense region remains at $\phi = 0.9$, close to the maximum packing fraction of disks but also that there are two peaks around 0.84 and 0.77 which correspond to particles around the edges of clusters and around vacancies (as shown in figure 3.19(c)).

If one compares this to the probability density distributions in (d), those from simulations with the much softer WCA potential, one can see that we no longer see the fingerprint of the structure of the cluster and no longer have a constant maximum packing fraction. WCA potentials have been used in simulations of MIPS where the clusters appeared crystalline as measured by the structure factor in the work of Redner *et al.* for example [1]. However we can

[9] Their effective radius is larger for larger diffusion.

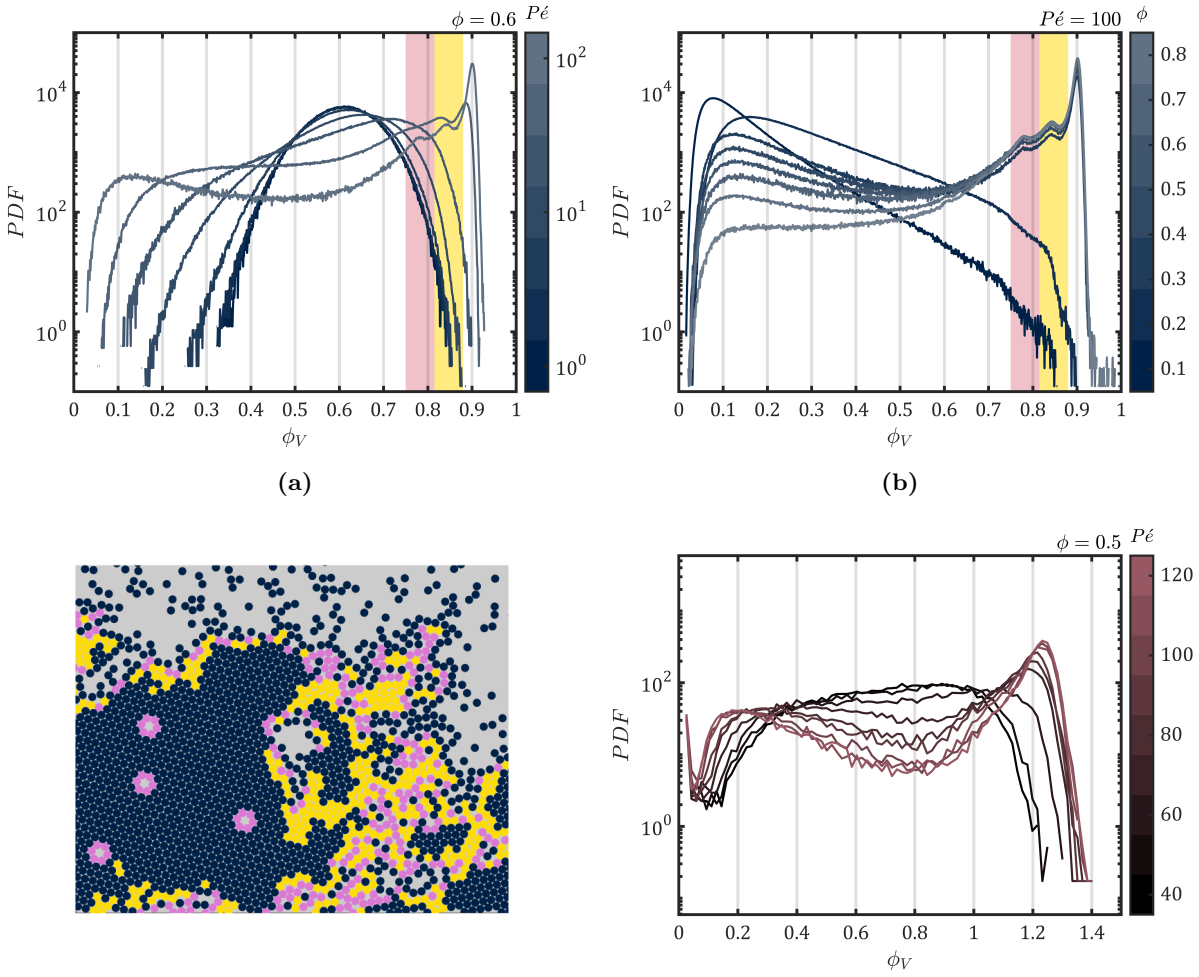

Figure 3.19: Voronoi density probability density distributions for various simulations. (a) PDFs of particles simulated via the SCP method at various Péclet numbers for a total area fraction of $\phi = 0.6$. (b) PDFs of particles simulated via the SCP method at various packing fractions for $Pé = 100$. (c) An image of a simulation at $\phi = 0.6$ and $Pé = 100$. The colours in (c) (pink and yellow) correspond to the bands shown in (a) and (b). (d) PDFs of particles simulated with a WCA potential at various Péclet numbers for a total area fraction of $\phi = 0.6$. Data in (d) is from the work of Martin-Roca *et al.* [2]. The lines for the phase boundaries are equidistant between the last non-separated and the first separated points.

see from these results that a WCA potential is too soft to be classed as a hard potential when compared to the SCP method.

3.3.2 Properties of MIPS via the SCP method at usual Péclet Numbers

As we have shown in the previous section, the SCP method enables us to examine MIPS with a consistent interaction regardless of Péclet number and allows one to observe details of cluster organisation. Therefore we compare our simulations to previous results using metrics which are

traditionally used for analysing MIPS.

As has been previously mentioned, it is difficult to distinguish between nucleation and growth and spinodal decomposition in these types of systems. We will therefore use the terminology around nucleation and growth to explain our results. In figure 3.20(a), we see a single nucleation event which leads to the growth of a single large cluster. This occurred at all of our simulations at a packing fraction of $\phi = 0.3$. This behaviour, although linked to the size of the simulation box, would agree with our findings that the boundary of the MIPS region is essentially flat around that packing fraction for the SCP potential with $\Delta t = \tau \times 10^{-5}$ or $\Delta t = 2.5\sigma/v_a \times 10^{-3}$. This is because nucleation is rare near the phase boundary and once a cluster begins to form, the probability of forming a second in the dilute phase decreases.

Deeper into the phase diagram, before the particles constitute a majority of the area of the simulation box, our systems can nucleate multiple initial clusters. This, as shown in figure 3.20(b), is when multiple clusters form at once before they coarsen into one large cluster. Because they do so by evaporating, the process is similar to what is known as Ostwald ripening.

If the packing fraction is over 0.5, then the notion of a cluster is no longer viable. In figure 3.20(c) we show a simulation at a packing fraction of 0.7 where the dense phase rapidly forms and is able to cross the entirety of the simulation box and reconnect with itself. This could also be thought as nucleations of the dilute region in a larger dense phase.

In figure 3.21, we show the cluster fractions of the simulations at $\phi = 0.3$ and 0.4. (a) shows the phases of growth from nucleation to the steady state. Because only one cluster appears there is no coarsening regime. The coarsening phase in (b) is at the beginning of the plateau in the cluster fraction. These are very similar to previous results like those of Redner *et al.* [1]. A point of note is that the length of the coarsening phase, when no more cluster are nucleating, will depend on the size of the simulation box. In our case, because we use only 8192 particles the coarsening regime is short [10].

We compare the progression of the simulations at three area fractions in figure 3.22. In (a), one can see that the base cluster fraction of our simulations, shown in the black lines, depends on the total packing fraction; this is because our definition of a cluster and/or the dense phase is density dependent. The curves at $\phi = 0.3$ all have a lag time before phase separation which

[10] Using optimised codes packages such as LAMMPS and HOOMD, previous works have gone up to 512 000 particles.

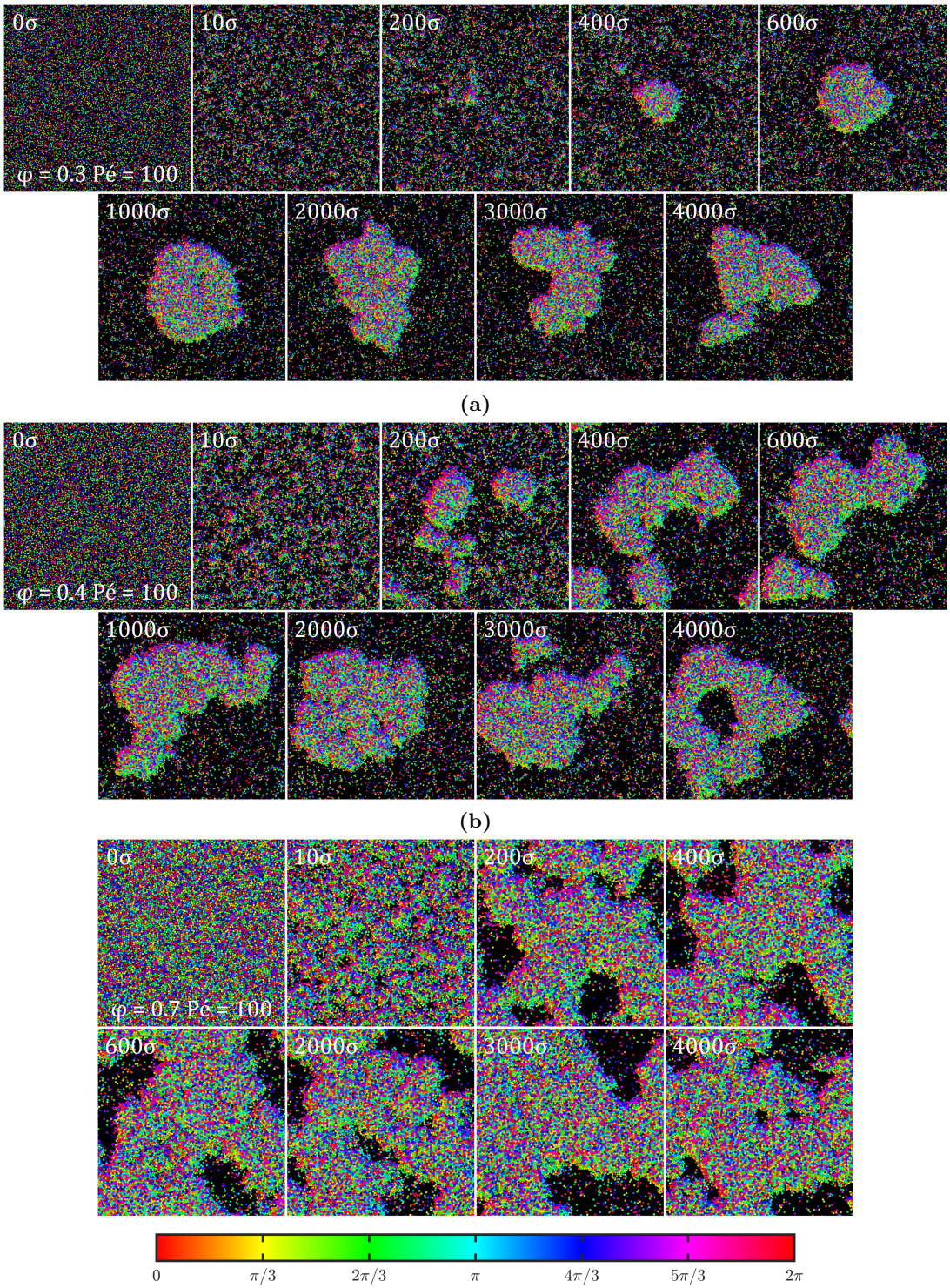

Figure 3.20: Three representative simulations presented as a series of images. All three are at a Péclet number of 100 with (a) at $\phi = 0.3$, (a) at $\phi = 0.4$ and (c) at $\phi = 0.7$. The colours of the particles represent the angle they make with the simulation box as shown by the colour bar at the bottom of (c). The nucleation of a single cluster is shown in (a), multiple clusters in (b) and a large dense region which spans the entirety of the simulation box in (c).

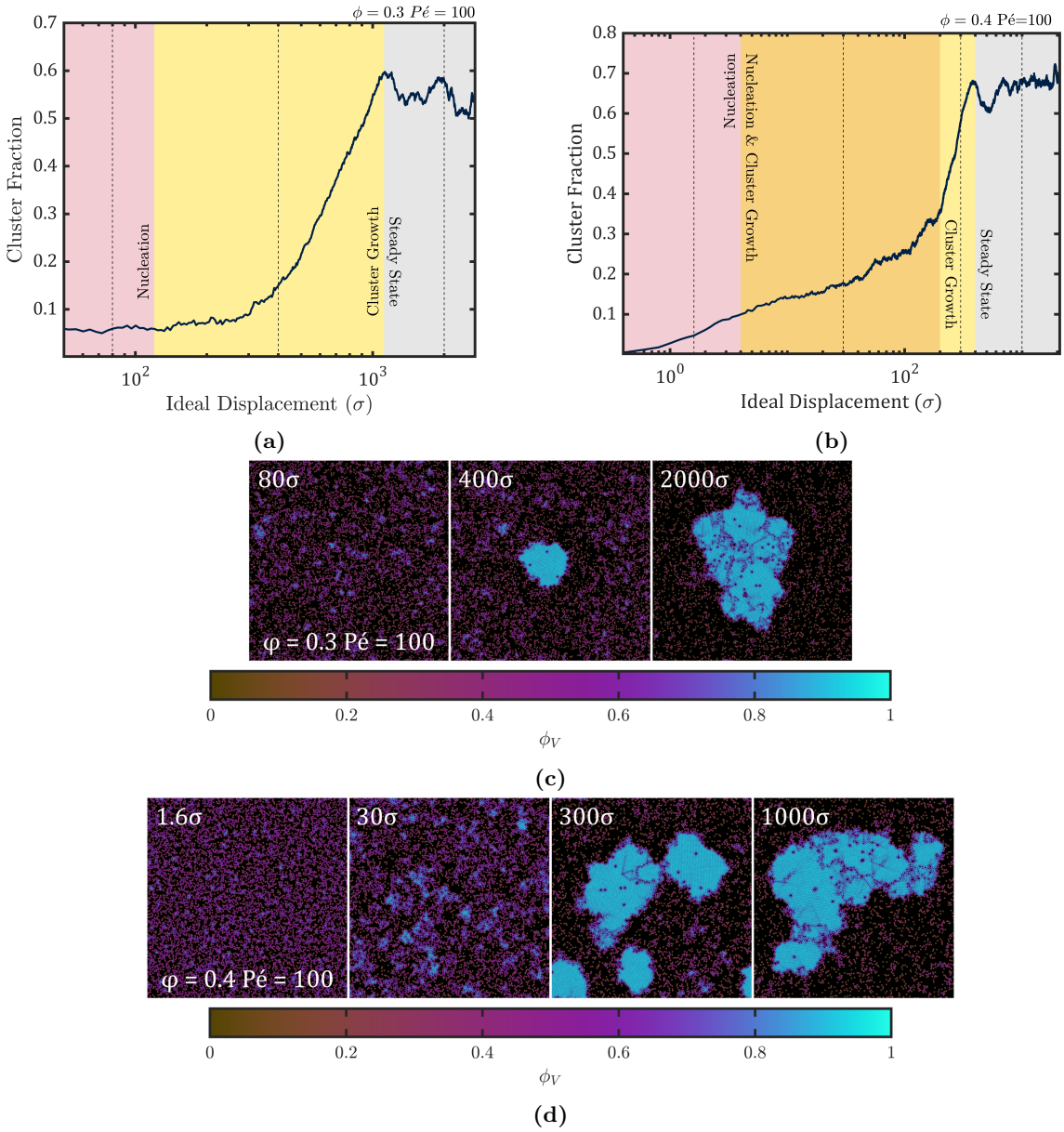

Figure 3.21: The difference in progression when multiple clusters initially nucleate. (a) and (b) are the cluster fractions, the proportion of crystalline particles determined by $\phi_V > 0.7$, of simulations at $Pé = 100$ and $\phi = 0.3$ and 0.4 respectively. The regimes are shown as colour patches in the background with corresponding images of the dashed lines shown in (c) and (d). (c) and (d) show the densities of the particles via for each of the highlighted points in (a) and (b).

shows the existence of the kinetic barrier whilst the others do not. A second point of note is the rate of growth. Because only one cluster forms at $\phi = 0.3$ its growth is the fastest; this is because the particles are never hindered and efficiently arrive at the interface at the optimal angle for remaining the longest time. The slowest growth is at $\phi = 0.7$ as the structure of the dense phase, which covers the whole of the box, prevents efficient particle motion and it takes a while for a neat dense phase to form.

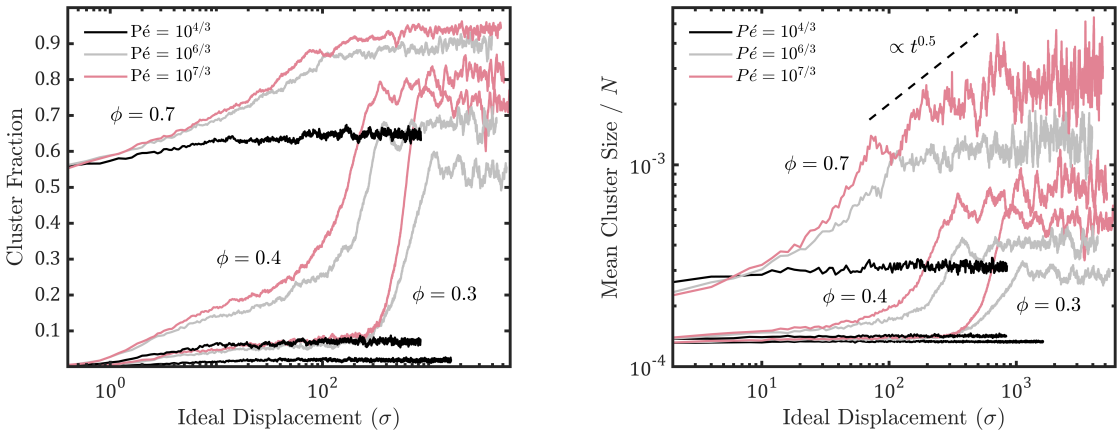

Figure 3.22: A comparison of cluster size and cluster fractions between simulations at different packing fractions and Péclet numbers. (a) The cluster fraction of a set of simulations labelled in the legend of the figure over time. (b) The mean normalised cluster size over time of the same set of simulations shown in (a).

In figure 3.22(b), we show the mean cluster size. Here we can be confident that, despite having few particles, we do not see a large deviation in the characteristic scaling from previous works of the mean cluster size, $t^{1/2}$, in the coarsening phase (the last stage before the mean cluster size no longer changes but the cluster fraction has already plateaued, around where the dashed line is for $\phi = 0.7$).

In figure 3.23(a) we show the structure factor at $\phi = 0.4$ and $Pé = 100$. Due to the small size of our simulation box, around 100 times our particle size, we are unable to isolate any peaks where k is smaller than 1 [11]. The size of the box can be clearly seen in the oscillatory form of the line at 4000σ. We therefore choose not to investigate our systems with the structure factor.

Because the radial distribution function is in real space, it is much less affected by the size of the box. In figure 3.23(b) we can see how $g(r)$ changes as the system phase separates. As

[11] Being smaller than one in reciprocal space would correspond to distance larger than the particle diameter in real space, the region where a cluster size would arise. Typically clusters need to be many orders of magnitude larger than a particle (coarse grained).

has been seen before, the peak at $r = 2\sigma$ is amplified in the nucleation phase (due to the activity creating collisions) and when the system phase separates the crystalline dense phase dominates [187].

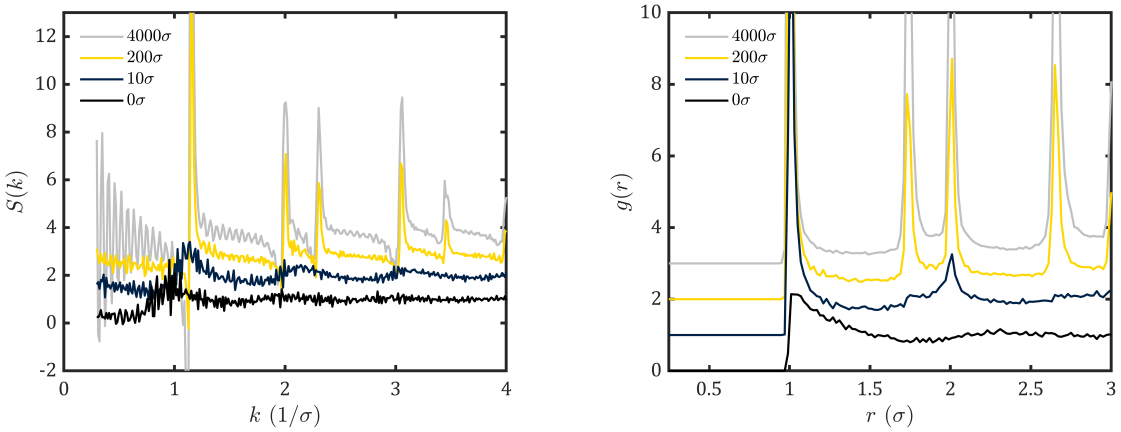

Figure 3.23: The structure inside a simulation over time. (a) The static structure factor over time. (b) The radial distribution function over time. Both graphs are of a simulation at $\phi = 0.4$ and $Pé = 100$ where each line corresponds to the time in the legend. Due to the constraints of the simulation box size, we are unable to obtain much information from the static structure factor. The radial distribution function shows characteristic MIPS behaviours.

As has been done before, we look at the relation of the velocity of our particles and their local density in figure 3.24. The relation is expected to be linear [5] in the nucleation regime (before phase separation occurs) as is the case for figure 3.24(a) and the short times in (c) and (e). Previous works have not looked into the evolution of this relation as the simulation progresses. This is because the theory, as presented in the beginning of this chapter, requires that perturbations which lead to phase separation occur before the transition occurs and that previous interaction potentials led to overlap and invalid measurements of local densities. However, we are able to show that the relation between velocity and density changes with the system. In (c) one can see that the curve at long times has a steeper negative gradient. We speculate that particles which end up in dense regions are not only affected by their neighbours but by a cluster as a whole. For example, a particle at the edge of a cluster will be significantly hindered (having to push a whole cluster) compared to one which nearly forms a successful nucleation event. We are able to compare these graphs due to how the SCP methods presents us with consistent behaviours regardless of active velocity.

In figure 3.24 we also show the evolution of probability profiles of local particle density. By

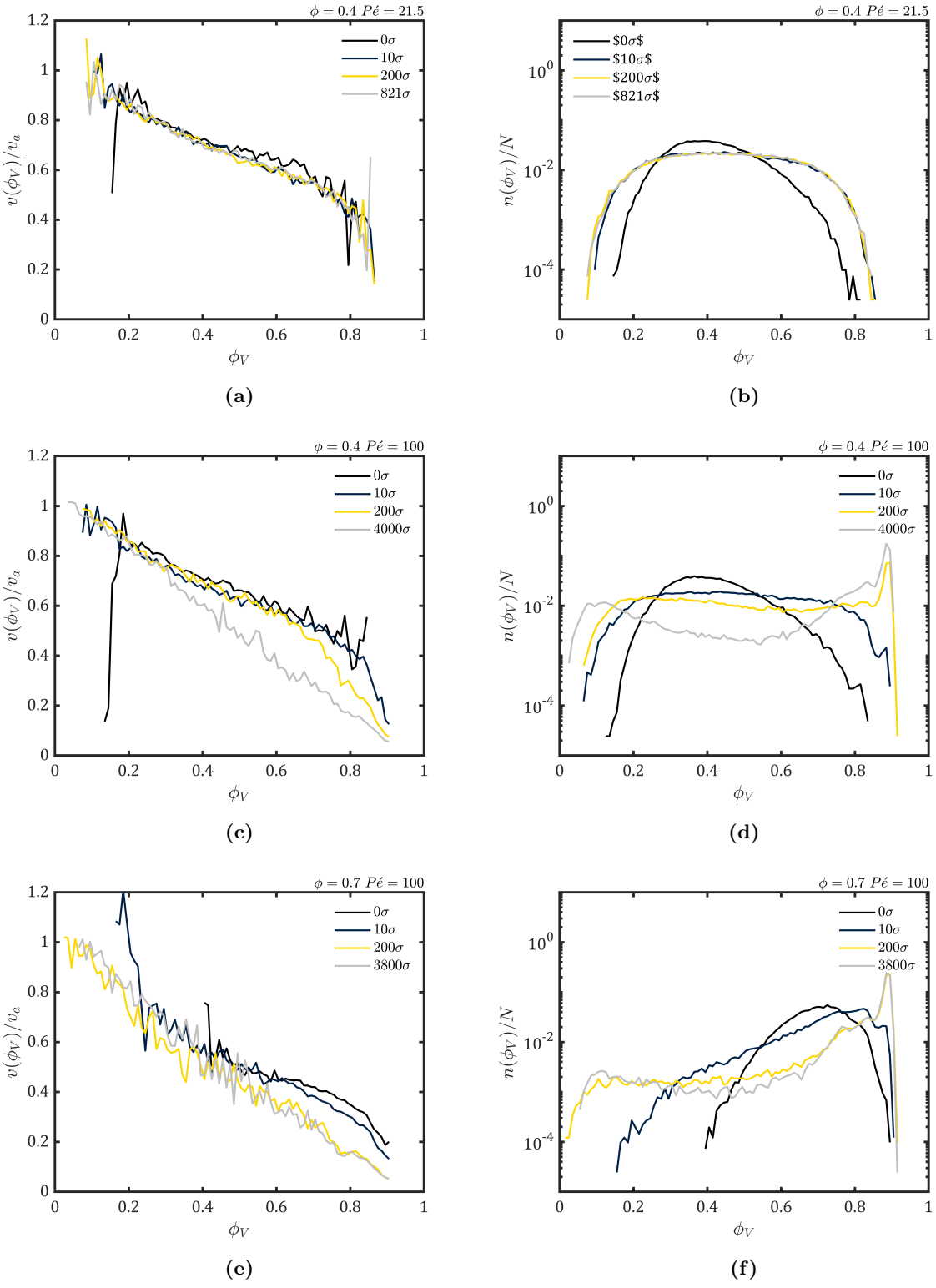

Figure 3.24: The evolution of the relation between velocity and density in MIPS. (a), (c) and (d) show the relation between particle velocity and local density. Velocity is measured as the total displacement over 1σ and normalised by the input velocity of each simulation. This to avoid diffusion distorting the data. (b), (d) and (f) show the evolution of probability profiles of local particle density. The densities and Péclet numbers of the simulation are next to each graph and the times in the legend.

comparing (b) and (d), we can see that the main difference is that the data for the simulation which does not phase separate has far fewer particles near the area fraction of close packing (0.9071). These graphs show that the perturbation theory and the theory analogous to passive phase separation [12] may require additional parameters because the velocity density relation is not constant (equation 3.14).

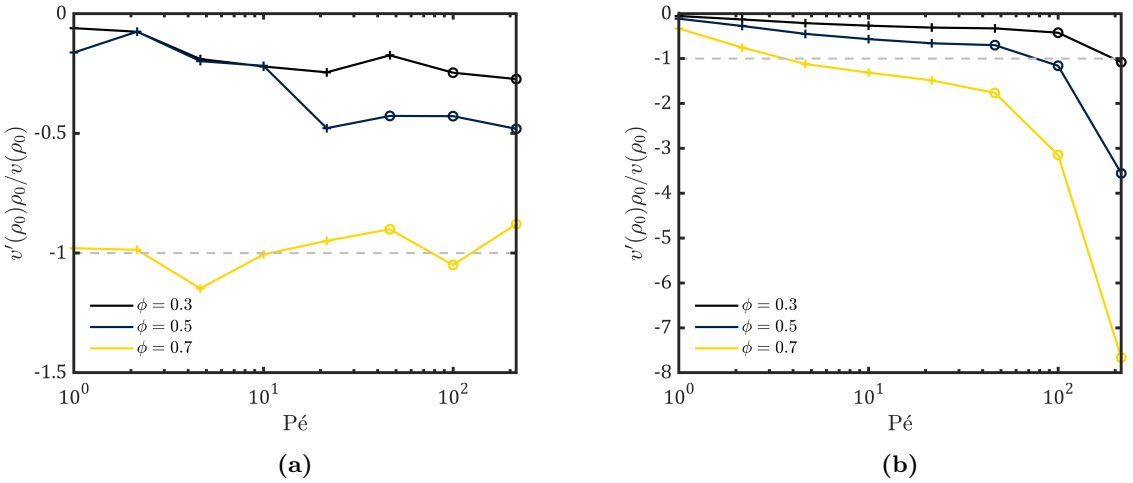

Figure 3.25: The perturbation explanation for MIPS seems to fail. (a) The value of the left hand side of equation 3.54 when the relation between velocity and local density is measured before phase separation. (b) The value of the left hand side of equation 3.54 when the relation between velocity and local density is measured in the steady state. Points denoted by circles are where we see phase separation.

Our measurements of the relation between local density and velocity allow us to test the inequality derived in the introduction of this chapter:

$$\frac{v'(\rho_0)\rho_0}{v(\rho_0)} < -1. \tag{3.54}$$

In figure 3.25 we plot the the value of the left hand side of equation 3.54 before phase separation (a) and after (b). In (a) we see that we would not predict that any system would separate until high densities (close to $\phi = 0.7$). Note that this analysis is affected by the error in determining $v'(\rho_0)$. In (b), because we use the steady state we have much better statistics from a much larger number of independent frames over which we can average. One can see that the theory works decently well despite being used on a steady state and not initial conditions. This suggests that the scaling relation via perturbation may require additional considerations. We suggest that this is not dependent on the potential but rather to do with the kinetics of nucleation which are

[12] Those derived by Cates and Tailleur [4].

not encompassed in the theory.

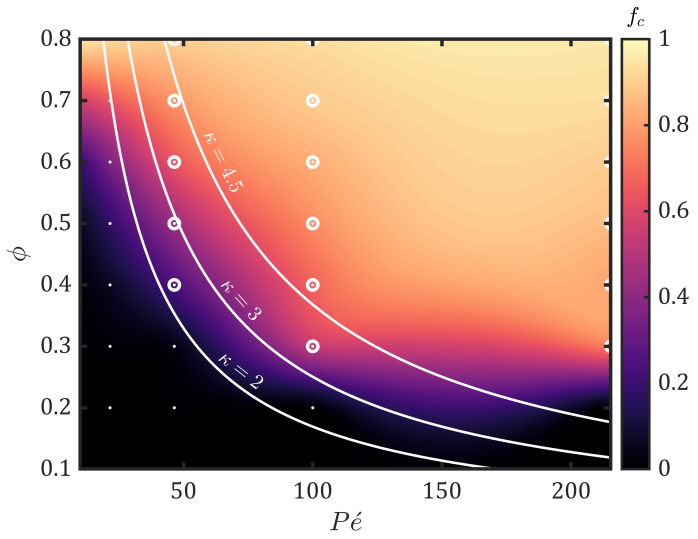

Figure 3.26: A phase diagram created by measuring the cluster fractions of systems in steady state compared to the kinetic theory of MIPS by Redner *et al* [1]. The results of equation 3.55 using f_c as 0.15 with various values for κ are shown on top of a fitted surface. The dots are systems which do not separate and the circles are those that do. Regardless of κ, the equation fails to map correctly. Cluster fractions are enhanced where the probability of having crystalline particles is increased (above $\phi = 0.5$).

The final theory we can test using the SCP method is the kinetic description presented by Redner *et al.* [1]. By measuring the cluster fraction of each simulation and plotting a contour plot alongside equation 3.55, as is done in figure 3.26, we can compare how the theory holds up. In figure 3.26 we use $f_c = 0.15$ which was determined empirically to fit around the simulations which were observed to phase separate.

$$Pé = \frac{f_c 6\sqrt{3}\pi\kappa\phi - 3\pi^2\kappa}{4\phi(f_c - 1)}. \tag{3.55}$$

In their work, Redner *et al.* mapped their equation to a range of ϕ between 0.1 and 0.7 and $Pé$ between 40 and 150 (figure 3.3). Over this range the model worked well when $\kappa = 4.5$. One can see in figure 3.26 that, given a certain value of κ, either the prediction can only fit a small region [13]. This would again suggest that the model is too simplified or that κ is not a constant and could depend on either packing fraction or the Péclet number. We expect that a harder potential would lead to better organisation in the dense phase resulting in a slight reduction of evaporation pushing the value of κ down for low Péclet numbers.

[13] Here we compare a much larger part of the phase diagram. $\phi = 0.7$ in a WCA simulation corresponds to $\phi = 0.55$ when using SCP.

3.3.3 Dynamics in MIPS at High Péclet Numbers

Due to the scaled contact potential we use in our simulations, we are able to increase the Péclet number without consideration of which method we use or if our particles no longer remain "hard". Most studies up to this point have not studied systems with Péclet numbers higher than around 270 with one exception; that of the work done by Fily *et al.* [5]. In their work, they noticed that if they increased F_a too much then the repulsion forces between the particles became negligible and MIPS was disrupted (maximum overlap). Although increasing the Péclet number could in theory be done by changing D_r such that the repulsion forces do not become negligible, in practice, the results would then depend on the F_a to $\frac{dU}{dr}$ (inter-particle force) ratio and therefore would not be universal.

In figure 3.27 we show $Pé/\phi$ phase diagrams for systems using the SCP potential with (a) $\Delta t = \tau \times 10^{-5}$ coupled with $\Delta t = 2.5\sigma/v_a \times 10^{-3}$ and (b) with $\Delta t = \tau \times 10^{-4}$ coupled with $\Delta t = 2.5\sigma/v_a \times 10^{-2}$. The choice of these time-steps was set as explained in the methods section of this chapter.

The extent to which MIPS occurs has been measured using our MIPS development parameter. As laid out in the method section, this parameter is measured from the difference in the local density probability density distributions as shown in figure 3.28(a) with resulting values also shown in (b) of the same figure (section 3.2.5).

As was presented in figure 3.18, using a softer potential changes the shape of the phase separated region. However, unlike with the comparison between PHS and WCA, the critical Péclet number of the transition is unchanged. This is because our particles have the same diameter regardless of how hard they are. A second point of note is that, as expected, having a softer potential leads to an increase in the critical packing fraction because particles are less likely to nucleate when given more freedom to move whilst interacting with a softer potential.

The aforementioned points are true for systems with traditional values of Péclet numbers (40-270). However, we show another phenomenon which might not be as obvious directly from the phase diagram. At the highest Péclet number we have observed we can see that for the harder system, the line which determines the transition slightly rises and the value of the MIPS development parameter ω_M decreases. This is not seen for the softer system in (b). Although this seems similar to how Fily *et al.* observed a reduction in MIPS at high Péclet numbers, it

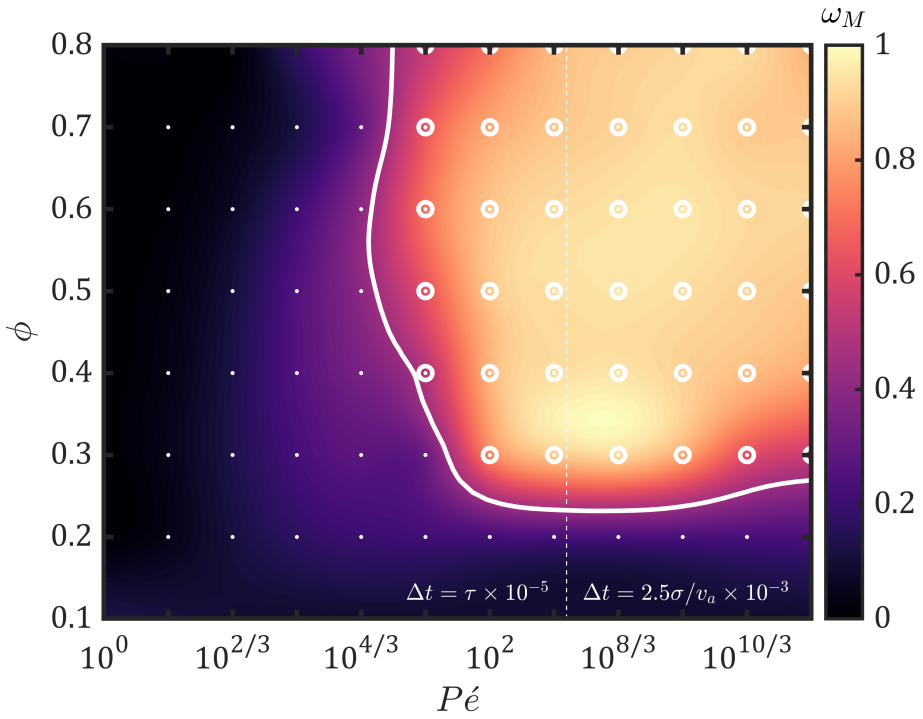

(a)

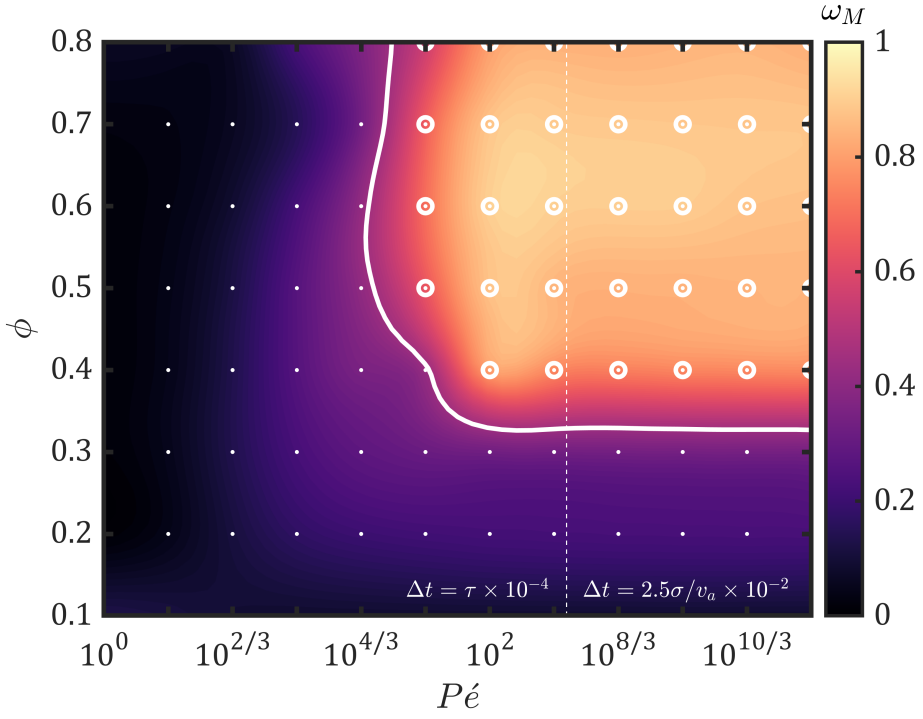

(b)

Figure 3.27: $Pé/\phi$ phase diagrams for systems using the SCP method up to very high Péclet numbers measured using the MIPS development parameter. (a) Harder systems, using $\Delta t = \tau \times 10^{-5}$ coupled with $\Delta t = 2.5\sigma/v_a \times 10^{-3}$. (b) Softer systems, using $\Delta t = \tau \times 10^{-4}$ coupled with $\Delta t = 2.5\sigma/v_a \times 10^{-2}$. The dots correspond to systems which do not phase separate and circles the ones that do. The white line corresponds to a value of ω_M of 0.45; taken to encompass all the simulations which do phase separate. Known differences are shown in the critical $Pé$ and ϕ values but a reduction in MIPS is shown at very high Péclet numbers in the harder system only.

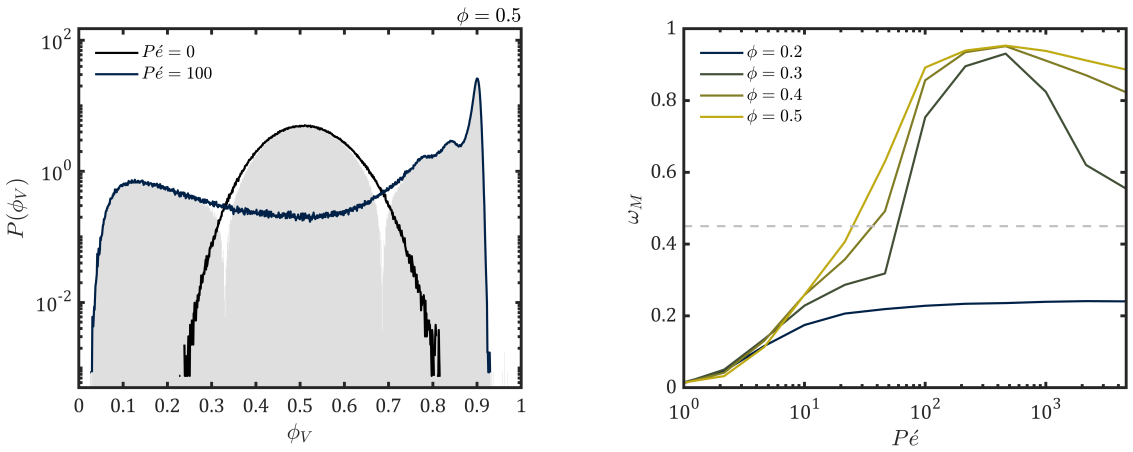

(a) **(b)**

Figure 3.28: The measurement of the MIPS development parameter ω_M. (a) The probability distributions of the local density of particles in the steady state for when no activity is present and a Péclet number of 100 using $\Delta t = \tau \times 10^{-5}$ coupled with $\Delta t = 2.5\sigma/v_a \times 10^{-3}$. The grey area shows the absolute of the difference between both which when integrated gives twice ω_M. (b) The values of the MIPS development parameters used for figure 3.27(a).

cannot be due to the same reasons because our particles keep a constant overlap.

A first approach to understanding the origin of this reduction is to look at the cluster fractions and mean cluster sizes of systems with high Péclet numbers. These are shown in figure 3.29. When we reach high Péclet numbers at $\phi = 0.3$ (figure (a)), we see that not only is the steady state less clustered but the growth of the system is significantly hindered. We also see in (c) that the mean cluster size seems to grow slower than for simulations at lower Péclet numbers [14] (figure 3.22(b)). However, due to the small size of our simulation box, the dynamics of the coarsening is difficult to measure. Nevertheless, these graphs suggest that there is a disruption to the formation of clusters and their stability.

Focussing on Péclet numbers, we can again measure the relation between velocity and local density. In figure 3.30(a) we show the relation before phase separation at two densities. We note that in all cases the profile is independent of the Péclet number but depends on average density (the structure in the system). In figure 3.30(b), (c) and (d) we show the relation in the steady state. In all three packing fractions shown, we note that the velocity at higher densities drops as the Péclet number increases, up to an optimal value, and subsequently rises again. This is not seen as much for the lower local area fractions as the structure and dynamics of the dense phase is that which changes the most. The reduction appears to be most significant at higher

[14] $t^{1/4}$ at high Péclet compared to the expected $t^{1/2}$.

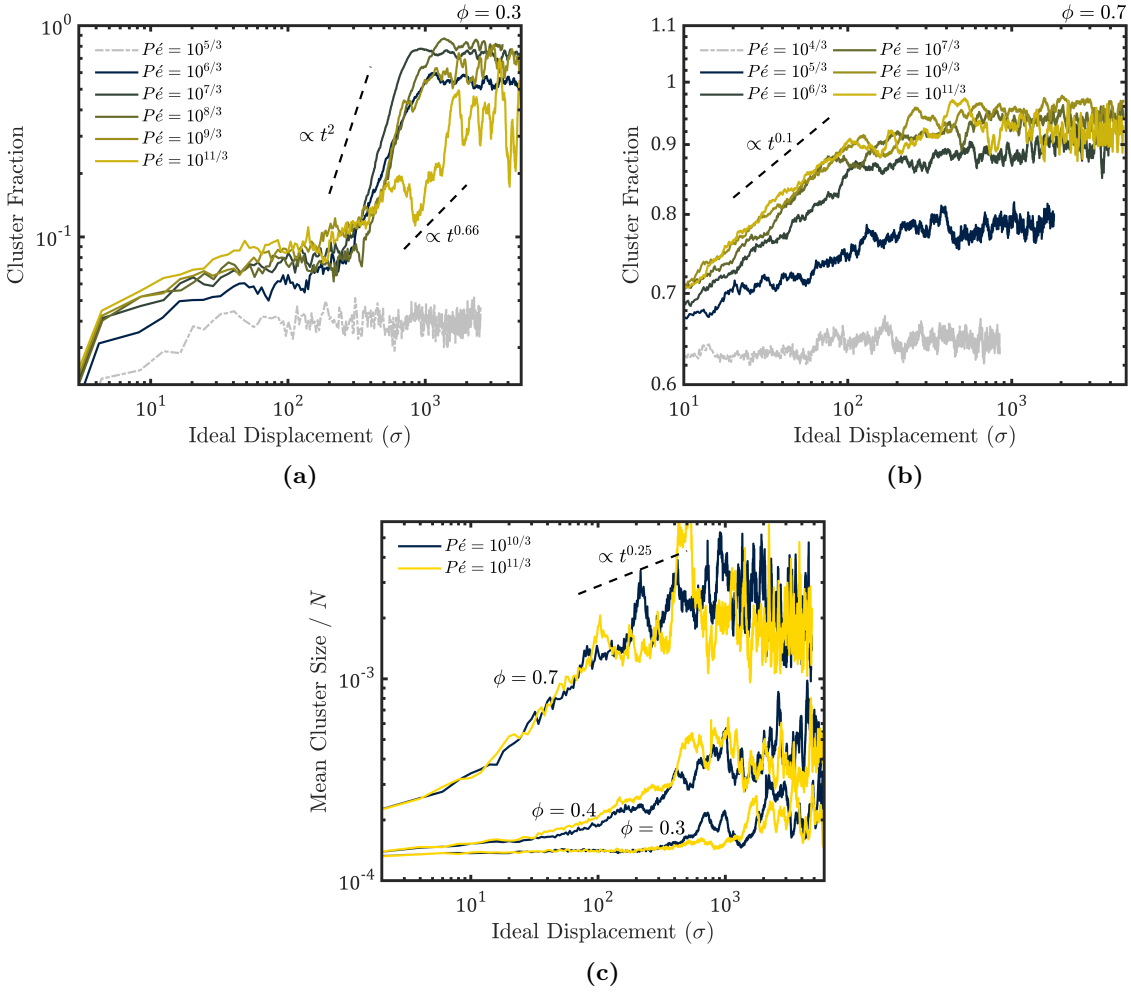

Figure 3.29: The progression of high Péclet systems measured by cluster fraction and mean cluster size. (a) The cluster fraction of various simulations at $\phi = 0.3$. (b) The cluster fraction of various simulations at $\phi = 0.7$. (c) The mean cluster size at high Péclet numbers at $\phi = 0.3$, 0.4 and 0.7. The reduction in growth rate and cluster fraction in the steady state hint towards a mechanism which destabilises clusters. The scalings in time are shown to be compares to those in figure 3.5. The mean cluster size scaling should follow t 0.5 in the coarsening regime like in figure 3.22.

densities which is most likely due to clusters reaching around the periodic boundary conditions due to their shape which covers most of the simulation box. A minor point is that at a value just under $\phi_V = 0.8$ there seems to be an extra dip; most likely linked to vacancies as shown in figure 3.19.

These results again suggest that there is a mechanism which disrupts clusters. From figure 3.30, we can state that the disruption is not just a change in the system structure, which is only what picked up by the MIPS development parameter analysis in figure 3.27. We can also suggest that the theory set out in the beginning of this chapter needs to have an input which includes the dependence of $v(\rho)$ on the Péclet number.

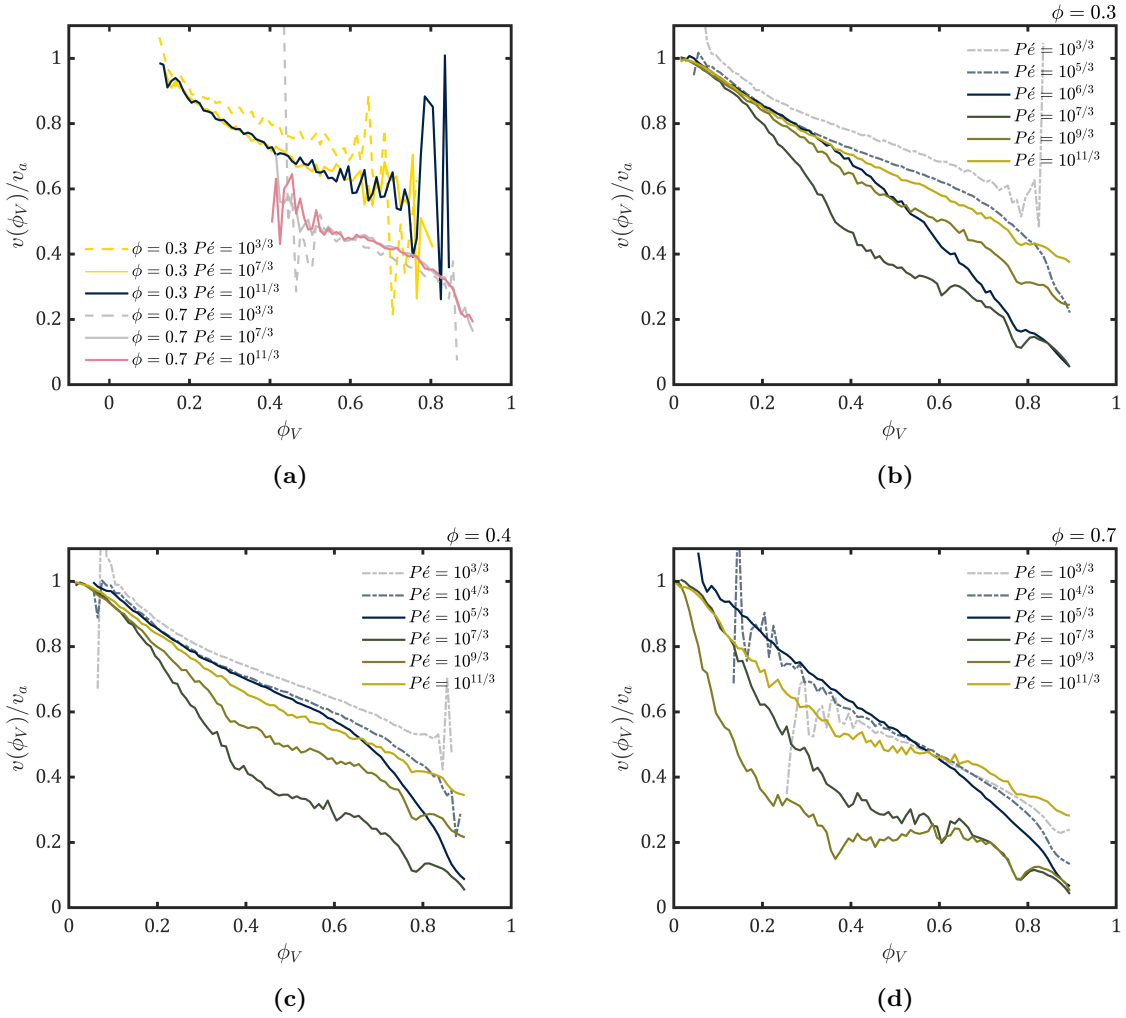

Figure 3.30: The progression of the relation between velocity and local packing fractions as Péclet changes. (a) The velocity as a function of local particle density measured over the first 1σ in time. It shows that it is the structure of the system and not the velocity of the particles which affects the relation. The relation between velocity and local particle density in the steady state for (b) $\phi = 0.3$, (c) 0.4 and (d) 0.7 respectively. Increasing Péclet reduces the velocity until a critical value where it begins to rise again.

Examining Cluster Rotation

In figure 3.31, we show the usual behaviour of a cluster formed in a system at $\phi = 0.3$ and $Pé = 215$. In figure (a), we can see that the cluster is not perfectly formed. It has reached a size over a time in which the particles have become orientationally decorrelated. This results in a single cluster with two grains (shown in (b) and (d)). If we use the average position of the intersects of the normals to the particle motion to determine the centres of rotation of this cluster, we can see, from (c), (i) and (j), that, on top of not being near to the centre of mass, the centre of rotation is not near the two most likely positions. This is because of the two grains.

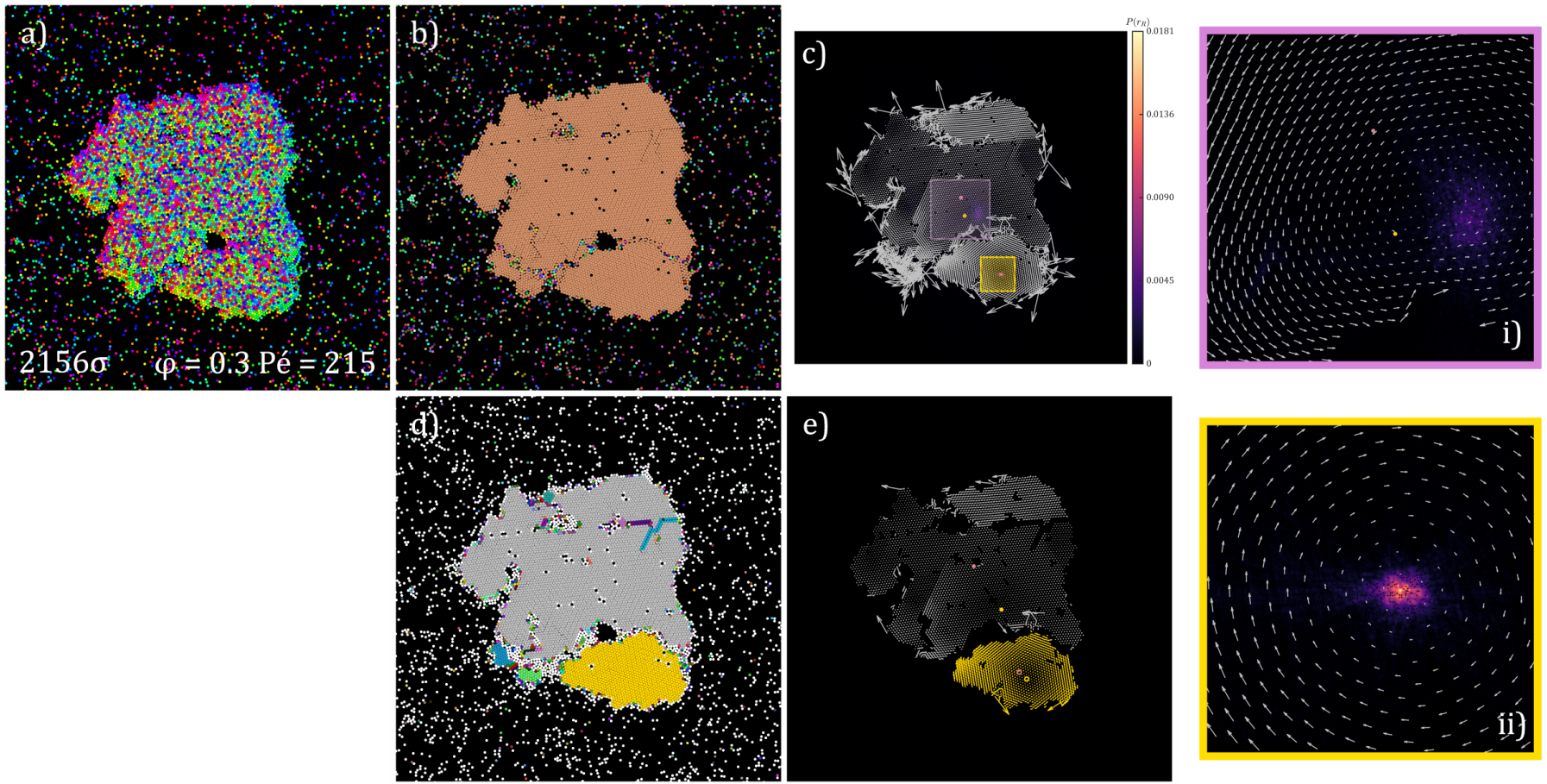

Figure 3.31: The behaviour of a typical cluster at a lower Péclet number. (a) A snapshot of a simulation with $\phi = 0.3$ and $Pé = 215$ at $t = 2156\sigma$. The colours of the particles indicate their orientation following the same colour scheme as figure 3.20. (b) The same snapshot as (a) but where the colours represent cluster IDs. (c) A vector field diagram on top of a colour map showing the direction of motion of all the particles in the cluster and the probability distribution of the intersections of the normals to the particle motion where the pink dot is the centre of mass and the yellow dot the average position of all the intersections of the normals to the vector field. (d) The same as (b) but with grain IDs. (e) The vector field diagram with the same as (c) but with each major grain identified. (i) and (j) are enlarged parts of figure (c) corresponding to the same colour.

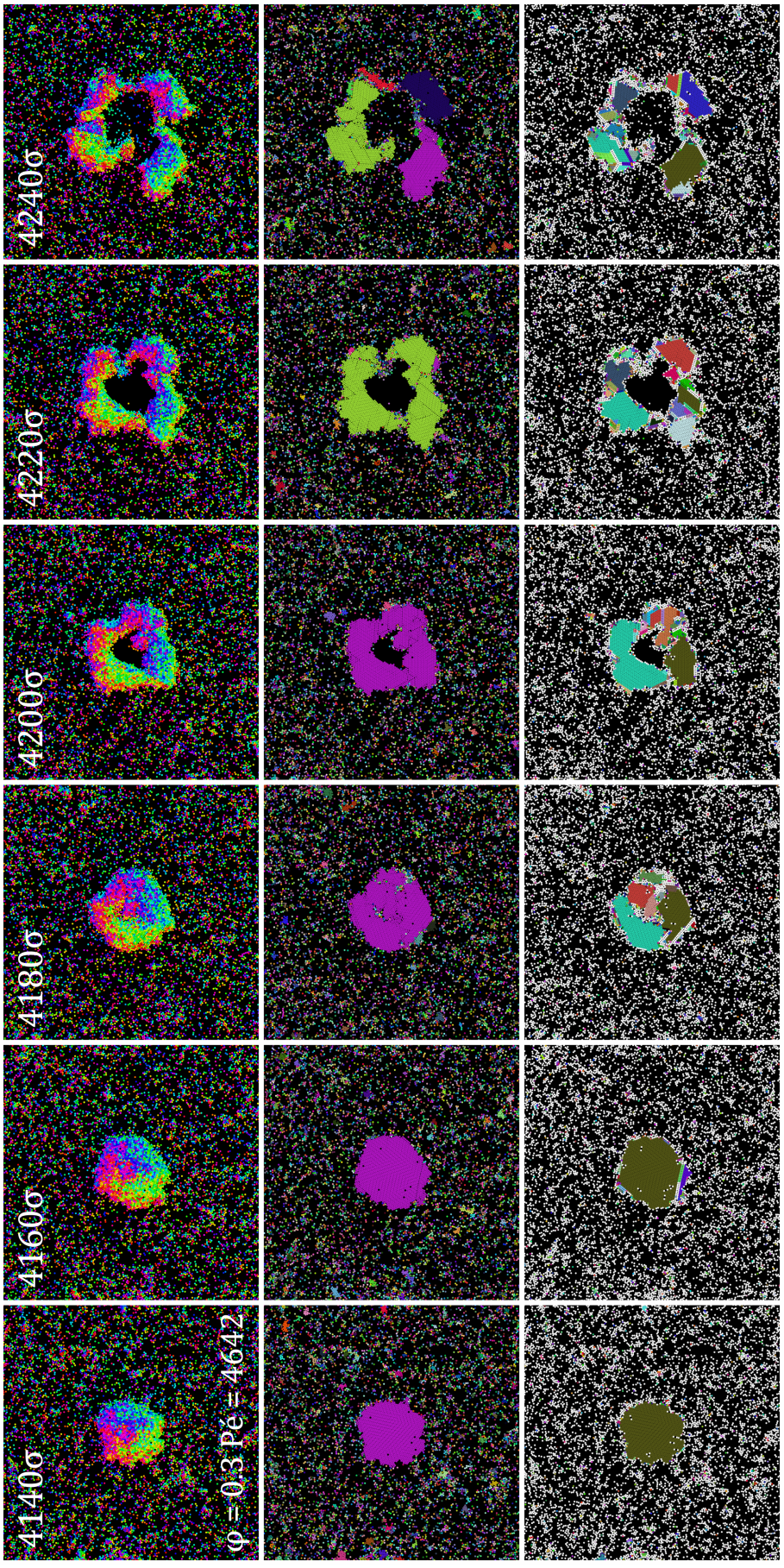

Figure 3.32: Snapshots of a cluster exploding at a high Péclet number. A time series from a simulation at $\phi = 0.3$ and $Pé = 4642$. The first row indicates the particle orientation by colour, again using the colour scheme of figure 3.20. The second row indicates individual clusters by colour. The third row indicates each grain. The cluster is seen to explode just after multiple grains have formed.

Despite the grains being part of a single cluster, they are able to move independently as long as their motion does not significantly disrupt the cluster.

If we observe the motion of the grains, as seen in (i) and (j), we notice that each grain has a centre of rotation which corresponds to the region where most of the normals intersect. In fact the direction of rotation of the grains are opposed (the direction of the vector fields in (i) and (j)). This indicates that the ability for the dense phase to crystallise, due to how hard the particles are in this case, can leads to extra dynamics in MIPS systems.

If we simply observe a similar cluster but at a much higher Péclet number, as shown in figure 3.32, we see that, unlike the cluster in figure 3.31, this one is unstable. Around $t = 4200\sigma$, a void grows in the centre of the cluster and the cluster separates. This also seems to coincide with the formation of multiple grains in a cluster.

In this case, because the Péclet number is much higher (over an order of magnitude), this occurs before the particles have reoriented themselves. This can be seen in the first row of the figure. This would suggest that clusters are unstable if their constituent particle are unable to find a way to cancel out their motion. Looking closely at the first row of the figure, one can see that the particles are mostly aligned with their neighbours. Following the green section, where particles are oriented at $2\pi/3$ or 60°, it moves from the bottom left of the cluster, where the particles would be oriented to the centre of the cluster, to the other side where no particles would oppose their motion.

In figure 3.33(a) we present the vector field diagram of the motion of the particles on top of the contour map of the probability density of the intersections of the normals to the motion at $t = 4200\sigma$. It is noticeable, because the grains have already formed, that the centre of rotation of the whole cluster is not where most normals intersect. However, each grain is moving/rotating in the same direction causing the cluster to split. In figure 3.33(b), we show the graphs of the torque of the cluster in figure 3.32 and its size over time. The grey region is the span of time shown in figure 3.32. As the cluster grows so does its torque. When the cluster has had time to rotate and not enough particles are join the cluster to stabilise it, it breaks and the size of the cluster drops (around 4000σ). This also coincides with a drop of the torque. This occurs once again in the grey region.

The formation and explosion of clusters is therefore at the origin of the reduction of the MIPS

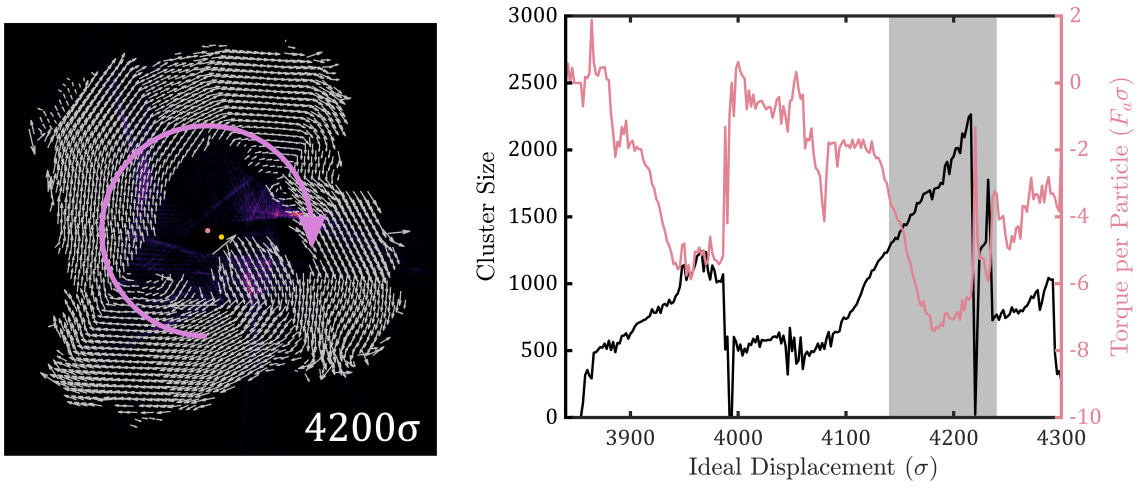

(a) **(b)**

Figure 3.33: The link between the rotation of a cluster and its size which then leads to cluster explosion. (a) The vector field of particle displacements over 1σ (amplified for visualisation) on top of a contour map of the probability density of the location of the intersections of the normals to particle motion. (b) A graph of the size of the cluster in figure 3.32 and its torque per particle over time. The link between the two lines in (b) show how the rotation of a cluster leads to its eventual demise.

development parameter mentioned at the beginning of this section. Although cluster are able to form, they have a tendency to be disrupted as the net forces, and more importantly torque, are not able to be cancelled out by either new particles joining the cluster or the particles in the core of the cluster reorienting themselves. One could think of this in terms of the kinetic model of MIPS. Seeing as the clusters are able to explode, then the parameter κ in equation 3.39, which represents the number of particles leaving a cluster per event, must be larger and dependent on Péclet number. This may be why the model mapped our results poorly in figure 3.26 but would have worked on softer systems which could not exhibit cluster dynamics, despite being at lower Péclet numbers.

In figure 3.34, we present the polar order parameter as a function of inter-particle distance at three different packing fractions in the steady state. It is clear that the higher the Péclet number the more the system is organised. This arises in the low area fractions because of the aforementioned mechanisms. Particles can only join a cluster if they are facing it and therefore at high Péclet numbers where the persistence lengths of the particles is long, particles which join the same region of a cluster have the same orientation. They accumulate and are only released when a cluster explodes. This results in grains of particles with similar orientations. These then loop around the periodic boundary and collide with other grains. Over time the particles sort

themselves and a type of collective motion is achieved.

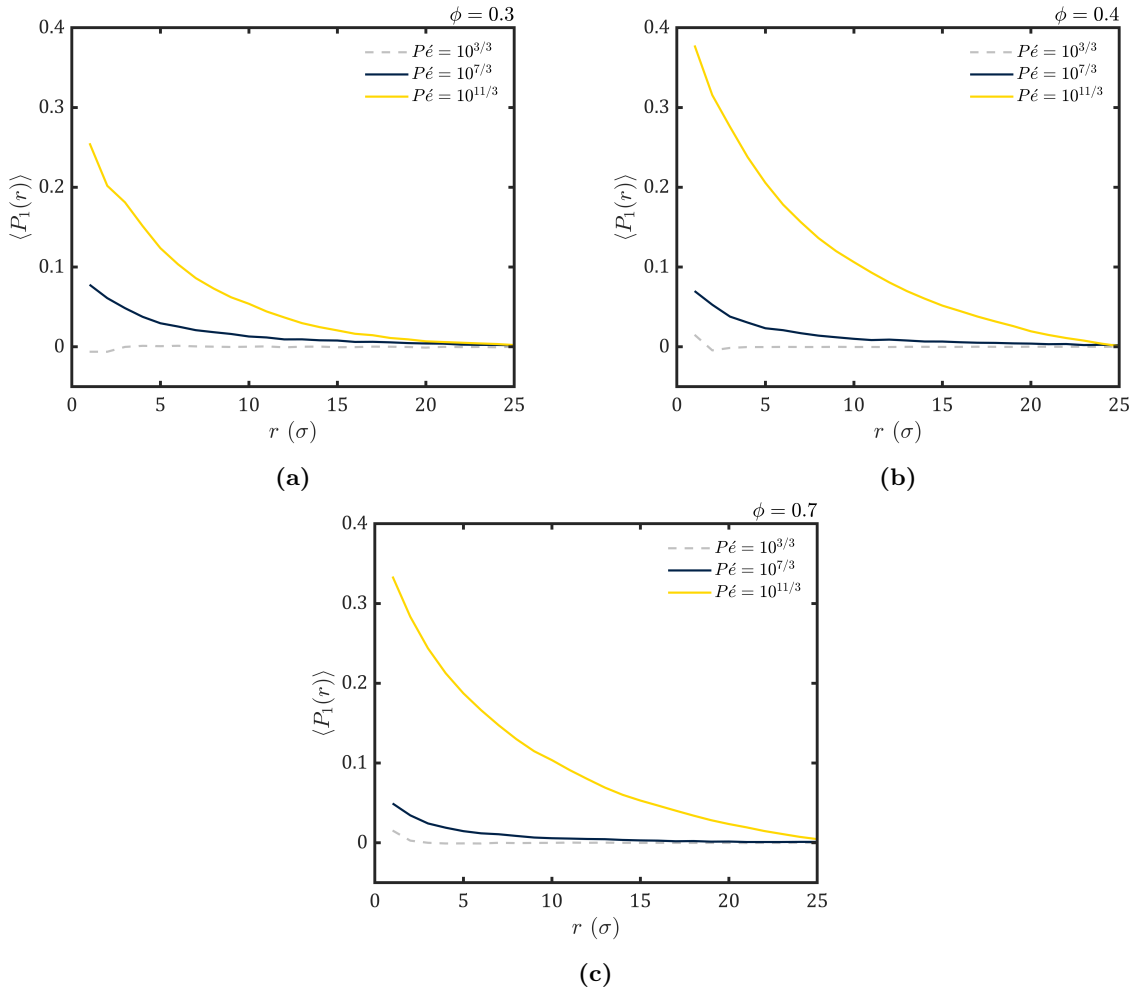

Figure 3.34: How the polar order parameter as a function of inter-particle distance depends on the Péclet number. (a), (b) and (c) are all graphs of the polar order parameter as a function of inter-particle distance with packing fractions of 0.3, 0.4 and 0.7 respectively. The increase in the order parameter at short distances at higher Péclet number indicates a sorting mechanism which leads to partial collective motion.

Although this explanation may seem unsuited for the more dense systems, it still occurs. Looking at the snapshots presented in figure 3.35, there is a noticeable difference between simulations at $Pé = 215$ and 4642. The orientations of the particles at the higher Péclet number are again similar to their neighbours. The grains inside the cluster are able to move around despite the large cluster anchoring to itself across the periodic boundary. Therefore, particle orientations can still be filtered.

This sorting phenomenon is similar to the systems of Wysocki *et al.* where they observed a more liquid like dense phase in three dimensions rearrange itself in a similar manner [171]. In our case, the two dimensional systems does remain crystalline but the grain boundaries and the

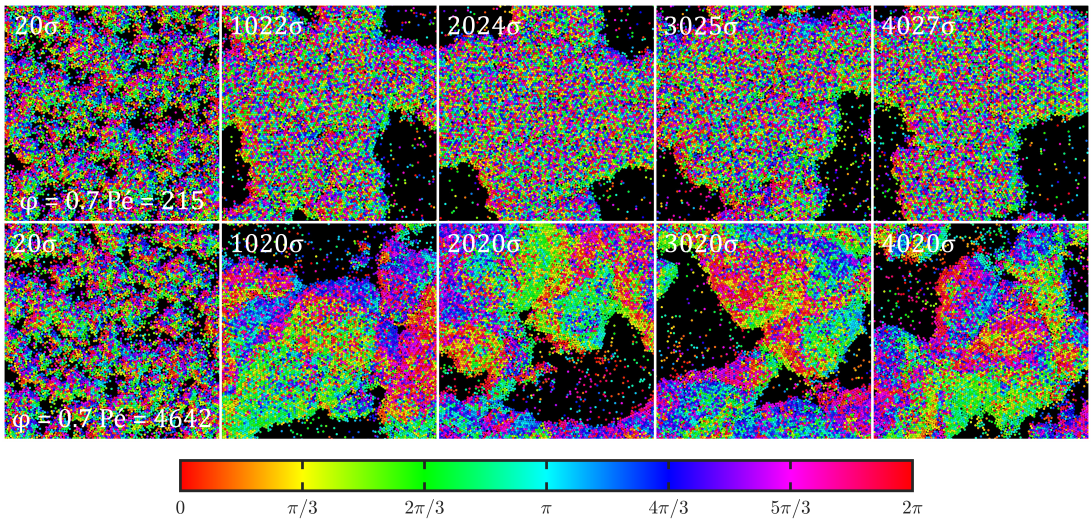

Figure 3.35: The difference in dynamics due to a change in Péclet number for dense systems. Snapshots of two systems of particles at different Péclet numbers (215 and 4642) where the orientation of the particles is denoted by colour according to the colour bar. The high Péclet system is still able to reorganise due to grain boundaries.

long persistence lengths of the particle trajectories lead to a very similar effect.

3.3.4 Adding Rotational Friction into the System

Clusters at high Péclet numbers are able to explode because their particles maintain their orientation during the lifetime of the cluster. More realistic systems would not only have interactions in translation but also in rotation such as friction. In this section we investigate the effect of particles having a physically motivated empirical model for rotational friction where our parameter $\mu_f = 1$ in equation 3.52; "sticky" disks. This is done as laid out in the last part of the methods section of this chapter.

In figure 3.36, we plot the same phase diagram as in figure 3.27(a) but now for "sticky" particles. The critical Péclet number, the vertical part of the phase boundary, decreases. This can be explained using the kinetic model. Particles are partially hindered in their rotations when at the edge of a cluster, therefore, they are less prone to reorienting themselves such that they can leave the cluster. This explanation partially maps onto the reason why the critical packing fraction decreases. If a particle keeps its orientation it is less likely to have a long lasting collision with another. However, if the particles are sticky, their relative angles are maintained for longer; those which led to the collision and the reduction in velocity in the first instance.

Furthermore, the value we obtain for the MIPS development parameter across the whole phase diagram is increased. This would suggest that the packing fraction of the dilute phase is reduced by the particles being more likely to adhere to a cluster. A final difference is that we no longer see the reduction of ω_M at high Péclet numbers, meaning the clusters do not explode.

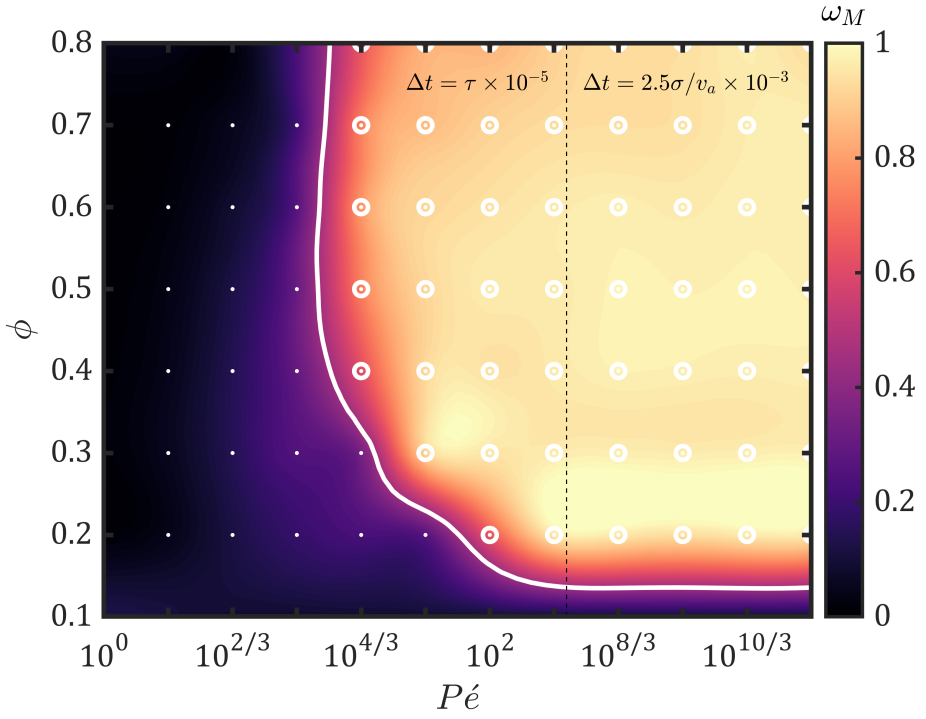

Figure 3.36: The phase diagram for sticky particles in $Pé/\phi$ space. Simulations which phase separate are shown with a circle and those that do not with a dot. The colours in the plot represent a thin-plate spline fit of the values of ω_M with magnitudes which follow the colour bar. The white line is representative of the spinodal and is where $\omega_M = 0.45$. The simulations use $\Delta t = \tau \times 10^{-5}$ coupled with $\Delta t = 2.5\sigma/v_a \times 10^{-3}$.

As in the previous section, we can begin by analysing these differences by looking at the cluster fractions and mean cluster size. In figure 3.37(a) and (b) we show the cluster fractions for simulations with various Péclet numbers at packing fractions of $\phi = 0.3$ and 0.7. In (a), there is no change in the rate of growth. This is because there is only one cluster growing at $\phi = 0.3$ therefore the growth is most linked to the rate of particles joining the cluster. At both densities the simulations always reach cluster fractions close to one which is because the packing fraction of the dilute phase is much lower when rotational friction is involved as previously described.

In figure 3.37(c), we see that the mean cluster size seems to scale close to $t^{0.5}$ for all Péclet numbers at $\phi = 0.7$. This again suggests that the effects at high Péclet in systems with no rotational friction are no longer present (they seemed to reduce the scaling before).

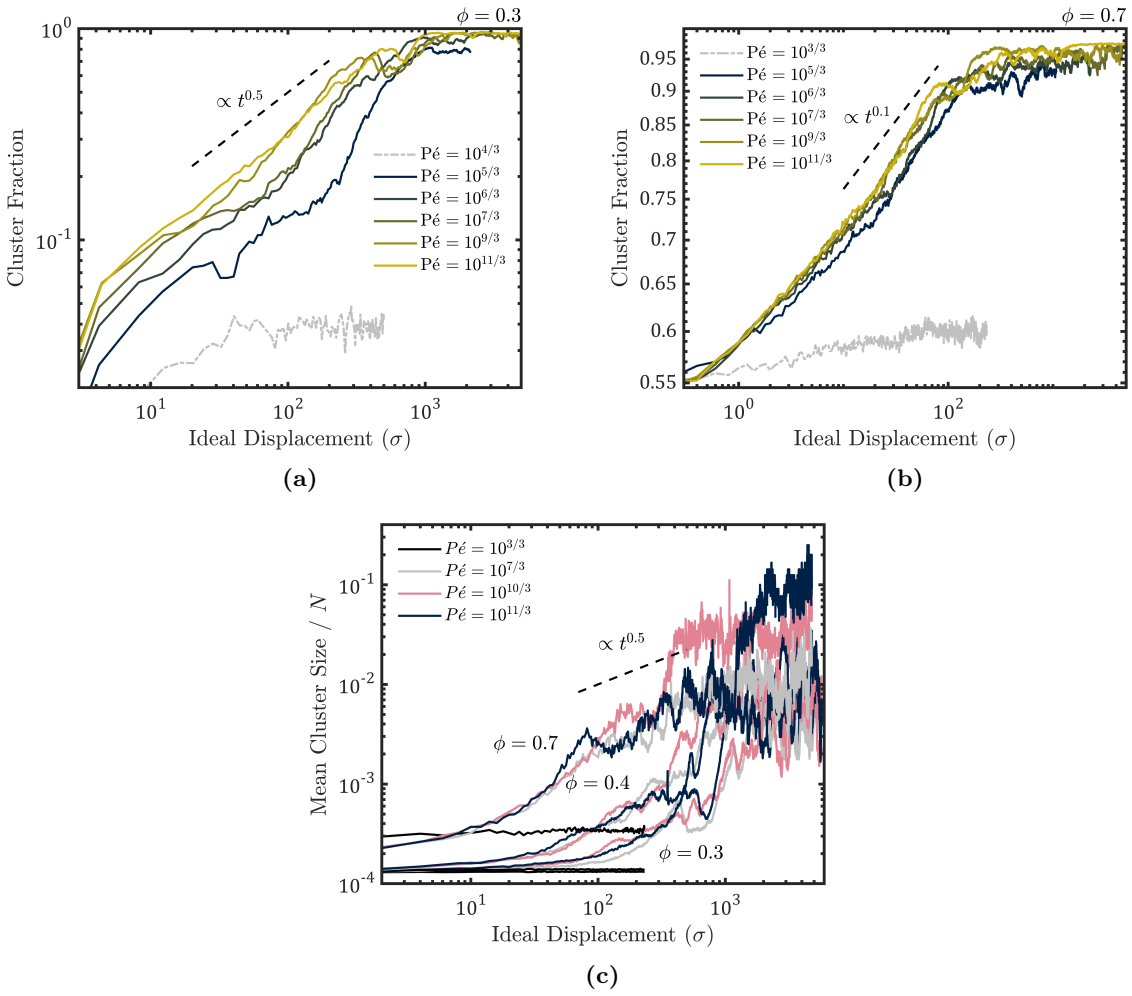

Figure 3.37: The progression of MIPS shown in the cluster fraction and mean cluster size of various simulations. The cluster fraction of simulations with (a) $\phi = 0.3$ and (b) 0.7 respectively with Péclet numbers shown in the colour bar. (c) The mean cluster size for various simulations labelled on the figure. The lack of difference between simulations with usual Péclet numbers and those with high Péclet numbers suggests that rotational friction quenches the effects seen in systems without rotational friction.

In figures 3.38(a) and (b), we see how the relation between velocity and density changes due to the presence of rotational friction. The most obvious point is that the velocity is significantly reduced over the range of Péclet numbers. It is also the case that the velocity does not rise again at the higher values of $Pé$. This again shows how the aforementioned effects are reduced. The drastic reductions in the velocities at low local packing fractions are related to the how the collision angle is maintained for longer due to the rotational friction.

Because we do not see the effects of cluster explosions when rotational friction is added, we should also be able to see this in the motions of the clusters. In figure 3.39 we investigate the angular motions of a cluster at $\phi = 0.3$, $Pé = 4642$ and $\mu_f = 1$. Along the first row in (a), it is

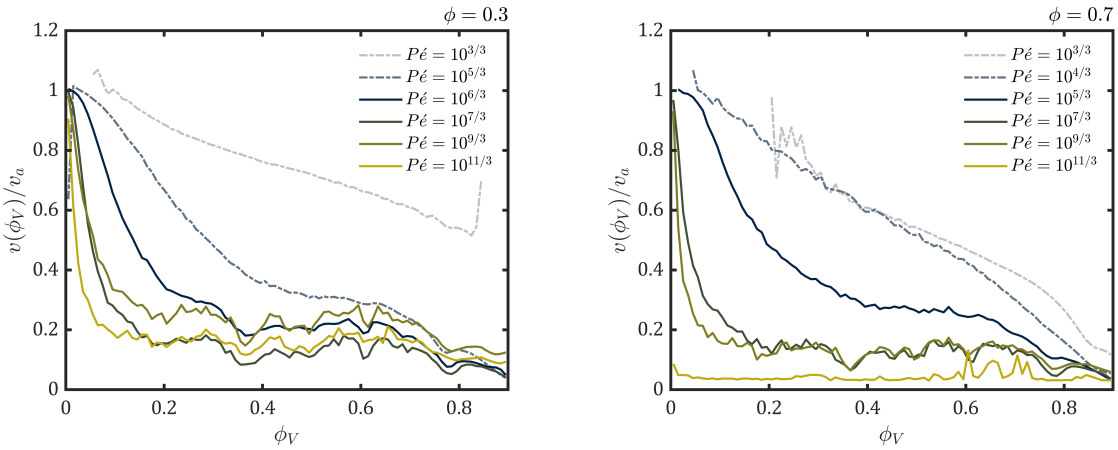

Figure 3.38: The drastic reduction in velocities due to the presence of rotational friction. The relation between velocity and local packing fraction for hard systems with rotational friction for (a) $\phi = 0.3$ and (b) 0.7. The consistent drastic reduction in friction can be associated with a retention in collision angle and is the reason why the dynamics at high Péclet numbers are not seen.

noticeable that the orientations of the particles in the cluster are less correlated. This is partly due to the ability for the cluster to rearranges its grains as seen in the third row as the colours of the grains change over time.

The rearrangements of the grains can still be seen at later times. In figure 3.39(b), not only is the cluster seen to rotate overall with a centre of rotation close to the majority of the intersections, but in the right hand image, the vector field is in two parts centred around the two large densities of intersections. They also are rotating in opposite directions indicating the cluster is still able to rearrange. Translational motion is not fully hindered by our addition of rotational friction.

Quite strikingly in figure 3.39(c) we see that the torque of the cluster, once it has finished growing, does not continue to grow as it does in the frictionless case. However, before the cluster has finished its growth it is shown to lose some of its particles indicating that the increased stability of the clusters due to the rotational friction is not absolute and improves for larger clusters; more particles leads to more jamming.

As far as the correlation of angles is concerned, the addition of rotational friction reduces the polar order parameter over short distances for systems with large Péclet numbers. This is because although grains can rotate and rearrange amongst themselves they keep the arrangement of particle orientations they were formed with which are mostly random to begin with and

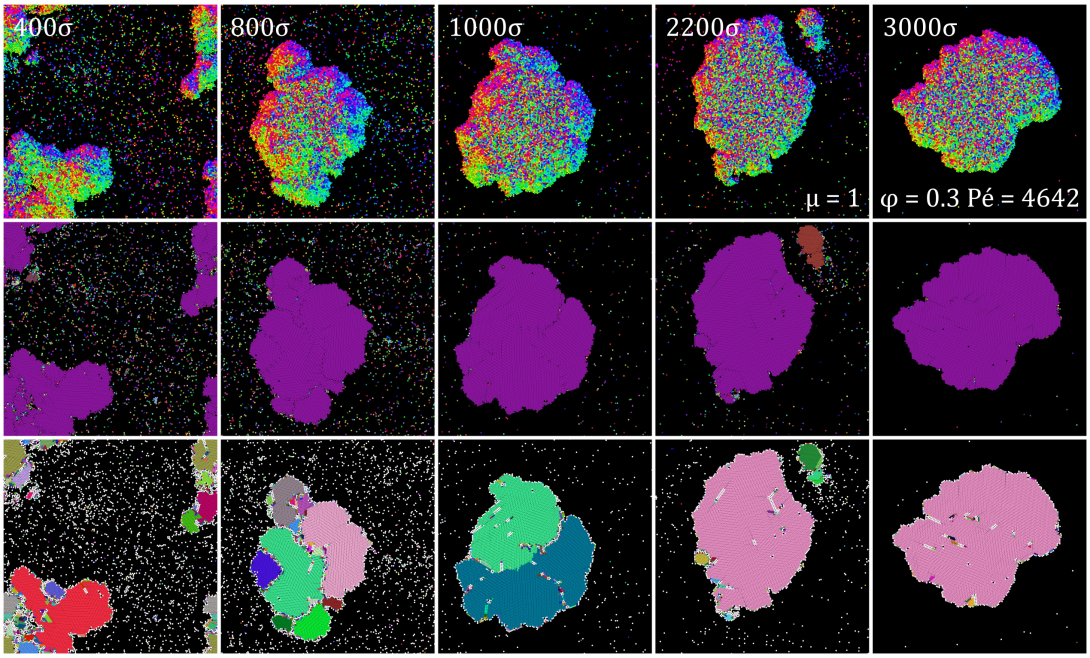

(a)

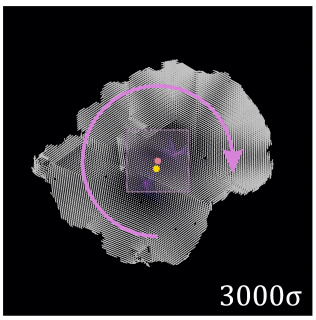

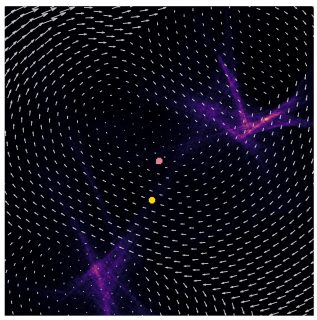

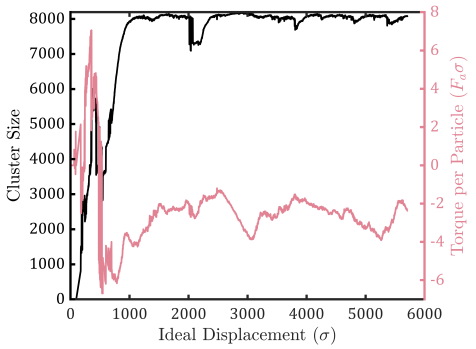

(b) (c)

Figure 3.39: The progression of clusters with rotational friction. (a) A time series of images of clusters showing the orientation of the individual particles on the first row, the identities of the clusters in the seconds, and the grains in the third. (b) The rotation of a cluster shown by a vector field on top of the probability density of the intersections. The yellow dot is the centre of rotation and the pink dot the centre of mass. (c) The cluster size of the major cluster and its torque over time. The cluster is shown to rearrange its grains until it is stabilised and able to rotate freely without breaking.

particles are able to change their orientations within grain boundaries. It is also the case that because clusters are not able to explode the collective motion at the origin of the increased orientational correlation is not present.

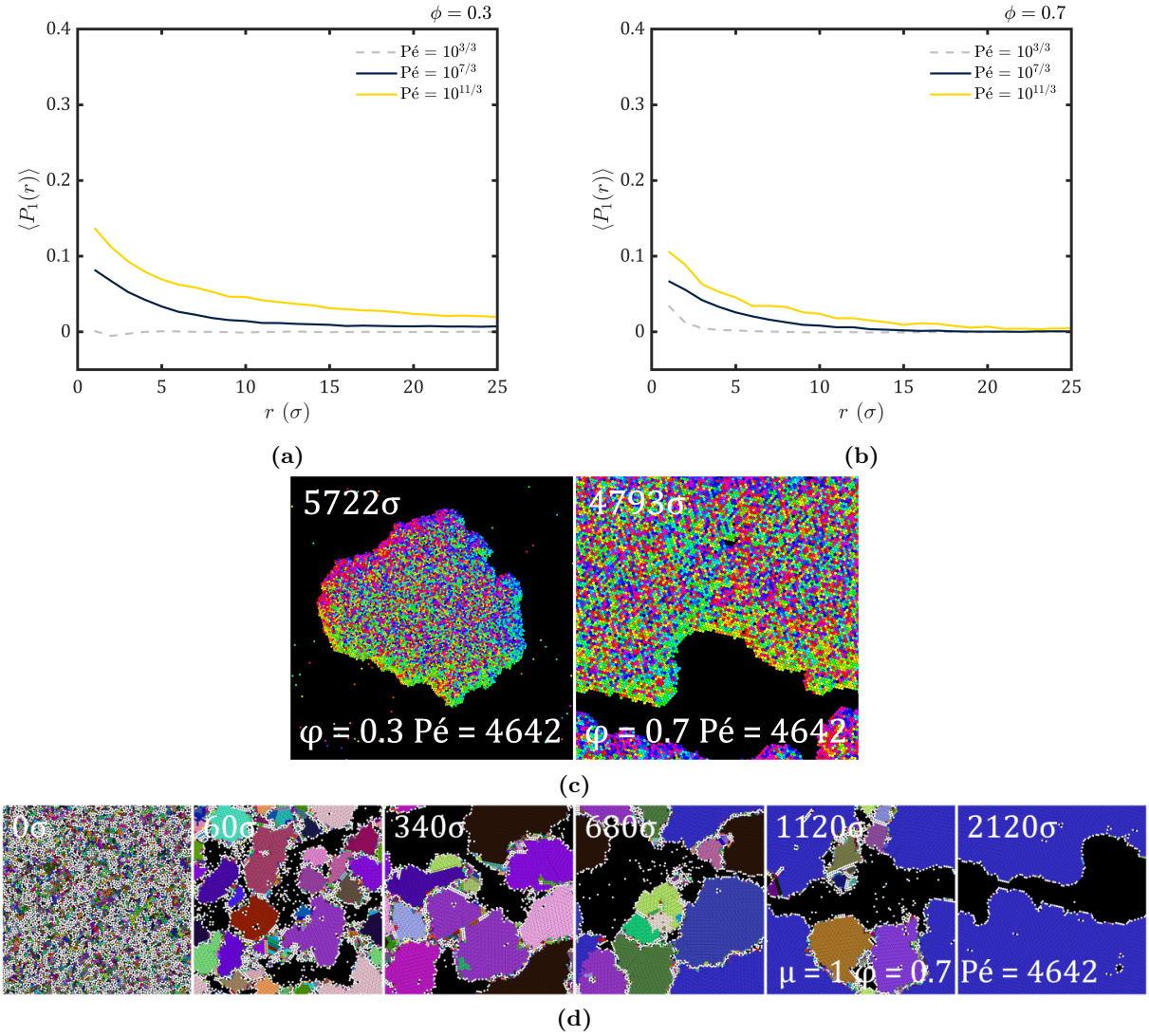

Figure 3.40: The reduction in orientation correlation at high Péclet due to the rotational friction. The polar order parameter as a function of distance between particles for systems at (a) $\phi = 0.3$ and (b) 0.7. (c) Snapshots of simulations in the steady state where friction is present. (d) Snapshots of the simulation at $\phi = 0.7$, $\mu_f = 1$ and $Pé = 4642$ where the grains are indicated by colour.

3.4 Summary and Conclusions

After comparing phase diagrams of ABPs in $Pé/\phi$ space using the SCP method, the WCA potential and the PHS potential, we have shown that not only does the SCP method provides us with the means of creating effectively harder systems than those which have been previously used, but that it also achieves consistency regardless of Péclet number. In addition to this, we have also shown that our approach solves the question as to which method one chooses to alter the Péclet number and gives us the same results regardless of which is chosen.

With this we were able to recover the same behaviours which have previously been studied in systems with Péclet numbers below 300. We show that the mechanisms of phase separation still occur and are in fact promoted by the harder interaction. We have furthermore been able to test the predictions presented by Tailleur and Cates [4] and find that we do not quite recover the expected values in the linear instability as measured from the relation between velocity and local density before phase separation. We also show how the kinetic approach to explaining MIPS falters when a wider range of Péclet numbers and packing fractions are used, despite remaining in the region of the phase diagram which is usually studied.

The novel part of the chapter involves the study of MIPS of hard particles at higher Péclet numbers than in previously studied systems. With the exception of the work of Fily *et al.*, where their repulsive interaction is overcome by their active force essentially meaning that their particles are not hard and overlap is excessive [5], previous studies have not looked into systems where the Péclet number exceeds 300.

We show that at high Péclet numbers (large velocity and slow rotational diffusion), the MIPS phase becomes disrupted through cluster fractions, which rise slower and are less stable in the steady state, and the mean cluster size which also appears to grow more slowly ($t^{0.25}$ compared to the usual $t^{0.5}$). Through the relation between velocity and the local packing fraction of the particles, we were able to show that the disruption of the dense phase arises due to a mechanism which leads to a less significant reduction in velocities for more crowded particles.

It becomes clear through the observation of cluster in these systems and the grains they contain that the disruption of the dense phase is due to a cooperative motion of particles within grains with similar orientations. These particles have correlated angles due to the way in which clusters form and their large persistence lengths. We show that the torque of a cluster and its freedom to rotate are at the origin of how they are able to explode.

A phenomenon which arises as a consequence of these extra behaviours is that the system as a whole becomes more ordered and collective motion can occur. The formation and destruction of clusters leads to particle sorting such that there is a high degree of polarity in systems where there is no orientational interaction. This phenomenon is similar to what has previously been observed in three dimensional systems where dense fluid-like phases of particles can rearrange [171]. However, in our case it is not a fluid-like nature of the dense phase which enables it but the ability to form highly crystalline grains with grain boundaries which allow motion.

To investigate how important cluster explosions are to this phenomenon, we study systems of "sticky" particles where we add a phenomenological/empirical model for rotational friction. Particles are forced to maintain their orientation relative to their coordination shell (scaled by the number of neighbours). Because of the rotational friction the critical values of ϕ and $Pé$ of the binodal are reduced. On top of this, the behaviours of our hard ABPs at high Péclet numbers no longer occur. The growth of the cluster fraction and mean cluster size are no longer inhibited by cluster instabilities whilst also preventing a significant degree of angular correlations between particles. We see by the observations of grains that clusters, whilst remaining stable, are still able to reorganise such that their constituent particles have more disordered orientations and do not lead to large cluster torques.

From the results of this chapter, the validity of the models used to describe MIPS, namely those introduced in the start of the chapter, have been examined; as has been previously done with other phenomena [76, 173, 177–179]. The most obvious case is that of the kinetic model. Although the promotion of MIPS by adding rotational friction can easily be explained by the model, the reduction in phase separation at high Péclet numbers provides evidence that κ, the constant used as the average number of particles which leave per break-off event, is most likely dependent on Péclet. With respect to the energetic description by Cates and Tailleur, we have noticed that the relation between velocity and local density which we measure does not recover expected results when used in the theory and that it is highly structure dependent. Most importantly, neither model predicts a reduction in the phase separation as Péclet increases due to the explosion of clusters.

3.5 Appendix

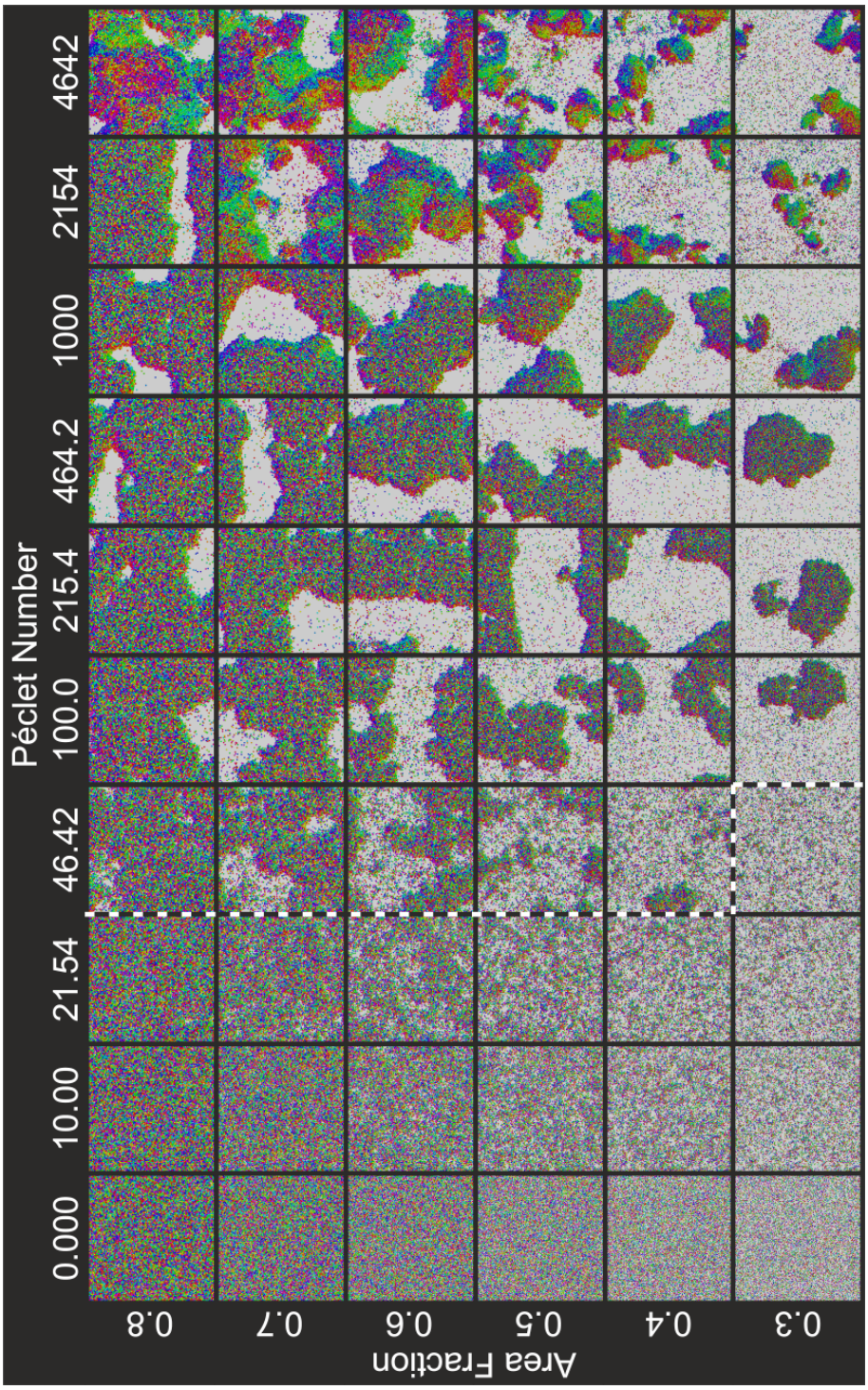

Figure 3.41: A full phase diagram of Hard active Brownian disks. The snapshots are taken in the steady state of simulations. The superimposed colours correspond to the interpolated ω_M surface from figure 3.28(c). The dashed line shows the transition line. Particles are simulated using $\Delta t = \tau \times 10^{-5}$ or $\Delta t = 2.5\sigma/v_a \times 10^{-3}$.

Chapter 4

Motility-Induced Phase Separation: Experiments of Phase Separating Active Particles

Abstract

In this chapter, we tested the hypotheses laid out in the previous chapter on an experimental system of active Janus particles. For their tunability and behavioural diversity, we chose to use induced-charge electrophoretic particles. After careful optimisation, we were able to investigate the phase behaviour of these systems over a range of area fractions and Péclet numbers. We discovered, by comparison with the results for the numerical simulations, that the flows and interactions generated in the propulsion of the particles are never negligible. We do still recover many of the aspects of systems of repulsive active particles observed in our and previous work.

4.1 Introduction

We being by bringing to the attention of the reader the nature of colloidal particles and how they can be approximated to interact in a hard manner. This is explained using DLVO theory of such interactions in electrolytic solvents. Before moving onto the mechanism of electrophoresis, the conditions for which are setup in the DLVO theory, we describe previously obtained results from experimental systems of active particles with regards to phase separation. As well as describing the propulsion mechanism for our ICEP particles, we also cover interactions which have been observed in systems of such particles also induced by the external electric field. We end our introduction with a summary of ICEP particles in experiment.

In the methods section we cover the nature of our experimental setup. We cover the creation of samples including particle and electrode synthesis. We end with a description of the reflection microscopy we employed and our numerical methods of particle detection allowing us to track the positions of particles in two dimensions and their orientations.

We begin the results section with a study in the measurement of the Péclet number for our systems, covering the measurements of velocity and rotational diffusion and highlighting complications for a range of electric field amplitudes and frequencies. Once this has been achieved, we present our data in the form of a phase diagram which mimics those in the previous chapter (in $Pé/\phi$ space). The final section of our results examines the dynamics of clusters using the same tools as laid out in chapter 3.

4.1.1 Colloidal Interactions

The aforementioned "hard" interactions can only truly exist in numerical simulations. Experimentally, no particles are isolated from their environment such that they are truly hard. In the case of colloidal particles, they are in suspension and therefore are exposed to their solvent. They are also solid particles and electrostatic interactions cannot be avoided.

Due to the nature of atoms and molecules, any solid will interact with another via Van der Waals forces. These can lead to attractions when summed over a body [188]. From a colloidal perspective, these are interactions which need to be confronted to avoid the aggregation of particles [189, 190].

There are many ways in which Van der Waals interactions can be avoided which include the use of a polar solvent [191], matching the index of refraction of the particle to that of the solvent [192] and the use of polymers grafted to the surface of the particles [193, 194]. In aqueous solution, the stability of particles can be tuned by simply changing the concentration of free ions. Larger concentrations of ions allows the Van der Waals interaction to take over leading to aggregation.

For a surface with a given charge or ζ potential [1] in aqueous solution, there will be an associated density of co-ions and counter-ions which balances the exposed charge called a double layer. To describe the distribution of ions around a surface, we can point towards the Gouy-Chapman model. This model assumes that the potential of mean force and the average electrostatic potential are identical, that the ions are point charges, and that the electrolyte is an ideal solution with uniform dielectric properties [2] [79]. It gives us the Poisson-Boltzmann equation for the electrostatic potential in ionic solutions:

$$\epsilon\epsilon_0 \nabla^2 \psi = -e \sum_{1}^{N} z^k n_b^k \exp(-ez^k \psi / k_B T), \tag{4.1}$$

where $\epsilon\epsilon_0$ is the permittivity of the solution, ψ is the electrostatic potential, e the fundamental charge, N the number of ionic species, z^k the valence of the kth ionic species, n_b^k is the concentration of the kth ionic species in the bulk, and the distribution of ions associated with the potential follows:

$$n^k = n_b^k \exp(-ez^k \psi / k_B T). \tag{4.2}$$

When we consider a flat surface and a symmetric electrolyte, equation 4.1 becomes,

$$\frac{d^2\psi}{dx^2} = \frac{2ez}{\epsilon\epsilon_0} n_b \sinh(ez\psi / k_B T), \tag{4.3}$$

One can linearise the sinh function (linearised Poisson-Boltzmann) and this leads to the Debye-

[1] The electrostatic potential at the slipping plane of a colloidal particle [195]

[2] "The potential of mean force is the potential whose gradient gives the average force acting on an ion whereas the local average electrostatic potential is the canonical ensemble average of the electrostatic potential" [196].

Hückel approximation,

$$\frac{d^2\psi}{dx^2} = \frac{2e^2z^2n_b}{\epsilon\epsilon_0 k_B T}\psi. \tag{4.4}$$

The square root of the inverse of the prefactor to ψ on the right hand side of equation 4.4 is equal to the Debye length,

$$\kappa^{-1} = \lambda_D = \left(\frac{\epsilon\epsilon_0 k_B T}{2e^2z^2n_b}\right)^{\frac{1}{2}}, \tag{4.5}$$

and is a characteristic length scale over which the surface charge is shielded from its environment and effectively neutralised [79]. Raising the concentration of salt reduces the Debye length, shortening the range of the surface based electrostatic interactions between particles.

Solutions to the Poisson-Boltzmann equation for a spherical surface can only be approximated as analytical solutions do not exist. In 1961, Loeb, Overbeek and Wiersema published the first tabulated numerical results for spherical systems [197]. However, for a qualitative understanding, in the limit of large spheres, one can simply used the results for a surface, taking the Debye length as a valid characteristic length scale.

The presence of an electrolyte and the formation of a screening double layer leads to a short/medium range repulsive potential (compared to a repulsion in a vacuum). In conjunction with the Van der Waals interaction, this leads to what is known as DLVO theory named after its creators; Derjaguin and Landau and Verwey and Overbeek [198, 199]. Under the DLVO scheme, the Van der Waals interaction between to spheres can be derived, for $r << \sigma$, as [189]:

$$U_{VdW}(r) = -\frac{A\sigma}{2r}, \tag{4.6}$$

where A is the Hamaker constant, a coefficient which accounts for the properties of the particles interacting via Van der Waals. The electrostatic contribution from the double layer repulsion between two spheres in DLVO theory can be approximated with [189]:

$$U_{DL}(r) = 2\pi\sigma\psi_s\epsilon\epsilon_0 \exp(-\kappa r), \tag{4.7}$$

where ψ_s is the charge at the surface.

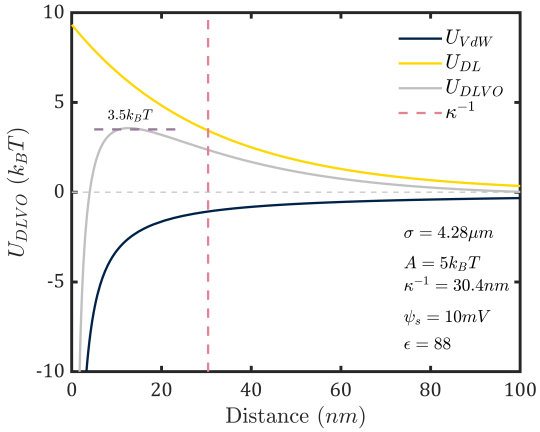

Figure 4.1: The repulsive barrier created by double layer propulsion according to DLVO theory. The Van der Waals potential, the double layer repulsion potential and the DLVO potential for a pair of particles with the given properties in the figure using equations 4.6 and 4.7. The repulsion creates a barrier to the Van der Waals regime of around $3.5k_BT$.

Under the correct conditions, the repulsive double layers results in suspensions of colloidal particles which remain stable for long periods of time and, because the Debye length is generally orders of magnitude smaller than the diameter of the particles in question [3], they behave as if they interact with a hard potential [106, 200, 201].

4.1.2 Motility-Induced Phase separation in Experiment

As mentioned in the introduction of this thesis, there are many methods which have been used to create colloidal active particles. The most important of which are those activated by light [202], the decomposition of hydrogen peroxide [203] and those propelled by an interaction with an electric field [204]; this list is by no means exhaustive [53, 205]. All three of the aforementioned mechanisms of propulsion have been employed to create systems which phase separate.

The first examples of the study of phase separating active particles come from the use of bacteria, [183, 206]. These studies came before the term motility-induced phase separation had taken hold. Although bacterial systems can be tuned with methods such as genetic modification and the control of nutrients, choosing the Péclet number of the swimmers can be difficult and as such many have turned to synthetic alternatives.

Although the systems propelled by the decomposition of hydrogen peroxide were where clusters were first reported [51] (figure 4.2(a)), it quickly became evident that due to the consumption

[3] κ^{-1} is typically 1 to 25 nm compared to the colloidal length scale of 100 to 10 000 nm

of the fuel and the low speed of the particles ($v = 1 - 5\sigma s^{-1}$) that using other methods are better for MIPS. Then came the first study where larger clusters of particles emerged [52] (figure 4.2(b)). These clusters were shown to be reversible by how they separated when the light was turned off. In both of the mentioned studies they discovered that the size of the clusters had a linear relation with velocity [57, 204].

The system created by Gangwal *et al.* [207] of induced-charge electrophoretic particles, which was first conceptualised by Squires and Bazant in 2006 [208, 209], was then used by Yan *et al.* to create active particles with tunable velocities, controllable electrostatic interactions and none of the previous flaws that other synthetic particles had; namely being difficult to use in dense systems. They created four behavioural regimes; gas, swarms, chains and clusters (figure 4.2(c)). Through a comparison of the magnitude of forces in the system, they deduced that the interactions between the particles were mainly electrostatic from the quadrupoles in the particles induced by the external electric field.

Soon after came an article on the dynamics of clusters of electrophoretic Janus particles by van der Linden *et al.* [7]. Their system, almost identical to that used in for the results in this chapter, is composed of 4.28 µm silica particles half-coated in 35 nm of titanium followed by 15 nm of silica between two indium tin oxide (ITO) electrodes coated in 25 nm of silica separated by 95 µm. The particles, at an area fraction of 0.29, were propelled by an alternating electric field at $f = 10kHz$ and $a_V = 10V$ to $20\sigma s^{-1}$ with a "negligible" rotational diffusion (giving an approximate Péclet number of 350).

The clusters in this system were able to translate efficiently and also frequently break (figure 4.3). It was explained that these clusters would break due to the stresses generated by their motion acting on the weak grain boundaries formed by the history of aggregation; much like our results in chapter 3 and the results on numerical systems published later by Caprini *et al.* [176]. On top of this the correlated alignment of particles was said to be controlled by the electrostatic interactions of the particles in the system which occasionally made particles follow each other [4]. Particles were prone to finding regions on the surface of their electrodes to bind to when the electric field was on and thus led to limited experimental statistics. This chapter is an attempt to build on this work.

Since the work of van der Linden *et al.*, there has been a second article which has shown

[4] Much like the chains in the work of Yan *et al.* [57] in figure 4.2(c).

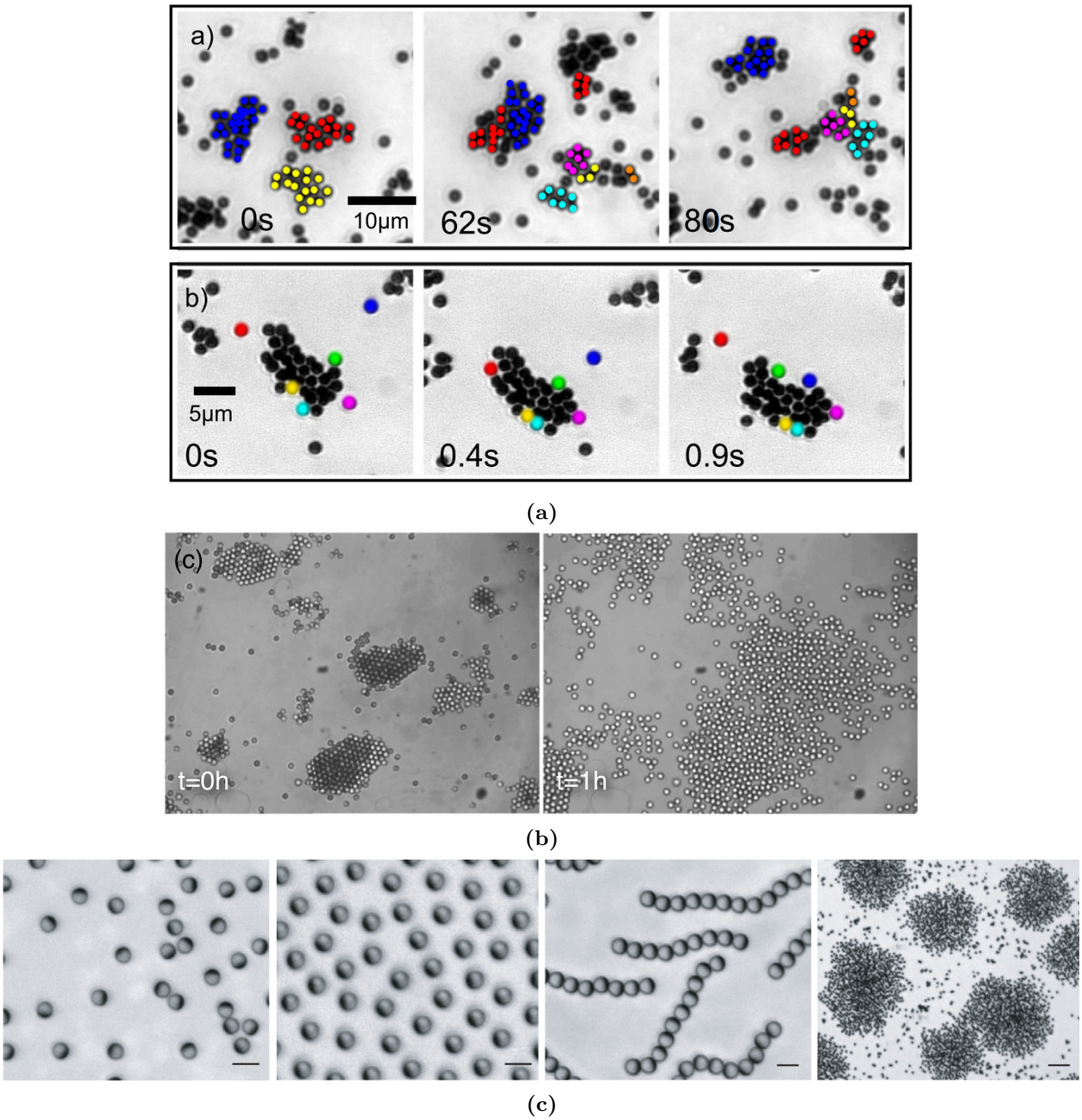

Figure 4.2: Some key examples of motility-induced phase separation in experiment. (a) Dynamic clusters observed in a $\phi = 0.5\%$ and $C_{H_2O_2} = 0.1\%$. The images are obtained in the transmission mode with a $63x$ objective. An illustration of the dynamics between clusters and the dynamics inside a cluster. Marked particles show exchanges between clusters, a dynamic exchange between the gas phase and the cluster, and internal reorganisation of the cluster. From Theurkauff *et al.* [51]. (b) At high densities ($\phi = 0.27$ and $v = 0.77\sigma s^{-1}$), phase separation into a few big clusters and a dilute phase occurs. The aggregation is completely reversible: The snapshots show how the clusters dissolve after the illumination has been turned off. From Buttinoni *et al.* [48]. (c) Illustrative images of gas, swarms, chains and clusters observed experimentally. The first three images are obtained in deionized water. The cluster phase is obtained in 0.1 mM NaCl solution at f equal to 40 kHz. Scale bars are 5 µm in the first three images and 30 µm in the last. From Yan *et al.* [57].

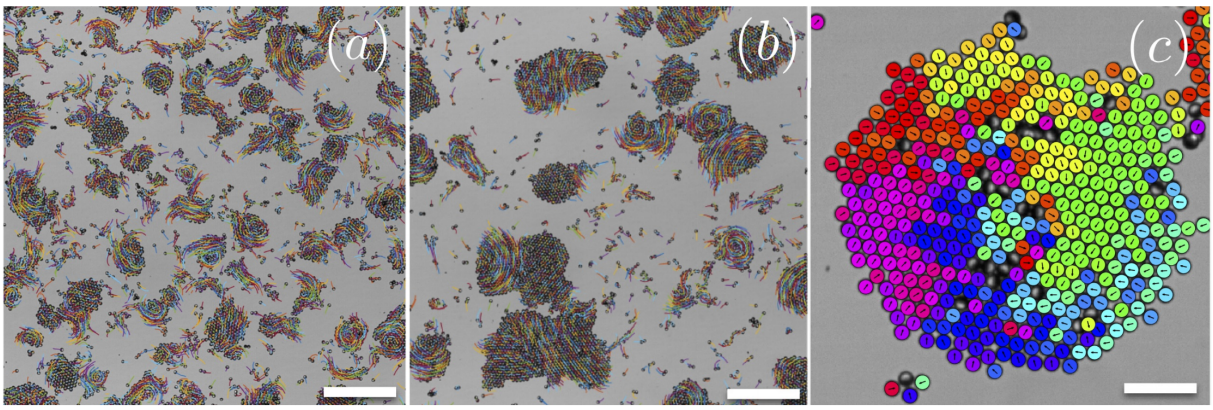

Figure 4.3: A dynamic system of active clusters. (a)-(b) Snapshots at times $t = 8s$ and $t = 42s$, with traces of the particles integrated over $\Delta t = 0.4s$. Scale bar is 100 µm. (c) The colloids orientations inside one cluster. Scale bar is 25 µm. Adapted from van der Linden *et al.* [7].

dynamic clusters. In the work of Karani *et al.* [54], they studied dense suspensions of Quincke rollers [53, 210]. These propel themselves due to spontaneous symmetry breaking of the charge distribution at their surface leading to an electrostatic torque and swim in a similar fashion to bacteria (run and tumble). They showed that the dynamics of their clusters strongly depended on the run time and turn time of their particles.

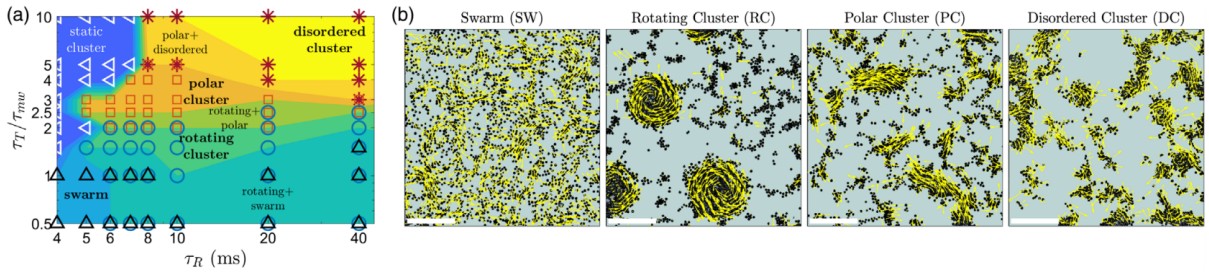

Figure 4.4: Cluster variations in systems of Quincke rollers. (a) Collective states formed by Quincke random walkers with different run and turn times (τ_R, τ_T). Symbols indicate: left triangles are static clusters, upwards triangles are swarms (SW), circles are rotating clusters (RC), squares are polar clusters (PC), stars are disordered clusters (DC). (b) Snapshots of the SW ($\tau_T/\tau_M W = 3$, $\tau_R = 4ms$), RC ($\tau_T/\tau_M W = 1.5$, $\tau_R = 5ms$), PC ($\tau_T/\tau_M W = 0.5$, $\tau_R = 8ms$), and DC ($\tau_T/\tau_M W = 10$, $\tau_R = 40ms$) phases from the experiments. Scale bar is 1 mm. Velocity vectors are superimposed to the particles. Particle area fraction and pulse amplitude are constant in all experiments and are equal to $\phi \approx 0.15$ and $E = 2.08MV/m$, respectively. Adapted from van der Karani *et al.* [54].

4.1.3 Induced-Charge Electrophoretic Particles

For the purpose of using the Janus particles as active particles in experiment, a detailed description of their propulsion mechanism is not necessary. We will, in the remaining parts of this section cover, the necessary theory which describes their mechanism of motion. We start with the principles of electro-osmosis, the motion of fluid induced by an electric field along a

surface. We then extend this to a cylinder in aqueous solution and finally a Janus particle in a time-averaged alternating electric field. We then cover two additional effects, that of electrohydrodynamic repulsion and electrostatic interactions (including the complexities of polarisation). We do this because these are the types of interactions we observe in these systems which we have tuned our setup to avoid.

Electro-Osmosis and Electrophoresis

Any electrostatic double layer induced by a surface charge will lead to flow of ions and accompanying fluid in a perpendicular electric field (figure 4.5). The resulting flow slips outside the screening double layer; the slip velocity is given by the Helmholtz-Smoluchowski (HS) formula [209]:

$$\vec{u}_s = -\frac{\epsilon\epsilon_0\zeta}{\eta}\vec{E}_{\parallel}, \tag{4.8}$$

where ζ is the zeta potential given by $\zeta = q\kappa^{-1}/\epsilon\epsilon_0$, $\vec{E}_{\parallel}$ is the tangential component of the bulk electric field to the surface.

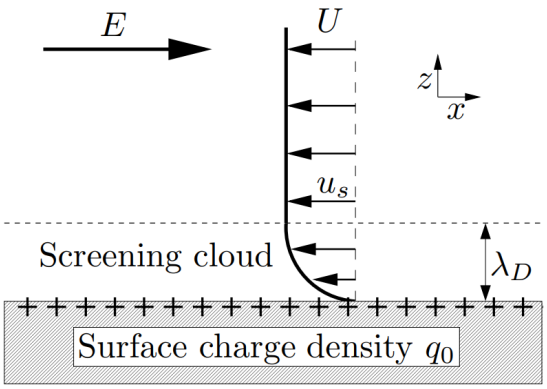

Figure 4.5: Electro-osmosis. A charged solid surface in an electrolytic solution attracts an oppositely-charged "screening cloud" of width $\approx \lambda_D$. An electric field applied tangent to the charged solid surface gives rise to an electro-osmotic flow. From Squires and Bazant [209].

When a charged particle is affected and not a surface, the name of this effect term changes to electrophoresis (motion of the freely moving particle) and the HS formula becomes:

$$\vec{U} = \frac{\epsilon\epsilon_0\zeta}{\eta}\vec{E}_{\infty} \equiv \mu_e\vec{E}_{\infty}, \tag{4.9}$$

where $\vec{U}$ is the new electrophoretic velocity of the particles propulsion, $\vec{E}_{\infty}$ is the external electric

field and μ_e is the electrophoretic mobility. This equation remains valid as long as:

$$\frac{\kappa^{-1}}{a} \exp\left(\frac{ze\zeta}{2k_BT}\right) \ll 1, \tag{4.10}$$

where a is the radius of curvature of the surface. When this inequality is not satisfied, surface conduction becomes important and the electrophoretic mobility has to be modified by a dimensionless ratio of the surface and bulk conductivities called the "Dukhin number" Du and other phenomena occur such as bulk concentration gradients alongside non-uniform charge distributions which lead to extra diffusiophoresis and concentration polarisation. More on this theory can be found in the work of Lyklema [211] and Dukhin [212].

Induced-Charge Electrophoresis

The theory in the previous section is based on particles which have a net non-zero surface charge. In fact, with a few adjustments, it can be extended to those which have surface charges that have been induced by an external field. Unlike simple electrophoresis (EP), induced-charge electrophoresis (ICEP) is able to propel particles in alternating and static fields [209].

First we will describe the case for static fields. Once an electric field is applied to a polarisable particle, it will gain an ionic cloud as a response to it gaining induced surface charges, as shown in the first diagram in figure 4.6. This ionic cloud screens the particle and the electric field resembles that in the second part of figure 4.6. The electric field then interacts with the ionic cloud resulting in the flows shown in the third and fourth images where the third represents a zero net charged cylinder and the fourth a positively charged cylinder.

The quadrupolar slip velocity of the resulting flows can be written as:

$$\vec{u}_s = 2U_0 \sin(2\theta)\hat{\theta}, \tag{4.11}$$

with:

$$U_0 = \frac{\epsilon\epsilon_0 E_0^2 a}{\eta}, \tag{4.12}$$

where U_0 is the natural velocity scale for ICEP, E_0 is the magnitude of the external field and θ is the position on the surface of the sphere relative to the orientation of the electric field. A

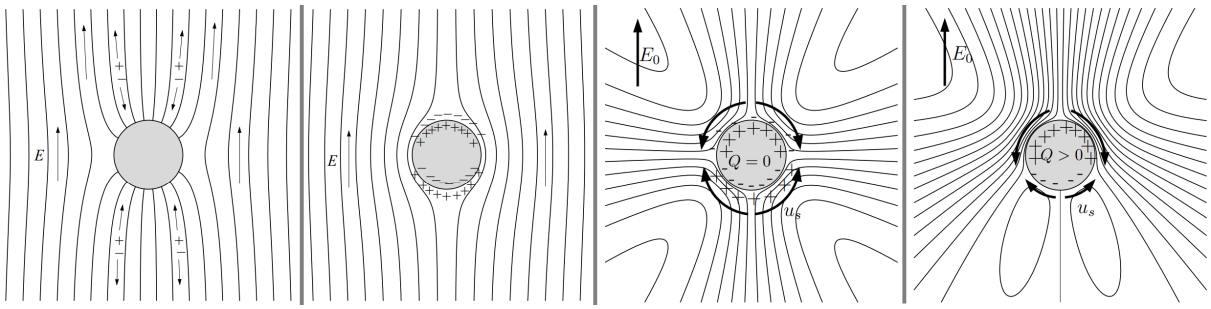

Figure 4.6: Mechanism of ICEP. The evolution of the electric field around a solid, ideally polarisable conducting cylinder immersed in a liquid electrolyte, following the imposition of a background static field. Over a charging time $\tau_c = \kappa^{-1}a/D$, a dipolar charge cloud forms in response to currents from the bulk, reaching steady state when the bulk field profile is that of an insulator. The resulting zeta potential is non-uniform. The third and fourth images are the steady-state induced-charge electro-osmotic flows around (third) a conducting cylinder with zero net charge and (fourth) a positively charged conducting cylinder. The ICEP slip velocity depends on the product of the steady field and the induced zeta potential. From Squires and Bazant [209].

static surface charge on the particles will couple to the polarisation and alter the magnitudes of these effects, although this would be minor in the larger electric field amplitudes used in this work.

When an alternating field described by $\vec{E} = E_0 \exp(i\omega t)$ is concerned, where ω is the alternating frequency, the zeta potential and ICEP become time dependent:

$$\zeta = 2E_0 a \cos(\theta) Re\left(\frac{\exp(i\omega t)}{1 + i\omega\tau_c}\right), \tag{4.13}$$

$$\vec{u}_s = 2U_0 \sin(2\theta)\left[Re\left(\frac{\exp(i\omega t)}{1 + i\omega\tau_c}\right)\right]^2 \hat{\theta}, \tag{4.14}$$

and:

$$\langle \vec{u}_s \rangle = \frac{U_0 \sin(2\theta)}{1 + \omega^2\tau_c^2}\hat{\theta}, \tag{4.15}$$

where τ_c is the characteristic charging time of the cylinder and $\langle \vec{u}_s \rangle$ is averaged over time.

This analysis requires that $\omega \ll \tau_D^{-1}$, where $\tau_D = (\kappa^{-1})^2/D_i = \epsilon\epsilon_0/\sigma_c$, D_i the ion diffusivity and σ_c is the conductivity of the ions, i.e. that the double-layer changes quasi-steadily. It is also the case that in the high-frequency limit that the particle will not have time to charge up and will attain a maximum magnitude, $(\omega\tau_c)^2$, with a $\pi/2$ phase shift. It is also necessary that the charging time is much larger than the diffusion across the double layer: $\tau_c > \tau_D$. The charging time also needs to be much smaller than the diffusion time of the particle.

For this work, it is important to note that at large voltages many of the aforementioned effects become more complex. Not only does the initial charging process change but the ideal polarisability of the particle can be altered and chemical reactions can occur at the surface.

So far, we have only covered the case where a particle is made of a uniform polarisable material. Squires and Bazant also presented theory when one side of a particle was a dielectric; a Janus particle. In this case (represented in figure 4.7) the velocity of the particle becomes:

$$\vec{v}_a = -\frac{4}{3\pi} U_0 \hat{x}, \tag{4.16}$$

if at low electric field frequencies and amplitudes.

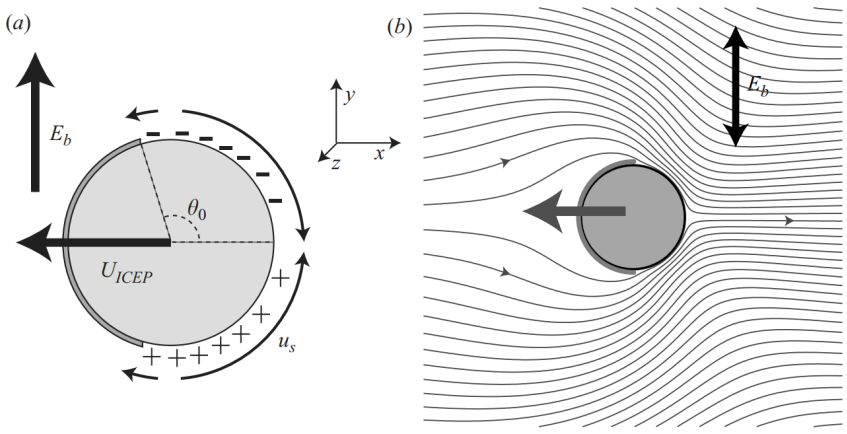

Figure 4.7: Mechanism of ICEP for a Janus particle. (a) Induced-charge electrophoretic motion of a partially coated cylinder with a partial dielectric coating that breaks left–right symmetry. (b) Streamlines (in the co-moving frame) for the ICEO flow around a conducting cylinder whose left-hand side is coated with a dielectric layer that suppresses ICEO flow. The cylinder moves in the direction of its coated end. From Squires and Bazant [208].

Additional Electrohydrodynamic Effects

ICEP is not the only method to generate flows around particles in electric fields. In a 2004 article by Ristenpart *et al.* [213], the phenomenon by which identical passive particles would aggregate in alternating electric fields was theoretically described. These fields had frequencies between 100 Hz and 10 kHz and opposed the repulsions from Coulombic interactions and induced dipoles. The flows towards the particles is given by:

$$\vec{u} \cdot \vec{t} \approx \frac{3\epsilon\epsilon_0\kappa^{-1}}{\eta} \frac{E_0^2}{4(h/2)^2} \left(C_0' + \frac{D_i}{\omega(\kappa^{-1})^2} C_o'' \right) \tag{4.17}$$

where h is the electrode plate separation and C_0 is the dimensionless complex dipole coefficient for polarisation. The effect of this phenomenon can be seen in figure 4.8. Particles reversibly aggregate. As shown by the specific frequencies used for this phenomenon, we chose to use frequencies which would avoid this interaction and keep our particles "hard".

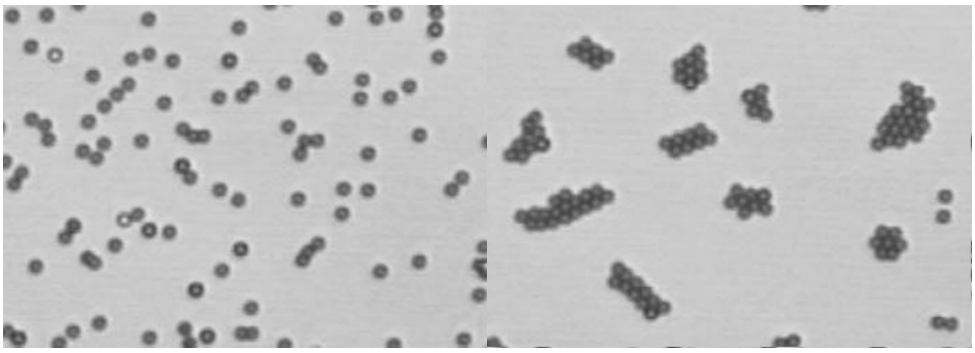

(a) **(b)**

Figure 4.8: Lateral aggregation in response to an electric field. Particles are 2.7 µm polystyrene in 1 mM KCl. The applied field is 500 Hz and 6 V, oriented out of the page. (a) Initially there are 407 isolated particles dispersed throughout the field of view. (c) After 30 s, only 19 solo particles remain. Adapted from Ristenpart *et al.* [213].

Complex Dipole Coefficients

A final important aspect of a system of electrophoretic Janus particles is that, as was pointed out in the works of Yan *et al.* [57], it is not the case that the dielectric component (SiO_2) of the particles is non-polarisable: it is just significantly less so than the metallic side. Therefore to understand the interactions between their induced quadrupoles/dipoles we must understand their polarisibility.

The polarisability of a material can be described using the Clausius-Mossotti factor otherwise known as the dimensionless complex dipole coefficient. Yan *et al.* used the work of García-Sánchez *et al.* [214] and Shilov *et al.* [215] to predict these coefficients as shown in figure 4.9.

Due to the complexity of the system, trying to describe it theoretically in its entirety is beyond the scope of this thesis. This polarisation can lead to electrostatic interactions which can prevent our particles from behaving as hard particles. Therefore our system is chosen to minimise these interactions whilst still inducing electrophoresis by using frequencies close to where the real complex dipole coefficient for metals changes sign and whilst it remains negative to reduce attractions.

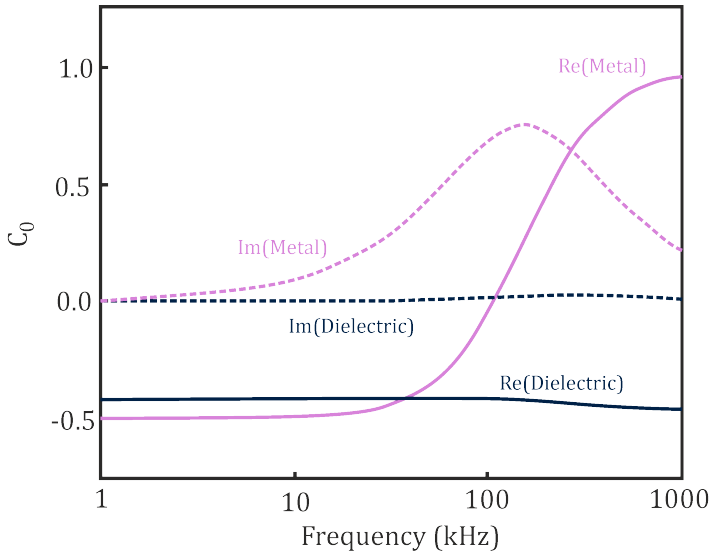

Figure 4.9: Real and imaginary parts of the dimensionless complex dipole coefficients for polarisable and dielectric particles. Solid and dotted curves represent the real and imaginary parts of the induced dipole coefficients for metal hemisphere (magenta) and dielectric hemisphere (blue) respectively at different frequencies. Adapted from Zhang *et al.* [216].

Behaviours in Experiment

The first use of induced-charge electrophoretic Janus particles in experiment can be found in the work of Gangwal *et al.* [207]. In their work, they studied a system where the electric field was aligned with the plane the particles swam in. Crucially they showed that the relation between the electric field amplitude and the velocity of the particles followed the relation in equation 4.12 (figure 4.10(a)). They also showed that an increase in the ionic strength of the solution, the total concentration of ions in the solution, led to a decrease in the particle velocity. This is because a reduction in the Debye length leads to a reduction in the slip velocity.

The next work in the history of the use of ICEP Janus particles comes from the group of Masaki Sano. In the article by Nishiguchi and Sano [204], they showed that the flows generated by the particles when an electric field of 1 kHz and $2 \times 10^5\,\mathrm{V\,m^{-1}}$ led to short ranged velocity correlations between the particles which then led to active turbulence (figure 4.10(c) and (d)). In a later article, Nishiguchi *et al.* then showed that the velocity of Janus particles depends on the frequency of the electric field, inverting at a given frequency. This in conjunction with an attractive interaction between the metallic and the dielectric side of the particles lead to moving chains over a range of frequencies and salt concentrations (figure 4.10(e)). If one of the end particles becomes stuck to the surface then Nishiguchi *et al.* showed how the chains beat due to the electric field and the flows associated with their motion. In a much later article [218],

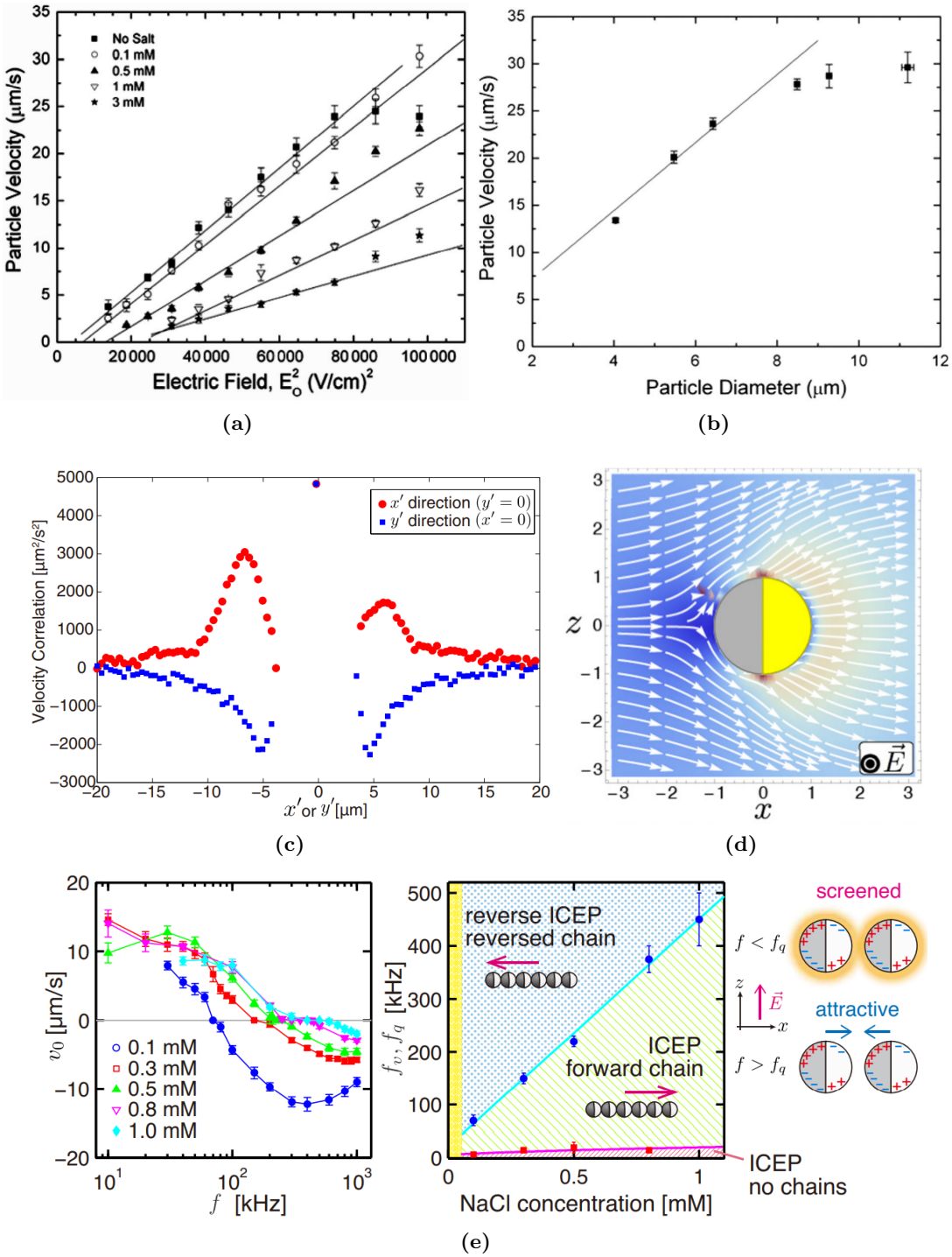

Figure 4.10: Typical behaviours of induced-charge electrophoretic Janus particles. (a) Velocity of 5.7 µm Janus particles as a function of electric field intensity squared (E_0^2) for various NaCl concentrations at 1 kHz. The linear fits generally agree with the experimental values for low intensities and start deviating for $E_0 > 280 V cm^{-1}$. (b) Average velocity of different size particles as a function of their average diameter at 300 V cm^{-1} in 0.1 mM NaCl at a field frequency of 1 kHz. Adapted from Gangwal *et al.* [207]. (c) Slices of the velocity correlation function at $y' = 0$ and $x' = 0$. Positive correlation in the x' direction indicates that the particles are following other particles in front of them. (d) Flows perpendicular to the electric field in the particle frame where the colour indicates the amplitude of the flow field. Adapted from Nishiguchi and Sano [204]. (e) Frequency dependence of self-propulsion velocity v_0 for different NaCl concentrations (1.2×10^3 V cm^{-1}) and the velocity reversal frequency f_v (blue circles) and the interaction switching frequency f_q (red squares) for different NaCl concentrations. Adapted from Nishiguchi *et al.* [217].

Iwasawa *et al.* (still in the same group) showed that swarms with long range orientational order could be achieved through the interactions at 1 MHz and 615 V cm^{-1}.

In parallel to the group of Sano, the group of Steve Granick also studied such particles. Over three articles, they showed that colloidal clusters could be made using mixtures of Janus and passive particles [216] (figure 4.11(a)) and that "dilute" clusters could be formed where particles were freely able to move [57, 219] (figure 4.11(b)).

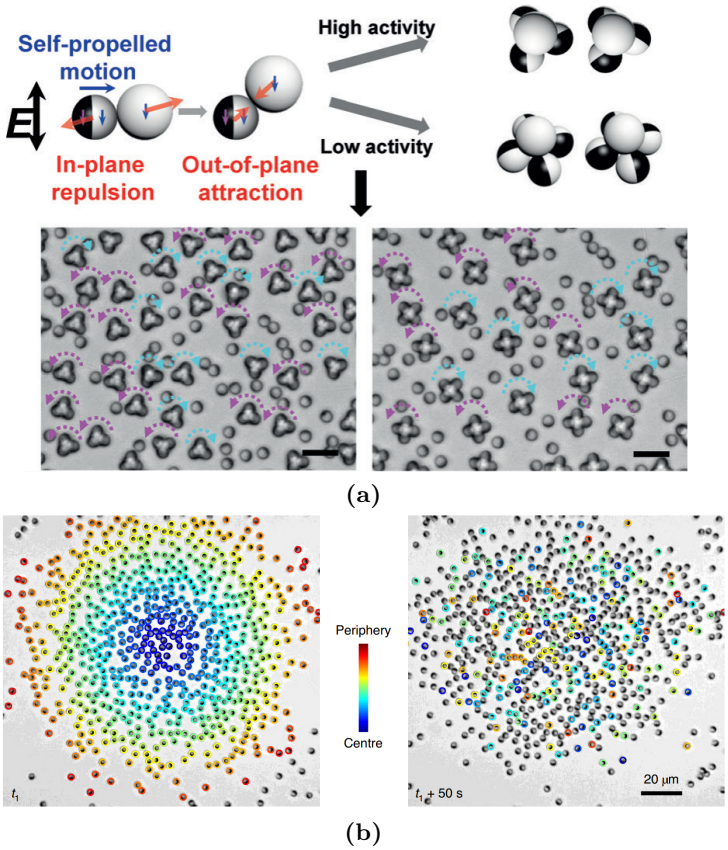

Figure 4.11: Dilute clustering with ICEP Janus particles. (a) Directed self-assembly of chiral colloidal active clusters. The Janus particles are 3 µm in diameter with an alternating electric field of 40 kHz and 400 V cm^{-1}. Adapted from Zhang *et al.* [216]. (b) Example of particle turnover between the gas and cluster states for a cluster whose total population is nearly constant over the experimental time window. Adapted from Zhang *et al.* [219].

An aspect which is both the advantage and disadvantage of using ICEP Janus particles and their downfall is that they can have many tunable iterations. They are affected by a multitude of factors, including particle size electrode composition, electrode separation, the nature of the dielectric and conductivity of the metal, the diffusivity and concentration of the ions and many more which all affect both the activity and the interactions of the particles. These are in principle controllable but difficult to fine-tune whilst also preventing particle from adhering to the surface.

In the next section, we present the methods used for the results of this chapter.

4.2 Experimental Methods

4.2.1 Experimental Setup

For all the experiments in this chapter we used 4.28 µm silica particles as a base to create Janus particles. To make the particles into Janus particles we first deposited them onto a glass slide. The glass slides are cleaned by sonication in 4 % Hellmanex solution at 45° Celsius. 400 µl of a solution of particles was spread on top of a glass slide resulting in an area fraction of 0.1. The glass slide was kept in an open container such that the water evaporates (using ethanol as a solvent instead of water speeds up the evaporation and can help to avoid particles clustering). The glass slides were then coated with 50 nm of titanium by vapour deposition, then coated with 15 nm of silica to avoid having the metal side exposed and submitting the particles to strong Van der Waals interactions. These particles were then removed by gentle sonication into a 0.1 mM solution at 37 Hz for 2 min. As particles break away from each other they can sometimes break a part of their coating. This makes them swim in a chiral fashion. The extent of this is discussed in the results section. Aqueous solutions were prepared by serial dilution by mass.

The observation cell is built as in figure 4.12. For the upper electrode, we used 15-30 $\Omega\,\mathrm{cm}^{-1}$ ITO cover slips from Diamond Coatings Ltd coated in 25 nm by vapour deposition at 0.03 $\mathrm{nm\,s}^{-1}$. Traditionally ITO slides have been used for both electrodes. We found that particles found regions of the surfaces to stick to once the electric field is on. In figure 4.13(a) we show a simple bright field microscopy image of a 2-15 $\Omega\,\mathrm{cm}^{-1}$ ITO cover slip where the crystalline nature of the ITO creates a rough surface which affects local electric fields. Based on this we chose to move to using gold electrodes.

Below a thickness of 40 nm, a gold electrode is partially transparent but far more fragile. In figure 4.13(b), we plot a measurement of the resistivity of the gold electrodes over 1 cm. It shows that at least 40 nm of gold is required to reach the same resistivity that ITO has. We therefore chose to use 80 nm gold electrodes to get low resistivity, and a more solid surface. To be able to record images we then used reflection microscopy as the gold electrode is not transparent at this thickness. Because the transparency of the electrode was no longer of concern, we then added

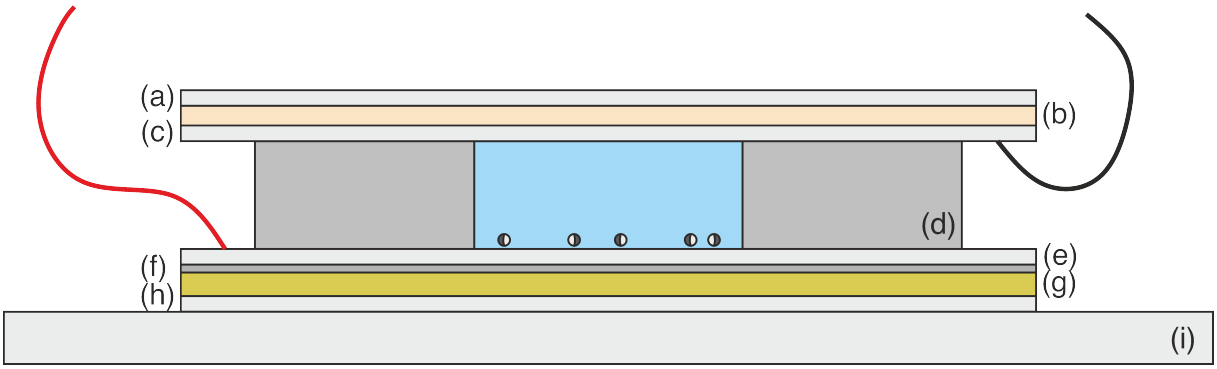

Figure 4.12: A scheme of an observation cell. (a) Cover slip, (b) ITO electrode, (c) 25 nm silica, (d) spacer with UV glue, (e) 25 nm silica, (f) 5 nm chromium, (g) 80 nm gold, (h) cover slip and (i) glass slide. Wires are connected with tape.

5 nm of chromium to stabilise the connection between the gold and the additional 25 nm of silica to prevent Van der Waals interactions between the gold and the coated particles. All coatings were done by vapour deposition at a rate of $0.03\,\mathrm{nm\,s^{-1}}$ apart from the gold which is done by thermal evaporation at $0.3\,\mathrm{nm\,s^{-1}}$. Slow deposition ensures a more even coating.

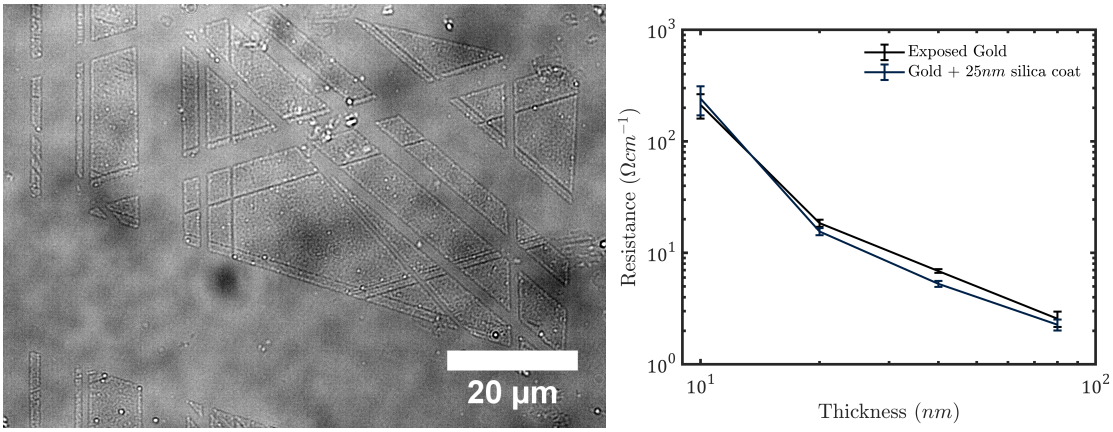

(a) **(b)**

Figure 4.13: Properties of electrodes. (a) A bright field microscopy image of a 2-15 $\Omega\,\mathrm{cm^{-1}}$ ITO cover slip where the structure of the ITO can be seen; the origin of many of the particle sticking issues. (b) The resistivity over one centimetre of gold electrodes at various thicknesses.

The gold cover slip was mounted onto a glass slide using Norland optical UV glue. Specac Omni Cell spacers from Merck of a width of 60 µm were used with UV glue to enclose the cell. The upper cover slip was pressed before the glue was cured. This left a gap of (110 ± 010) µm between the electrodes.

An alternating potential difference was passed through the electrodes through the wires which are attached to exposed surfaces of the electrodes past the spacers. Using a signal generator, we created a square waved signal at a chosen frequency and amplitude.

The conditions described in this section were assembled after testing a preliminary broad parameter space.

4.2.2 Reflection Microscopy

Due to the non-transparent gold electrode, typical bright field microscopy is not an option for imaging our particles. Instead we opted to use reflection microscopy, exploiting the reflective properties of the 80 nm of gold.

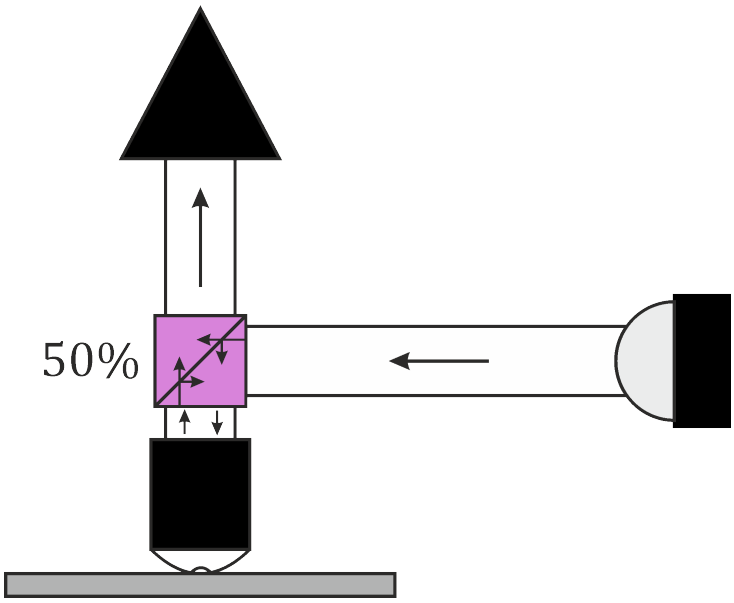

Figure 4.14: Reflection microscopy setup. Light passed through a 50:50 beam splitter and is reflected through the objective (acting as a condenser) and onto the sample. The light passes through the particles is reflected and comes back into the objective after which it passes again through the beam splitter before going to the camera.

The beam splitter shown in pink in figure 4.14 is the BS013 50:50 beam splitter from Thorlabs. The objective we used was an Olympus UPLXAPO 20X oil immersion Objective with a numerical aperture of 0.8. Because the light passed through the objective before hitting the sample, the numerical aperture of the "condenser" and the objective was the same meaning that the final image is not uniform if the whole field of view is used. The signal of the particles we obtain is also not the same as those usually seen in bright field experiments. Therefore, we use a custom detection algorithm.

To record our images we used a $4.2 MPix$ XIMEA camera which passed images into $\mu Manager$ software to record a video with a constant frame-rate (a maximum of $10.3 fps$ limited by the rate of transfer to the computer).

4.2.3 Particle Detection

Particle detection is a crucial step in the analysis of individual colloidal particles. A large step in the detection of particles from numerical images was done by Crocker and Grier in 1995 [220]. They were studying uniform passive particles. They established a procedure which first found the peaks of intensity, then used a bandpass filter to iron out noise in the image and then ended with a Gaussian fit on the particles to obtain a sub-pixel level of accuracy. There exist a few procedures already in the scientific literature for the detection of Janus particles but we choose to use our own as reflection microscopy gives us a different signal compared to previous studies [221].

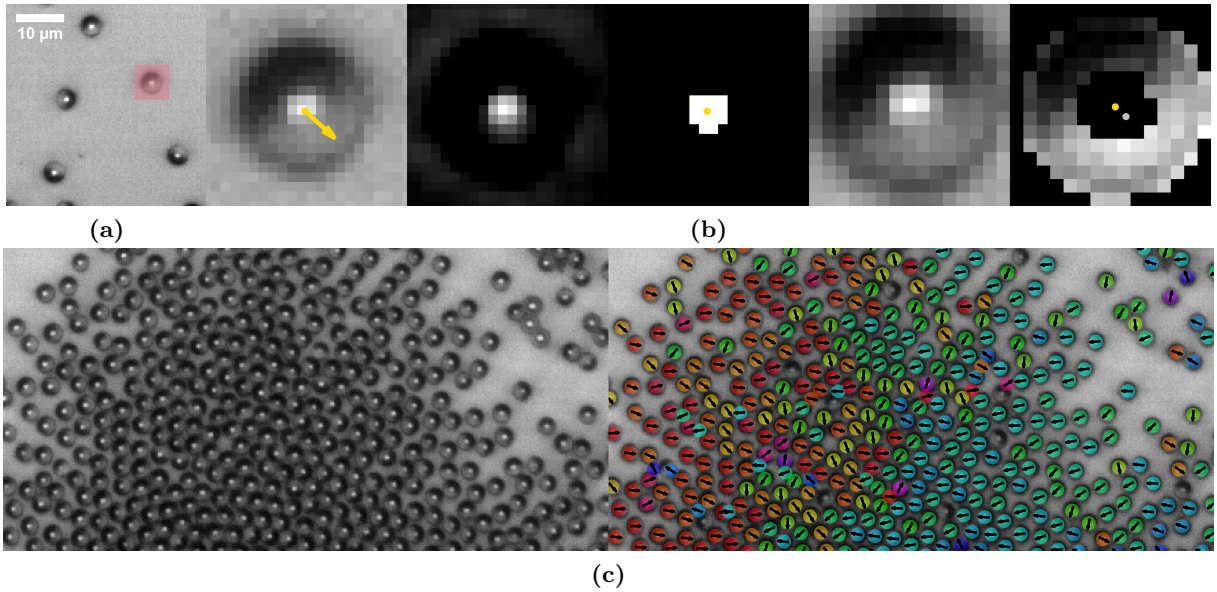

Figure 4.15: Particle detection procedures. (a) A suspension of active 4.28 µm ICEP Janus particles on an electrode observed by reflection microscopy with the electric field turned on. The pink square in (a) corresponds to the particles shown in (b). (b) The step by step detection of an active particle going from the raw image (with the final position and angle of detection), to one after a bandpass, to one of the binarised image from which the weighted centre of mass of the pixels is calculated, to a raw image pre cut for determining the angle to the final image where the central and outer pixels are cut to obtain the angle. (c) A comparison of a raw image and the detection super imposed. Colours denote the angles given by the arrows.

In figure 4.15(a), we show what Janus particles look like once an electric field has been turned on and the particles rise to align with it. We see a bright spot in the centre which comes from light reflecting off part of the metal cap and directly through the particle. We made use of this. To avoid using the slow peak-finding and Gaussian fitting procedures, we first began with a bandpass filter before binarising each frame of a video. Subsequently, we used the "regionprops"

inbuilt function in MATLAB to determine the centre of mass of the pixels of the bright region belonging to a particle, weighted by their intensity in the original image. This procedure is around ten times faster than the traditional Crocker and Grier method. A step by step example is shown in figure 4.15(b).

Due to the an-isometry of the Janus particles, we implement an algorithm to obtain the angle of the particle. We first crop each particle out of the image (fourth image in figure 4.15(b)). We then crop out pixels either more than the radius of the particle (2.14 µm) or less than 0.87 µm to obtain the pixels pertaining to the particle without the bright centre. By using a weighted centre of mass of the leftover pixels, we determine the second point in the fourth image of figure 4.15(b). We then create a vector between the two points shown to obtain the orientation. All of our subsequent analysis is based on the positions and angles of the particles over time.

We find that, although our methods are relatively robust, there can be some errors. These are typically associated in the dense regions where particles interfere with each others' signal or create a lensing effect between them which creates ghost particles. It is also the case that the tracking procedure fails when the particles are moving quickly. This is because the distance they travel between subsequent frames is large it is harder to correlate their positions (this is limited in our case by our camera's recording speed).

4.3 Results

4.3.1 Péclet Number vs Density Phase Diagram in Experiment

To be able to compare the results of our experiments to each other and to those of our simulations, a crucial aspect of the system we need to measure is the Péclet number. To do this we need a measure of the mean velocity of the particles and the rotational diffusion coefficient (alongside their distributions). This is because we measure the Péclet number in this work with the following equation and ignore the contribution from translational Brownian motion [159]:

$$Pé = \frac{3v_a}{\sigma D_r}, \tag{4.18}$$

One can obtain the velocity of the particles with a study of dilute systems where particle interactions/collisions can be neglected. Although this presents us with an easier method from an analysis point of view, it does not mean we have an exact measure of the motion of the particles in the systems we wish to look at and also assumes, unless proven otherwise, that our experiments are consistent with one another. Instead, we choose to directly take measurements of the important aspects of our system such that we know precisely how our particles behave and to avoid needing to consider experimental inconsistencies, such as the distance between our electrodes, which can be difficult to control.

We present measurements in the next sections using the videos from which the snapshots in figure 4.16 are taken.

Measuring Velocity

A velocity is defined simply as the distance a particle travels over a certain time. In an ideal world this would mean that we could choose any time interval and distance covered from which to calculate a mean. To obtain the most detail we would simply choose the smallest time interval and distance possible. In practice, as with any measurement, we must take care as to when and where we take it; also considering any effects which can alter the value we obtain.

In the case of measuring the velocity of an active particle whose position we detect from numerical images, we must consider two extra facets of its motion; noise and angular motion.

In figure 4.17(a), we plot the trajectory of a particle in an 8 kHz 100 V cm^{-1} electric field. This particle has a given velocity but also a combination of translational diffusion and noise in the detection shown in the roughness of the line. If we then look at (b) of the same figure, we see that at short time intervals the mean velocity decreases until it reaches a plateau. The plateau is the true mean velocity of the particle [5].

If one considers the limit where the time interval is infinitesimally small, then one essentially takes a measurement of a distance between two points on a two dimensional Gaussian distribution. The mean of the probability density function of the distances between two points on the same Gaussian has a value of 1.74 standard deviations [222]. This means that if a velocity is measured there will be a significant positive contribution from the noise (a very large number

[5] We have tested this via a numerical approach.

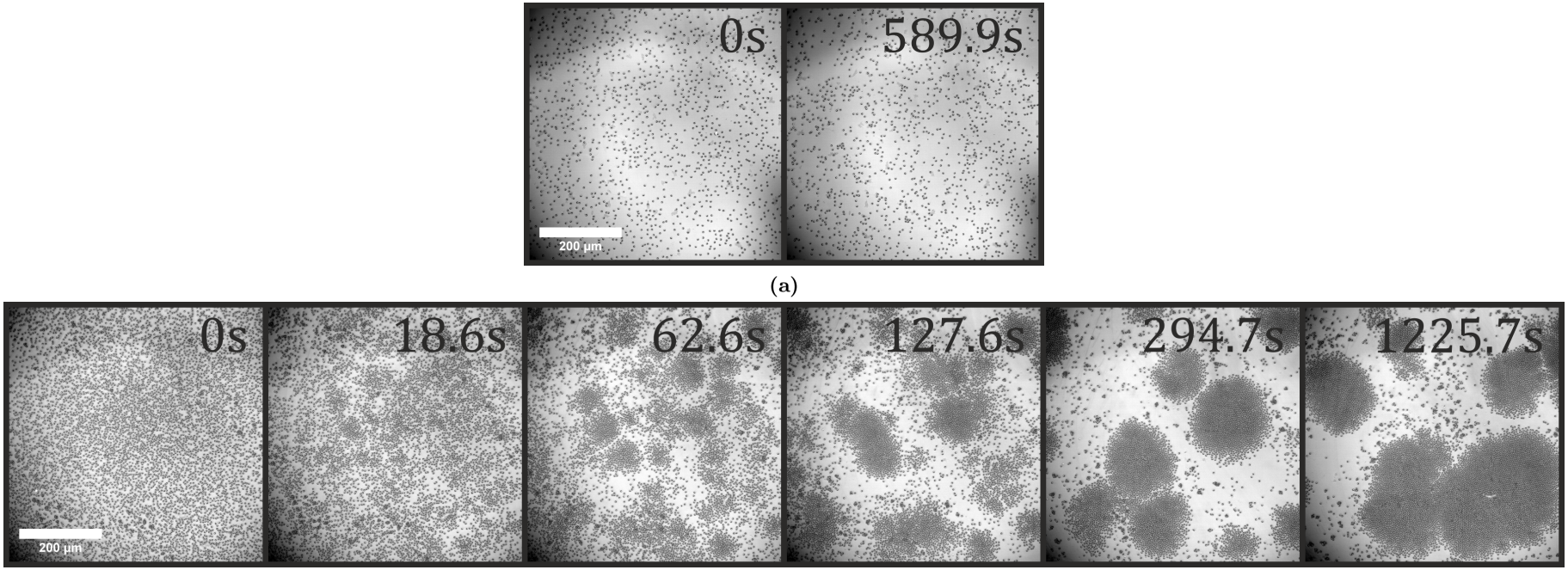

Figure 4.16: Snapshots of example recordings. (a) $\phi = 0.05$, 8 kHz and 100 V cm^{-1}. (b) $\phi = 0.32$, 8 kHz and 250 V cm^{-1}.

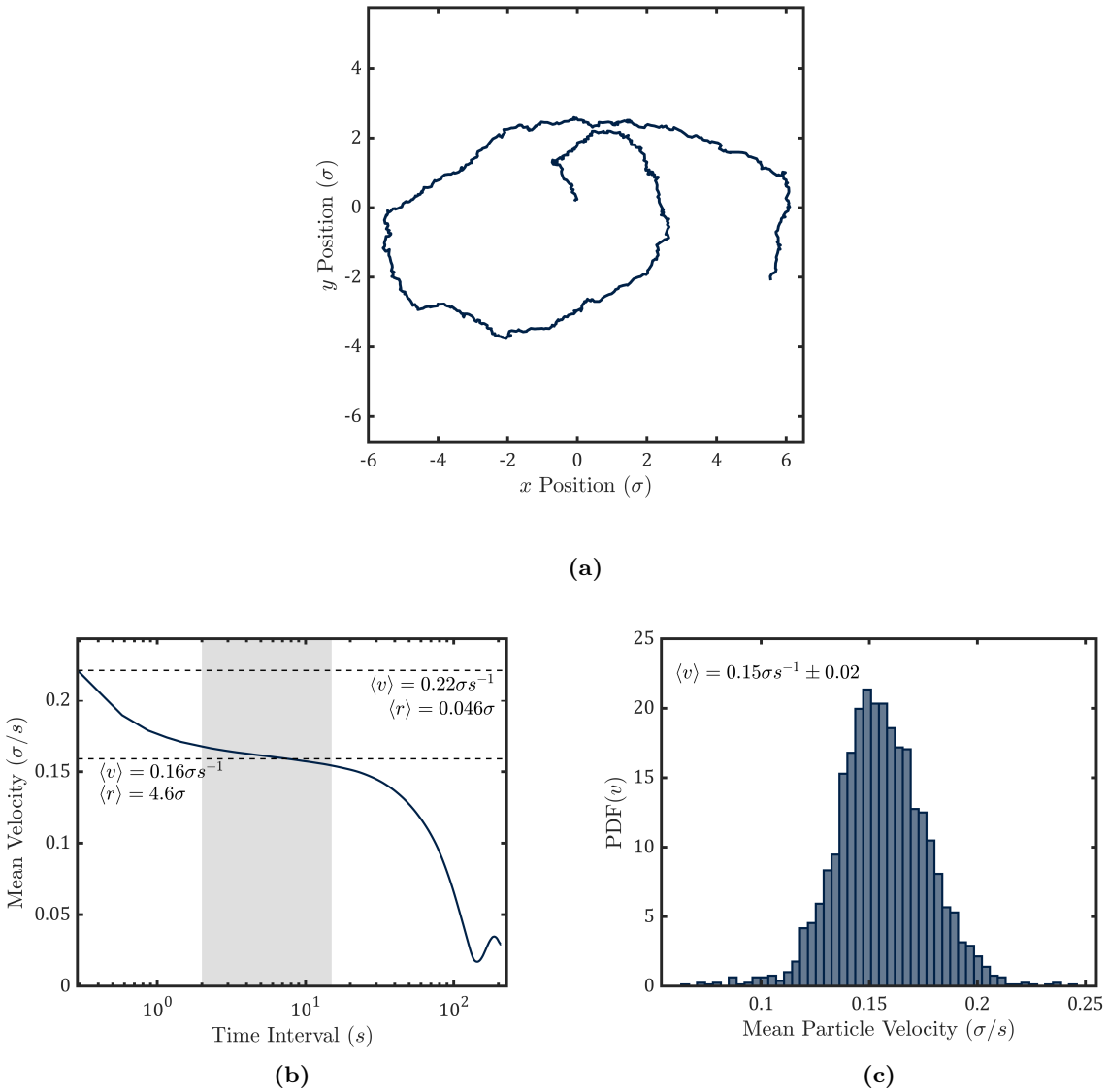

Figure 4.17: Mean velocity measurement of a particle. (a) The trajectory of an ICEP Janus particle in an 8 kHz 100 V cm^{-1} electric field. (b) The mean measured instantaneous velocity of the particle in (a) as a function of the time interval used. The dependence of the measured mean velocity on the time interval chosen shows that the best time interval for this particle is in the grey region (around 6 s or a mean of 4.6σ in displacement). (c) A histogram of the mean velocities of 2503 particles in the same conditions as (a).

seeing as a small time interval is used). As the time interval increases, this constant is divided by an ever larger time and vanishes leaving only the actual distance between two points as the velocity. At our smallest time interval the distance covered by the active component of the particle's motion is around 5 % of it diameter, which is most likely comparable to the Gaussian of the noise and the Brownian motion combined. On top of this, the rate at which the contribution from the noise becomes insignificant is dependent on the velocity of the particle itself. In the case of the particle shown in figure 4.17, if we were to blindly chose the smallest intervals we

would overestimate our velocity by 38 %.

A complication related to the angular motion of the particle arises at large time intervals. If a particle rotates, by either diffusion or an angular velocity (possible due to an uneven metal coating), then it may start to approach its original position. The distance between two points therefore reduces as seen in the right hand side of figure 4.17(b).

As a consequence of the aforementioned factors, a specific time interval is chosen such that the noise and angular contributions are not included for the majority of particles for a given recording. This typically falls around 0.2 to 15 s depending on the velocity of the particles. We can, as a consequence, obtain velocity distributions as shown in figure 4.17(c).

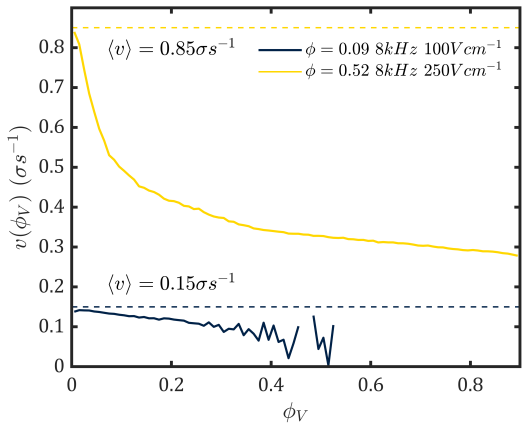

Figure 4.18: Mean velocity measurement from the relation between velocity and density. The velocity as a function of the local area fraction of the particles measured over an appropriate interval chosen for each video. The legend shows the conditions of the particles which correspond to those shown in figure 4.16. The mean velocity can be extrapolated from where the curve would cross the y axis.

In addition to the issues regarding the time intervals over which to average the velocities of particles, we must also consider the fact that we measure the velocities of particles in systems which are colliding and phase separating. However, once the optimal interval has been determined we can use it to determine the velocity of all particles in the steady state. The only consideration needed is that of when particles are submitted to collisions, joining the dense region or joining the dilute region. Thankfully, the collision rate in the dilute region is low, the rate of "evaporation" is low and the rate of "condensation" is low in the steady state when compared to the frame rate. The systems which do phase separate are the faster ones which have smaller time intervals for measuring velocities. Therefore we can simply plot the relation of velocity as a function of local area fraction and extrapolate from the low area fraction region

of the curve to determine the actual propulsion velocity devoid of particle interactions.

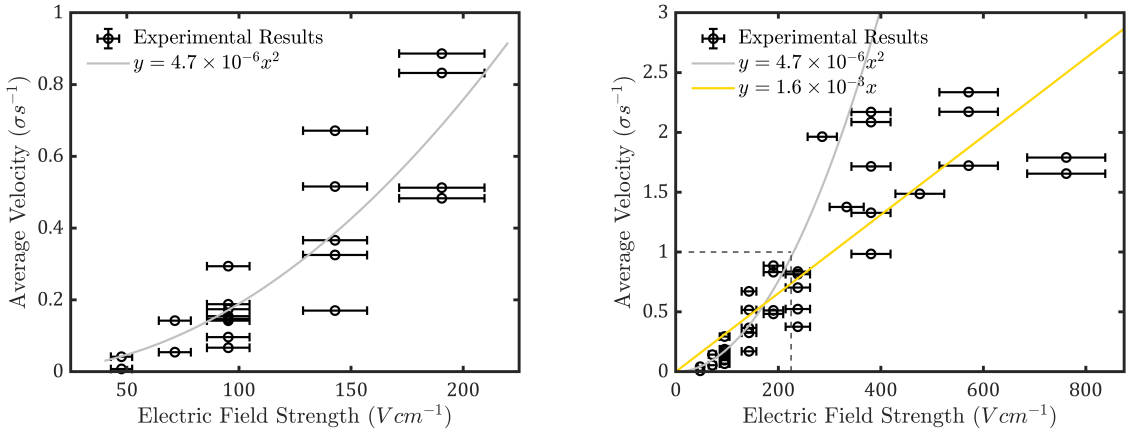

Figure 4.19: The break down of the relation between electric field amplitude and velocity. (a) The fit of the data points for all experiments where a velocity was recorded at 8 kHz with a fit showing the square relation expected form the Einstein-Smoluchowski equation foe ICEP particles (4.12). (b) The linear fit through all the point, including those at high field strengths show how the squared relation falters (as predicted in the theory in the introduction of the chapter). The error bars in the field amplitude come from the measured deviation in cell height ((105 ± 10) µm).

In figure 4.18 we plot the mean velocity as a function of local area fraction for the systems shown in figure 4.16. First, one can note that the velocity obtained from the intersect of the y axis for the curve at the lower area fraction (the one which does not phase separate) is in agreement with the analysis from figure 4.17. This corroborates our approach. We also show the curve for a system which has undergone phase separation. In this case, we see that the relation between velocity and local area fraction is not linear. It also shows that we obtain a mean velocity of $0.85\sigma s^{-1}$ for this system. The fact we have data at high area fractions also shows that the system has phase separated; this is not seen in the curve at the lower area fraction.

In figure 4.19 we plot the measured mean velocities of all the systems we could measure a velocity for as a function of the input electric field strength. At low field strengths the squared relation from equation 4.12 appears. This relation is only valid for low amplitudes as stated in the theory section. The error bars show the estimated errors in our field strengths from how we prepare our observations. Our error in our measurement is dominated by the variety of speeds in each sample and is therefore not shown. These distributions resemble those in figure 4.17(c) and are a combination of thermal fluctuations, variations in material polarisibility and metal cap shape.

Measuring the Rotational Diffusion Coefficient

Because, when Brownian motion is concerned, the mean position and velocity of a particle is equal to zero we cannot use the same method to measure the rotational motion of our particles as we do for the active velocity. The mean squared displacement is often used to measure a rotational diffusion coefficient following:

$$MSD_x = 2_x^n D_x t^{\gamma_x} + 2^n D_\zeta, \tag{4.19}$$

where in the case of angular motion in a two dimensional uniformly Brownian system $x = \theta$, the number of angular dimensions $n = 1$, the diffusion coefficient is the rotational diffusion coefficient $D_x = D_r$, the exponent is $\gamma_x = 1$ and D_ζ is the contribution from the error in the detection of orientation. D_ζ is equal to the y intercept because the contribution from the noise is time independent.

In our case, we do not have an ideal system. Although the particles are relatively monodisperse, their coatings can be uneven which may lead to various degrees of ballistic character. It is also the case that the fact we create flows around the particles may lead to a diversion from Brownian dynamics; especially as we change the electric field strength which may lead to multiple effects and regimes.

Using the method to calculate the MSD of a system described in section 2.2.6 requires the combination of averaging the time intervals of a given particle's trajectory before averaging all of the time intervals for all particles. This works well for systems with homogeneous behaviour. This is why, unless an extraordinary amount of time is spent individually selecting and cropping particle trajectories we are unable to measure the rotational diffusion coefficient in systems which phase separate.

The averaging also has a significant effect if the particles, despite being in an isotropic system, behave differently. This is the case in our experiments. Because we are able to track our particles over long times we can use a single particle's trajectory to obtain an MSD. We can then categorise how Brownian or ballistic this particle's angular motion is.

In figure 4.20, we show the trajectory of two particles, their orientation over time as well as their mean squared and mean displacements. The first particle in yellow is that which we would

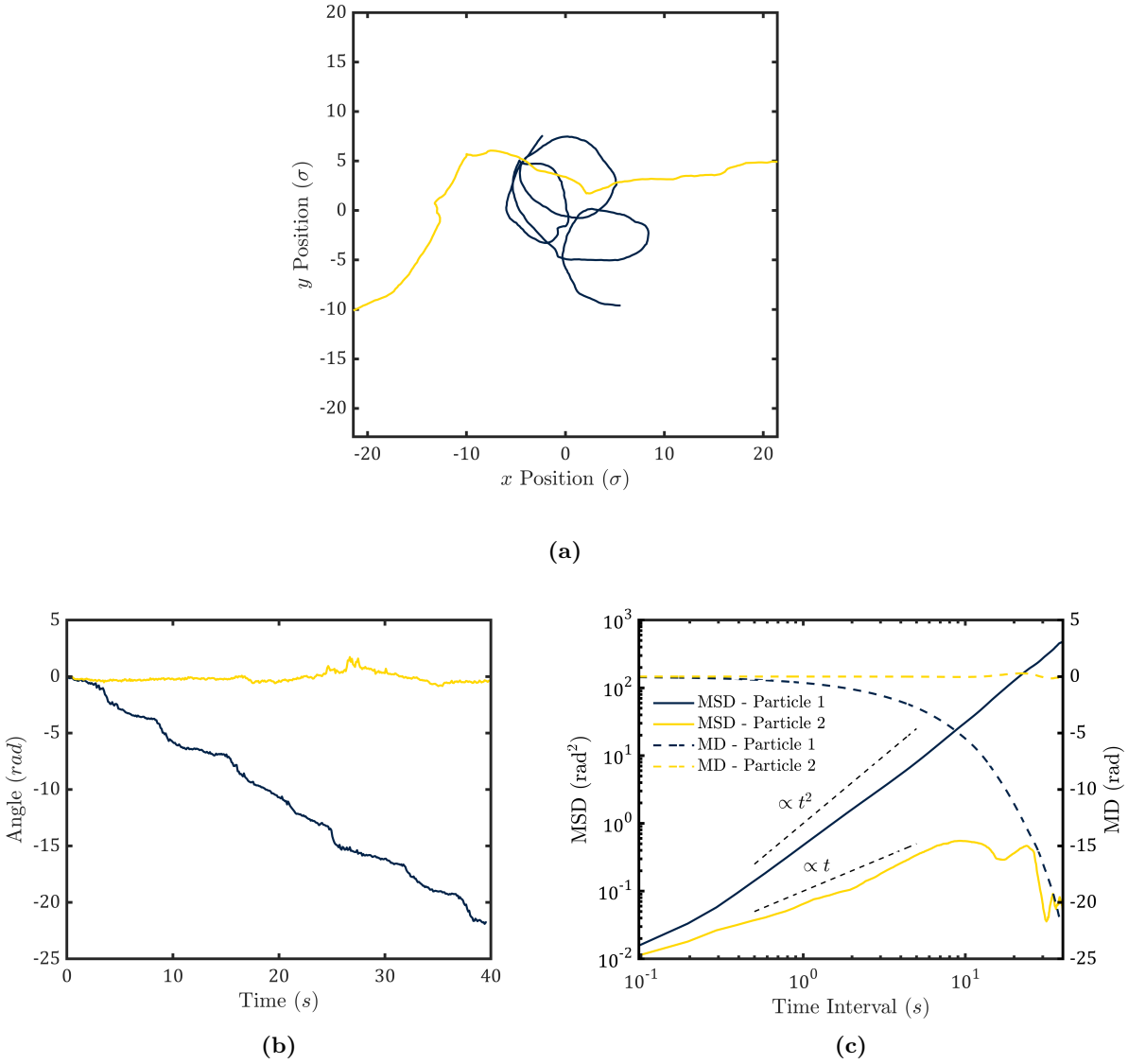

Figure 4.20: The characterisation of the angular motion of example particles. (a) The trajectories of two particles in a system at 8 kHz and 381 V cm^{-2}. (b) The renormalised orientation of the same particles over time. (c) The mean angular displacement and the mean squared angular displacement of the same particles over all the time intervals of the trajectories.

expect from a particle which has diffusive rotation and ballistic translation. The trajectory is straight on short timescales, the mean change in angle is zero, the MD is close to zero and the MSD is proportional to t. On the other hand, the blue particle behaves in a mostly ballistic fashion. Its trajectory is rounded, its angle has a relatively constant change over time, its MD is biased in one direction and its MSD is proportional to t^2. For each particle we are able to obtain this information and characterise them along the prefactor and the exponent in their MSD. Specifically we choose to fit the MSD curve where the MD curve is less than 0.3 rad or if there are too few data points which fit, we take the first ten time intervals.

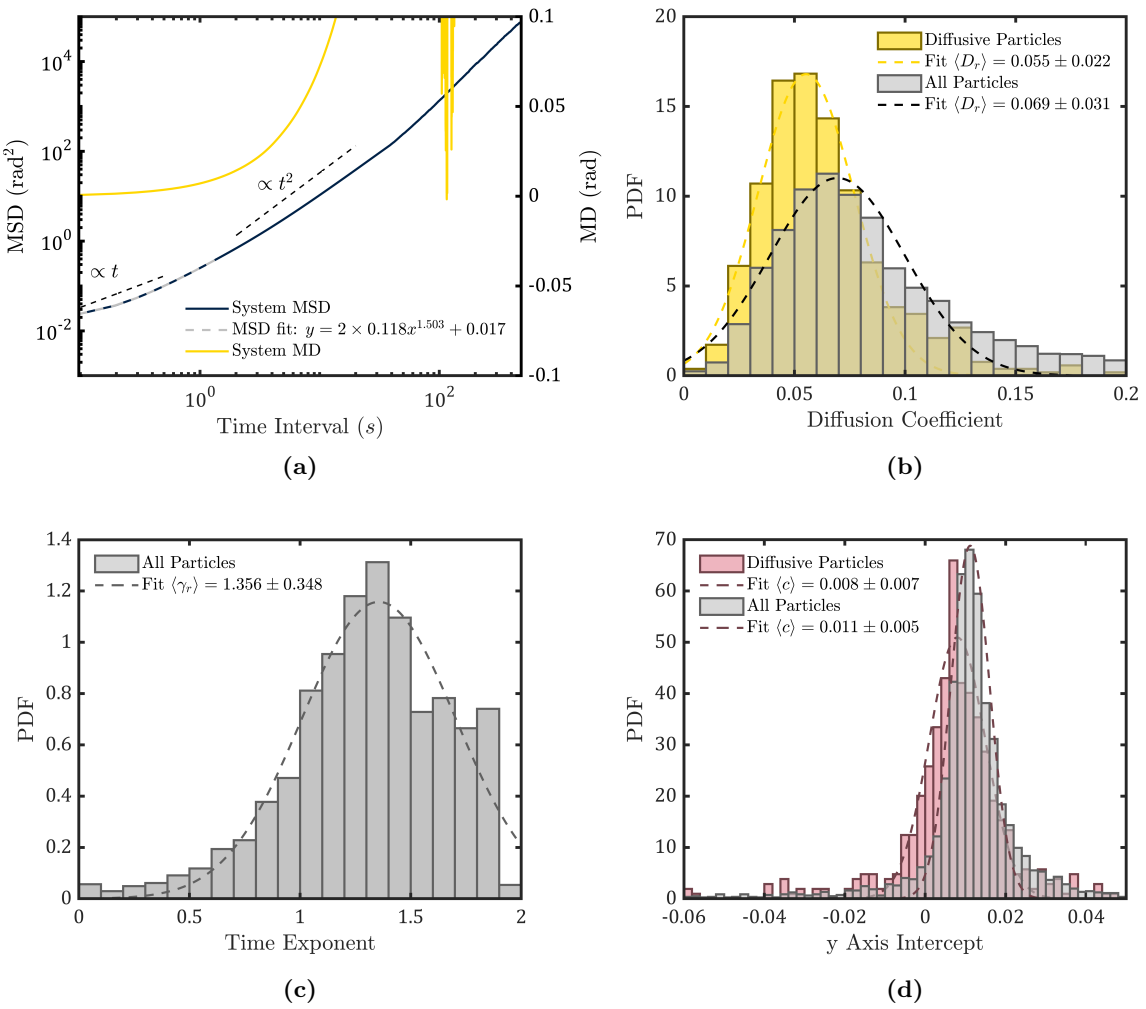

Figure 4.21: The characterisation of the angular motion of a given system by the properties of the each particle. (a) The total mean and mean squared angular displacement of all particles at $\phi = 0.061$, 8 kHz and 381 V cm^{-2}. The fit is chosen to pass over the points where the MD is less than 1 %. (b) The probability density distribution of the measured diffusion constants for all and the diffusive particles. (c) The time PDF of the time exponents for all particles. (d) The intercept of the y axis of the fits of all and the diffusive particles. The total MSD curve seems to over estimate all of the measurable constant of the system shown in the latter three graphs. Diffusive particles are defined as those with time exponents between 0.9 to 1.1.

In figure 4.21, we plot the results for all the particles of the system at $\phi = 0.061$, 8 kHz and 381 V cm^{-2}; the experiment where we observed the most ballistic particles. We first look at the MSD and MD curves in (a). The values for the free parameters in the fit where the MD is below 1 % are larger than those measured from the distributions as shown in all three cases from (b) to (d). We predict that this is due to the fact that the particles with the higher exponents have an effectively larger weighting in the average of the MSD. We therefore use the distributions of the values for all the particles as the measurements of the angular behaviour in our systems.

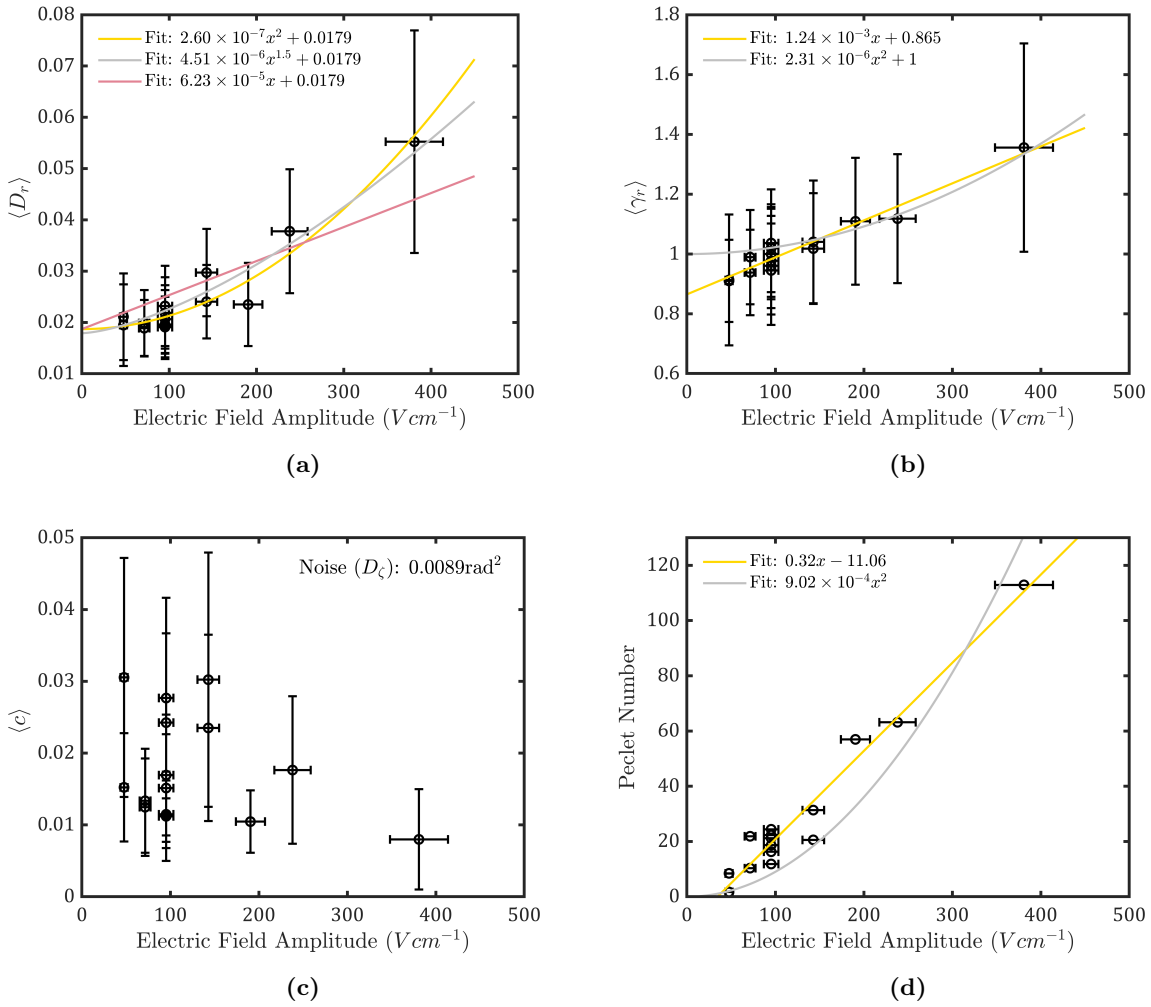

Figure 4.22: The measured properties from the fits to the individual particle MSD curves for all systems where particle tracking was possible and MIPS was not observed. (a) The mean diffusion constant as a function of the amplitude of the electric field. We plot three fits to compare which scaling the diffusion coefficient has. The y intercept is fixed to the theoretical value for the diffusion coefficient following Stoke's laws. (b) The mean time exponent as a function of the amplitude of the electric field. Again we show a couple of fits as we do not have a large data set. (c) The mean value of the y intercept for the fits. This shows the average D_ζ to be around $0.0089\,\mathrm{rad}^2$. (d) The measured Péclet number as a function of the amplitude of the electric field using γ_r to maintain a dimensionless value. We plot two fits to show how the data points scale with the amplitude. The trends in (a) and (b) are somewhat unexpected.

The measurements for the set of data points where MIPS was not observed and the particles were slow enough be tracked are shown in figure 4.22. In (a), we show the relation between the diffusion constant and the field amplitude. One may have expected there to be no relation, however it is clear from the data that there is an increase in the diffusion rate as the amplitude increases. We have also plotted various fits through the data whilst fixing the y intercept to the theoretically predicted value when no field is present ($D_0 = 0.0187 rad^2 s^{-1}$). The curve which fits the best is that when $D_r \propto E^2$. This, as is the case in the Einstein-Smoluchowski

equation for the velocity ICEP particles, must mean that the friction forces on the particle are significantly affected by the flows generated by electrophoresis.

In figure 4.22(b), we show the relation between the mean exponent and the amplitude of the electric field. Here, we again see an unexpected increase. Although both of the fitted curves fit the data well, the one where the y intercept is fixed to 1 is perhaps more realistic. This is because for there to be a mean sub-diffusive behaviour there would have to be a kind of hysteresis/friction generated by the flows, which are weaker as amplitude decreases.

The average error in the detection of the particles is shown to be relatively constant in figure 4.22(c). This is good from the perspective of our methods but also tells us that the mean value is significantly less than the measured diffusion rates and therefore can be neglected.

Finally, we show in (d) the resulting Péclet numbers for the systems. To obtain these values we divide the mean measured velocity from figure 4.19 to the power of γ_r from figure 4.22(b) by the measured mean angular diffusion rate in figure 4.22(a). Here we see that an increase in the electric field amplitude does increase the Péclet number. However, due to the changing relation between the amplitude and the velocity form the ES relation to a more complex one and the probable squared relation between the amplitude and the rates of angular diffusion, we obtain a relation which seems mostly linear.

The distributions of measurements we obtain is quite large. This again comes from the range of behaviours the particles have in the system and not our measurement methods. Although this does not aid out confidence in the results, we still recover a significant trend over the range of our points in each case.

To estimate the Péclet numbers of our more dense and faster systems, we use the relation in the first fit of figure 4.22(d):

$$Pé \approx 0.32 \times E - 11.06. \tag{4.20}$$

To verify the effects of the electric field and the flows around the particles, we recorded systems at $381\,\mathrm{V\,cm^{-1}}$ and $\phi \approx 0.17$ and varied the electric field frequency. This is to reach the inversion frequency, where the velocity of the particles is equal to zero despite there being a field present. We plot the velocity as a function of field frequency in figure 4.23(a). We see that

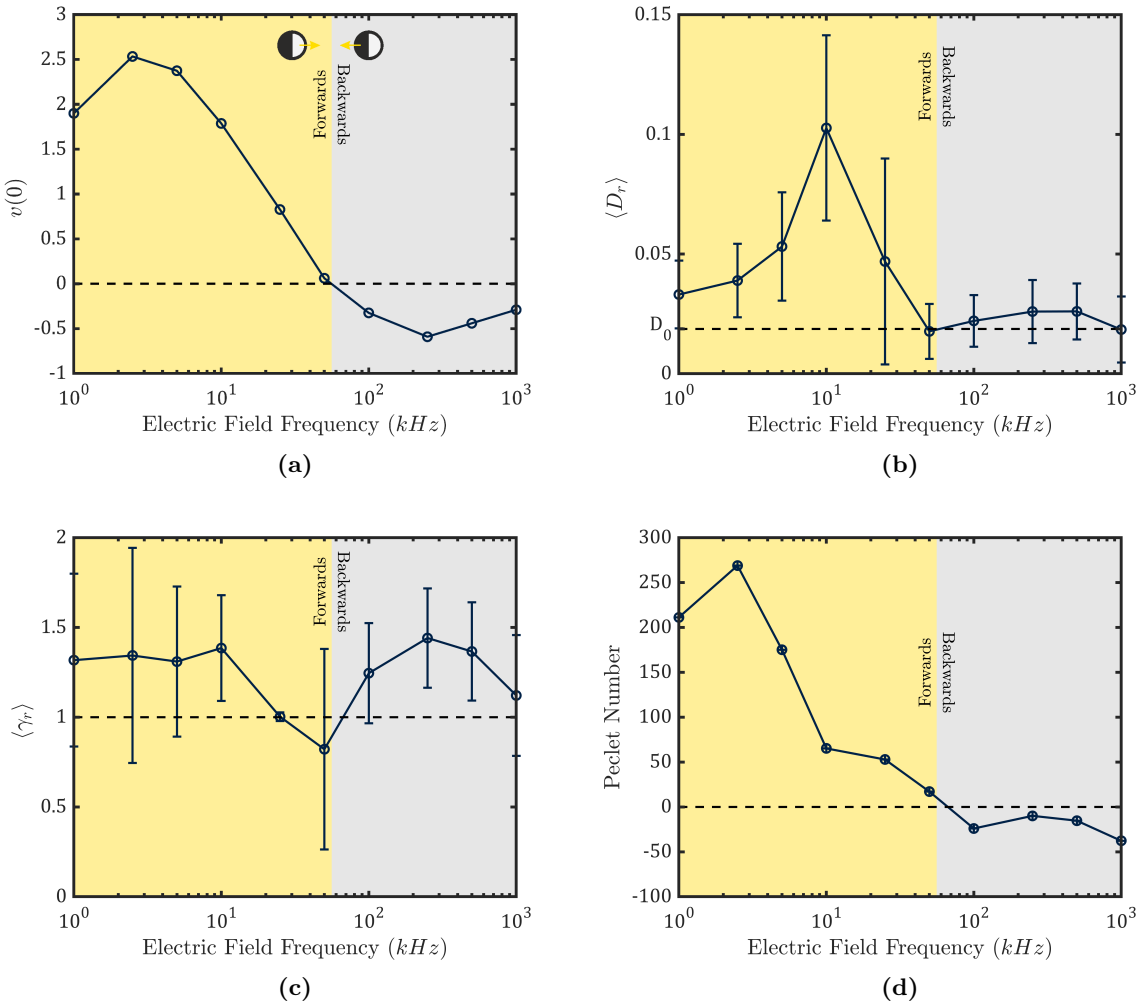

Figure 4.23: The measured properties of systems at a range of electric field frequencies at $381\,\mathrm{V\,cm^{-1}}$ **and** $\phi \approx 0.10$**.** (a) The mean velocity taken from the extrapolation of the relation between velocity and local density as a function of field frequency. We see the characteristic inversion of velocity at 56 kHz. (b) The angular diffusion rate as a function of electric field frequency. Close to the inversion frequency the angular diffusion matches that which is predicted by Stoke's law. (c) The mean time exponent of the particles as a function of frequency. When the field causes the particles to move, at this amplitude, the particles have some ballistic character. (d) The measured Péclet number as a function of frequency.

the inversion frequency of this system is 56 kHz, which is very similar to previously measured values [217], where the ionic strength of the solution is important (0.1 mM). What is more surprising is the trend in the diffusion rate. We crucially see that, when there are no net flows (near the inversion frequency), the diffusion rate and time exponents match those for diffusive particles predicted by Stokes' laws. This shows that it is indeed the flows which affect the change in the character of the angular motion. These measurements result in the Péclet numbers shown in (d) which are unsurprisingly strongly linked to the velocity with the dip around 10 kHz. In this figure, we again see the wide bars for each point which are associate with the breadth of

behaviours. We still again are able to discuss these trends as they do not exceed the trends such as in (c) where the distributions are completely above the expected value of 1.

Final Péclet number vs Area Fraction Phase Diagram

Using the above relation and a simple measure of the initial area fraction of all our systems, we can create the phase diagram shown in figure 4.24.

When we compare these results to those obtained from chapter 3, we note a few differences. Without counting what appears to be overlap between the regions, which can be attributed to experimental errors (stuck particles, errors in measurement and deviations in cell height), one can see that the critical Péclet numbers and area fractions are lower than predicted. We attribute this difference mostly due to inaccuracies in our method of determining Péclet numbers and friction forces between particles which we did show help to reduce the critical Péclet numbers and area fractions. We have, however, shown that the crucial dependency of MIPS on $Pé$ and ϕ which we observe in simulation is at worst qualitatively equal to real systems of tunable hard Janus spheres.

4.3.2 Dynamics of Clusters

Very much as was presented in the work of van der Linden *et al.* [7], we observe a plethora of dynamics both on the individual particle level and on the level of the clusters. To bring the dynamics of our system in the context presented by the results of chapter 3, we present in figure 4.25 the evolution of many of the measurable properties of the system. We begin with the cluster fraction in (a). Here, as in chapter 3, we have defined a particle to be in the dense phase as one with a local area fraction above 0.7. This works well in this case as the system of concern has an average area fraction of 0.29. As in the simulated systems the growth of the higher Péclet number systems is faster reaching similar but increasing final cluster fractions.

We can use this data to determine where the clusters no longer begin to nucleate. This occurs, for example, at around 10σ for $Pé = 232$, where the cluster fraction hits a plateau. In 4.25(b), we plot the mean cluster size over time. This tells us that our systems are similar to those at lower Péclet numbers in chapter 3 because the scaling of the growth follows $t^{1/2}$ in the initial coarsening process.

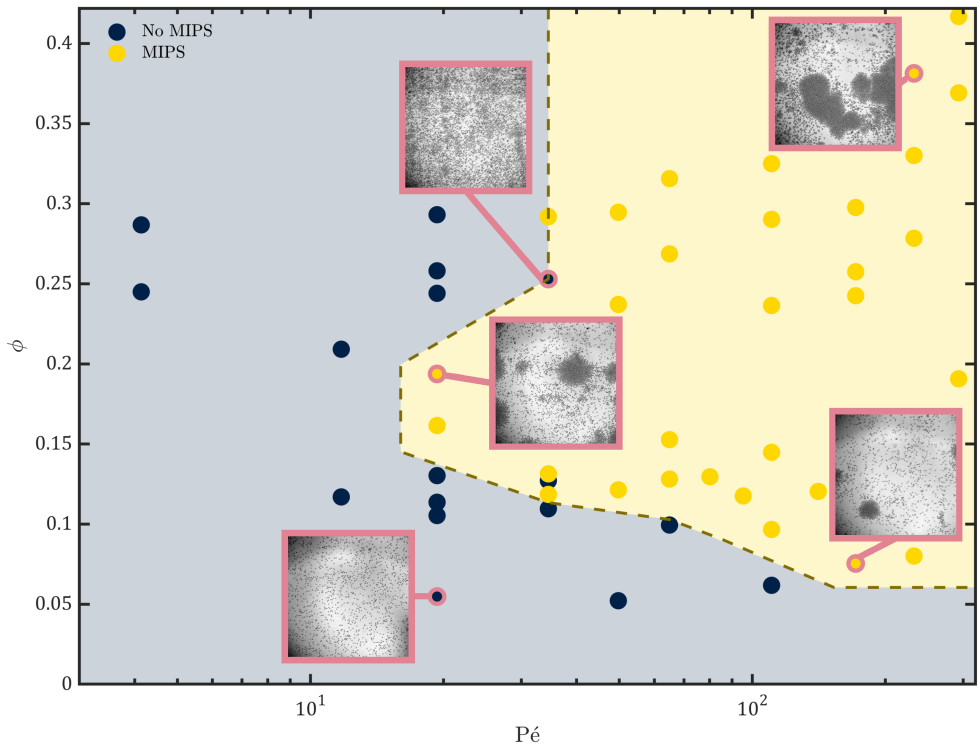

Figure 4.24: The $Pé/\phi$ phase diagram for our experimental system of ICEP Janus particles in an 8 kHz square wave alternating field. The MIPS and non-MIPS data points, determined by an observation of if clusters form are shown in yellow and blue respectively. The grey line denotes an estimate of the phase transition. The MIPS region appears to be at lower ϕ and lower $Pé$ than for numerical systems (chapter 3). The inserts are snapshots of the corresponding data points in the steady state; each field of view is 626 by 626 µm.

Another similarity we obtain is that of the probability distributions of the local area fractions in 4.25(c). Like in all MIPS systems, phase separation is distinguished from the formation of two peaks in this graph. However, if we compare the PDFs of the bond orientational order parameter (ψ_6) in figure 4.25(d) we notice that the first of the systems to phase separate (at $Pé = 65$) does not in fact form highly crystalline clusters and the PDF resembles that at $Pé = 21.26$ of the simulations. This effect is also seen in how the dense peak in (c) is not pronounced for this Péclet number. One could attribute the formation of these "dilute" clusters (similar to those formed in the work of Zhang *et al.* [219]) to the electrohydrodynamic interactions observed in passive systems and the induced electrostatic repulsions.

In 4.25(e) and (f), we explore the characteristics which we previously used to describe the way in which the systems at high Péclet numbers were unable to fully phase separate. We first look at the relation between velocity and the local area fraction of the particles. As before,

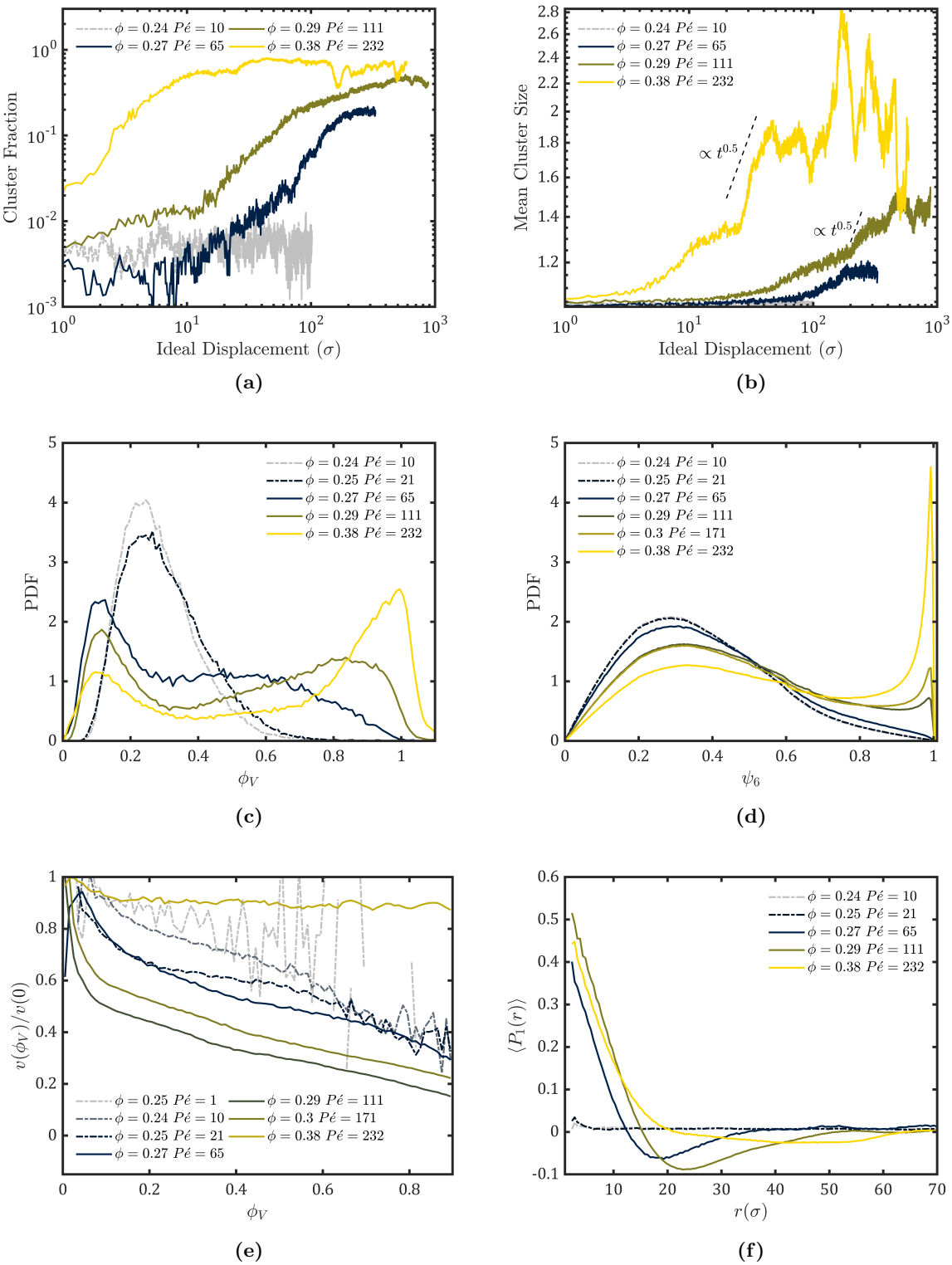

Figure 4.25: The changes in measurable properties of systems as a whole as a function of Péclet number. The evolution of (a) the cluster fraction, (b) the mean cluster size, (c) the probability density functions of the local area fractions, (d) the probability density functions of the bond orientational order parameter, (e) the normalised velocity as a function of the local area fraction determined by Voronoi tessellation and (f) the correlation in particle orientations in the steady state at various Péclet numbers and $\phi = 0.29$. The changes in velocity mimic those found in simulation. Solid lines are phase separating systems and dashed lines are not.

we notice that, upon entering the MIPS region of the phase diagram, we see a reduction in the velocity of particles at high local area fractions. The rise also seems to be different to the velocity/density lines in simulation. At high Péclet numbers it eventually completely flattens.

Our explanation for this kind of effect in the previous chapter was based around how the increased persistence length of the particles lead to local alignment of particles in clusters. This is why we plot the polar order parameter as a function of distance again in (f). Here not only do we see enhanced ordering, but it is the case even for the lower Péclet numbers. The ordering is such that we also see a significant anti-correlation above $r = 10\sigma$. This corresponds to the size of the clusters which grows as Péclet number increases. Having such a large correlation would suggest that there may be an interaction between the particles which leads to alignment. Such an interaction has been observed before. In the work of van der Linden *et al.* [7], it was used to explain certain dynamics as particles following each other in a fashion similar to the chains formed by Nishiguchi *et al.* [217] were observed. In our case we do not observe interactions in the dilute region as the conditions were chosen specifically to avoid them. However, our results in (f) would suggest that particles are still able to do this within the dense regions. The dissipation of the effect a particle's environment has on its velocity comes therefore from the mechanism shown in figure 4.27(c); the ability for a cluster to translate as a single body due to the orientational alignment.

In figure 4.26 we show the appearance of characteristic clusters at different Péclet numbers. In all three cases we can see the correlation of orientations. We also see the local area fraction of the particles increase as is shown in figure 4.25. The crystallinity increasing allows for clearer cluster identification, defined with the same methodology as in chapter 3, with a larger proportion of particles in the dense phase. We can also see that the size of the grains in the last column of the figure increases with the size and pressure of the dense regions.

We show the images in figure 4.27 as illustrations of the motion/dynamics within our systems. In (a), we show how, at lower Péclet numbers, the clusters remain static as a whole but that, like in the work of Zhang *et al.*, the particles around the outside can mostly translate whilst those in the centre do not, something not observed by Zhang *et al.* [219]. We attribute this difference to having our system tuned differently. Figure 4.27(b) shows how a cluster at an intermediary Péclet number of 111 is able to explode in the same fashion as those in chapter 3. The particles in the cluster are initially partially orientationally ordered leading to a degree of cluster torque.

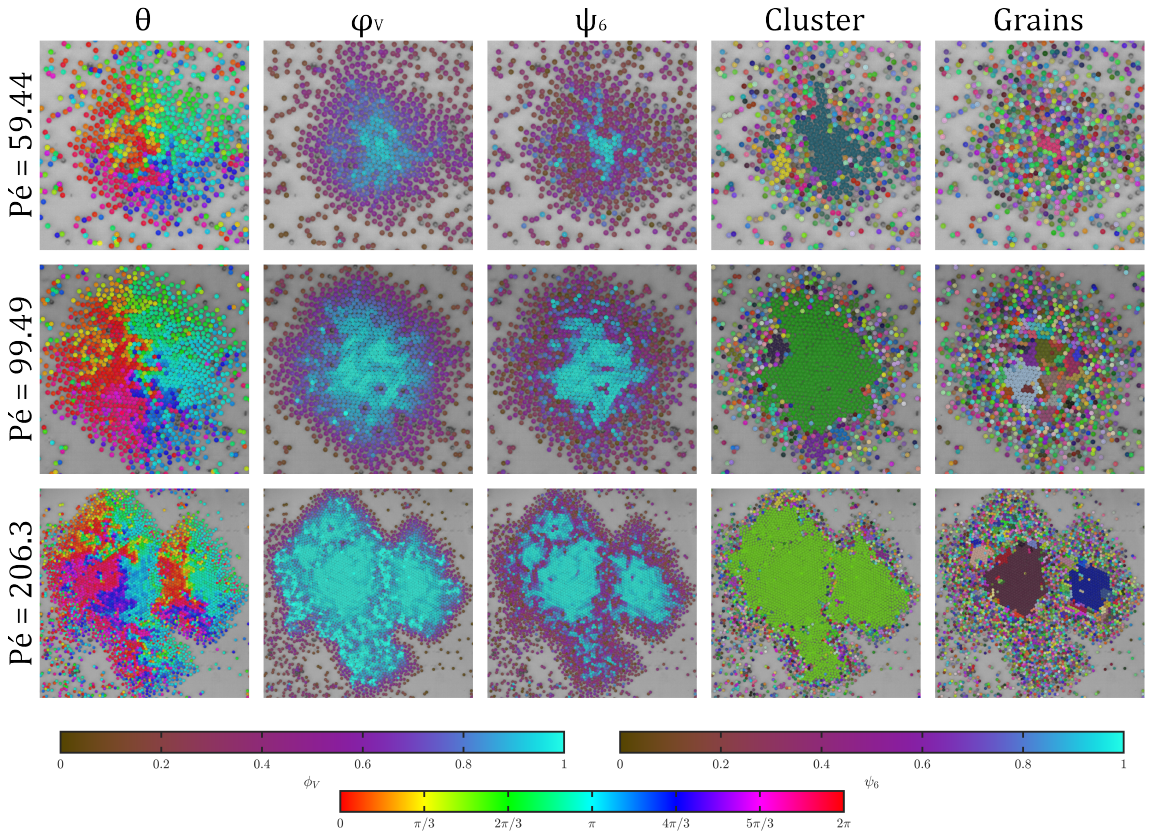

(a)

Figure 4.26: Snapshots of characteristic clusters at a given Péclet number to illustrate the changes in figure 4.25. Each column of images corresponds to the data type labelled above them; orientation, local area fraction, bond orientational order parameter, cluster number and grain number. The snapshots at $Pé = 65$ are 40σ (173.0 µm) wide, at $Pé = 111$ are 45σ (195.7 µm) wide and at $Pé = 232$ are 74σ (318.2 µm) wide.

The cluster then rotates before dissolving. The region of green particles ($\theta \approx 2\pi/3$) swims downwards and outwards off the bottom of the image for example. The final set of images is at $Pé = 232$. Here, we show how the largest cluster [6] translates and rotates whilst maintaining most of the particles inside it. We do see two break off events where the second largest cluster in the image (in dark blue) leaves the cluster. This breaking of the cluster is similar although not exactly the same as the mechanism described in chapter 3 (figure 3.32). This translation only occurs at the higher Péclet numbers we recorded. This kind of motion was only observed in our numerical simulations when friction was added. This would suggest that the flows generated around the particles are able to couple with one another when a crystalline cluster forms and velocities are not necessarily annihilated by collisions.

[6] The colours of the clusters are shown by size and not tracked in this system as our camera was unable to operates at a high enough frame rate for efficient particle tracking.

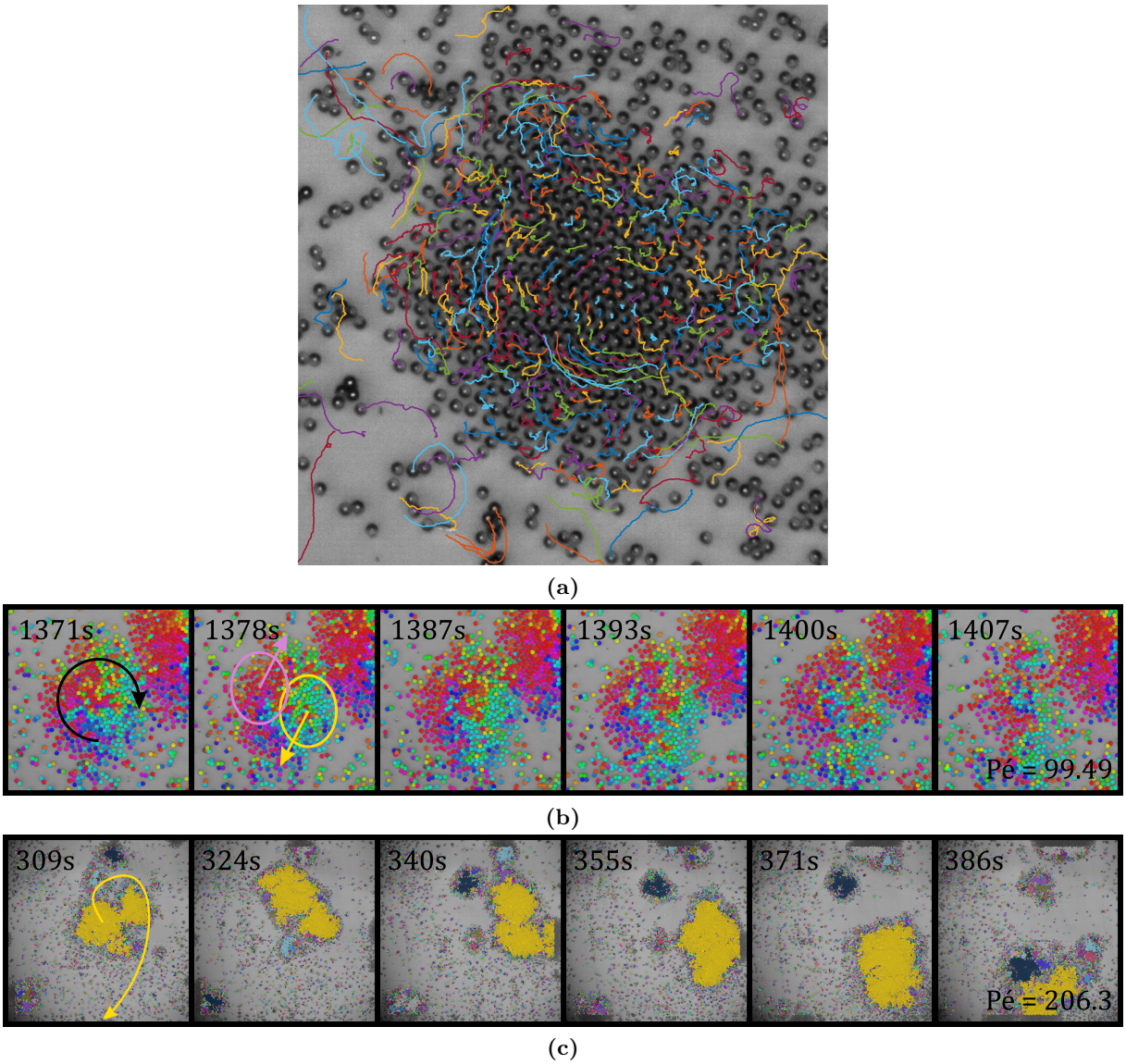

(a)

(b)

(c)

Figure 4.27: The motion of particles in clusters and of clusters themselves. (a) An image of a cluster at $Pé = 65$ with the trajectories of the particles over 29 s on top. (b) The dissolution of a cluster at $Pé = 111$ in a similar mechanism to the explosion of clusters in chapter 3. (c) The translational motion of a large crystalline cluster at $Pé = 232$. The sizes of the images in (a), (b) and (c) are 29s 40σ or 173.0 µm, 45σ or 195.7 µm and 146σ or 626.1 µm respectively. The times shown in (b) and (c) are with respect to when the electric field is turned on.

4.4 Summary and Conclusions

The purpose of the work in this chapter was to create an experimental system to compare to our results on the dynamics of MIPS at high Péclet numbers in simulation from chapter 3. We have shown that we are able to create systems of ICEP Janus particles with tunable differences to those which have been previously studied [7, 57, 204, 217, 219]. A key result of our work is that we were able to create a $Pé/\phi$ phase diagram akin to those typically created in simulated

systems. We could do this because of how we optimised the system using gold electrodes and reflection optical microscopy.

An essential part to creating the phase diagram is the measurement of the Péclet number. We were able to to this for many of the systems which we recorded. We could not measure velocities or rates of angular diffusion for certain systems due to the limitations of our setup. However, the methodology we developed, namely the dissection of the mean squared angular displacement, allowed us to determine the effect of the AC electric field amplitude and frequency on the orientational motion of the particles to eventually extrapolate the motions of the systems which could not be measured directly. We have shown that the flows generated around the particle by the electric field not only affect the activity but also add sub-diffusive and super-diffusive character to the angular motion of the particles as reflected in the varying value of γ_r the time exponent.

Thanks to the analysis developed in the ideal simulated case in chapter 3, we were able to determine the effects in the system which lead to the interesting dynamics we observe. The most important of which is the ability for a cluster to translate. This phenomenon was observed in the work of van der Linden *et al.* [7] and it was suggested that it interrupted MIPS. We have shown that the velocity of the particles need to be high enough to allow for this mechanism to occur and that it is most probably linked to the propulsion mechanism or electrostatic alignment. We have also shown that the interactions between the particles, which can be electrohydrodynamic or electrostatic in origin, can be reduced but are ultimately unavoidable. Despite this, the ICEP Janus particle system remains one of the most versatile synthetic active systems.

Chapter 5

Active Brownian Dynamics Simulations with Additional Interactions

Abstract

Using our experimental results and previous numerical studies as sources of inspiration, we develop interactions between particles in conjunction with the SCP method to simulate particles with additional interactions. We investigate the effect of strong dipolar interactions between the front and back hemispheres of particles where the SCP interaction keeps our particles hard for strong attractions. We also demonstrate that by using these methods, even more complex simulations, such as a simulated predator-prey relationship, can be easily made. We end with a study into the effect of altering the 1-1 collisions such that velocities are not annihilated if particles do not collide head-on.

5.1 Introduction

As touched upon in previous chapters, one of the main attributes in simulating active particles is the ability to tailor particle interactions. There have been many attempts to bring numerical simulations from being purely simple systems to incorporating more realistic interactions. For example, the use of Lattice Boltzmann simulations is commonplace when including hydrodynamic interactions in simulated active matter [65, 223, 224]. The Lattice Boltzmann method is a scheme used for solving non-linear coupled equations such as Navier-Stokes and advection-relaxation equations [225].

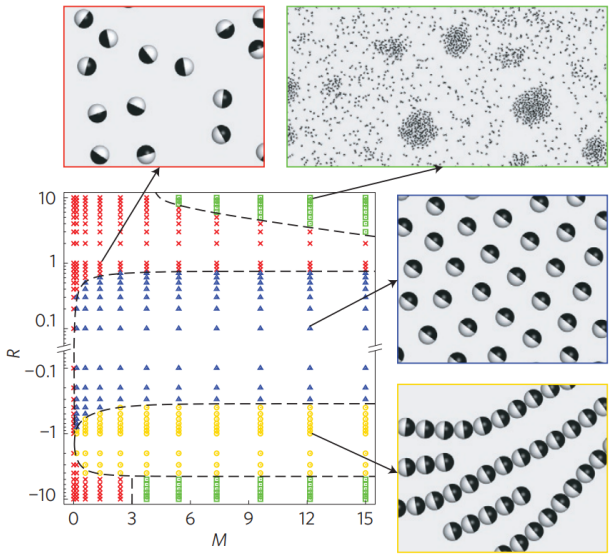

Figure 5.1: Dynamic state diagram from 2D simulations. R is the ratio of the dipole moments on the front and back hemispheres. M is the dipolar repulsive force between two spheres at contact. Simulation snapshots for the four different phases are shown, and the corresponding parameter choices (R, M) are indicated by the arrows. From Yan *et al.* [57].

Due to the flexibility of Brownian dynamics simulations, they are also used to create evermore complex systems [174]. Real world active systems are often a source of inspiration for interactions used in such simulation. The Vicsek model, and subsequent models derived from it, are attempts to mimic the collective dynamics of groups of animals building up from basic interactions [37,46]. Inspired by ICEP Janus particles, Yan *et al.* made an initial investigation into the effect of quadrupolar interactions on the phase behaviour of active particles [57]. They discovered that by tuning the relative strength of dipoles situated on either hemisphere of Janus particles, they could recreate the chains, clusters and polar swarms seen in experiment.

In this chapter we make our own investigation into systems which have additional interac-

tions. We use a similar approach of using two dipoles on a Janus particle to attempt to recreate the dynamics observed in the experimental systems of chapter 4. We also begin to probe the effect of coupling the friction/velocities of particles via a modification of the SCP method.

5.2 Methods

5.2.1 Quadrupolar Interactions between Spheres

Each Janus particle is chosen to have two dipoles; one in its front hemisphere (head) and one at its back hemisphere (tail). The positions of these dipoles are determined by the mean centre of mass of a hemisphere which results in a distance of $3/16\sigma$ from the centre of the particle [216].

The electric field in the plane perpendicular to the centre of a dipole in the far field approximation follows [226]:

$$\vec{E} = \frac{kp}{r^3}, \tag{5.1}$$

where k is a constant, p is the magnitude of the dipole moment and r is the distance from the dipole.

The interaction potential between a dipole and an electric field is the dot product between its dipole moment and the electric field. Therefore, the potential energy of a dipole in the presence of another in the same perpendicular plane is:

$$U = \frac{k\vec{p}_2 \cdot \vec{p}_1}{r^3}. \tag{5.2}$$

The force between the two then becomes:

$$\vec{F}_{p_1,p_2} = -\frac{dU}{dr} = 3\frac{k\vec{p}_2 \cdot \vec{p}_1}{r^4}\hat{r}. \tag{5.3}$$

where $\vec{p}_1$ and $\vec{p}_2$ are the dipole moments for the first and second dipoles respectively and $\hat{r}$ the unit vector in the inter-particle direction. The force is fixed to be positive as the opposite dipoles attract each other.

We implement this force on the positions of the dipoles in each particle, between each head and tail, resolving a force in the direction of the motion of the particle and a torque [1]:

$$\vec{r_i}(t+\Delta t) = \vec{r_i}(t) + \Delta t \lambda_t \Bigg(\sum_{j \neq i}^{N} \big((\vec{F}_{p_i^h, p_j^t} \cdot \hat{u}_i(t)) \hat{u}_i(t) \big) + \sum_{j \neq i}^{N} \big((\vec{F}_{p_i^t, p_j^h} \cdot \hat{u}_i(t)) \hat{u}_i(t) \big) \Bigg), \tag{5.4}$$

$$\hat{u}_i(t+\Delta t) = \hat{u}_i(t) + \Delta t \lambda_r \Bigg(\sum_{j \neq i}^{N} \big(\vec{F}_{p_i^h, p_j^t} \times \frac{3}{16} \sigma \hat{u}_i(t) \big) + \sum_{j \neq i}^{N} \big(\vec{F}_{p_i^t, p_j^h} \times \frac{3}{16} \sigma \hat{u}_i(t) \big) \Bigg), \tag{5.5}$$

where $\vec{r_i}(t)$ is the initial position of particle i, N the number of particles within range of the force cut-off distance, p_i^h the dipole in the head of the particle, p_j^h the dipole in the tail of the particle, $\hat{u}_i(t)$ the initial orientation vector of the particle and σ the diameter of the particles. The distance cut-off is determined by taking the distance between two points where the magnitude of the dipolar force is equal to 0.5 % of the active force.

A key feature of using the SCP method is that we are able to tune the interaction between particles to keep them hard regardless of the other inter-particle interactions. In this case, we must choose an appropriate time step and adjust the distance threshold of the interaction based on the attraction as it may lead to overlap. The time step is set to be $0.0025 \times \tau_c$ where τ_c is the characteristic time that the dipolar attraction moves a particle over one diameter ($\sigma\lambda_t/((3kp_i^h p_j^t)^4/\sigma^4)$). As in the modification of to the SACP method, we add twice the displacement cause by the attraction at contact $\sigma^* = \sigma + 2v_a\Delta t + 2(kp_i^h p_j^t \Delta t)/(\sigma^4 \lambda_t)$.

5.2.2 Maintaining Velocities by a Modification of the SCP Method

Inspired by the translating clusters in chapter 4, we devised a method of preventing the annihilation of velocities upon particle collisions in Brownian dynamics. To explain what is meant by this, one can consider what happens in Brownian dynamics when an active particle collides with a passive one. In a given time step the passive particle essentially does not move and the active particle creates a degree of overlap. This overlap is then resolved by displacing the passive particle and the active particle along by half the overlap in the direction the active one is swimming (around half the displacement from the activity). The final result is that both the active and the passive particle have half the velocity of the input active velocity necessarily

[1] We do not include the repulsions between the heads of particles and tails of particles unless explicitly stated otherwise. This is to fix and vary only one aspect of the interaction and it gives the same behaviour with a slight offset.

leading to reduced active motion in clusters.

To modify this we alter the method by which the overlap is resolved. Instead of giving each particle half of the overlap, the displacements are weighted by the relative angle between the particle orientation and the collision vector (between the two particle centres):

$$s_{SACP}(t) = \left(-\frac{1}{2}r + \frac{\sigma + 2v_a\Delta t}{2} \right) \times \big(-\cos(\theta_C) + 1 \big), \quad r < \sigma + 2v_a\Delta t, \tag{5.6}$$

where most of the equation is the same as equation 3.42 in chapter 3 but with the modification which depends on θ_C which is the difference between a particle's orientation and its collision vector.

This results in a system where the velocities of the particles do not cancel out in a collision between two particles unless they collide head-on. This can be thought of in two ways. Either the back of the particles are marginally softer than the front or that the propulsion of the particles are not inhibited by the collisions.

5.3 Results

5.3.1 Head to Tail Attraction

We can begin analysing our simulations of phase separating active particles using the same measurements which we defined and used in chapter 3 and 4; those shown in figure 5.2. Beginning with (a), we can see the effect electrostatic interaction between the heads and tails of particles has on the progression of the phase separation. The black line is the reference line where no interaction is added. Comparing this to the blue line, we see the smaller interaction begin to accelerate the growth of the dense phase early on in the progression (after around 3σ). Increasing the magnitude of the interaction increases the rate of growth. In addition to the rate the yellow and grey lines, those where the interaction is greatest, appear to have more stable cluster fractions at long times, most likely due to adhesion of the clusters due to the attractive force dominating. It can also be said that there is a slightly larger final cluster fraction from the interaction, likely due to a reduction in the ability for particles to leave clusters, offsetting the steady state position. This is small as the cluster fraction with no interaction is already high.

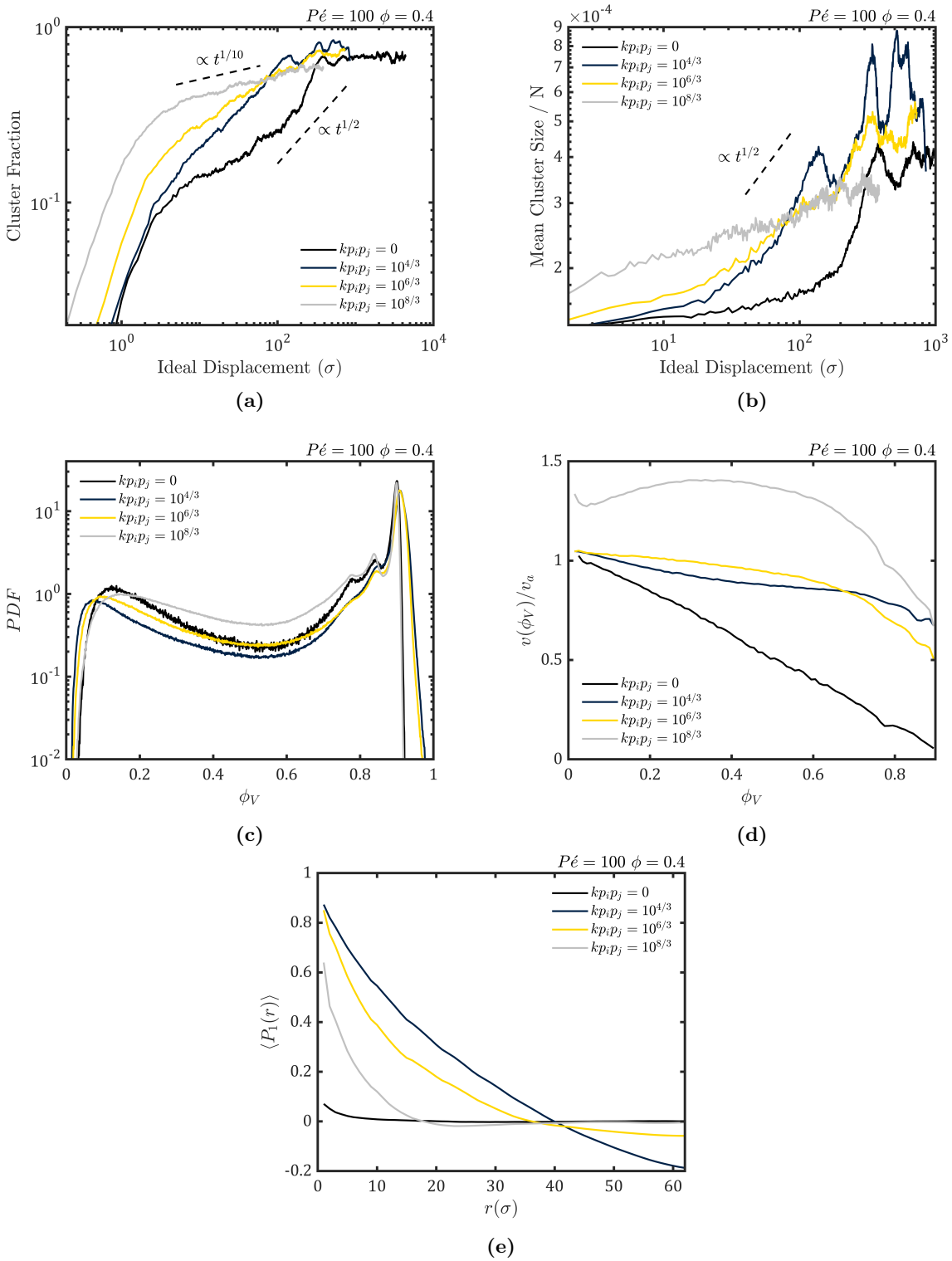

Figure 5.2: The changes in measurable properties of systems with growing attractive dipolar attractions between the heads and tails of particles. The evolution of (a) the cluster fraction, (b) the mean cluster size, (c) the probability density functions of the local area fractions, (d) the normalised velocity as a function of the local area fraction in the steady state determined by Voronoi tessellation and (e) the correlation in particle orientations in the steady state at various interactions strengths. $Pé = 100$ and $\phi = 0.4$. The results show that there are any similarities when the interaction is comparable to the activity to systems at high Péclet numbers.

It can however be seen in the concentration of the dilute region of figures 5.3(a) and (b). As the interaction increases the attraction dominates the activity and it results in systems which resemble those in figure 5.3(c) which appear to have straighter interfaces.

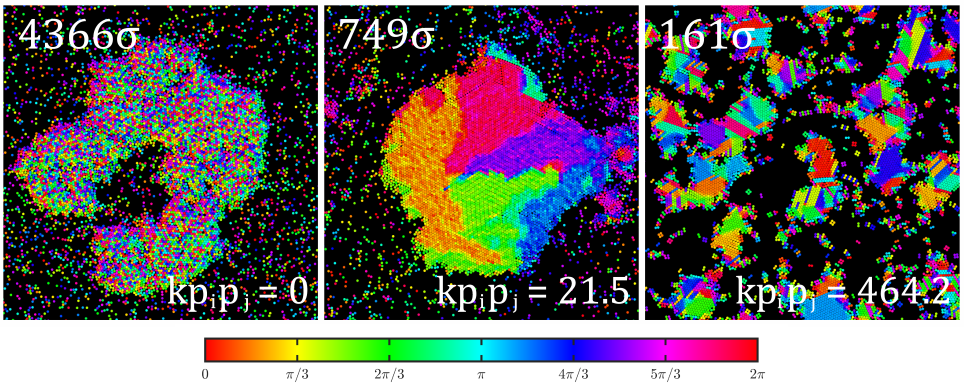

Figure 5.3: Example snapshots of simulations used to generate the data in figure 5.2. The particles are coloured according to their orientation and correspond to the colours in the colour bar. With no interaction the particles are not correlated in orientation. Smaller interactions lead to orientationally correlated clusters which are able to coarsen. Stronger interactions lead to the rapid formation of smaller clusters which have to collide for the system to coarsen. $Pé = 100$ and $\phi = 0.4$.

Moving on to figure 5.2(b), we see that in the steady state where $kp_ip_j = 10^{4/3}$ is less stable; this resembles the fluctuations in mean cluster size in systems with high Péclet numbers. The initial growth in cluster size in the system, where $kp_ip_j = 10^{8/3}$ and the attractive electrostatic force dominates, is much faster. However, after initial nucleation, the growth is slower than when clusters coarsen by activity. This is because particles cannot individually leave clusters; their orientations are locked and clusters have to come together as units.

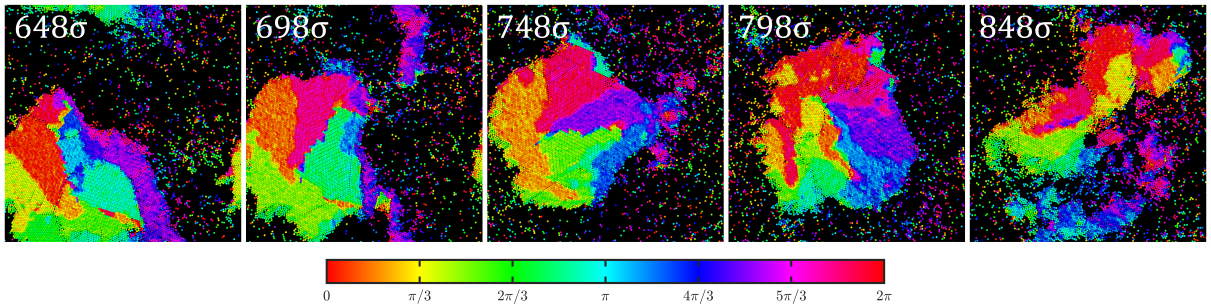

Figure 5.4: Snapshots of a simulation showing a cluster rotating. At $kp_ip_j = 10^{4/3}$ clusters are able to rotate and explode much like in systems with high Péclet numbers. $Pé = 100$ and $\phi = 0.4$.

Although not much can be said from figure 5.2(c), where the distributions of particle densities are similar, figure 5.2(d) has a lot of information about these systems. Going from the system with no interactions (black) to the one at $kp_ip_j = 10^{4/3}$, there is a drastic rise in the velocities at high densities. Much like the variation in the mean cluster size in (b), this is similar to the

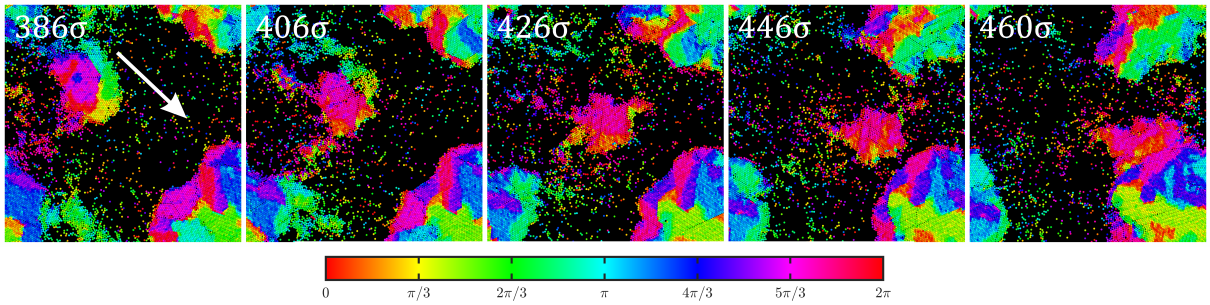

Figure 5.5: Snapshots of a simulation showing a cluster translating. At $kp_ip_j = 10^{4/3}$ clusters are able to translate leading to an increased mean velocity of particles with high local packing fractions.

systems at high Péclet numbers of chapter 3. If we look into the orientations of the particles in the clusters of these systems, as seen in figures 5.3(b), 5.4 and 5.5, we see a large correlation. This is also confirmed in figure 5.2(e) via the distance dependent polar order parameter. Looking more closely at the motion of the cluster in figure 5.4, we see that the main cluster is able to rotate and explode like the clusters at high Péclet number. This suggests that the correlations of the orientations, when coupled with activity are able to disrupt MIPS as long as there are no interactions which prevent clusters from exploding, such as a strong electrostatic attraction or significant angular friction.

Something which is different in the $kp_ip_j = 10^{4/3}$ system compared to those at high Péclet numbers, is the motion of these clusters before and after they break. The cluster in figure 5.4 translates over almost half the simulation box before it breaks. In figure 5.5 we show a cluster that, whilst it is breaking, ends up with nearly all its particles in the same orientation which subsequently leads to an efficient and significant translation. These observations suggest that the increase in velocity at high local area fractions in figure 5.2(d) may, on top of the rotations of clusters as in the systems at high Péclet number, be from the collective motion of particles in clusters.

Two final points which can be made from figure 5.2(d) is that of the bulge in the centre of the grey line, where the electrostatic attraction is dominant, and the increase at the lowest local area fractions. The bulge come from the velocity induced by the attractions. Because these are distance dependent, the particles which are closer together will be affected most. However, the excluded volume of the particles in the denser phases still leads to the eventual reduction. The increase at low area fractions are due to these same attractions pulling particles together against their activity.

The length scales over which the polar order parameter in figure 5.2(e) becomes negative are related to the cluster sizes. When the attraction becomes greater, the clusters tend to be smaller, as coarsening is hindered. The simulation box size also becomes important if a cluster dominated most of the space.

5.3.2 Predator Prey Interactions

As has already been covered throughout this thesis, the field of active matter has also been motivated to mimic the interactions of animals in the real world with only basic interactions. To show the scope of the SCP method, we also created a system where a larger and faster particle, a predator, is designed to interact with smaller particles, prey. We chose to use dipolar electrostatic repulsions between the tails of the prey such that they would turn inwards and create deformable clusters whilst turning away from the dilute region; mimicking using numbers for survivability [227]. The predator has a dipolar electrostatic attraction from its head to the tails of all the prey. This is to make the predator prioritise the closest prey or regions where there are many.

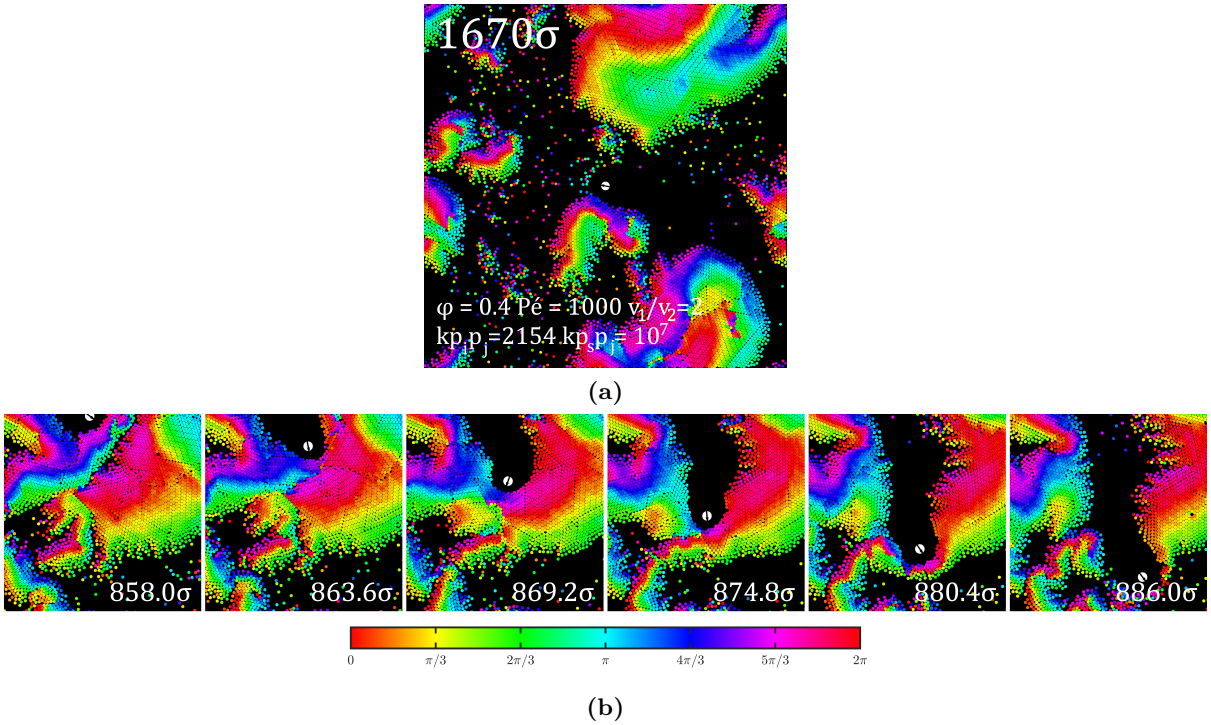

Figure 5.6: Snapshots of a predator-prey simulation. (a) A snapshot of the whole simulation box showing a predator and many prey which form orientationally correlated clusters. (b) A series of snapshots showing how the predator is able to attack a cluster and part it.

We show snapshots of a predator-prey simulation in figure 5.6. Although we have not performed any quantitative study on such as system, we are able to confirm that our methods are flexible enough to be expanded on in such a way. This system was only used as a preliminary test and would need to be rigorously tested before making statements about any observable effects. Moreover, it can be said that they do resemble many other attempts to mimic the collective behaviour we see in nature but that current advances in the field provide more detailed and representative approaches .

5.3.3 Altering the SCP Method by Collision Angle

Using the method of altering the collisions explained previously, we obtain the results in figure 5.7. It is clear from all the graphs in this figure that our modification has nearly no effect. The most significant change is in (d), where the mean velocity increases for all local area fractions. This result could arise from the fact that the structure of these clusters remains the same and the forces within are dissipated throughout. Although each particle is pushing its neighbours with its own active force, the sum total of the forces a collision exerts on a particle is not only from the active force of its neighbour but also those not directly connected to it. This study and those in previous chapters have however shown that the SCP method and active Brownian dynamics, despite only resolving one to one collisions, do not hinder collective pressures in clusters.

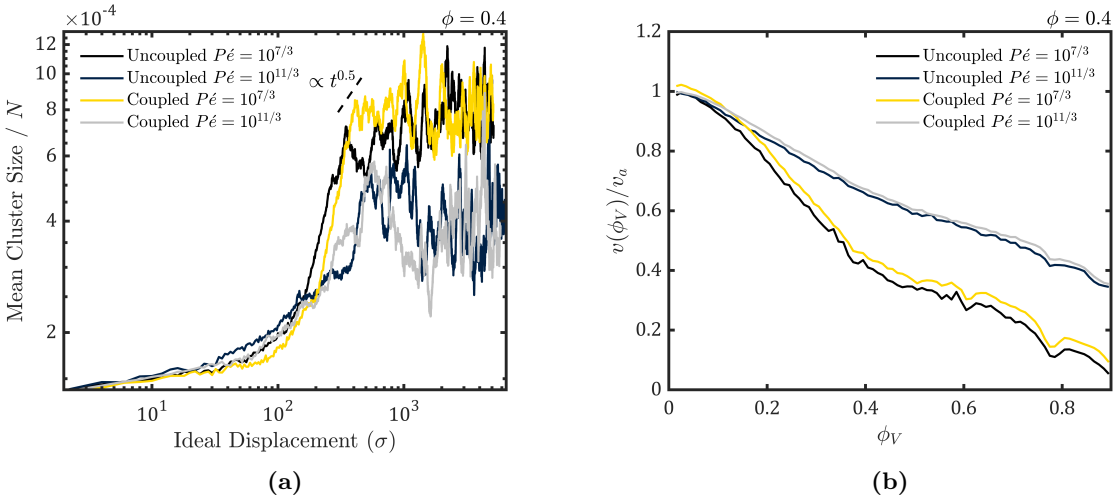

Figure 5.7: The changes in measurable properties of systems where the SCP method is modified. (a) The evolution of the cluster fraction over time. (b) The normalised velocity as a function of the local area fraction in the steady state determined by Voronoi tessellation. $\phi = 0.4$. The "coupled" systems are those with the SCP modification.

5.4 Summary and Conclusions

This work done for this chapter came mainly from the incentive of showing that the SCP method is valuable in systems with more complex interactions and not just in resolving Brownian motion and active motion. After creating systems with electrostatic dipolar interactions, a system with a predator and those with altered collisions, we have shown that our methods remain stable even with extremely large attractive forces.

In our results on the effect of adding a dipolar attraction between the fronts and backs of particles, inspired by the electrostatic effects described in chapter 4, we have shown that we can recreate a system with very similar dynamics to systems of ICEP Janus particles. Not only doe we see the increase in the mean velocity at high densities, the disruption of MIPS in the progression of the mean cluster size and the spatially correlated orientations, but we are able to visualise the motions of clusters which rotate and translate in a similar fashion to the experimental ones in chapter 4.

From our work, we would suggest that more in depth analyses of active systems with various interactions potential can be done. The interplay between excluded volume, long range attractions and orientational interactions still have a lot to be uncovered. Although our approach towards extra particle interactions in this chapter is not novel, by using the SCP method we have shown again [2] that activity can have an effect on systems even when one aspect, such as the attractions in this case, is dominant.

[2] Like in chapter 3 where the activity dominates.

Summary, Conclusions and Outlook

In this thesis, we report on motility-induced phase separation (MIPS) in both simulation and experiment. We dedicate a large part of our work to developing and testing a novel particle interaction to mimic a hard interaction in Brownian dynamics simulations which we call the scaled contact potential (SCP). We cover the structure of passive particle simulations and the structure and dynamics of active particle simulations. Because of the benefits of using our SCP method, we are able to investigate systems at high Péclet numbers and with additional strong dipolar interactions. We also optimise a system of electrophoretic Janus particles for use in experiment. By controlling the conditions we use, we are able to alter the inter-particle interaction such that particles remain hard. From this, we then make comparisons between our results in simulation and experiment.

In the introduction we cover the origin of the study of active matter in the field of soft condensed matter and give a general overview of the study of active particles in simulation and experiment. We end with a brief description of MIPS, how it first arose in the literature and where current research stands. We develop these points further in the thesis.

In chapter 2, we describe the theory behind the structure and dynamics of systems of hard particles focussing on the pair distribution function and the mean squared displacement of Brownian particles. We then present the fundamentals of numerical simulations to set up our methods. Subsequently, we derive and describe our scaled contact potential method in Brownian dynamics and the importance of the time-step in our simulations. We round off our methods section with the details of how we measure the pair distribution function and the mean squared displacement in our systems. In the results section, we focus on the structure of our systems. Through a comparison of the contact value of the pair distribution functions from our simulations an Monte Carlo data, we show first that adding an extra motion step reduces how hard the SCP

method is but leads to a better overall structure of the system. We then show that for the same computation time, our methods provide us with a harder interaction than those currently used in active Brownian simulations and that our systems are independent of temperature, an aim in the derivation of the SCP method. We end with brief comparison of the motion of the particles which shows that it is important for an such repulsive potentials to give particles a consistent and predictable size.

The results of chapter 2 show that the aims of the SCP method are indeed fulfilled. The two main important points being the disconnection with temperature and the consistent particle diameter (figure 2.10). Both of these show that linking the potential to the time-step and considering overlap is a valid and successful method to create an effectively hard potential in a type of simulation with discrete motions. Much like how Heyes *et al.* [145, 147, 149] used a similar method for simulating systems under a constant shear and how we use it in active systems in subsequent parts of the thesis, we predict that such approaches could be used more universally in numerical approaches when studying systems of discrete repulsive particles. This is important because, although some methods like Monte Carlo simulations are in fact in many ways more efficient than Brownian dynamics, they are hindered when it comes to systems with more complex and less predictable interactions, the types of systems the SCP method could be used for.

In chapter 3, we move on to show how the SCP method can be used in active systems. After a theoretical description of the motion of ballistic particles, an important framework for quantifying systems of active Brownian particle, we lay out the theory used to describe MIPS as derived by Tailleur and Cates [4]. The key points in this theory are the result that it is based on theory for equilibrated systems that undergo spinodal decomposition, that density and velocity are inversely proportional to one another (equation 3.14) and that the free energy is dependent on the relation between density and velocity. We also bring in the relation derived by Redner *et al.* [1] based on a kinetic interpretation of particles joining and leaving the dense phase. We round off the introduction to this chapter by highlighting key findings on MIPS from the scientific literature. As in chapter 2, we present our methods beginning with the manner with which we perform our simulations. In this case, linking the active motion to the overlap and the time-step is key to calibrating the SCP method. We then also cover how we measure crystallinity using Voronoi tessellation and the bond-orientational order parameter, angular correlations via the

polar radially averaged polar order parameter, the progress of MIPS with a new development parameter, a procedure to identify and track clusters/grains, torque and rotation within clusters and a method to create what we call "sticky" disks (a physically motivated empirical model to include rotational friction).

The key results of this thesis are in the results section of chapter 3. After showing that the SCP methods provides us with more consistent, stable and harder systems than previously studied in the literature (figure 3.19), we eventually move on to show that we can directly measure the relation between local particle density and velocity (figure 3.24). This is made possible because are particles keep a consistent diameter regardless of initial conditions. We show that both the description based on perturbation presented by Tailleur and Cates [4] and the kinetic description by Redner *et al.* [1] both have their flaws (figures 3.25 and 3.26). However, it is not until we explore the phase diagram at much higher Péclet numbers do we really find novel and convincing arguments for requiring additional terms in such theories. In examining the progression of MIPS, via the traditional parameters such as cluster fraction and mean cluster size (figure 3.29), as well as the relation between local particle density and velocity (figure 3.30), we find a mechanism, then confirmed by observing the rotation of clusters, which leads to cluster instability and an inhibition of MIPS. Due to the long persistence lengths of the particles' trajectories, particles do not have time to reorient before a cluster has had time to form and obtain a net torque. Then, due to a lack of rotational interactions, particles which once joined a cluster end up on the opposite side with no other particles preventing them from escaping. This is enabled because particles which join a cluster from a specific side have similar orientations (figure 3.32). This then results in a type of collective motion and long distance correlations in angles as particles remain close to neighbours with similar orientation. Surprisingly, this occurs at all area fractions (figure 3.34). We test this phenomenon further by introducing our empirical model of rotational friction between the particles. It shows us, by inhibiting cluster disruption, that it is indeed the freedom of rotation which particles have in conventional Brownian simulations which enables the disruption in MIPS we observe (figure 3.38). Our results go to show that, although simple dynamical simulations are useful to understand certain phenomena, the regimes we observe, or may be limited to by methodology, may need to be expanded for a full interpretation of certain systems. We also add to the list of phenomena which do not fit well with current theory [76, 173, 177–179] creating further motivation and evidence for a more encompassing theory to be derived in future.

In chapter 4, we optimise and test a systems of induced-charge electrophoretic (ICEP) particles. We introduce basic colloidal interactions to put the motivations of using colloidal particles as active particles into context. We then do an overview of how MIPS has been performed in experiment and the difficulties which have been encountered up to now in the literature. We end the introduction to the chapter with a brief description of the propulsion mechanism of our particles and previously observed interactions in this kind of system and how others have used them to explore activity. Essential considerations systems of ICEP particles are vast, including particle size, material, solvent ionic strength, electrode synthesis and electric field properties. We cover the conditions of our experiments in the beginning of the methods section. We also include our reflection microscopy technique and how we detect particles. Analysis methods used in this chapter are described in both chapter 2 and 3 except for how to measure a Péclet number which we have considered as part of the results section.

Measuring a velocity is simple in principle but can be complex in practice, especially when particle interactions/behaviours and noise are involved. We consider the correct time-interval over which to measure a distance and then obtain the relation between velocity and local particle density (figure 4.18). This allows us to predict the average propulsion velocity in the absence of interactions and to directly measure velocities regardless of system area fraction. Our first result is that we recover the squared relation predicted in theory [208] and previously obtained in experiment [204] for low field strengths. However, above around $300\,\mathrm{V\,cm^{-1}}$, this relation appears to falter and seems to becomes linear (figure 4.19). In measuring the rotational motion of our particles we find a significant degree of non-diffusive behaviour. By analysing the mean squared angular displacement of each particle, we obtain distributions for the diffusion coefficients, the time exponents and the noise levels in various experiments. From this we obtain an empirical measure for the Péclet number as a function of electric field strength (figure 4.22). When looking across a range of frequencies we also find that the behaviour changes. A change in rotational behaviour accompanies the previously described inversion of velocity at higher frequencies (figure 4.23). Crucially, we are then able to create a $Pé/\phi$ phase diagram and observe that the critical Péclet number for the transition is similar to results from simulations but that the critical area fraction is much lower in our experimental system (figure 4.24). We attribute this to experimental phenomena such as stuck particles, the non-diffusive rotational behaviour and unavoidable particle interactions. The final result in this chapter is a demonstration that through particle alignment and a probable synchronisation of induced flows, that clusters are

able to efficiently translate like in the work of van der Linden *et al.* [7]. We also show an example of a cluster exploding via a mechanism akin to those we observe at high Péclet numbers in our simulations (figure 4.27).

Despite many experimental barriers, such as overcoming particles adhering to the surfaces of electrodes, we have shown that ICEP particles provide us with tunable and versatile active systems. We predict that through careful manipulation of the experimental conditions, such as using a variety of particle sizes and materials, one could extend the already substantial collection of phenomenology. We predict that this system could be the first to be used as an synthetic active component in advanced materials, perhaps competing with biological counterparts which are often viable options for creating active matter.

Our final chapter, chapter 5, is a brief study on simulations with extra interactions. After an overview of active systems with additional interactions seen in the scientific literature, we test the stability of the SCP method with experimentally inspired dipolar interactions, similar to the work of Yan *et al.* [57]. Because of the SCP method, we are able to again explore an extended phase space with large interaction potentials. We show that these dipolar interactions could be at the origin of the translating clusters seen both in our work and the work of van der Linden *et al.* [7] (figure 5.5). We also show how one could create active gels, where the specific magnitudes of all the forces plays a key role (figure 5.3). We then go to show how this dipolar model can be used to create systems with pseudo predator-prey relationships, a key motivation for the study of active particles (figure 5.6). We end with a study on the effect of altering how the velocities of particles are distributed in collisions. Although we do see a minor effect, the density and organisation of the dense phases in these systems tend to average out collisions such to reduce velocities regardless of how they are distributed in a one to one interaction (figure 5.7). The main outlook from this chapter is that the SCP method is indeed modifiable for a variety of systems. We potentially see that it could be used with any interaction; attractive ones being of most significance. As a general concept, we do believe that the collisions in Brownian dynamics should be carefully considered in such systems if one is to make any physical conclusion from such studies. This is even more true if using a coarse grained time-step appears to rectify many potential issues in simulations.

With this thesis, we have achieved our initial goals of expanding the $Pé/\phi$ phase diagram of repulsive active disks and provided our simulation results with more concrete experimental

ones. This work is the first time such a phase diagram has been created in experiment. We hope that our experimental methods could be a source for inspiration for pushing the phase diagram further or adding additional interactions.

In the longer term we foresee that the SCP method, perhaps after being implemented in the more advanced and commercialised software packages, could be used in a wide variety of simulations. Other interaction potentials have always brought with them some degrees of difficulty such as the inconsistencies shown in the work of Martin-Roca *et al.* [2]. Using the SCP method could be a way to find more common ground in the study of "hard" active particles. The ratification of our results with our experiments also give promise to the study of active systems of growing into more practical fields of study. Through our work, we hope that more experimental systems of active particles can be conceived both practically, conceptually and in applications, perhaps including the higher Péclet phenomena we observed in simulation.

Bibliography

[1] Gabriel S. Redner, Michael F. Hagan, and Aparna Baskaran. Structure and dynamics of a phase-separating active colloidal fluid. *Phys. Rev. Lett.*, 110:055701, Jan 2013.

[2] José Martin-Roca, Raul Martinez, Lachlan C. Alexander, Angel Luis Diez, Dirk G. A. L. Aarts, Francisco Alarcon, Jorge Ramírez, and Chantal Valeriani. Characterization of MIPS in a suspension of repulsive active brownian particles through dynamical features. *The Journal of Chemical Physics*, 154(16):164901, April 2021.

[3] J. Tailleur and M. E. Cates. Statistical mechanics of interacting run-and-tumble bacteria. *Phys. Rev. Lett.*, 100:218103, May 2008.

[4] Michael E. Cates and Julien Tailleur. Motility-induced phase separation. *Annual Review of Condensed Matter Physics*, 6(1):219–244, March 2015.

[5] Yaouen Fily and M. Cristina Marchetti. Athermal phase separation of self-propelled particles with no alignment. *Phys. Rev. Lett.*, 108:235702, Jun 2012.

[6] Joakim Stenhammar, Davide Marenduzzo, Rosalind J. Allen, and Michael E. Cates. Phase behaviour of active brownian particles: the role of dimensionality. *Soft Matter*, 10(10):1489–1499, 2014.

[7] Marjolein N. van der Linden, Lachlan C. Alexander, Dirk G. A. L. Aarts, and Olivier Dauchot. Interrupted motility induced phase separation in aligning active colloids. *Phys. Rev. Lett.*, 123:098001, Aug 2019.

[8] Ivo Buttinoni, Giovanni Volpe, Felix Kümmel, Giorgio Volpe, and Clemens Bechinger. Active brownian motion tunable by light. *Journal of Physics: Condensed Matter*, 24(28):284129, June 2012.

[9] M Doi. *Soft matter physics*. Oxford University Press USA, Oxford, 2013.

[10] Maurice Kléman. *Soft matter physics : an introduction*. Springer, New York, 2003.

[11] Carmelo Giacovazzo. *Fundamentals of crystallography*. International Union of Crystallography Oxford University Press, Chester, England Oxford New York, 1992.

[12] Yoshiaki Sugimoto, Pablo Pou, Masayuki Abe, Pavel Jelinek, Rubén Pérez, Seizo Morita, and Óscar Custance. Chemical identification of individual surface atoms by atomic force microscopy. *Nature*, 446(7131):64–67, March 2007.

[13] Jean Perrin. Les atomes. *Nature*, 91(2280):473–473, June 1913.

[14] Albert Einstein. Über einen die erzeugung und verwandlung des lichtes betreffenden heuristischen gesichtspunkt. *Annalen der Physik*, 322(6):132–148, 1905.

[15] James Davis, Yi-Hsuan Hsieh, and Hung-Chi Lee. Humans perceive flicker artifacts at 500 hz. *Scientific Reports*, 5(1):7861, February 2015.

[16] Mitsuhiro Shibayama, Xiang Li, and Takamasa Sakai. Gels: From soft matter to BioMatter. *Industrial & Engineering Chemistry Research*, 57(4):1121–1128, January 2018.

[17] Sylvie Roke. Nonlinear optical spectroscopy of soft matter interfaces. *ChemPhysChem*, 10(9-10):1380–1388, July 2009.

[18] Young-Ki Kim, JungHyun Noh, Karthik Nayani, and Nicholas L. Abbott. Soft matter from liquid crystals. *Soft Matter*, 15(35):6913–6929, 2019.

[19] Bi cheng Wu, Brian Degner, and David Julian McClements. Soft matter strategies for controlling food texture: formation of hydrogel particles by biopolymer complex coacervation. *Journal of Physics: Condensed Matter*, 26(46):464104, October 2014.

[20] François A. Lavergne, Dirk G. A. L. Aarts, and Roel P. A. Dullens. Anomalous grain growth in a polycrystalline monolayer of colloidal hard spheres. *Phys. Rev. X*, 7:041064, Dec 2017.

[21] Sriram Ramaswamy. The mechanics and statistics of active matter. *Annual Review of Condensed Matter Physics*, 1(1):323–345, August 2010.

[22] B. A. Finlayson and L. E. Scriven. Convective instability by active stress. *Proceedings of the Royal Society of London. A. Mathematical and Physical Sciences*, 310(1501):183–219, May 1969.

[23] John Tyler Bonner and L. J. Savage. Evidence for the formation of cell aggregates by chemotaxis in the development of the slime mold dictyostelium discoideum. *Journal of Experimental Zoology*, 106(1):1–26, October 1947.

[24] Ofer Feinerman, Itai Pinkoviezky, Aviram Gelblum, Ehud Fonio, and Nir S. Gov. The physics of cooperative transport in groups of ants. *Nature Physics*, 14(7):683–693, May 2018.

[25] J. Prost, F. Jülicher, and J-F. Joanny. Active gel physics. *Nature Physics*, 11(2):111–117, February 2015.

[26] D. Dell'Arciprete, M. L. Blow, A. T. Brown, F. D. C. Farrell, J. S. Lintuvuori, A. F. McVey, D. Marenduzzo, and W. C. K. Poon. A growing bacterial colony in two dimensions as an active nematic. *Nature Communications*, 9(1):4190, October 2018.

[27] D. M. Bloor and E. Wyn-Jones, editors. *The Structure, Dynamics and Equilibrium Properties of Colloidal Systems*. Springer Netherlands, 1990.

[28] Thomas Speck. Stochastic thermodynamics for active matter. *EPL (Europhysics Letters)*, 114(3):30006, May 2016.

[29] Sarah Eldeen, Ryan Muoio, Paris Blaisdell-Pijuan, Ngoc La, Mauricio Gomez, Alex Vidal, and Wylie Ahmed. Quantifying the non-equilibrium activity of an active colloid. *Soft Matter*, 16:7202–7209, 2020.

[30] Larissa Conradt. When it pays to share decisions. *Nature*, 471(7336):40–41, March 2011.

[31] Avraham Be'er, Bella Ilkanaiv, Renan Gross, Daniel B. Kearns, Sebastian Heidenreich, Markus Bär, and Gil Ariel. A phase diagram for bacterial swarming. *Communications Physics*, 3(1):66, April 2020.

[32] Manuele Brambilla, Eliseo Ferrante, Mauro Birattari, and Marco Dorigo. Swarm robotics: a review from the swarm engineering perspective, 2012.

[33] Dirk Helbing. Traffic and related self-driven many-particle systems. *Reviews of Modern Physics*, 73(4):1067–1141, December 2001.

[34] Joseph Wang and Wei Gao. Nano/microscale motors: Biomedical opportunities and challenges. *ACS Nano*, 6(7):5745–5751, July 2012.

[35] Gandhimohan. M. Viswanathan, Marcos G. E. da Luz, Ernesto P. Raposo, and H. Eugene Stanley. *The Physics of Foraging: An Introduction to Random Searches and Biological Encounters*. Cambridge University Press, 2011.

[36] John Toner and Yuhai Tu. Flocks, herds, and schools: A quantitative theory of flocking. *Physical Review E*, 58(4):4828–4858, October 1998.

[37] Tamás Vicsek, András Czirók, Eshel Ben-Jacob, Inon Cohen, and Ofer Shochet. Novel type of phase transition in a system of self-driven particles. *Physical Review Letters*, 75(6):1226–1229, August 1995.

[38] W. Bialek, A. Cavagna, I. Giardina, T. Mora, E. Silvestri, M. Viale, and A. M. Walczak. Statistical mechanics for natural flocks of birds. *Proceedings of the National Academy of Sciences*, 109(13):4786–4791, March 2012.

[39] Abul K. Tarafder, Andriko von Kügelgen, Adam J. Mellul, Ulrike Schulze, Dirk G. A. L. Aarts, and Tanmay A. M. Bharat. Phage liquid crystalline droplets form occlusive sheaths that encapsulate and protect infectious rod-shaped bacteria. *Proceedings of the National Academy of Sciences*, 117(9):4724–4731, February 2020.

[40] Jie Zhang, Erik Luijten, Bartosz A. Grzybowski, and Steve Granick. Active colloids with collective mobility status and research opportunities. *Chemical Society Reviews*, 46(18):5551–5569, 2017.

[41] Markus Bär, Robert Großmann, Sebastian Heidenreich, and Fernando Peruani. Self-propelled rods: Insights and perspectives for active matter. *Annual Review of Condensed Matter Physics*, 11(1):441–466, March 2020.

[42] Anupam Sengupta. Microbial active matter: A topological framework. *Frontiers in Physics*, 8, 2020.

[43] Wang Xi, Thuan Beng Saw, Delphine Delacour, Chwee Teck Lim, and Benoit Ladoux. Material approaches to active tissue mechanics. *Nature Reviews Materials*, 4(1):23–44, December 2018.

[44] Clemens Bechinger, Roberto Di Leonardo, Hartmut Löwen, Charles Reichhardt, Giorgio Volpe, and Giovanni Volpe. Active particles in complex and crowded environments. *Rev. Mod. Phys.*, 88:045006, Nov 2016.

[45] Achini Opathalage, Michael M. Norton, Michael P. N. Juniper, Blake Langeslay, S. Ali Aghvami, Seth Fraden, and Zvonimir Dogic. Self-organized dynamics and the transition to turbulence of confined active nematics. *Proceedings of the National Academy of Sciences*, 116(11):4788–4797, February 2019.

[46] D. J. G. Pearce, A. M. Miller, G. Rowlands, and M. S. Turner. Role of projection in the control of bird flocks. *Proceedings of the National Academy of Sciences*, 111(29):10422–10426, July 2014.

[47] Walter F. Paxton, Kevin C. Kistler, Christine C. Olmeda, Ayusman Sen, Sarah K. St. Angelo, Yanyan Cao, Thomas E. Mallouk, Paul E. Lammert, and Vincent H. Crespi. Catalytic nanomotors: autonomous movement of striped nanorods. *Journal of the American Chemical Society*, 126(41):13424–13431, October 2004.

[48] Ivo Buttinoni, Julian Bialké, Felix Kümmel, Hartmut Löwen, Clemens Bechinger, and Thomas Speck. Dynamical clustering and phase separation in suspensions of self-propelled colloidal particles. *Phys. Rev. Lett.*, 110:238301, Jun 2013.

[49] Steve Granick, editor. *Janus Particle Synthesis, Self-Assembly and Applications*. Royal Society of Chemistry, 2012.

[50] Jérémie Palacci, Benjamin Abécassis, Cécile Cottin-Bizonne, Christophe Ybert, and Lydéric Bocquet. Colloidal motility and pattern formation under rectified diffusiophoresis. *Phys. Rev. Lett.*, 104:138302, Apr 2010.

[51] I. Theurkauff, C. Cottin-Bizonne, J. Palacci, C. Ybert, and L. Bocquet. Dynamic clustering in active colloidal suspensions with chemical signaling. *Phys. Rev. Lett.*, 108:268303, Jun 2012.

[52] J. Palacci, S. Sacanna, A. P. Steinberg, D. J. Pine, and P. M. Chaikin. Living crystals of light-activated colloidal surfers. *Science*, 339(6122):936–940, January 2013.

[53] Antoine Bricard, Jean-Baptiste Caussin, Nicolas Desreumaux, Olivier Dauchot, and Denis Bartolo. Emergence of macroscopic directed motion in populations of motile colloids. *Nature*, 503(7474):95–98, November 2013.

[54] Hamid Karani, Gerardo E. Pradillo, and Petia M. Vlahovska. Tuning the random walk of active colloids: From individual run-and-tumble to dynamic clustering. *Phys. Rev. Lett.*, 123:208002, Nov 2019.

[55] G. Quincke. Ueber rotationen im constanten electrischen felde. *Annalen der Physik und Chemie*, 295(11):417–486, 1896.

[56] Ryo Soma, Bokusui Nakayama, Masashi Kuwahara, Eiji Yamamoto, and Toshiharu Saiki. Phase-change janus particles with switchable dual properties. *Applied Physics Letters*, 117(22):221601, November 2020.

[57] Jing Yan, Ming Han, Jie Zhang, Cong Xu, Erik Luijten, and Steve Granick. Reconfiguring active particles by electrostatic imbalance. *Nature Materials*, 15(10):1095–1099, July 2016.

[58] M. Reza Shaebani, Adam Wysocki, R. Winkler, Gerhard Gompper, and Heiko Rieger. Computational models for active matter. *Nature Reviews Physics*, pages 181—-199, 10 2020.

[59] Howard C. Berg. The rotary motor of bacterial flagella. *Annual Review of Biochemistry*, 72(1):19–54, June 2003.

[60] Giorgio Volpe, Sylvain Gigan, and Giovanni Volpe. Simulation of the active brownian motion of a microswimmer. *American Journal of Physics*, 82(7):659–664, July 2014.

[61] H. H. Wensink and H. Löwen. Aggregation of self-propelled colloidal rods near confining walls. *Phys. Rev. E*, 78:031409, Sep 2008.

[62] H H Wensink and H Löwen. Emergent states in dense systems of active rods: from swarming to turbulence. *Journal of Physics: Condensed Matter*, 24(46):464130, October 2012.

[63] Isabella Petrelli, Pasquale Digregorio, Leticia Cugliandolo, G. Gonnella, and Antonio Suma. Active dumbbells: dynamics and morphology in the coexisting region. *The European Physical Journal E*, 41:128, 05 2018.

[64] Robin van Damme, Jeroen Rodenburg, René van Roij, and Marjolein Dijkstra. Interparticle torques suppress motility-induced phase separation for rodlike particles. *The Journal of Chemical Physics*, 150(16):164501, April 2019.

[65] Dóra Bárdfalvy, Shan Anjum, Cesare Nardini, Alexander Morozov, and Joakim Stenhammar. Symmetric mixtures of pusher and puller microswimmers behave as noninteracting suspensions. *Phys. Rev. Lett.*, 125:018003, Jul 2020.

[66] Alice L. Thorneywork, Joshua L. Abbott, Dirk G. A. L. Aarts, and Roel P. A. Dullens. Two-dimensional melting of colloidal hard spheres. *Phys. Rev. Lett.*, 118:158001, Apr 2017.

[67] A G Thompson, J Tailleur, M E Cates, and R A Blythe. Lattice models of nonequilibrium bacterial dynamics. *Journal of Statistical Mechanics: Theory and Experiment*, 2011(02):P02029, February 2011.

[68] Julian Bialké, Hartmut Löwen, and Thomas Speck. Microscopic theory for the phase separation of self-propelled repulsive disks. *EPL (Europhysics Letters)*, 103(3):30008, August 2013.

[69] Demian Levis and Ludovic Berthier. Clustering and heterogeneous dynamics in a kinetic monte carlo model of self-propelled hard disks. *Phys. Rev. E*, 89:062301, Jun 2014.

[70] Iago Grobas, Marco Polin, and Munehiro Asally. Swarming bacteria undergo localized dynamic phase transition to form stress-induced biofilms. 2020.

[71] Nicolas Bain and Denis Bartolo. Dynamic response and hydrodynamics of polarized crowds. *Science*, 363(6422):46–49, January 2019.

[72] M E Cates. Diffusive transport without detailed balance in motile bacteria: does microbiology need statistical physics? *Reports on Progress in Physics*, 75(4):042601, March 2012.

[73] M. E. Cates and J. Tailleur. When are active brownian particles and run-and-tumble particles equivalent? consequences for motility-induced phase separation. *EPL (Europhysics Letters)*, 101(2):20010, January 2013.

[74] Silke Henkes, Yaouen Fily, and M. Cristina Marchetti. Active jamming: Self-propelled soft particles at high density. *Phys. Rev. E*, 84:040301, Oct 2011.

[75] Ricard Matas-Navarro, Ramin Golestanian, Tanniemola B. Liverpool, and Suzanne M. Fielding. Hydrodynamic suppression of phase separation in active suspensions. *Phys. Rev. E*, 90:032304, Sep 2014.

[76] Suvendu Mandal, Benno Liebchen, and Hartmut Löwen. Motility-induced temperature difference in coexisting phases. *Phys. Rev. Lett.*, 123:228001, Nov 2019.

[77] Ahmad K. Omar, Katherine Klymko, Trevor GrandPre, and Phillip L. Geissler. Phase diagram of active brownian spheres: Crystallization and the metastability of motility-induced phase separation. *Phys. Rev. Lett.*, 126:188002, May 2021.

[78] Giuseppe Gonnella, Davide Marenduzzo, Antonio Suma, and Adriano Tiribocchi. Motility-induced phase separation and coarsening in active matter. *Comptes Rendus Physique*, 16(3):316–331, April 2015.

[79] W. Russel, D. A. Saville, and W. R. Schowalter. *Colloidal dispersions*. Cambridge University Press, Cambridge New York, 1989.

[80] J-P. Hansen and I. R. McDonald. *Theory of simple liquids : with applications to soft matter*. Academic Press, Amsterdam Boston, 2013.

[81] M. P. Allen and D. J. Tildesley. *Computer simulation of liquids*. Clarendon Press Oxford University Press, Oxford England New York, 1987.

[82] J. A. Barker and D. Henderson. What is "liquid"? understanding the states of matter. *Rev. Mod. Phys.*, 48:587–671, Oct 1976.

[83] J. S. Rowlinson. *Molecular theory of capillarity*. Dover Publications, Mineola, N.Y, 2002.

[84] B. M. Axilrod and E. Teller. Interaction of the van der waals type between three atoms. *The Journal of Chemical Physics*, 11(6):299–300, June 1943.

[85] John C. Crocker and David G. Grier. Microscopic measurement of the pair interaction potential of charge-stabilized colloid. *Physical Review Letters*, 73(2):352–355, July 1994.

[86] Marco Polin, Yohai Roichman, and David G. Grier. Autocalibrated colloidal interaction measurements with extended optical traps. *Phys. Rev. E*, 77:051401, May 2008.

[87] Adam Edward Stones, Roel P. A. Dullens, and Dirk G. A. L. Aarts. Model-free measurement of the pair potential in colloidal fluids using optical microscopy. *Phys. Rev. Lett.*, 123:098002, Aug 2019.

[88] Mark Tuckerman. *Statistical mechanics : theory and molecular simulation*. Oxford University Press, Oxford, 2010.

[89] Jeppe C Dyre. Simple liquids' quasiuniversality and the hard-sphere paradigm. *Journal of Physics: Condensed Matter*, 28(32):323001, June 2016.

[90] Lars Onsager. The effects of shape on the interaction of colloidal particles. *Annals of the New York Academy of Sciences*, 51(4):627–659, May 1949.

[91] P. W. Bridgman. Change of phase under pressure. i. the phase diagram of eleven substances with especial reference to the melting curve. *Physical Review*, 3(3):153–203, March 1914.

[92] John G. Kirkwood. Molecular distribution in liquids. *The Journal of Chemical Physics*, 7(10):919–925, October 1939.

[93] John G. Kirkwood, Eugene K. Maun, and Berni J. Alder. Radial distribution functions and the equation of state of a fluid composed of rigid spherical molecules. *The Journal of Chemical Physics*, 18(8):1040–1047, August 1950.

[94] William G. Hoover and Francis H. Ree. Melting transition and communal entropy for hard spheres. *The Journal of Chemical Physics*, 49(8):3609–3617, October 1968.

[95] N. D. Mermin. Crystalline order in two dimensions. *Physical Review*, 176(1):250–254, December 1968.

[96] Jooyoung Lee and Katherine J. Strandburg. First-order melting transition of the hard-disk system. *Physical Review B*, 46(17):11190–11193, November 1992.

[97] John A. Zollweg and Geoffrey V. Chester. Melting in two dimensions. *Physical Review B*, 46(17):11186–11189, November 1992.

[98] Julio F. Fernández, Juan J. Alonso, and Jolanta Stankiewicz. One-stage continuous melting transition in two dimensions. *Physical Review Letters*, 75(19):3477–3480, November 1995.

[99] A. Jaster. Computer simulations of the two-dimensional melting transition using hard disks. *Physical Review E*, 59(3):2594–2602, March 1999.

[100] Kurt Binder, Surajit Sengupta, and Peter Nielaba. The liquid-solid transition of hard discs: first-order transition or kosterlitz-thouless-halperin-nelson-young scenario? *Journal of Physics: Condensed Matter*, 14(9):2323–2333, February 2002.

[101] Etienne P. Bernard and Werner Krauth. Two-step melting in two dimensions: First-order liquid-hexatic transition. *Physical Review Letters*, 107(15), October 2011.

[102] Michael Engel, Joshua A. Anderson, Sharon C. Glotzer, Masaharu Isobe, Etienne P. Bernard, and Werner Krauth. Hard-disk equation of state: First-order liquid-hexatic transition in two dimensions with three simulation methods. *Phys. Rev. E*, 87:042134, Apr 2013.

[103] Rudolf Peierls. *Surprises in theoretical physics.* Princeton University Press, Princeton, N.J, 1979.

[104] David Nelson. *Defects and geometry in condensed matter physics.* Cambridge University Press, Cambridge New York, 2002.

[105] B. J. Alder and T. E. Wainwright. Phase transition in elastic disks. *Physical Review*, 127(2):359–361, July 1962.

[106] Alice L. Thorneywork, Roland Roth, Dirk G. A. L. Aarts, and Roel P. A. Dullens. Communication: Radial distribution functions in a two-dimensional binary colloidal hard sphere system. *The Journal of Chemical Physics*, 140(16):161106, April 2014.

[107] J M Kosterlitz and D J Thouless. Ordering, metastability and phase transitions in two-dimensional systems. *Journal of Physics C: Solid State Physics*, 6(7):1181–1203, April 1973.

[108] David R. Nelson and B. I. Halperin. Dislocation-mediated melting in two dimensions. *Physical Review B*, 19(5):2457–2484, March 1979.

[109] B. I. Halperin and David R. Nelson. Theory of two-dimensional melting. *Physical Review Letters*, 41(2):121–124, July 1978.

[110] A. P. Young. Melting and the vector coulomb gas in two dimensions. *Physical Review B*, 19(4):1855–1866, February 1979.

[111] J. K. Percus. Approximation methods in classical statistical mechanics. *Physical Review Letters*, 8(11):462–463, June 1962.

[112] Harry L. Frisch, Joel L. Lebowitz, and Stuart A. Rice. The equilibrium theory of classical fluids. *Physics Today*, 18(5):78–80, May 1965.

[113] M. Puoskari. Exact self-consistent integral equations for the distribution functions of classical fluids. *Physics and Chemistry of Liquids*, 39(2):201–225, March 2001.

[114] P. Langevin. *Sur la théorie du mouvement brownien.* 1908.

[115] Adolf Fick. Ueber diffusion. *Annalen der Physik und Chemie*, 170(1):59–86, 1855.

[116] Dirk G. A. L. Aarts. Liquids and solutions undergraduate lecture notes.

[117] Eric R Weeks and D.A Weitz. Subdiffusion and the cage effect studied near the colloidal glass transition. *Chemical Physics*, 284(1-2):361–367, November 2002.

[118] Wei Wang, Wentao Duan, Suzanne Ahmed, Ayusman Sen, and Thomas E. Mallouk. From one to many: Dynamic assembly and collective behavior of self-propelled colloidal motors. *Accounts of Chemical Research*, 48(7):1938–1946, June 2015.

[119] Maxime Woringer, Ignacio Izeddin, Cyril Favard, and Hugues Berry. Anomalous subdiffusion in living cells: Bridging the gap between experiments and realistic models through collaborative challenges. *Frontiers in Physics*, 8, 2020.

[120] P. N. Pusey and W. van Megen. Observation of a glass transition in suspensions of spherical colloidal particles. *Physical Review Letters*, 59(18):2083–2086, November 1987.

[121] Ludovic Berthier and Giulio Biroli. Theoretical perspective on the glass transition and amorphous materials. *Reviews of Modern Physics*, 83(2):587–645, June 2011.

[122] Daan Frenkel. *Understanding molecular simulation : from algorithms to applications.* Academic Press, San Diego, 2002.

[123] J. Jover, A. J. Haslam, A. Galindo, G. Jackson, and E. A. Müller. Pseudo hard-sphere potential for use in continuous molecular-dynamics simulation of spherical and chain molecules. *The Journal of Chemical Physics*, 137(14):144505, October 2012.

[124] Alice L. Thorneywork, Roberto E. Rozas, Roel P. A. Dullens, and Jürgen Horbach. Effect of hydrodynamic interactions on self-diffusion of quasi-two-dimensional colloidal hard spheres. *Phys. Rev. Lett.*, 115:268301, Dec 2015.

[125] E. Sanz and D. Marenduzzo. Dynamic monte carlo versus brownian dynamics: A comparison for self-diffusion and crystallization in colloidal fluids. *The Journal of Chemical Physics*, 132(19):194102, May 2010.

[126] B. Cichocki and K. Hinsen. Dynamic computer simulation of concentrated hard sphere suspensions. *Physica A: Statistical Mechanics and its Applications*, 166(3):473–491, July 1990.

[127] J. B. Gibson, A. N. Goland, M. Milgram, and G. H. Vineyard. Dynamics of radiation damage. *Phys. Rev.*, 120:1229–1253, Nov 1960.

[128] B. J. Alder and T. E. Wainwright. Phase transition for a hard sphere system. *The Journal of Chemical Physics*, 27(5):1208–1209, 1957.

[129] L. Filion, R. Ni, D. Frenkel, and M. Dijkstra. Simulation of nucleation in almost hard-sphere colloids: The discrepancy between experiment and simulation persists. *The Journal of Chemical Physics*, 134(13):134901, 2011.

[130] David R. Foss and John F. Brady. Brownian dynamics simulation of hard-sphere colloidal dispersions. *Journal of Rheology*, 44(3):629–651, 2000.

[131] D.C. Rapaport. *The Art of Molecular Dynamics Simulation*. Cambridge University Press, 2004.

[132] J. M. Haile. *Molecular dynamics simulation : elementary methods*. Wiley, New York, 1997.

[133] Julie A. McCormick, Carol K. Hall, and Saad A. Khan. The dynamics of single chains within a model polymer melt. *The Journal of Chemical Physics*, 122(11):114902, March 2005.

[134] Berk Hess, Carsten Kutzner, David van der Spoel, and Erik Lindahl. GROMACS 4: algorithms for highly efficient, load-balanced, and scalable molecular simulation. *Journal of Chemical Theory and Computation*, 4(3):435–447, February 2008.

[135] Steve Plimpton. Fast parallel algorithms for short-range molecular dynamics. *Journal of Computational Physics*, 117(1):1–19, March 1995.

[136] W. Smith and T.R. Forester. DL_POLY_2.0: A general-purpose parallel molecular dynamics simulation package. *Journal of Molecular Graphics*, 14(3):136–141, June 1996.

[137] James C. Phillips, Rosemary Braun, Wei Wang, James Gumbart, Emad Tajkhorshid, Elizabeth Villa, Christophe Chipot, Robert D. Skeel, Laxmikant Kalé, and Klaus Schulten. Scalable molecular dynamics with NAMD. *Journal of Computational Chemistry*, 26(16):1781–1802, 2005.

[138] John E. Stone, James C. Phillips, Peter L. Freddolino, David J. Hardy, Leonardo G. Trabuco, and Klaus Schulten. Accelerating molecular modeling applications with graphics processors. *Journal of Computational Chemistry*, 28(16):2618–2640, 2007.

[139] John D. Weeks, David Chandler, and Hans C. Andersen. Role of repulsive forces in determining the equilibrium structure of simple liquids. *The Journal of Chemical Physics*, 54(12):5237–5247, 1971.

[140] J E Jones. On the determination of molecular fields. —ii. from the equation of state of a gas. *Proc. R. Soc. Lond. A.*, 106(738):461–482, oct 1924.

[141] J E Lennard-Jones. Cohesion. *Proceedings of the Physical Society*, 43(5):461–482, sep 1931.

[142] J. Gao and J. H. Weiner. Excluded-volume effects in rubber elasticity. 1. virial stress formulation. *Macromolecules*, 20(10):2520–2525, October 1987.

[143] Basel F. Abu-Sharkh and Esam Z. Hamad. Simulation and model development for the equation of state of self-assembling nonadditive hard chains. *Macromolecules*, 33(4):1345–1350, February 2000.

[144] Basel F. Abu-Sharkh. Equation of state and phase separation in binary mixtures of non-additive chains. *Macromolecules*, 33(25):9437–9443, November 2000.

[145] D. M. Heyes and H. Okumura. Some physical properties of the weeks–chandler–andersen fluid. *Molecular Simulation*, 32(1):45–50, January 2006.

[146] A Mulero. *Theory and simulation of hard-sphere fluids and related systems*. Springer, Berlin, 2008.

[147] David M. Heyes and Hisashi Okumura. Equation of state and structural properties of the weeks-chandler-andersen fluid. *The Journal of Chemical Physics*, 124(16):164507, April 2006.

[148] Gustav Mie. Zur kinetischen theorie der einatomigen körper. *Annalen der Physik*, 316(8):657–697, 1903.

[149] D.M. Heyes and J.R. Melrose. Brownian dynamics simulations of model hard-sphere suspensions. *Journal of Non-Newtonian Fluid Mechanics*, 46(1):1–28, January 1993.

[150] P. Strating. Brownian dynamics simulation of a hard-sphere suspension. *Physical Review E*, 59(2):2175–2187, February 1999.

[151] W. Schaertl and H. Sillescu. Brownian dynamics of polydisperse colloidal hard spheres: Equilibrium structures and random close packings. *Journal of Statistical Physics*, 77:1007–1025, 1994.

[152] D. Beeman. Some multistep methods for use in molecular dynamics calculations. *Journal of Computational Physics*, 20(2):130–139, February 1976.

[153] Nicholas Metropolis, Arianna W. Rosenbluth, Marshall N. Rosenbluth, Augusta H. Teller, and Edward Teller. Equation of state calculations by fast computing machines. *The Journal of Chemical Physics*, 21(6):1087–1092, June 1953.

[154] Etienne P. Bernard, Werner Krauth, and David B. Wilson. Event-chain monte carlo algorithms for hard-sphere systems. *Phys. Rev. E*, 80:056704, Nov 2009.

[155] Adam Edward Stones, Roel P. A. Dullens, and Dirk G. A. L. Aarts. Communication: Contact values of pair distribution functions in colloidal hard disks by test-particle insertion. *The Journal of Chemical Physics*, 148(24):241102, June 2018.

[156] W. van Megen and H. J. Schöpe. The cage effect in systems of hard spheres. *The Journal of Chemical Physics*, 146(10):104503, March 2017.

[157] Juan Ruben Gomez-Solano and Francisco J Sevilla. Active particles with fractional rotational brownian motion. *Journal of Statistical Mechanics: Theory and Experiment*, 2020(6):063213, jun 2020.

[158] G. E. Uhlenbeck and L. S. Ornstein. On the theory of the brownian motion. *Physical Review*, 36(5):823–841, September 1930.

[159] Shibananda Das, Gerhard Gompper, and Roland G Winkler. Confined active brownian particles: theoretical description of propulsion-induced accumulation. 20(1):015001, jan 2018.

[160] John W. Cahn and John E. Hilliard. Free energy of a nonuniform system. i. interfacial free energy. *The Journal of Chemical Physics*, 28(2):258–267, February 1958.

[161] John W. Cahn and John E. Hilliard. Free energy of a nonuniform system. III. nucleation in a two-component incompressible fluid. *The Journal of Chemical Physics*, 31(3):688–699, September 1959.

[162] John W Cahn. On spinodal decomposition. *Acta Metallurgica*, 9(9):795–801, September 1961.

[163] John W. Cahn. Phase separation by spinodal decomposition in isotropic systems. *The Journal of Chemical Physics*, 42(1):93–99, January 1965.

[164] David S Dean. Langevin equation for the density of a system of interacting langevin processes. *Journal of Physics A: Mathematical and General*, 29(24):L613–L617, December 1996.

[165] A. J. Archer and R. Evans. Dynamical density functional theory and its application to spinodal decomposition. *The Journal of Chemical Physics*, 121(9):4246–4254, September 2004.

[166] Akira Onuki. *Phase transition dynamics*. Cambridge University Press, Cambridge New York, 2002.

[167] W. Van Negen and I. Shook. Equilibrium properties of suspensions. *Advances in Colloid and Interface Science*, 21(1-2):119–194, September 1984.

[168] Julian Bialké, Thomas Speck, and Hartmut Löwen. Crystallization in a dense suspension of self-propelled particles. *Phys. Rev. Lett.*, 108:168301, Apr 2012.

[169] Ludovic Berthier. Nonequilibrium glassy dynamics of self-propelled hard disks. *Phys. Rev. Lett.*, 112:220602, Jun 2014.

[170] Yaouen Fily, Silke Henkes, and M. Cristina Marchetti. Freezing and phase separation of self-propelled disks. *Soft Matter*, 10(13):2132–2140, 2014.

[171] Adam Wysocki, Roland G. Winkler, and Gerhard Gompper. Cooperative motion of active brownian spheres in three-dimensional dense suspensions. *EPL (Europhysics Letters)*, 105(4):48004, February 2014.

[172] Adam Patch, David Yllanes, and M. Cristina Marchetti. Kinetics of motility-induced phase separation and swim pressure. *Phys. Rev. E*, 95:012601, Jan 2017.

[173] Adam Patch, Daniel M. Sussman, David Yllanes, and M. Cristina Marchetti. Curvature-dependent tension and tangential flows at the interface of motility-induced phases. *Soft Matter*, 14(36):7435–7445, 2018.

[174] Jie Su, Huijun Jiang, and Zhonghuai Hou. Inertia-induced nucleation-like motility-induced phase separation. *New Journal of Physics*, 23(1):013005, January 2021.

[175] Paul J. Steinhardt, David R. Nelson, and Marco Ronchetti. Bond-orientational order in liquids and glasses. *Physical Review B*, 28(2):784–805, July 1983.

[176] L. Caprini, U. Marini Bettolo Marconi, and A. Puglisi. Spontaneous velocity alignment in motility-induced phase separation. *Phys. Rev. Lett.*, 124:078001, Feb 2020.

[177] A. P. Solon, Y. Fily, A. Baskaran, M. E. Cates, Y. Kafri, M. Kardar, and J. Tailleur. Pressure is not a state function for generic active fluids. *Nature Physics*, 11(8):673–678, June 2015.

[178] Alexandre P. Solon, Joakim Stenhammar, Raphael Wittkowski, Mehran Kardar, Yariv Kafri, Michael E. Cates, and Julien Tailleur. Pressure and phase equilibria in interacting active brownian spheres. *Phys. Rev. Lett.*, 114:198301, May 2015.

[179] Julian Bialké, Jonathan T. Siebert, Hartmut Löwen, and Thomas Speck. Negative interfacial tension in phase-separated active brownian particles. *Phys. Rev. Lett.*, 115:098301, Aug 2015.

[180] H. H. Wensink, J. Dunkel, S. Heidenreich, K. Drescher, R. E. Goldstein, H. Lowen, and J. M. Yeomans. Meso-scale turbulence in living fluids. *Proceedings of the National Academy of Sciences*, 109(36):14308–14313, August 2012.

[181] Chantal Valeriani, Martin Li, John Novosel, Jochen Arlt, and Davide Marenduzzo. Colloids in a bacterial bath: simulations and experiments. *Soft Matter*, 7(11):5228, 2011.

[182] A. Suma, G. Gonnella, D. Marenduzzo, and E. Orlandini. Motility-induced phase separation in an active dumbbell fluid. *EPL (Europhysics Letters)*, 108(5):56004, December 2014.

[183] Fernando Peruani, Jörn Starruß, Vladimir Jakovljevic, Lotte Søgaard-Andersen, Andreas Deutsch, and Markus Bär. Collective motion and nonequilibrium cluster formation in colonies of gliding bacteria. *Phys. Rev. Lett.*, 108:098102, Feb 2012.

[184] Samuel R. McCandlish, Aparna Baskaran, and Michael F. Hagan. Spontaneous segregation of self-propelled particles with different motilities. *Soft Matter*, 8(8):2527, 2012.

[185] S Chandrasekhar. *Liquid crystals*. Cambridge University Press, Cambridge England New York, NY, USA, 1992.

[186] P Dillmann, G Maret, and P Keim. Polycrystalline solidification in a quenched 2d colloidal system. *Journal of Physics: Condensed Matter*, 20(40):404216, September 2008.

[187] Julian Jeggle, Joakim Stenhammar, and Raphael Wittkowski. Pair-distribution function of active brownian spheres in two spatial dimensions: Simulation results and analytic representation. *The Journal of Chemical Physics*, 152(19):194903, May 2020.

[188] Johannes Diderik van der Waals. *Over de continuiteit van den gas- en vloeistoftoestand (On the Continuity of the Gaseous and Liquid States) (doctoral dissertation)*. Universiteit Leiden, 1873.

[189] Jacob Israelachvili. *Intermolecular and surface forces*. Academic Press, Burlington, MA, 2011.

[190] Lei Wu, Carlos P. Ortiz, and Douglas J. Jerolmack. Aggregation of elongated colloids in water. *Langmuir*, 33(2):622–629, January 2017.

[191] Navid Bizmark and Marios A. Ioannidis. Effects of ionic strength on the colloidal stability and interfacial assembly of hydrophobic ethyl cellulose nanoparticles. *Langmuir*, 31(34):9282–9289, August 2015.

[192] Gregory N. Smith, Matthew J. Derry, James E. Hallett, Joseph R. Lovett, Oleksander O. Mykhaylyk, Thomas J. Neal, Sylvain Prévost, and Steven P. Armes. Refractive index matched, nearly hard polymer colloids. *Proceedings of the Royal Society A: Mathematical, Physical and Engineering Sciences*, 475(2226):20180763, June 2019.

[193] T. A. Witten and P. A. Pincus. Colloid stabilization by long grafted polymers. *Macromolecules*, 19(10):2509–2513, October 1986.

[194] A. Kohut, A. Voronov, and W. Peukert. An effective way to stabilize colloidal particles dispersed in polar and nonpolar media. *Langmuir*, 23(2):504–508, January 2007.

[195] Giovanni Giupponi and Ignacio Pagonabarraga. Determination of the zeta potential for highly charged colloidal suspensions. *Philosophical Transactions of the Royal Society A: Mathematical, Physical and Engineering Sciences*, 369(1945):2546–2554, June 2011.

[196] Donald McQuarrie. *Statistical mechanics*. University Science Books, 1976.

[197] A.L. Loeb. *Electrical Double Layer around a Spherical Colloidal Particle*. Mit Pr, City, 1961.

[198] B Derjaguin and L Landau. Theory of the stability of strongly charged lyophobic sols and of the adhesion of strongly charged particles in solutions of electrolytes. *Acta Physicochimica U.R.S.S.*, 14:633–662, 1941.

[199] E. J. W. Verwey. Theory of the stability of lyophobic colloids. *The Journal of Physical and Colloid Chemistry*, 51(3):631–636, March 1947.

[200] Jorrit Mellema. Experimental rheology of model colloidal dispersions. *Current Opinion in Colloid & Interface Science*, 2(4):411–419, August 1997.

[201] C. Patrick Royall, Wilson C. K. Poon, and Eric R. Weeks. In search of colloidal hard spheres. *Soft Matter*, 9(1):17–27, 2013.

[202] Hong-Ren Jiang, Natsuhiko Yoshinaga, and Masaki Sano. Active motion of a janus particle by self-thermophoresis in a defocused laser beam. *Phys. Rev. Lett.*, 105:268302, Dec 2010.

[203] A Erbe, M Zientara, L Baraban, C Kreidler, and P Leiderer. Various driving mechanisms for generating motion of colloidal particles. *Journal of Physics: Condensed Matter*, 20(40):404215, September 2008.

[204] Daiki Nishiguchi and Masaki Sano. Mesoscopic turbulence and local order in janus particles self-propelling under an ac electric field. *Phys. Rev. E*, 92:052309, Nov 2015.

[205] Julien Deseigne, Olivier Dauchot, and Hugues Chaté. Collective motion of vibrated polar disks. *Phys. Rev. Lett.*, 105:098001, Aug 2010.

[206] Andrey Sokolov, Igor S. Aranson, John O. Kessler, and Raymond E. Goldstein. Concentration dependence of the collective dynamics of swimming bacteria. *Phys. Rev. Lett.*, 98:158102, Apr 2007.

[207] Sumit Gangwal, Olivier J. Cayre, Martin Z. Bazant, and Orlin D. Velev. Induced-charge electrophoresis of metallodielectric particles. *Phys. Rev. Lett.*, 100:058302, Feb 2008.

[208] Todd M. Squires and Martin Z. Bazant. Breaking symmetries in induced-charge electro-osmosis and electrophoresis. *Journal of Fluid Mechanics*, 560:65, July 2006.

[209] Todd M. Squires and Martin Z. Bazant. Induced-charge electro-osmosis. *Journal of Fluid Mechanics*, 509:217–252, June 2004.

[210] Antoine Bricard, Jean-Baptiste Caussin, Debasish Das, Charles Savoie, Vijayakumar Chikkadi, Kyohei Shitara, Oleksandr Chepizhko, Fernando Peruani, David Saintillan, and Denis Bartolo. Emergent vortices in populations of colloidal rollers. *Nature Communications*, 6(1):7470, June 2015.

[211] J Lyklema. *Fundamentals of interface and colloid science*. Academic Press, London San Diego, California, 2000.

[212] S.S. Dukhin. Non-equilibrium electric surface phenomena. *Advances in Colloid and Interface Science*, 44:1–134, May 1993.

[213] W. D. Ristenpart, I. A. Aksay, and D. A. Saville. Assembly of colloidal aggregates by electrohydrodynamic flow: Kinetic experiments and scaling analysis. *Phys. Rev. E*, 69:021405, Feb 2004.

[214] Pablo García-Sánchez, Yukun Ren, Juan J. Arcenegui, Hywel Morgan, and Antonio Ramos. Alternating current electrokinetic properties of gold-coated microspheres. *Langmuir*, 28(39):13861–13870, September 2012.

[215] V.N. Shilov, A.V. Delgado, F. Gonzalez-Caballero, and C. Grosse. Thin double layer theory of the wide-frequency range dielectric dispersion of suspensions of non-conducting spherical particles including surface conductivity of the stagnant layer. *Colloids and Surfaces A: Physicochemical and Engineering Aspects*, 192(1-3):253–265, November 2001.

[216] Jie Zhang, Jing Yan, and Steve Granick. Directed self-assembly pathways of active colloidal clusters. *Angewandte Chemie International Edition*, 55(17):5166–5169, March 2016.

[217] Daiki Nishiguchi, Junichiro Iwasawa, Hong-Ren Jiang, and Masaki Sano. Flagellar dynamics of chains of active janus particles fueled by an AC electric field. *New Journal of Physics*, 20(1):015002, January 2018.

[218] Junichiro Iwasawa, Daiki Nishiguchi, and Masaki Sano. Algebraic correlations and anomalous fluctuations in ordered flocks of janus particles fueled by an ac electric field. *Phys. Rev. Research*, 3:043104, Nov 2021.

[219] Jie Zhang, Ricard Alert, Jing Yan, Ned S. Wingreen, and Steve Granick. Active phase separation by turning towards regions of higher density. *Nature Physics*, 17(8):961–967, May 2021.

[220] John C. Crocker and David G. Grier. Methods of digital video microscopy for colloidal studies. *Journal of Colloid and Interface Science*, 179(1):298–310, Apr 1996.

[221] Stephen M. Anthony, Minsu Kim, and Steve Granick. Single-particle tracking of janus colloids in close proximity. *Langmuir*, 24(13):6557–6561, June 2008.

[222] Benjamin Thirey and Randal Hickman. Distribution of euclidean distances between randomly distributed gaussian points in n-space. *Department of Mathematical Sciences United States Military Academy, West Point*, 08 2015.

[223] Dóra Bárdfalvy, Henrik Nordanger, Cesare Nardini, Alexander Morozov, and Joakim Stenhammar. Particle-resolved lattice boltzmann simulations of 3-dimensional active turbulence. *Soft Matter*, 15(39):7747–7756, 2019.

[224] Zaiyi Shen, Alois Würger, and Juho S. Lintuvuori. Hydrodynamic interaction of a self-propelling particle with a wall. *The European Physical Journal E*, 41(3):39, March 2018.

[225] Livio Nicola Carenza, Giuseppe Gonnella, Antonio Lamura, Giuseppe Negro, and Adriano Tiribocchi. Lattice boltzmann methods and active fluids. *The European Physical Journal E*, 42(6):81, June 2019.

[226] B. B. Laud. *Electromagnetics*. J. Wiley, New York, 1987.

[227] Davide Thambithurai, Jack Hollins, Travis Van Leeuwen, Anita Rácz, Jan Lindström, Kevin Parsons, and Shaun S. Killen. Shoal size as a key determinant of vulnerability to capture under a simulated fishery scenario. *Ecology and Evolution*, 8(13):6505–6514, June 2018.

Acknowledgements

I would like to thank Dirk first and foremost. He has provided me with, maybe not intentionally at first, a unique opportunity and has propped my studies up to achieve what is not meant to be possible despite many difficulties and changes.

Then comes Adam, the office buddy I didn't know I needed. He has shown me that I have no need to doubt myself and has been a source of inspiration and solidarity in my work.

The rest of the Oxford Colloid Group have also been of great help. They remained welcoming and open despite my regular absence. I give special thanks to Carla, Nick, Taiki and Roel who on top of creating a pleasant atmosphere for me were always helpful. I can't remember the number of times I bothered Arran for help and he delivered.

I would like to thank Paco, Chantal and the rest of my Madrid based collaborators who have given their experienced eye over my work when it was needed.

I would like to thank Christ Church for keeping me around for so long and the department for the whole experience.

These things can't be done without family. I would like to put my brother forward for the best brother anyone could ask for award and my parents for the best support award.